Zwitterionic Phosphorylcholine Polymer-Supported Ionic Liquid Gel Electrolytes

A dissertation submitted by

Mossab Khalid A Alsaedi

in partial fulfillment of the requirements for the degree of

Doctor of Philosophy

in

Chemical Engineering and Materials Science and Engineering

Tufts University

February 2026

Advisor: Professor Matthew J. Panzer

© 2026, Mossab Khalid A Alsaedi

Abstract

Energy storage devices, such as batteries, are ubiquitous. They are found in electric vehicles, airplanes, and portable electronics, to name a few. One aspect of battery research that has been of major importance is battery safety, especially in applications where batteries could directly impact users. A battery's electrolyte, which is an ionically-conductive and electronically-insulating medium that connects the cathode to the anode, is one component where safety could be improved. Most conventional batteries have electrolytes that are liquids, such as propylene carbonate (PC) and ethylene carbonate (EC), which could leak, and, in the case of PC and EC, are flammable. Researchers have investigated replacing liquid electrolytes with solid ones to eliminate the risk of leakage, but solid electrolytes have poor ionic conductivity compared to liquid ones. This dissertation looks at developing gels, which are part liquid and part solid, as electrolytes. Using gels as electrolytes combines liquid-like ionic conductivity and solid-like mechanical robustness.

This dissertation specifically looks at ionic liquid-based gels, also known as *ionogels*, that contain a zwitterionic polymer as its solid phase. Ionic liquids, being thermally stable and having a higher decomposition temperature threshold, eliminate the safety concerns with current liquid electrolytes. Zwitterionic polymers, having positively and negatively charged moieties, introduce solid scaffolds that provide mechanical integrity without compromising ionic conductivity via favorable ion-ion interactions. The mechanical, electrochemical, and ionic-transport properties of these gels are analyzed via a suite of characterization techniques, including electrochemical impedance spectroscopy (EIS), dynamic mechanical analysis (DMA), Raman spectroscopy, and pulsed field gradient nuclear magnetic resonance (PFG NMR).

Acknowledgements

This dissertation is the final milestone of my Ph.D. journey and is the result and culmination of years of scientific discussions, experiments, and research. This dissertation would not have come to full fruition without the support of many individuals.

Firstly, I want to thank my Ph.D. advisor and mentor, Professor Matthew J. Panzer, for all the guidance and support he has provided me with throughout my studies at Tufts. During one of our conversations in my early years as a Ph.D. student, he mentioned that one of the main reasons he became a professor was that he wanted to be able to train students to think independently and become independent researchers. I admire such approach to mentoring graduate students, and I commend him for it. He taught me how to develop scientific intuition and how to approach scientific and engineering problems with a science fundamentals-oriented mindset; stripping complex problems down to the basic scientific principles they are based on, then building up from there to reach the solution. Most importantly, he showed me that one can be a professor and possess deep knowledge in and understanding of one's field and still be humble, friendly, and approachable. Our biweekly one-on-one research update meetings sometimes felt like casual conversations where we discussed science.

I would also like to thank Professor Sameer Sonkusale, whose lab I worked in during the first couple of years of my studies at Tufts. During my time under Professor Sonkusale's wing, I came to appreciate his creativity and approach to problem solving. He showed me that science and engineering are fun, and even more fun when we think outside the box. I will always fondly remember our meetings in which we brainstormed multiple ways to tackle research problems. And I will always appreciate his mindset towards scientific research; no specific type of research is

better than other types of research, we are all trying to push the boundaries of our respective fields, and for that we should all be commended.

I want to also extend my gratitude to my thesis committee members, Professor Ayse Asatekin, Professor Jeffrey Guasto, and Professor Lauren Marbella for all their feedback and suggestions throughout my Ph.D. research journey. Professor Asatekin was one of the first professors to reach out to me when I first got admitted into the ChBE Ph.D. program at Tufts with a heartwarming email welcoming me into the department. She was also an integral part of my Ph.D. as she is a polymers expert whose office door was always open for me to barge through whenever I had questions or wanted candy from the bucket of candy on her desk that seemingly never ran out. I want to thank Professor Guasto, who I was fortunate to meet by being one of the students in a course he taught at Tufts. Professor Guasto made me appreciate physical sciences and mathematics more and demonstrated how math can neatly and precisely explain physical phenomena we encounter in our daily lives. Throughout my Ph.D. journey, Professor Guasto was generous with his time, not only by being on my thesis committee, but also by offering me advice on post-Ph.D. endeavors and discussing my potential career options. I want to also thank Professor Marbella for always bringing up interesting and creative ideas pertaining to electrolyte research and advising me on how I could push my research to be more groundbreaking. I would also like to thank Professor Graham Leverick for training me on his lab's Raman spectrometer, for walking me through the tedious process of spectral deconvolution, for taking the time to look at my experimental data and discussing them with me, and for always being very nice and kind to me no matter how many questions I had or how many times I barged into his office unannounced.

I want to extend my heartfelt gratitude and appreciation to my mother Haifaa, my father Khalid, my sisters Ohoud and Najoud, my brother Faisal, my sister-in-law Shadin, my brothers-

in-law Abdulaziz and Mubarak, and my lovely nieces and nephew Haifaa, Basma, and Abdullah. I would not have been able to complete my Ph.D. without their unconditional and unwavering love and support. They have truly been my backbone during my life in the U.S. despite the distance.

I also want to thank my friends in my hometown of Riyadh, Saudi Arabia and in the Northeastern United States. Firstly, I want to thank my childhood best friend and graduate school roommate, Abdulrahman Nakshabandi, for all the support and for being a constant reminder of my roots and where I came from. I also want to extend my gratitude to my friends Salam Alabdullatif, Demetrios Stoukides, Michael Saad, Yasmeen Alfaraj, Sarah Alnegheimish, Moulay Zaidane Draidia, Briana Lino, Rebecca Hershman, Sean Williams, Faisal Alghariri, Abdallah Alazzaz, Baraa Bin Battal, Faisal Alzamil, Raed Hashem, Ibrahim Aldabbagh, Majid Alturki, Nibras Hijazi, Michael Lange, Igantius Alepede, Denis Nalbantov, Ashleigh Herrera, Pomai Yamaguchi, Ryan O'Hara, Karl Wieck, Ho Yi Lam, Bricker Like, Kritee Sangroula, Ebrahim Aljohani, Alejandra Herreros de Tejada, Abdullah Alomar, Yasmin Alkhowaiter, Mohammed Alsobay, Faisal Aldilaijan, Hessa Alyahya, Majid Aldohan, Abdullah Aljohani, Reyouf Almuhayya, Emad Alibrahim, Omar Sagga, Ibraheem Alsaab, Noura Islam, and Hanan Wali. Whether they were scientific discussions, long video calls, coffee and ice cream runs, or soccer scrimmages, they were all an integral part of my Ph.D. journey. To my friends in the Boston area, thank you for making Boston feel like home.

Dedication

I dedicate this dissertation to my beloved mother, Dr. Haifaa Alnasser. Thank you for instilling gratitude, integrity, and the principles of great work ethic in me from a young age. In the instances where you took me with you to work, I saw you treat your patients with care and tend to their needs with passion and saw how friendly you were to them. You will forever be my role model. Thank you for always supporting me and reminding me that nothing is difficult if I put my mind to it. Thank you for instilling in me the importance of and the appreciation for education. And lastly, thank you for passing down your old white coats to me whenever you received a fresh set when I was a kid, for trimming them down to fit me, and for allowing me to wear them in my bedroom pretending like I was in a lab. Because of that, I have always worn and will always wear my lab coats with a sense of pride and fulfillment, for I know that six-year-old Mossab would be over the moon to know that he would get to work in research labs for most of his twenties and more.

I also dedicate this dissertation to my late friend Mohammad Alshahrani. Mohammad was a cornerstone to my educational journey throughout college and graduate school. He was always supportive of my educational and professional endeavors and generous with his time and advice. He always celebrated my accomplishments, no matter how insignificant I thought they were. Mohammad championed my decision to apply to Ph.D. programs and supported my commitment to the Ph.D. program at Tufts. I am certain he would have been proud of this dissertation.

Table of Contents

Abstract…….. ii

Acknowledgements…… iii

Dedication…….. vi

Table of Contents…….. vii

List of Tables……. xii

List of Figures…… xvi

Chapter 1: Introduction…….. 1

1.1 Batteries for Energy Storage…….. 1

1.2 Ionic Liquids……... 4

1.3 Solid-State Electrolytes for Batteries…… 6

1.4 Zwitterions and Zwitterionic Polymer-Supported Ionic Liquid Electrolytes…… 7

1.5 Dissertation Outline……... 10

1.6 References…….. 12

Chapter 2: Experimental Methods and Characterization……..... 18

2.1 Sample Preparation……..... 18

2.1.1 UV-initiated in situ Free Radical Polymerization of Zwitterionic Monomers in Ionic Liquids (ILs)…….. 18

2.2 Electrical Characterization……..... 21

2.2.1 Alternating Current (AC) Electrochemical Impedance Spectroscopy (EIS)…… 21

2.2.2 Coin Cell Preconditioning, Direct Current (DC) Polarization, and Lithium Current Fraction……... 25

2.3 Spectroscopic Characterization…….. 29

2.3.1 Raman Spectroscopy…… **29**

2.4 Mechanical Characterization…… **33**

2.4.1 Compression Testing…… **33**

2.5 References…….. **35**

Chapter 3: Zwitterionic Polymer Ionogel Electrolytes Supported by Coulombic Cross-Links: Impacts of Alkali Metal Cation Identity…….. **37**

3.1 Abstract……..... **38**

3.2 Introduction…… **38**

3.3 Methods…….. **43**

3.3.1 Materials……..... **43**

3.3.2 Ionic Liquids Electrolyte (ILE) Preparation……..... **43**

3.3.3 Ionogel Preparation…….. **44**

3.3.4 Dynamic Mechanical Analysis (DMA)……..... **45**

3.3.5 Ionic Conductivity Measurements……..... **46**

3.3.6 Molecular Dynamics Simulations……..... **46**

3.3.7 Radial Distribution Functions…….. **47**

3.4 Results and Discussion…….. **48**

3.5 Conclusions…… **62**

3.6 Author Contribution and Acknowledgements…….. **62**

3.7 References…….. **63**

Chapter 4: Understanding the Effects of Li^+ Salt Concentration and Zwitterion/Li^+ Stoichiometry on Ion Coordination in Zwitterionic Polymer-Supported Ionogel Electrolytes…….. **68**

4.1 Abstract……..... **69**

4.2 Introduction…… **70**

4.3 Experimental Methods……... **72**

4.3.1 Materials……... **72**

4.3.2 LiTFSI/BMP TFSI Solution Preparation……... **72**

4.3.3 Ionogel Precursor Solution Preparation…….. **73**

4.3.4 Total Ionic Conductivity Measurements…….. **73**

4.3.5 Ionogels for Mechanical Analysis……... **74**

4.3.6 Raman Spectroscopy…… **75**

4.4 Results and Discussion……... **76**

4.5 Conclusions…… **88**

4.6 Author Contribution and Acknowledgements……... **89**

4.7 References……... **89**

Chapter 5: The Role of Li^+ Ions in Polyzwitterionic Ionogels: a Gelator or Mobile Charge Carrier?..... **95**

5.1 Abstract……... **96**

5.2 Introduction…… **96**

5.3 Materials and Methods……... **101**

5.3.1 Materials……... **101**

5.3.2 Ionogel Preparation…….. **101**

5.3.3 Dynamic Light Scattering (DLS)…….. **102**

5.3.4 Ionic Conductivity…… **103**

5.3.5 NMR Spectroscopy and Pulsed-Field Gradient NMR (PFG NMR)…….. **103**

5.3.6 Raman Spectroscopy…… **104**

5.3.7 Dynamic Mechanical Analysis…… **105**

5.4 Results and Discussion…….. **105**

5.4.1 In Situ Polymerization and Molecular Weight……... **105**

5.4.2 Ionic Conductivity…… **108**

5.4.3 Diffusion Coefficients of the Constituents…….. **110**

5.4.4 Li^+ Ion Apparent Transference Number…….. **112**

5.4.5 ^7Li NMR Spectra and Spin-Spin Relaxation Rates…… **115**

5.4.6 Raman Spectroscopy…… **117**

5.4.7 Dynamic Mechanical Analysis (DMA)……... **121**

5.4.8 Discussion of Li^+ Sites…….. **123**

5.4.9 Implications for Transport……... **130**

5.5 Conclusions…… **131**

5.6 Author Contribution and Acknowledgements…….. **132**

5.7 References…….. **132**

Chapter 6: Future Work…… **139**

6.1 Characterizing the Solid-Electrolytes Interphase (SEI) Layer…… **139**

6.2 Non-Ionic Liquid-Based Polyzwitterion-Containing Gel Electrolytes…… **144**

6.3 Non-Polymerizable Zwitterionic Phosphorylcholine Molecules in Lithium-Containing Ionic Liquid-Based Electrolytes…… **148**

6.4 References…….. **153**

Appendix A: Supplementary Information Concerning Chapter 3…….. **155**

Appendix B: Supplementary Information Concerning Chapter 4…….. **192**

Appendix C: Supplementary Information Concerning Chapter 5…….. **205**

Appendix D: Smart Sensing Flexible Sutures for Glucose Monitoring in House Sparrows…… **222**

Appendix E: Supplementary Information Concerning Appendix D……..... **254**

Appendix F: Soft Injectable Sutures for Dose-Controlled and Continuous Drug Delivery…….. **258**

Appendix G: Supplementary Information Concerning Appendix F……..... **287**

List of Tables

Table 5.1. Stokes diameter and polydispersity index measured by dynamic light scattering for dissolved p(MPC) extracted from polymer/LiTFSI-in-IL samples of varying composition.

Table 5.2. Collection of resulting parameters, detailing the distribution of Li^+ on different sites as a function of p(MPC) content.

Table 6.1. I_0, I_{ss}, and I_{ss}/I_0 as a function of mol MPC / mol Li^+ for 0.5 M, 1 M, and 2 M salt concentration ionogels.

Table A.1. Simulation details for LiTFSI single-salt ionogel precursor solutions at different MPC weight percentage values (W_{MPC}).

Table A.2. Simulation details for NaTFSI single-salt ionogel precursor solutions at different MPC weight percentage values (W_{MPC}).

Table A.3. Simulation details for NaTFSI and LiTFSI (equimolar) mixed-salt ionogel precursor solutions at different MPC weight percentage values (W_{MPC}).

Table A.4. Atom type, Lennard-Jones parameters, and partial charges for MPC. Dashes indicate that the value from the previous line is repeated.

Table A.5. Atom type, Lennard-Jones parameters, and partial charges[19, 20] for $TFSI^-$. Dashes indicate that the value from the previous line is repeated.

Table A.6. Atom type, Lennard-Jones parameters, and partial charges[19, 20] for BMP^+. Dashes indicate that the value from the previous line is repeated.

Table A.7. Atom type, Lennard-Jones parameters, and partial charge for Li^+.

Table A.8. Equilibrium bond lengths and spring constants for MPC. Dashes indicate that the value from the previous line is repeated.

Table A.9. Equilibrium bond lengths and spring constants[19, 20] for $TFSI^-$.

Table A.10. Equilibrium bond lengths and spring constants[19, 20] for BMP^+.

Table A.11. Equilibrium bond angles and spring constants for MPC.

Table A.12. Equilibrium bond angles and spring constants[19, 20] for $TFSI^-$.

Table A.13. Equilibrium bond angles and spring constants[19, 20] for BMP^+.

Table A.14. Ryckaert-Bellemans dihedral potential constants for MPC. Dashes indicate that the value from the previous line is repeated.

Table A.15. Fourier dihedral potential[19, 20] constants for BMP^+ and $TFSI^-$. Dashes indicate that the value from the previous line is repeated.

Table A.16. Improper dihedral constants.

Table B.2. Calculated polymer volume fraction values based on experimental measurements of salt solution and ionogel densities via Eq. 4.2.

Table B.3. Molar compositions of ionic species in LiTFSI/BMP TFSI salt solutions (1 L basis) and calculated Li^+ coordination numbers (with $TFSI^-$).

Table B.4. Molar compositions of ionic species in 0.5 M LiTFSI/BMP TFSI salt solution and ionogels (1 L solution basis) and calculated Li^+ coordination numbers (with $TFSI^-$).

Table B.5. Molar compositions of ionic species in 1 M LiTFSI/BMP TFSI salt solution and ionogels (1 L solution basis) and calculated Li^+ coordination numbers (with $TFSI^-$).

Table B.6. Molar compositions of ionic species in 2 M LiTFSI/BMP TFSI salt solution and ionogels (1 L solution basis) and calculated Li^+ coordination numbers (with $TFSI^-$).

Table C.1. Molar ratios of different constituents (MPC, Li^+, and $TFSI^-$) for varying weight percent of p(MPC).

Table C.2. Integral ratios of the Raman peaks obtained through spectral deconvolution, quantifying the coordinated fraction of anions and coordination numbers resulting from Eq. (C.3).

List of Figures

Figure 1.1. Schematic of an operating Li-ion battery with its typical components.

Figure 1.2. A table showing the glass transition temperature, melting temperature, ionic conductivity (at 20 and 90 ^{o}C), molar conductivity (at 20 and 90 ^{o}C), and decomposition temperature of ILs, Li-containing ILs, and Li salts.

Figure 1.3. Illustration of the different ways zwitterions could improve electrolyte properties. Figure is an illustration and does not satisfy charge neutrality.

Figure 2.1. Precursor solution preparation and characterization method-specific molds (pre-polymerization)

Figure 2.2. A phase angle-frequency plot for an ionogel from Chapter 3.

Figure 2.3. A 12-well PTFE board. Each well has gold pins connected to wires. This board is used to test room temperature ionic conductivity.

Figure 2.4. Chronoamperometry curve (current with respect to time) for a 7 wt. % MPC ionogel under 80 mV DC polarization. The I_{ss}/I_o value for this ionogel is 0.11.

Figure 2.5. Coin cell assembly with the electrolyte in Whatman separator between lithium discs and stainless-steel current collectors.

Figure 2.6. Raman spectrum for a Li^+-containing ionic liquid sample (from Chapter 4).

Figure 2.7. An ionogel in a glass vial for Raman spectroscopy.

Figure 2.8. Vial containing ionogel in sample holder inside Raman spectrometer.

Figure 2.9. A typical stress-strain curve of an ionogel that is compressed to 15% strain. The elastic modulus of this ionogel is ~2500 kPa which was calculated by fitting a line through the curve from 4% to 10% strain.

Figure 3.1. (a) Chemical structures of the zwitterionic monomer, 2-methacryloyloxyethyl phosphorylcholine (MPC), and the ionic liquid ions, 1-butyl-1-methylpyrrolidinium (BMP^+) and bis(trifluoromethylsulfonyl)imide ($TFSI^-$). (b) Schematic illustrations of: an MPC monomer/ionic liquid electrolyte ion cluster centered around an alkali metal cation (Li^+ or Na^+) within the ionogel precursor solution (top); the post-UV photopolymerization poly(MPC) ionogel scaffold that is supported by Coulombic, alkali metal cation-mediated cross-links between polymer chains (bottom).

Figure 3.2. (a) Room temperature ionic conductivity values of poly(MPC)-supported ionogels synthesized in situ using 0.5 M LiTFSI in BMP TFSI ("Li^+"), 0.5 M NaTFSI in BMP TFSI ("Na^+"), or 0.5 M LiTFSI:NaTFSI (1:1 molar mixture) in BMP TFSI ("1:1 mix"). Neat ILE conductivity values for each electrolyte are shown at 0 wt.% poly(MPC) content. Values displayed are an

average of 3 samples, with error bars indicating one standard deviation. (b) Normalized ionic conductivity values for the same ionogels (relative to the ionic conductivities of their base ILEs).

Figure 3.3. (a) Elastic modulus values of poly(MPC)-supported ionogels synthesized *in situ* using 0.5 M LiTFSI in BMP TFSI ("Li^+") or 0.5 M NaTFSI in BMP TFSI ("Na^+"). (b) Elastic modulus values of ionogels with low poly(MPC) contents for Li^+, Na^+, or 0.5 M LiTFSI:NaTFSI (1:1 molar mixture) in BMP TFSI ("1:1 mix") ILE. Values displayed are an average of 3 samples, with error bars indicating one standard deviation.

Figure 3.4. Radial distribution functions calculated for (a) Li^+ and ZI[-] and (b) Na^+ and ZI[-] at five different weight percentages of MPC monomer (W_{MPC}) in the single-salt ionogel precursor solutions. ZI[-] represents the anionic portion (PO_4^-) of the MPC molecule.

Figure 3.5. Radial distribution functions calculated for (a) Li^+ and $TFSI^-$, and (b) Na^+ and $TFSI^-$ at five different weight percentages of MPC monomer fraction (W_{MPC}) in the single-salt ionogel precursor solutions.

Figure 3.6. Number of clusters versus cluster size calculated for precursor solutions containing different weight percentages of MPC monomers (W_{MPC}): (a) 3 wt.%, (b) 6 wt.%, (c) 8 wt.%, (d), 11 wt.%, and (e) 13 wt.%. ZI[-] and X^+ represent the anionic portion (PO_4^-) of the MPC molecule and the alkali metal ion(s), respectively.

Figure 3.7. Schematic illustration showing the qualitative difference between the simulated alkali metal cation–MPC cluster sizes within ionogel precursor solutions, which lead to different experimentally-observed ionogel elastic modulus values: (a) Li^+ only ILE, (b) Na^+ only ILE.

Figure 4.1. Room temperature (25 °C) total ionic conductivity values of 0.5 M, 1 M, and 2 M LiTFSI/BMP TFSI solutions and their pMPC-supported ionogels. **(a)** Total ionic conductivity plotted versus pMPC wt.%. **(b)** Normalized total ionic conductivity (with respect to the salt solution value) plotted versus pMPC wt.%. **(c)** Total ionic conductivity plotted versus the molar ratio of zwitterionic monomer repeat units to lithium cations (mol MPC/mol Li^+). **(d)** Normalized total ionic conductivity plotted versus the MPC/Li^+ molar ratio.

Figure 4.2. Characteristics of noncovalently cross-linked pMPC ionogel networks. (a) Elastic modulus, (b) cross-link density, and (c) estimated percentage of non-cross-linked Li^+ cation values.

Figure 4.3. Raman spectra of liquid electrolyte and ionogel samples. (a) Neat BMP TFSI, 0.5 M, 1 M, and 2 M LiTFSI/BMP TFSI solutions. (b) 0.5 M LiTFSI solution and ionogels, (c) 1 M LiTFSI solution and ionogels, and (d) 2 M LiTFSI solution and ionogels. Ionogels were created from each LiTFSI solution at 0.25, 0.5, and 0.75 mol MPC/mol Li^+.

Figure 4.4. Percentage of total $TFSI^-$ anions coordinating with either BMP^+ or Li^+, calculated from deconvoluted Raman spectra. (a) Neat BMP TFSI, 0.5 M, 1 M, and 2 M LiTFSI/BMP TFSI solutions. (b) 0.5 M LiTFSI solution and ionogels, (c) 1 M LiTFSI solution and ionogels, and (d) 2 M LiTFSI solution and ionogels.

Figure 4.5. Number of $TFSI^-$ anions coordinating per Li^+ cation (Li^+ coordination number) calculated for LiTFSI solutions and ionogels, plotted as a function of either: (a) pMPC wt.%, or (b) MPC/Li^+ molar ratio.

Scheme 5.1. Structures of the main electrolyte components (top) and illustration of different Li^+ species within a p(MPC)-supported ionogel: bridging Li^+ that acts as noncovalent cross-linker between ZI units, non-bridging Li^+ coordinated to a single ZI unit, and mobile Li^+ in solution (bottom).

Figure 5.1. Total ionic conductivity at room temperature (25 °C) as a function of p(MPC) wt %.

Figure 5.2. (a) Self-diffusion coefficients of the nuclei (^1H, ^{19}F, ^7Li) obtained from PFG-NMR at room temperature (25°C) as function of p(MPC) content. (b) Activation energies of diffusion as a function of p(MPC) content measured over a temperature range of 25-65°C. The dotted lines are merely guides to the eye.

Figure 5.3. Li^+ ion apparent transference number as function of p(MPC) content.

Figure 5.4. (a) ^7Li NMR spectra, (b) peak integral, (c) line width, and (d) ^7Li spin-spin relaxation rate R_2 determined by a stimulated echo sequence (black) and R_2^* determined by linewidth analysis (red star) for 1M LiTFSI/BMP TFSI solution (0 wt % p(MPC)), 2 wt % p(MPC) solution, and 4-8 wt % p(MPC) free-standing ionogels.

Figure 5.5. (a) Raman spectra and (b) Li^+ coordination number (coordinated anions per Li^+) as extracted from the fraction of coordinated anions in dependence on p(MPC) content. The green dotted line in a) marks the position of the band of coordinated $TFSI^-$ and the black arrow represents the increase in p(MPC) content from 2 wt % (green spectrum) to 14 wt % (dark blue).

Figure 5.6. (a) Elastic modulus values for ionogels containing 4 to 14 wt % p(MPC). (b) Calculated cross-link density within the ionogels, representing the number of Li^+ ion-mediated noncovalent cross-links per nm^3, and (c) the corresponding fraction of Li^+ that is not participating in noncovalent cross-links.

Figure 5.7. (a) Distribution of Li^+ in different sites; (b) – (d) Li^+ coordination scenarios at 0, 8, and 14 wt % p(MPC), showing free, immobilized, and cross-linking Li^+ ions. For a legend of the symbols, see Scheme 1. Note that the MPC:Li^+ molar ratio and number of coordinating anions are shown according to scale, while the total number of IL cations and anions is not to scale to enhance clarity.

Figure 6.1. I_{ss}/I_0 for 0, 0.25, 0.5, and 0.75 mol MPC / mol Li^+ in 0.5 M, 1 M, and 2 M LiTFSI in BMP TFSI salt solution.

Figure 6.2. Chemical structure of gamma-valerolactone (GVL) (left) and propylene carbonate (PC) (right).

Figure 6.3. Total ionic conductivity for 1, 2, and 4 m LiTFSI/GVL solutions.

Figure 6.4. Chemical structure of L-alpha-Glycerylphosphorylcholine (α-GPC).

Figure 6.5. a) Ionic conductivity and b) normalized ionic conductivity of α-GPC-containing electrolytes with different LiTFSI/BMP TFSI concentrations (0.5 M, 1 M, and 2 M).

Figure 6.6. The ionic conductivity of pMPC ionogels and α-GPC-containing LiTFSI/BMP TFSI solutions in a) 0.5 M, b) 1 M, and c) 2 M LiTFSI/BMP TFSI solution concentrations.

Figure A.1. Photographs of NaTFSI solutions prepared in BMP TFSI at 0.5 M (left) and 1 M (right). White oblong object is a stir bar.

Figure A.2. (a) Natural logarithm of ionic conductivity plotted as a function of inverse absolute temperature for 5 wt.% and 10 wt.% poly(MPC) single salt ionogels. (b) Apparent activation energy of ionic conductivity values measured for Li^+ and Na^+ ILEs (0 wt.% poly(MPC)), as well as the 5 wt.% poly(MPC) and 10 wt.% poly(MPC) single salt ionogels.

Figure A.3. Top series: photographs showing (a) 3 wt.% MPC monomer in neat BMP TFSI (white oblong object is a stir bar), and (b) post-photopolymerization specimen of the same 3 wt.% MPC in neat BMP TFSI, vial inverted. The opacity of both samples indicates the poor solubility of MPC and poly(MPC) in neat ionic liquid, in the absence of alkali metal salt. Bottom image: (c) photograph of representative 5 wt.% poly(MPC)-supported ionogels containing 0.5 M NaTFSI (left, Na^+) or 0.5 M LiTFSI (right, Li^+). The freestanding, transparent ionogels were synthesized in cylindrical-shaped molds, then removed.

Figure A.4. Atom naming scheme for (a) MPC, (b) BMP^+ and (c) $TFSI^-$ molecules.

Figure A.5. Number of clusters in ionogel precursor solutions as a function of weight percentages of MPC monomers (W_{MPC}) for cluster sizes of (a) 2, (b) 3, (c) 4 and (d) 5. ZI[-] and X^+ represent the anionic portion of the MPC molecule and the alkali metal ion(s), respectively.

Figure A.6. The alkali metal cation-MPC intermittent association lifetimes, $\tau_c^{X^+ - MPC}$ in (a) single- and (b) 1:1 mixed-salt ionogel precursor solutions.

Figure A.7. Molecular dynamics (MD) snapshots of Li^+ only system simulation boxes with increasing mass fraction of MPC monomer, W_{MPC}. MPC molecules (orange) and Li^+ ions (purple) are displayed in the simulation snapshots. The ionic liquid ions, BMP^+ and $TFSI^-$, have been removed from the snapshots for ease of viewing MPC and Li^+.

Figure A.8. Molecular dynamics (MD) snapshots of Li^+ only system simulation boxes with increasing mass fraction of MPC monomer, W_{MPC}. MPC molecules (orange) and Na^+ ions (green) are displayed in the simulation snapshots. The ionic liquid ions, BMP^+ and $TFSI^-$, have been removed from the snapshots for ease of viewing MPC and Na^+.

Figure A.9. Molecular dynamics (MD) snapshots of 1:1 mixed Li^+/Na^+ system simulation boxes with increasing mass fraction of MPC monomer, W_{MPC}. MPC molecules (orange), Li^+ ions (purple), and Na^+ ions (green) are displayed in the simulation snapshots. The ionic liquid ions, BMP^+ and $TFSI^-$, have been removed from the snapshots for ease of viewing MPC, Li^+, and Na^+.

Figure B.1. Elastic modulus values of ionogels prepared using 0.5 M, 1 M, and 2 M LiTFSI/BMP TFSI solutions plotted versus pMPC wt.%.

Figure B.2. Raman spectra for an equivolume mixture of IL (BMP TFSI) with methanol (MeOH) (black curve) and for a 5 wt. % pMPC solution prepared in the same equimolar mixture via UV-initiated *in situ* free radical polymerization (red curve). Methanol was used here to adjust the solvent quality in order to dissolve the MPC monomer, which is not soluble in the neat BMP TFSI ionic liquid.

Figure B.3. Deconvoluted Raman spectra showing the BMP^+-coordinated $TFSI^-$ and Li^+-coordinated $TFSI^-$ sub-peaks for: **a)** BMP TFSI, **b)** 0.5 M LiTFSI/BMP TFSI solution, **c)** 1 M LiTFSI/BMP TFSI solution, and **d)** 2 M LiTFSI/BMP TFSI solution.

Figure B.4. Deconvoluted Raman spectra showing the BMP^+-coordinated $TFSI^-$ and Li^+-coordinated $TFSI^-$ sub-peaks for ionogels prepared from a 0.5 M LiTFSI/BMP TFSI solution containing: **a)** 0.25 mol MPC/mol Li^+ , **b)** 0.5 mol MPC/mol Li^+, and **c)** 0.75 mol MPC/mol Li^+.

Figure B.5. Deconvoluted Raman spectra showing the BMP^+-coordinated $TFSI^-$ and Li^+-coordinated $TFSI^-$ sub-peaks for ionogels prepared from a 1 M LiTFSI/BMP TFSI solution containing: **a)** 0.25 mol MPC/mol Li^+ , **b)** 0.5 mol MPC/mol Li^+, and **c)** 0.75 mol MPC/mol Li^+.

Figure B.6. Deconvoluted Raman spectra showing the BMP^+-coordinated $TFSI^-$ and Li^+-coordinated $TFSI^-$ sub-peaks for ionogels prepared from a 2 M LiTFSI/BMP TFSI solution containing: **a)** 0.25 mol MPC/mol Li^+ , **b)** 0.5 mol MPC/mol Li^+, and **c)** 0.75 mol MPC/mol Li^+.

Figure B.7. Percentage of total $TFSI^-$ anions that are coordinating with Li^+ cations in the LiTFSI/BMP TFSI solutions plotted versus Li^+ concentration. Extrapolation of the best-fit linear regression to the data through the origin (equation shown) predicts 100% of the $TFSI^-$ anions will be Li^+-coordinated for a LiTFSI concentration of approximately 2.7 M.

Figure C.1. ^1H NMR spectra of the dissolved p(MPC) ionogels in D_2O. The lack of peaks related to the CH_2=CH- bonds between 5-6 ppm indicates the full conversion of p(MPC).

Figure C.2. Temperature dependent diffusion coefficients for ^1H and ^{19}F for the different compositions of p(MPC) varying from 2 wt % p(MPC) to 14 wt % p(MPC). Data points: Experimental values, solid lines: Arrhenius fits.

Figure C.3. (a) ^7Li spin-lattice relaxation rate R_1 determined by inversion recovery pulse sequence (b) Relaxation rate ratios for 1M LiTFSI/BMP TFSI solution (0 wt % p(MPC)), 2 wt % p(MPC) solution, and 4-8 wt % p(MPC) ionogels.

Figure C.4. Raman spectra of BMP TFSI, neat 1M LiTFSI/BMPTFSI solution, and ionogels containing varying wt % of p(MPC) in the spectral region between 700 cm^{-1} and 800 cm^{-1}. The blue and green lines are obtained by deconvolution by Voigt profiles where f_{TFSI^-} represents free $TFSI^-$ ions and c_{TFSI^-} represents the coordinated $TFSI^-$ ions.

Figure C.5. Ratio of diffusion coefficients D_+ of BMP versus D_- of TFSI, showing a slight loss of their coupling with increasing p(MPC) content.

Figure D.6. Sensor layers and characterization. **a)** A schematic showing a sensor's cross-section with conductive layers (gold and Prussian blue) and enzyme-immobilization layers (chitosan and glucose oxidase). Microscopic images of **b)** pristine Polysorb^{TM} suture (COVIDIEN 5-0), **c)** the suture coated with gold, and **d)** the suture coated with Prussian blue (blue arrows represent an order of coating sequence). **e)** A scanning electron microscopy (SEM) image of the gold-coated suture.

Figure D.2. FTIR spectra for **a)** gold-coated suture, **b)** Prussian blue-coated suture, and **c)** enzyme-polymer matrix-coated suture.

Figure D.3. a-d) bending a gold-coated suture to radii of curvature of 2.0, 1.5, and 1.0 cm from its original 3 cm length. **e)** normalized change in resistance as a function of radius of curvature. **f-i)** bending a glucose sensing suture (fully functionalized) to radii of curvature of 2.0, 1.5, and 1.0 cm from its original 3.0 cm length. **e)** Normalized change in resistance as a function of radii of curvature (n=3, multiple sensors) **j)** Current readout for two different glucose concentrations (0.10 mM and 0.30 mM) as a function of radius of curvature (n=3, multiple sensors).

Figure D.4 Sensor calibration and real-time glucose monitoring: a) Sensor calibration curve showing the change in current with changing glucose concentration in 1X PBS-based solution (n

= 4, one sensor). b) Real-time glucose sensing by monitoring the current as the glucose concentration was increased every ~10 minutes (0, 0.10, 0.20, then 0.30 mM glucose in 1X PBS).

Figure D.5. Sensor interference, repeatability, and stability tests. **a)** Sensor interference/selectivity test showing the change in current in 1X PBS and after the addition of 0.10 M glucose, 18.0 mM lactate, 18.0 mM NaCl, and 18 mM KCl (added sequentially with five-minute intervals). **b)** Sensor repeatability test showing the current read by the sensor in 0.62 mM glucose (first measurement), 36.4 mM glucose (first measurement), 0.62 mM glucose (second measurement), then 36.4 mM glucose (second measurement). (1) and (2) in the legend of **b** represent the first and the second measurement, respectively, obtained for each of the two glucose concentrations. **c)** Sensor stability showed as a comparison between the current read by the sensor for two glucose concentrations (0.62 and 3.71 mM glucose) on days one and five from sensor fabrication.

Figure D.6. Glucose monitoring in euthanized house sparrows (*Passer domesticus*) (n = 3, multiple sensors). Chronoamperometric measurements were obtained by a two-electrode system implanted in house sparrows for monitoring glucose. The concentration of glucose around the sensing region was changed by infusing 1X PBS-glucose solutions of known concentrations (x-axis) and the current was recorded after each infusion.

Figure E.1. Absorbance as a function of time for the electrodeposition of gold on a glass slide (one cycle) using the same procedure used to deposit gold on sutures.

Figure E.2. Energy dispersive spectroscopy (EDS) on gold-coated suture showing the presence of carbon, oxygen, and gold.

Figure E.3. Cyclic voltammetry (CV) plot for the deposition of Prussian blue onto the gold-coated suture. The redox peaks for Prussian blue are at 0.165 V and 0.145 V.

Figure F.7. a) Illustration and comparison of transdermal (microneedles and injectable) and dermal drug delivery platforms. Soft injectables are smart surgical sutures that are either loaded with the drug (method 1) or carry drug from a wearable reservoir into the skin (method 2). **b)** Illustration of suture-based drug-delivery wearable device. **c)** Table comparing hypodermic needles, microneedles, and soft injectable sutures. **d)** Wearable device delivering dye (rhodamine B) from drug reservoir to a skin model gel through a surgical suture.

Figure F.8. SEM images of **a)** polyester thread, **b)** polyester suture, **c)** cotton thread, and **d)** Polysorb^{TM} suture (scale bars = 300 μm). **e)** Water uptake of polyester thread, polyester suture, cotton thread, and Polysorb^{TM} suture (n=7).

Figure F.9. Qualitative assessment of drug release: release of rhodamine B dye (drug model) from polyester suture into agarose gel (skin model) and porcine skin. Pictured is a polyester suture **a)** before dye loading, **b)** after dye loading, and **c)** after complete release of dye (a-b scale bars = 0.4 mm). Images in **d** show the release of dye from a polyester suture in an agarose gel at different time points (scale bars = 2.5 cm). Images **g** and **f** pertain to the release of dye from a polyester suture that was brought to contact with the surface of the skin patch: images in **g** (scale bars = 0.5 cm) are top view images of the porcine skin patch at different time points and **f** is the cross-sectional image (UV-illuminated sideview) of the same porcine skin patch after 180 seconds. Images **g** and **h** pertain to the release of dye from a polyester suture that was inserted in a horizontal incision made in the center of the skin patch: images in **g** (scale bars = 0.5 cm) are top view images

of the porcine skin patch at different time points and **h** is the cross-sectional image (UV-illuminated sideview) of the same porcine skin patch after 180 seconds.

Figure F.10. Chemotherapeutic soft injectables. **a)** Release of 5-fluorouracil from polyester sutures of different lengths into 1X PBS (n=3). **b)** 5-FU release as percent of total amount of loaded onto 0.6, 6, and 60 into 1X PBS (n=3). **c)** Cell viability of HeLa cells 48 hours after incubating with bare and cancer-drug-loaded polyester sutures of different lengths. Ordinary one-way ANOVA was used for **c** (*** p value < 0.001, **** p value < 0.0001).

Figure F.5. Long-term continuous delivery. **a)** Schematic of experimental setup used to obtain results. Parafilm and deep eutectic solvent or DES based gelatin gel constitute the skin model. **b)** Images of gel on day 0, after 30 days, and after 63 days. **c)** Volume of rhodamine B delivered to gel by sutures of different conformations in the gel (straight and U-shaped, n=3) after 6 days. Unpaired t-test was used in **c** (* p value < 0.1). **d)** Volume of rhodamine B dye delivered from reservoir to gel by sutures in the span of 63 days (n=3).

Figure F.6. a) Cross-sectional view of the drug-delivery wearable device showing the upper and lower parts of the device, the O-ring, and the screw-lock assembly. **b)** Increase in mass of DES gelatin gel connected to delivery reservoir via polyester suture over a period of 66 hours. Images of DES gelatin gel connected to delivery reservoir via polyester suture at **c)** 0 hours and **d)** after 2 hours.

Figure G.1. a) Release profile of cresol red dye (drug model) from polystyrene threads of different lengths, b) qualitative assessment of total drug released from polystyrene threads of different lengths, c) color of thread before coating, after coating, and after dye release, d) correlation

between total drug released and different length of the thread. This figure was previously published by members of our group as part of a conference paper (H.R. Nejad, A. Sadeqi, and S. Sonkusale, The 24th International Conference on Miniaturized Systems for Chemistry and Life Sciences (μTAS 2020).[25]

Figure G.2. Microscopic images of cultured HeLa cells (dead cells circled in red) after 48 hours of incubation with a) a bare polyester suture and b) a drug-loaded suture.

Figure G.3. Experimental setup for long-term continuous delivery. Gelatin gel and parafilm constistute a skin tissue model. Acrylic disc offers physical support. Acrylic box prevents evaporation and contamination.

Figure G.4. Cross-section photos of the reservoir design (left) and the 3-D printed reservoir (right). Left image breakdown: yellow is the top part, pink is the lower part, and orange is the O-ring.

Figure G.5. Design of (left) and 3-D printed socket (right) in which the lower part of the reservoir is placed to facilitate wearing the device. For example, inserting a velcro strap will allow for wrapping the reservoir around the arm as shown in Figure F.1.

Figure G.6. Design cross-section of (left) and 3-D printed (right) lower part of the reservoir.

Figure G.7. Design of (left) and 3-D printed upper part of the device. The locking knob locks the reservoir by sliding in the locking slots in the lower part (visible in Fig. S6). The closing lid can be opened to refill the reservoir with desired drug.

Figure G.8. Design of (left) and 3D-printed part that goes into the inside of the upper part (Fig. S7) that gets in contact with the lower part and holds the O-ring from the top.

Figure G.9. Locking knobs and slots that keep the reservoir sealed. The knobs slide into the slots by physically rotating the top and bottom part in opposite angular directions. This locks the reservoir in place.

Figure G.10. Design of the needle guide placed upright for clarity. The surface facing the skin is on the left.

Figure G.11. A close-up of the needle holding compartment in the needle guide.

Figure G.12. 3-D printed needle guide with a suture (green) and a curved needle.

Figure G.13. Reservoir assembly (left to right): Insert the none-needle suture end into the reservoir through the thread hole. Place and press the O-ring into the designated slot while ensuring the thread end is inside the inner wall. Close the reservoir. Then press and turn the upper part to lock and seal the reservoir.

Figure G.14. Procedure to administer the drug carrying suture using the Assist device: Using needle guide and piercing through skin (top left to bottom right): Place the needle in the needle guide and screw the bolt such that the needle is fixated. Place the needle guide at the correct height. Use the built-in skin level for a skin depth of 1 mm. Rotate the needle guide for the needle to pierce the skin. Once the needle resurfaces, unscrew the bolt and lift the upper lid with a pair of tweezers

(use the release slots to slide the tweezers in). The needle should now be free from the guide and can be grabbed with a needle holder and pulled. Pull the thread to the end such that there is no gap between the reservoir and the skin. The leftover thread can be cut, and the incision can be closed with a bandage. On the reservoir, the lid can be unscrewed, and, with a Teflon Filter, the reservoir can be filled with the desired drug. After filling, screw the lid back on.

Chapter 1: Introduction

1.1 Batteries for Energy Storage

There is an ever-increasing demand on energy due to the growing population and growing number of devices and machines that consume energy (electronics, vehicles, etc.). This increasing demand is coupled with an increasing reliance on renewable energy sources. In 2016, the global energy generation increased by 2.1%[1]. Almost half of that percentage is from renewable energy sources. For example, more communities are now being supplied by solar energy stored in grids. Also, electric vehicles are gradually replacing gasoline-powered ones. In 2016 also, there was a 40% increase in the electric vehicles market[1]. Therefore, the need to develop more efficient energy-storage devices, especially batteries, is essential. The increase in producing and consuming portable electronics has also been a key catalyst in the development of more efficient and environmentally sustainable batteries[2]. The development of Li-ion batteries (figure 1.1) in the late 20th century provided lightweight batteries with improved energy density[2]. In a Li-ion battery, Li^+ is stripped from the surface of the $LiCoO_2$ cathode during charging via oxidation, carried across the cell through the electrolyte, then plated onto the surface of the carbon anode via reduction. The discharging of the battery occurs in an opposite manner, where Li^+ is stripped off of the anode via oxidation and plated onto the cathode via reduction[3].

In general, batteries can be categorized in terms of chargeability as primary batteries or secondary batteries[2]. Primary batteries are ones that are not rechargeable, which can be found in remote controls and flashlights. Because primary batteries are one-time-use batteries, they produce waste upon disposal, which raises environmental concerns. Secondary batteries are ones that can

be charged, such as the batteries in phones, laptops, and electric vehicles. Li-ion batteries, for example, are secondary batteries.

One of the main components of a battery is its electrolyte. The electrolyte is an ionically conductive, but electronically insulating, medium that connects an anode and a cathode to each other. Electrolytes allow for ionic transport during charging/discharging. Therefore, the ionic conductivity of an electrolyte is an important parameter. In batteries that are widely used nowadays, such as Li-ion batteries, the electrolytes are liquid or liquid-like. Because organic liquid electrolytes, such as propylene carbonate and ethylene carbonate, are flammable, they are not particularly safe[4,5,6].

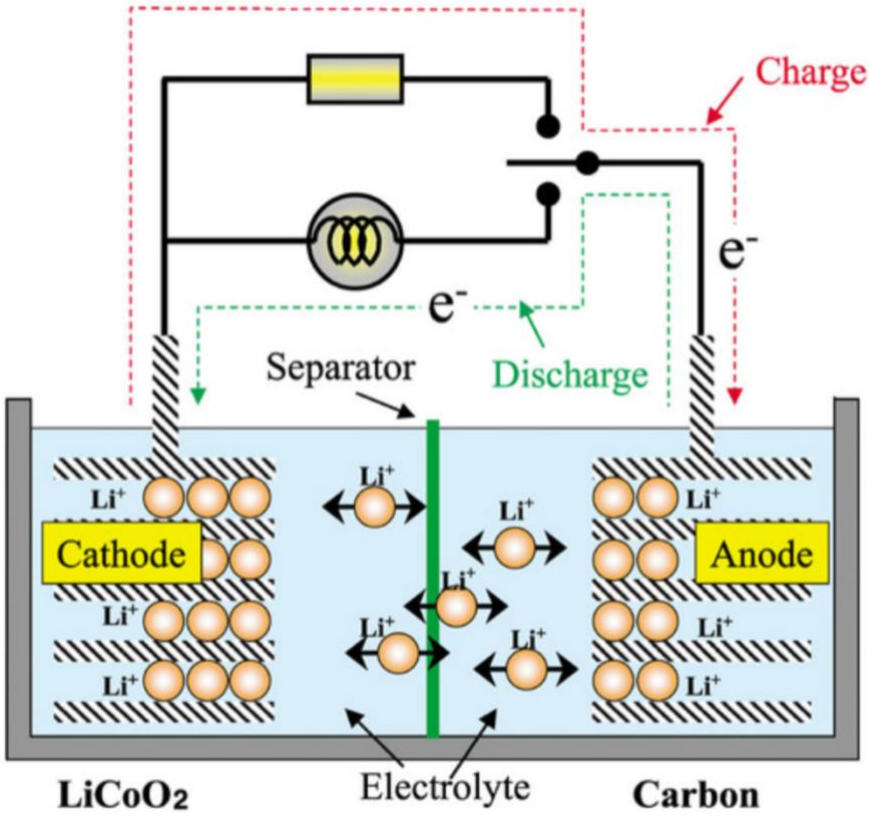


Figure 1.1. Schematic of an operating Li-ion battery with its typical components.

Reproduced from Nishi Y.[3]

1.2 Ionic Liquids

Ionic liquids (ILs) are a class of thermally stable materials[7,8] that are liquid at room temperature and melt below 100 ^{o}C[9]. ILs have high ionic conductivity and low volatility[10], making them suitable for battery applications. There are more than 1,000,000,000,000 possible ILs[8,11,12]. There are different combinations that could make up an IL by varying the species of the anions and the cations. For example, cations can be of the imidazolium, pyrrolidinium, or piperidinium families and anions can be bis(fluorosulfonyl)imide (FSI), bis(trifluoromethanesulfonyl)imide (TFSI), or hexafluorophosphate (PF_6^-)[8,13,14,15,16]. Organic solvents/diluents can also be added to ILs to enhance ionic transport[8,17,18], but their addition is counterproductive to the use of ILs at high temperatures[19]. Figure 1.2, which is a table from Kerner, M. *et al.*[8], shows some of the properties of ILs, Li-containing ILs, and Li salts[8]. Compared to organic solvent-based electrolytes, ILs have a higher threshold for their decomposition temperatures. While ILs address the flammability issue in battery electrolytes, they do not address the issue of potential leakage given that they are liquids.

Material	T_g [°C]	T_m [°C]	$\sigma_{20°C}$ [mS cm^{-1}]	$\sigma_{90°C}$ [mS cm^{-1}]	$\Lambda_{m\ 20°C}$ [S cm^2 mol^{-1}]	$\Lambda_{m\ 90°C}$ [S cm^2 mol^{-1}]	T_d [°C]
EMIFSI	—	−16	15.3	60.0	3.08	12.6	201
$Li_{0.1}EMI_{0.9}FSI$	−99	−29	6.6	27.0	1.27	5.43	178
$Li_{0.2}EMI_{0.8}FSI$	−97	−36	3.7	13.3	0.61	2.31	161
$LiTFSI_{0.1}EMIFSI_{0.9}$	−99	−28	4.6	17.1	0.90	3.50	211
$LiTFSI_{0.2}EMIFSI_{0.8}$	−92	−34	5.0	21.4	0.94	4.27	229
EMITFSI	−91	−18	5.3	23.5	1.38	6.39	302
$Li_{0.1}EMI_{0.9}TFSI$	−86	−22	2.8	12.9	0.68	3.32	288
$Li_{0.2}EMI_{0.8}TFSI$	−79	—	1.7	9.4	0.39	2.32	303
$LiFSI_{0.1}EMITFSI_{0.9}$	−88	−24	3.7	17.4	0.90	4.41	213
$LiFSI_{0.2}EMITFSI_{0.8}$	−87	—	2.6	13.2	0.58	3.14	199
LiFSI							160 315
LiTFSI							333

Figure 1.2. A table showing the glass transition temperature, melting temperature, ionic conductivity (at 20 and 90 °C), molar conductivity (at 20 and 90 °C), and decomposition temperature of ILs, Li-containing ILs, and Li salts.

Reproduced from Kerner, M. *et al.*[8]

1.3 Solid-State Electrolytes for Batteries

Incorporating solid materials in electrolytes has also been researched to eliminate safety concerns[6]. Solid-state electrolytes can fall under one of the following two categories: inorganic solid electrolytes and polymer electrolytes. Even though inorganic solid electrolytes offer high ionic conductivity at room temperature compared to organic liquid electrolytes, their rigidity gives rise to drawbacks, such as interfacial resistance and low ionic conductivity[6,20,21]. Such drawbacks can be resolved by realizing polymer electrolytes[6].

Polymer electrolytes can be further classified into three categories: solid-state polymer electrolytes (SPEs), gel polymer electrolytes (GPEs), and organic-inorganic composite polymer electrolytes (CPEs)[6,22]. Increasing ionic conductivity while maintaining solid-like mechanical integrity in electrolytes has been challenging[23]. Therefore, GPEs are particularly interesting as they combine liquid-like ionic transport with solid-like mechanical properties; they do not flow or leak, yet their large liquid fraction makes them highly conductive[24].

Using ILs as the liquid basis for a GPE results in an electrolyte that is thermally stable and mechanically robust. Such GPE would be typically called an ionogel[25,26,27,28]. An ionogel can be formed through different techniques. For example, polymerizing one of the ions of the IL can provide the polymeric scaffold of the ionogel[29,30,31,32]. Another method is incorporating nanoparticle-based scaffolds that are either polymeric or inorganic[33,34,35].

1.4 Zwitterions and Zwitterionic Polymer-Supported Ionic Liquid Electrolytes

Even though an ionogel can be mostly liquid, going from a fully-liquid electrolyte to a partially-liquid one means that there will be a reduction in ionic conductivity as the liquid fraction of the electrolyte is decreasing. One way to compensate for the reduction in liquid fraction is to select a solid scaffold that would interact with the IL in a way that would hinder the reduction of ionic conductivity, or in some cases, boost ionic conductivity.

Zwitterions (ZIs), which are molecules that have equal number of positive and negative charges[36], have been found to achieve that[24]. In addition to enhancing ionic conductivity, the incorporation of ZIs in battery electrolytes has shown to promote ion-cluster dissociation[37,38] due to the large dipole moments that arise from the presence of the positive and negative charges, and improve electrode/electrolyte interfacial stability[39,37,40, 41] and mechanical properties[36] (figure 1.3). ZI dopants and polyzwitterionic ionogels were also shown to enhance selective ion transport[42,39] and boost Li^+ diffusivity[37]. Polyzwitterionic scaffolds also provide favorable mechanical properties: increase noncovalent cross-links within a gel via Coulombic interactions between polymer chains[39,43,44] and alkali metal cation-mediated cross-links[45,24].

In 2005, Byrne *et al.* reported a boost in the diffusivity of Li^+ ions[37]. Using N-methyl-N-(butyl sulfonate)-pyrrolidinium (a zwitterion) and lithium bis(trifluoromethanesulfonyl)amide (LiTFSA) in N-methyl-N-propylpyrrolidinium bis(trifluoromethanesulfonyl)amide (P_{13}TFSA) (an ionic liquid), they were able to demonstrate enhanced Li^+ diffusivity via pulsed-field gradient nuclear magnetic resonance (PFG NMR) as well as improved solid-electrolyte interphase (SEI) layer via electrochemical impedance spectroscopy (EIS).

In 2010, Li *et al.* used MIm3S (a zwitterion) as an additive to an SPE that contained p(VdF-HFP) (a polymer) and $EMIBF_4$ (an ionic liquid) and demonstrated improved Li^+ transference, which is the fraction of current carried by Li^+)[42]. Furthermore, D'Angelo and Panzer in 2018 showed enhanced Li^+ transference in poly(MPC-co-SBVI) ionogels[39].

It is also hypothesized by Lee J. H. *et al*.[41] that having a zwitterionic polymer scaffold within an ionogel could enable the transport of Li^+ ions along the polymer by interacting with the zwitterionic moieties on the its backbone. In addition to enhanced transport, Li^+-mediated noncovalent cross-links between polymer chains within ionogels can also arise due to Li^+-ZI interaction[45]. These cross-links hold the gels together and contribute to their mechanical properties (elastic modulus).

Taylor *et al.*[46] reported in 2021 that strong Li^+-ZI interactions disrupt lithium salt ion clusters, which can be assessed by NMR (larger downfield ^7Li NMR peaks shifts indicate stronger interactions). They also reported that carboxybetaine- and phosphorylcholine-based zwitterionic monomers have larger peak shifts and greater Li^+ conductivity than sulfobetaine-based monomers, as the former have better solubility in LiTFS-containing conventional ionic liquids.

Although Li^+-based batteries are ubiquitous and Li^+-related properties for electrolytes are important, non-Li^+-containing batteries and electrolytes also exist. Sodium-ion batteries (SIBs) are a promising alternative to lithium-ion batteries because sodium and lithium are electrochemically similar and sodium is cheaper and more readily available than lithium.[47] One of the challenges that SIBs face is the mechanical damage and cracking the Sn-based electrodes undergo due to sodiation and desodiation.[48] ZI-based gel electrolytes could potentially overcome this challenge by providing a better interfacial contact at the electrode surface and minimizing the effects of the mechanical damage.

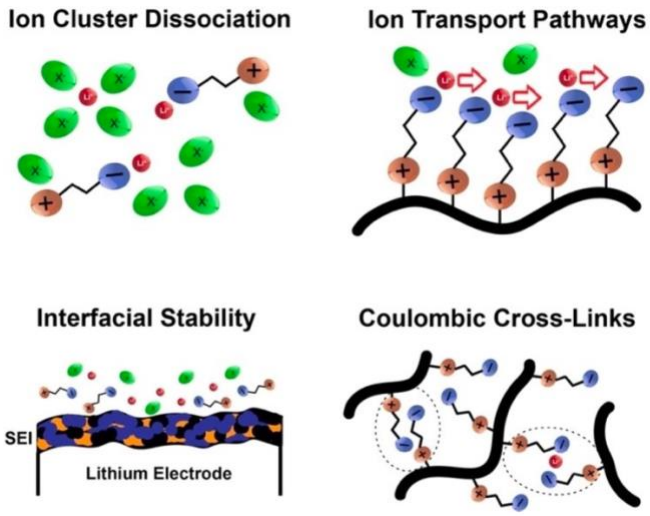


Figure 1.3. Illustration of the different ways zwitterions could improve electrolyte properties. Figure is an illustration and does not satisfy charge neutrality.

Reproduced from Alsaedi, M. K. *et al*.[36]

1.5 Dissertation Outline

Chapter 2 of this dissertation summarizes the experimental methods and characterization techniques used. Details pertaining to tools and equipment used and experimental processes are discusses. Chapter 2 includes an overview of UV-initiated *in situ* free radical polymerization, alternating current (AC) electrochemical impedance spectroscopy (EIS), coin cell preconditioning, direct current (DC) polarization, lithium current fraction calculation, Raman spectroscopy, and compression testing.

The studies in this dissertation – Chapters 3, 4 and 5 along with their appendices – all pertain to one type of ionogel electrolyte, which contains the following three components: poly(2-methacryloyloxyethyl phosphorylcholine) (pMPC), which is the polymer, 1-butyl-1-methylpyrrolidinium bis(trifluoromethylsulfonyl)imide (BMP TFSI), which is the ionic liquid, and lithium bis(trifluoromethylsulfonyl)imide (LiTFSI) and/or sodium bis(trifluoromethylsulfonyl)imide (NaTFSI), which are the lithium and sodium salts.

Chapter 3 looks at pMPC ionogels that are made with 0.5 M LiTFSI in BMP TFSI, 0.5 M NaTFSI in BMP TFSI, or a 0.5 M LiTFSI-NaTFSI in BMP TFSI. The pMPC weight percentage in the ionogels ranges from 0 (no polymer) to 15%. The Li only-containing ionogels exhibited different ionic conductivity and mechanical properties than the Na-containing ones. Molecular dynamics simulations were used to simulate the ionogel precursor solutions to better understand the effect of the alkali cation identity on the molecular coordination pre-polymerization, which, subsequently, explain the different properties of the ionogels prepared experimentally.

Similar to chapter 3, chapter 4 of this dissertation also looks at pMPC ionogels. However, the alkali cation salt was fixed to be LiTFSI, but the concentration of LiTFSI in BMP TFSI was varied (0.5 M, 1 M, and 2 M). The goal of the study in chapter 4 is to understand the effect of salt concentration and the stoichiometry (MPC-to-Li molar ratio) on the properties of ionogels. Ionic conductivity and elastic modulus values were measured, and cross-link density values were estimated. Raman spectroscopy was used to give insights on the coordination environment of TFSI anions, which complemented the aforementioned electrical and mechanical properties measured and estimated.

Chapter 5 of this dissertation focuses on a sinlge LiTFSI in BMP TFSI concentration (1 M) that was used to prepare pMPC ionogels. This chapter elucidates the role of Li in these gels and proposes the existence of three different Li species within these gels. This chapter utilizes pulsed field gradient nuclear magnetic resonance (PFG NMR), electrochemical impedance spectroscopy, dynamic mechanical analysis, and Raman spectroscopy to give insight on individual ion transport.

Chapter 6, the last of the main chapters of this dissertation, pertains to the future work that the work in chapter 3, 4, and 5 could lead to. Topics including resistance at the electrolyte/electrode interface, numerical modeling to predict ionogel elastic modulus values, and substituting ILs for green solvents (e.g. γ-valerolactone) are proposed with preliminary data.

Appendices A, B, and C contain supplementary information regarding chapters 3, 4, and 5, respectively. Appendix D showcases the fabrication and testing of an electrochemical glucose biosensor that was developed on the surface of polymer-based, medical sutures. Appendix E contains supplementary information regarding appendix D. Appendix F showcases the utilization

and testing of polyester sutures for drug delivery. Appendix G contains supplementary information regarding appendix F.

1.6 References

(1) Olabi, A. G.; Onumaegbu, C.; Wilberforce, T.; Ramadan, M.; Abdelkareem, M. A.; Al – Alami, A. H. Critical review of energy storage systems. *Energy* **2021**, *214*, 118987.

(2) Phogat, P.; Dey, S.; Wan, M. Powering the sustainable future: a review of emerging battery technologies and their environmental impact. *RSC Sustainability* **2025**, *3* (8), 3266-3306, 10.1039/D5SU00127G.

(3) Nishi, Y. The development of lithium ion secondary batteries. *The Chemical Record* **2001**, *1* (5), 406-413.

(4) Sasaki, Y. Organic Electrolytes of Secondary Lithium Batteries. *Electrochemistry* **2008**, *76* (1), 2-15.

(5) Tang, X.; Lv, S.; Jiang, K.; Zhou, G.; Liu, X. Recent development of ionic liquid-based electrolytes in lithium-ion batteries. *Journal of Power Sources* **2022**, *542*, 231792.

(6) Wu, F.; Zhang, K.; Liu, Y.; Gao, H.; Bai, Y.; Wang, X.; Wu, C. Polymer electrolytes and interfaces toward solid-state batteries: Recent advances and prospects. *Energy Storage Materials* **2020**, *33*, 26-54.

(7) Ye, Y.-S.; Rick, J.; Hwang, B.-J. Ionic liquid polymer electrolytes. *Journal of Materials Chemistry A* **2013**, *1* (8), 2719-2743, 10.1039/C2TA00126H.

(8) Kerner, M.; Plylahan, N.; Scheers, J.; Johansson, P. Ionic liquid based lithium battery electrolytes: fundamental benefits of utilising both TFSI and FSI anions? *Physical Chemistry Chemical Physics* **2015**, *17* (29), 19569-19581, 10.1039/C5CP01891A.

(9) Rogers, R. D.; Seddon, K. R. Ionic Liquids--Solvents of the Future? *Science* **2003**, *302* (5646), 792-793.

(10) Armand, M.; Endres, F.; Macfarlane, D. R.; Ohno, H.; Scrosati, B. Ionic-liquid materials for the electrochemical challenges of the future. *Nature Materials* **2009**, *8* (8), 621-629.

(11) Holbrey, J. D.; Seddon, K. R. Ionic Liquids. *Clean Products and Processes* **1999**, *1* (4), 223-236.

(12) Endres, F.; Zein El Abedin, S. Air and water stable ionic liquids in physical chemistry. *Physical Chemistry Chemical Physics* **2006**, *8* (18), 2101-2116, 10.1039/B600519P.

(13) Fernicola, A.; Scrosati, B.; Ohno, H. Potentialities of ionic liquids as new electrolyte media in advanced electrochemical devices. *Ionics* **2006**, *12* (2), 95-102.

(14) Garcia, B.; Lavallée, S.; Perron, G.; Michot, C.; Armand, M. Room temperature molten salts as lithium battery electrolyte. *Electrochimica Acta* **2004**, *49* (26), 4583-4588.

(15) Zhou, Q.; Henderson, W. A.; Appetecchi, G. B.; Montanino, M.; Passerini, S. Physical and Electrochemical Properties of N-Alkyl-N-methylpyrrolidinium Bis(fluorosulfonyl)imide Ionic Liquids: PY13FSI and PY14FSI. *The Journal of Physical Chemistry B* **2008**, *112* (43), 13577-13580.

(16) Sakaebe, H.; Matsumoto, H.; Tatsumi, K. Discharge–charge properties of Li/LiCoO2 cell using room temperature ionic liquids (RTILs) based on quaternary ammonium cation – Effect of the structure. *Journal of Power Sources* **2005**, *146* (1), 693-697.

(17) Lane, G. H.; Best, A. S.; MacFarlane, D. R.; Forsyth, M.; Bayley, P. M.; Hollenkamp, A. F. The electrochemistry of lithium in ionic liquid/organic diluent mixtures. *Electrochimica Acta* **2010**, *55* (28), 8947-8952.

(18) Bayley, P. M.; Lane, G. H.; Rocher, N. M.; Clare, B. R.; Best, A. S.; MacFarlane, D. R.; Forsyth, M. Transport properties of ionic liquid electrolytes with organic diluents. *Physical Chemistry Chemical Physics* **2009**, *11* (33), 7202-7208, 10.1039/B902200G.

(19) Arbizzani, C.; Gabrielli, G.; Mastragostino, M. Thermal stability and flammability of electrolytes for lithium-ion batteries. *Journal of Power Sources* **2011**, *196* (10), 4801-4805.

(20) Li, Y.; Zhou, W.; Xin, S.; Li, S.; Zhu, J.; Lü, X.; Cui, Z.; Jia, Q.; Zhou, J.; Zhao, Y.; et al. Fluorine-Doped Antiperovskite Electrolyte for All-Solid-State Lithium-Ion Batteries. *Angewandte Chemie International Edition* **2016**, *55* (34), 9965-9968.

(21) Xu, H.; Wang, S.; Wilson, H.; Zhao, F.; Manthiram, A. Y-Doped NASICON-type LiZr2(PO4)3 Solid Electrolytes for Lithium-Metal Batteries. *Chemistry of Materials* **2017**, *29* (17), 7206-7212.

(22) Janek, J.; Zeier, W. G. A solid future for battery development. *Nature Energy* **2016**, *1* (9), 16141.

(23) Amanchukwu, C. V.; Chang, H.-H.; Gauthier, M.; Feng, S.; Batcho, T. P.; Hammond, P. T. One-Electron Mechanism in a Gel–Polymer Electrolyte Li–O2 Battery. *Chemistry of Materials* **2016**, *28* (19), 7167-7177.

(24) Alsaedi, M. K.; Tadesse, M. Y.; Ganesan, V.; Panzer, M. J. Zwitterionic Polymer Ionogel Electrolytes Supported by Coulombic Cross-Links: Impacts of Alkali Metal Cation Identity. *The Journal of Physical Chemistry B* **2024**, *128* (13), 3273-3281.

(25) Le Bideau, J.; Viau, L.; Vioux, A. Ionogels, ionic liquid based hybrid materials. *Chemical Society Reviews* **2011**, *40* (2), 907-925, 10.1039/C0CS00059K.

(26) Chen, N.; Zhang, H.; Li, L.; Chen, R.; Guo, S. Ionogel Electrolytes for High-Performance Lithium Batteries: A Review. *Advanced Energy Materials* **2018**, *8* (12), 1702675.

(27) Néouze, M.-A.; Le Bideau, J.; Gaveau, P.; Bellayer, S.; Vioux, A. Ionogels, New Materials Arising from the Confinement of Ionic Liquids within Silica-Derived Networks. *Chemistry of Materials* **2006**, *18* (17), 3931-3936.

(28) Wang, M.; Zhang, P.; Shamsi, M.; Thelen, J. L.; Qian, W.; Truong, V. K.; Ma, J.; Hu, J.; Dickey, M. D. Tough and stretchable ionogels by in situ phase separation. *Nature Materials* **2022**, *21* (3), 359-365.

(29) Osada, I.; de Vries, H.; Scrosati, B.; Passerini, S. Ionic-Liquid-Based Polymer Electrolytes for Battery Applications. *Angew Chem Int Ed Engl* **2016**, *55* (2), 500-513.

(30) Qian, W.; Texter, J.; Yan, F. Frontiers in poly(ionic liquid)s: syntheses and applications. *Chemical Society Reviews* **2017**, *46* (4), 1124-1159, 10.1039/C6CS00620E.

(31) Zhang, S.-Y.; Zhuang, Q.; Zhang, M.; Wang, H.; Gao, Z.; Sun, J.-K.; Yuan, J. Poly(ionic liquid) composites. *Chemical Society Reviews* **2020**, *49* (6), 1726-1755, 10.1039/C8CS00938D.

(32) Tang, J.; Tang, H.; Sun, W.; Plancher, H.; Radosz, M.; Shen, Y. Poly(ionic liquid)s: a new material with enhanced and fast CO2 absorption. *Chemical Communications* **2005**, (26), 3325-3327, 10.1039/B501940K.

(33) Taylor, M. E.; Panzer, M. J. Fully-Zwitterionic Polymer-Supported Ionogel Electrolytes Featuring a Hydrophobic Ionic Liquid. *The Journal of Physical Chemistry B* **2018**, *122* (35), 8469-8476.

(34) Shaplov, A. S.; Marcilla, R.; Mecerreyes, D. Recent Advances in Innovative Polymer Electrolytes based on Poly(ionic liquid)s. *Electrochimica Acta* **2015**, *175*, 18-34.

(35) Lin, D.; Liu, W.; Liu, Y.; Lee, H. R.; Hsu, P.-C.; Liu, K.; Cui, Y. High Ionic Conductivity of Composite Solid Polymer Electrolyte via In Situ Synthesis of Monodispersed SiO2 Nanospheres in Poly(ethylene oxide). *Nano Letters* **2016**, *16* (1), 459-465.

(36) Alsaedi, M. K.; Like, B. D.; Wieck, K. W.; Panzer, M. J. Zwitterionic Materials for Enhanced Battery Electrolytes. *ChemPlusChem* **2024**, *89* (5), e202300731.

(37) Byrne, N.; Howlett, P. C.; Macfarlane, D. R.; Forsyth, M. The Zwitterion Effect in Ionic Liquids: Towards Practical Rechargeable Lithium-Metal Batteries. *Advanced Materials* **2005**, *17* (20), 2497-2501.

(38) Sun, J.; MacFarlane, D. R.; Byrne, N.; Forsyth, M. Zwitterion effect in polyelectrolyte gels based on lithium methacrylate-N,N-dimethyl acrylamide copolymer. *Electrochimica Acta* **2006**, *51* (19), 4033-4038.

(39) D'Angelo, A. J.; Panzer, M. J. Decoupling the Ionic Conductivity and Elastic Modulus of Gel Electrolytes: Fully Zwitterionic Copolymer Scaffolds in Lithium Salt/Ionic Liquid Solutions. **2018**.

(40) Woo, H.-S.; Son, H.; Min, J.-Y.; Rhee, J.; Lee, H.-T.; Kim, D.-W. Ionic liquid-based gel polymer electrolyte containing zwitterion for lithium-oxygen batteries. *Electrochimica Acta* **2020**, *345*, 136248.

(41) Lee, J. H.; Shin, J. C.; Kim, J.; Ho, J.-W.; Cho, W. J.; Park, M. J.; Yi, G.-R.; Lee, M.; Yoo, P. J. Zwitterionic surfactant–stabilized ionogel electrolytes with high ionic conductivity for lithium secondary batteries. *Journal of Power Sources* **2023**, *557*, 232565.

(42) Li, Z. H.; Xia, Q. L.; Liu, L. L.; Lei, G. T.; Xiao, Q. Z.; Gao, D. S.; Zhou, X. D. Effect of zwitterionic salt on the electrochemical properties of a solid polymer electrolyte with high temperature stability for lithium ion batteries. *Electrochimica Acta* **2010**, *56* (2), 804-809.

(43) D'Angelo, A. J.; Panzer, M. J. Design of Stretchable and Self-Healing Gel Electrolytes via Fully Zwitterionic Polymer Networks in Solvate Ionic Liquids for Li-Based Batteries. *Chemistry of Materials* **2019**, *31* (8), 2913-2922.

(44) Qin, H.; Panzer, M. J. Zwitterionic Copolymer-Supported Ionogel Electrolytes Featuring a Sodium Salt/Ionic Liquid Solution. *Chemistry of Materials* **2020**, *32* (18), 7951-7957.

(45) Wieck, K. W.; Panzer, M. J. Ionogel Electrolytes Supported by Zwitterionic Copolymers Featuring Lithium Ion-Mediated, Noncovalent Cross-Links. *ACS Applied Polymer Materials* **2023**, *5* (4), 2887-2894.

(46) Taylor, M. E.; Clarkson, D.; Greenbaum, S. G.; Panzer, M. J. Examining the Impact of Polyzwitterion Chemistry on Lithium Ion Transport in Ionogel Electrolytes. *ACS Applied Polymer Materials* **2021**, *3* (5), 2635-2645.

(47) Chayambuka, K.; Mulder, G.; Danilov, D. L.; Notten, P. H. L. From Li-Ion Batteries toward Na-Ion Chemistries: Challenges and Opportunities. *Advanced Energy Materials* **2020**, *10* (38), 2001310.

(48) Li, T.; Gulzar, U.; Bai, X.; Lenocini, M.; Prato, M.; Aifantis, K. E.; Capiglia, C.; Proietti Zaccaria, R. Insight on the Failure Mechanism of Sn Electrodes for Sodium-Ion Batteries: Evidence of Pore Formation during Sodiation and Crack Formation during Desodiation. *ACS Applied Energy Materials* **2019**, *2* (1), 860-866.

Chapter 2: Experimental Methods and Characterization

2.1 Sample Preparation

2.1.1 UV-initiated *in situ* Free Radical Polymerization of Zwitterionic Monomers in Ionic Liquids (ILs)

Polymers consist of repeat units known as monomers. When monomers polymerize, they form covalent bonds between each other that result in polymer chains. There are different ways to achieve polymerization, such as anionic polymerization, cationic polymerization, and free radical polymerization[1]. In this dissertation, the monomer 2-methacryloyloxethyl phosphorylcholine (MPC) is polymerized via UV-initiated *in situ* free radical polymerization while dissolved in a Li^+- and/or Na^+-containing ionic liquid (IL) solution. This photo-polymerization is achieved by using a photoinitiator[2], 2-hydroxy-2-methylpropiophenone (HOMPP). Once the HOMPP-containing monomer solution is exposed to UV light, radicals are formed on MPC that propagate to form covalent bonds with other monomers and eventually result in pMPC chains when all radicals have reacted.

In Chapters 3, 4, and 5 of this dissertation, all ionogels and viscous polymer solutions are prepared by dissolving MPC monomers in Li^+- and/or Na^+-containing ionic liquid at room temperature in a N_2-filled glovebox by stirring at 80 rpm. The ionic liquid of choice for this dissertation is 1-butyl-1-methylpyrrolidinium bis(trifluoromethylsulfonyl)imide, also known as BMP TFSI. Once MPC is fully dissolved, HOMPP is added to the liquid solution and stirred for ~10-20 seconds. Then, the solution is pipetted out into specific molds. The type of mold used is

dependent on the type of intended characterization method or test. We use polytetrafluoroethylene (PTFE) spacers for compression tests, PTFE wells that contain gold pins for room temperature ionic conductivity tests, rubber O-rings for temperature-dependent ionic conductivity and activation energy tests, and glass vials for Raman spectroscopy. Figure 2.1 is an illustration that shows the experimental procedure for gel precursor preparation and gel precursor casting. Once the relevant molds are filled, they are exposed to UV light for 10 minutes to initiate the free radical polymerization then are left to cure overnight in the glovebox.

The product of polymerization is either a viscous polymer solution or a free-standing gel. Chapters 3, 4, and 5 of this dissertation demonstrate the importance of the presence of alkali metal cations (Li^+ and/or Na^+) and the amount of monomers dissolved in the cation-containing IL in dictating whether or not a gel is formed. For one, alkali metal cations must be present in the IL for MPC to dissolve in it[3]. Also, alkali metal cations are crucial in bridging pMPC chains via noncovalent cross-links that, when abundant, produce a free-standing gel upon polymerization[3, 4]. Furthermore, the amount of monomer dissolved should be above a minimum threshold for the post-polymerization system to be a free-standing gel: more than ~2 wt. % MPC in 1 M Li^+-containing IL (Chapter 5).

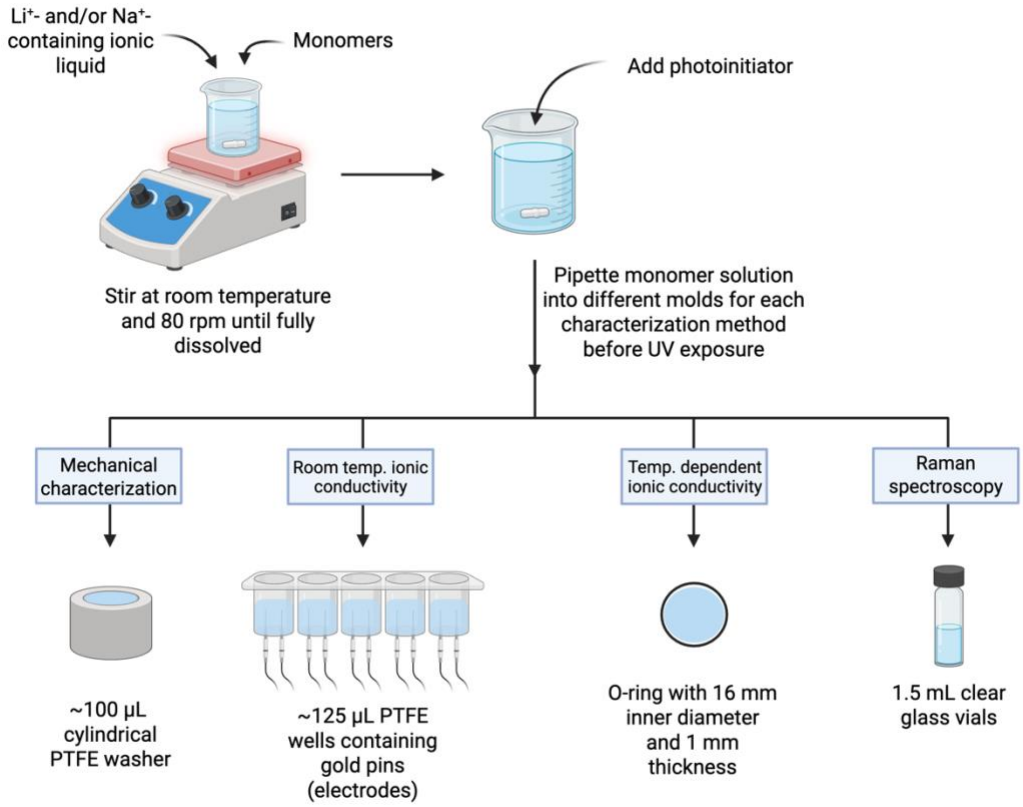


Figure 2.1. Precursor solution preparation and characterization method-specific molds (pre-polymerization)

2.2 Electrical Characterization

2.2.1 Alternating Current (AC) Electrochemical Impedance Spectroscopy (EIS)

AC EIS is used in this dissertation to measure electrolyte ionic conductivity. Using a potentiostat, the electrolyte is subjected to alternating voltage, which generates AC. The resulting impedance measured is a complex number with a real component and an imaginary one. By varying the frequency of the alternating voltage, one could glean information regarding the resistive and capacitive behavior of the electrolyte. Resistive behavior is dominant at high frequencies while capacitive behavior is at low frequencies. This can also be visualized using a phase angle-frequency plot (figure 2.2). Phase angles closer to -90^0 (theoretically) represent capacitive behavior (imaginary component) and those closer to 0^0 represent resistive behavior (real component). Therefore, phase angle-frequency plots tend to show low phase angles at higher frequencies and high phase angles at lower frequencies.

In Chapters 3, 4, and 5 of this dissertation, electrolytes were in PTFE wells that contain gold pins (shown in Figure 2.3). The alternating current frequency ranged between 1 and 200000 Hz. For each well, the impedance is calculated by averaging five impedance values: the impedance value at lowest phase angle (closest to 0^0) from the phase-frequency plot, two values above that value on the plot, and two values below that.

For each well, the ionic conductivity is calculated using equation 2.1[5]:

$$\sigma = \frac{t}{AR} \qquad \text{(Eq. 2.1)}$$

where σ is the ionic conductivity, t is the thickness of the electrolyte, A is the cross-sectional area through which the current passes, and R is the resistance (impedance at high frequency/low

phase angle). However, the t/A value for the PTFE wells used in this dissertation was calculated to be 3670 Ω mS cm^{-1} from previous calibration. So, equation 2.1 reduces to:

$$\sigma = \frac{3670}{R} \quad \text{(Eq. 2.2)}$$

In addition to room temperature conductivity, temperature-dependent conductivity of electrolytes can be measured. In Appendix A, temperature-dependent conductivity was used to report activation energies for ionogels. 16 mm diameter and 1 mm thickness gels were sealed in symmetric coin cells (CR 2032) and placed on a temperature-controlled optical microscopy stage that was connected to a potentiostat for EIS measurements. The impedance of the ionogels was calculated at different temperatures using equation 2.2. Then, equation 2.3 (an Arrhenius-type model for ionic conductivity) was used:

$$\sigma = \sigma_o e^{\left(\frac{-E_a}{RT}\right)} \quad \text{(Eq. 2.3)}$$

where E_a is the apparent activation energy of ionic conductivity, R is the universal gas constant, T is the temperature, and σ_o is a prefactor constant. Linearizing equation 2.3, plotting the natural log of ionic conductivity on the y-axis and the inverse of temperature (1/T) on the x-axis, then calculating the slope of the line gives $\frac{-E_a}{R}$, from which the apparent activation energy can be calculated.

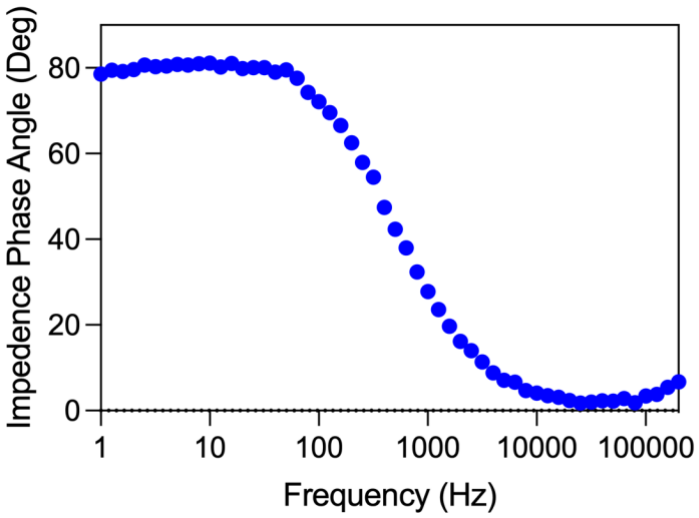


Figure 2.2. A phase angle-frequency plot for an ionogel from Chapter 3.

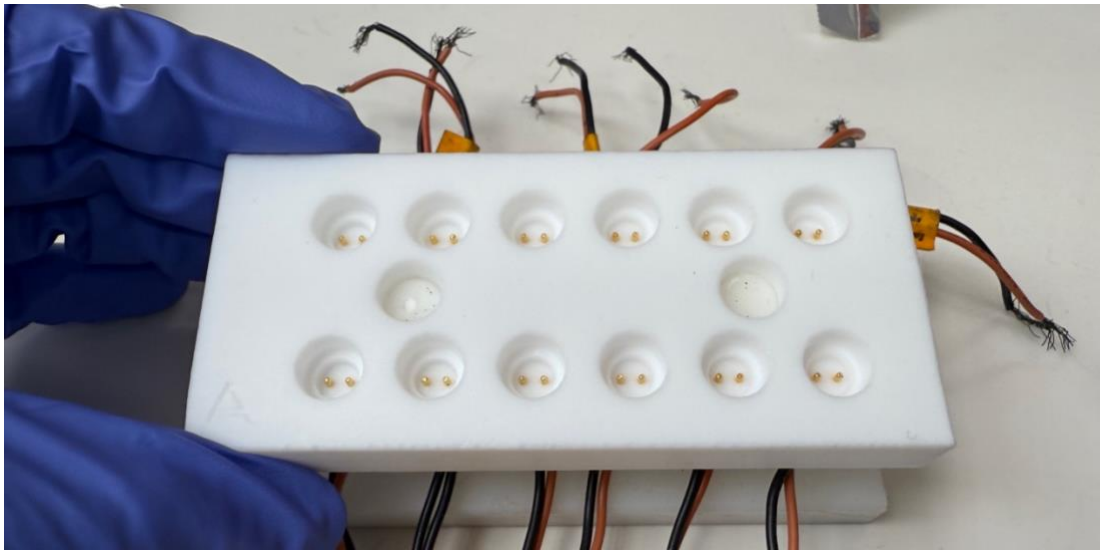


Figure 2.3. A 12-well PTFE board. Each well has gold pins connected to wires. This board is used to test room temperature ionic conductivity.

2.2.2 Coin Cell Preconditioning, Direct Current (DC) Polarization, and Lithium Current Fraction

The fraction of current carried by Li^+ compared to the total current carried by Li^+ and all the other ions in the electrolyte is a common way of quantifying the relative mobility of lithium in an electrolyte. It was measured via DC polarization (80 mV) and chronoamperometry. The initial current (I_o) is the current carried across the electrolyte by all mobile ions in the electrolyte (here recorded at 1 second). Once steady state is reached, the remaining current is known as the steady-state current (I_{ss}) (here recorded at 4 hours), which is the current carried by Li^+ ions due to the stripping and plating of Li^+ at the Li-electrolyte interface[6]. Figure 2.4 shows a typical chronoamperometry curve where current is changing with respect to time and the I_o plateaus off to I_{ss}. The current fraction value for the ionogel whose chronoamperometry data is shown in figure 2.3 is 0.11.

To perform DC polarization, the electrolyte is sandwiched between lithium metal on each side and stainless-steel (SS) current collectors and sealed in a coin cell (CR2032 coin cells, SS304 grade, MTI Corporation) as shown in figure 2.5. The electrolyte, in this case, is not in any of the molds shown in figure 2.1. Whatman separators (GF/A, Cytiva), which are porous, are submerged in the liquid precursor and placed under vacuum (-30 inHg) for 10 minutes. Then, the liquid precursor-filled Whatman separator is exposed to UV irradiation. This step ensures that the liquid fills the pores of the separator that would, post polymerization, be filled with the resulting polymer solution or gel. Coin cell assembly is done by stacking the components in figure 2.5 in the following order: The smaller half of the CR 2032 metallic coin cell cases, a SS current collector, a lithium chip, the electrolyte-containing separator, a second lithium chip, a second SS current collector, and finally the bigger half of the CR 2032 metallic coin cell cases. This assembly is then transferred to an electric coin cell crimper (MSK-160E, MTI Corporation) and crimped.

Coin cells containing the electrolytes are preconditioned before DC polarization. The coin cells were preconditioned right after sealing with a battery cycler. The preconditioning step is an 18-hour process and is as follows: A 2-hour charging step with 0.02 A current, a two-hour rest period (no current), a two-hour discharging step with -0.02 A current, then a 12-hour rest period (no current). Once preconditioning is done, the coin cell can then be polarized (under DC current) to measure the initial and steady-state current values and calculate the resulting current fraction.

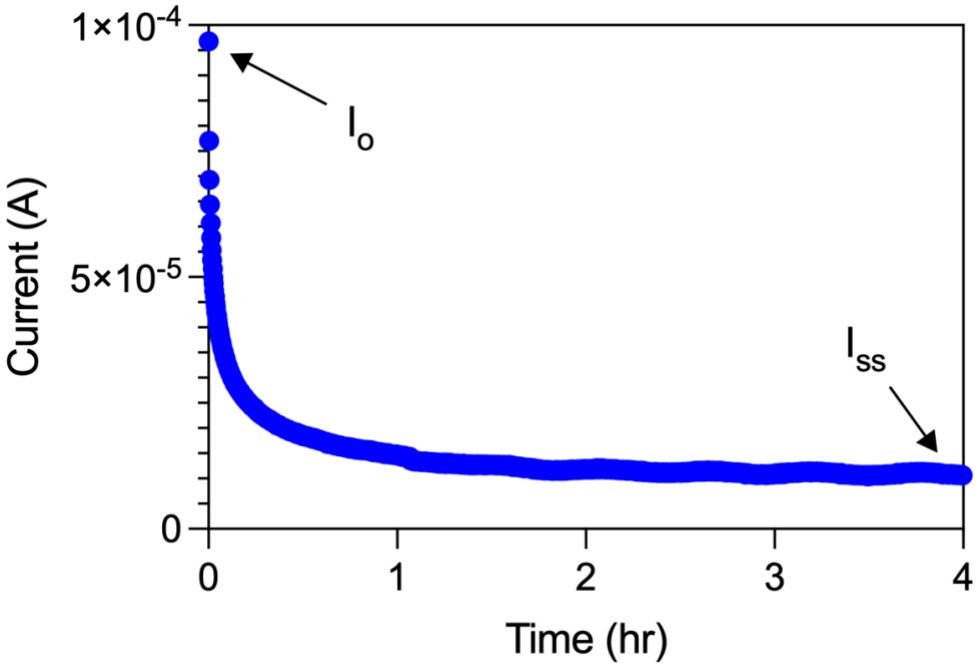


Figure 2.4. Chronoamperometry curve (current with respect to time) for a 7 wt. % MPC ionogel under 80 mV DC polarization. The I_{ss}/I_o value for this ionogel is 0.11.

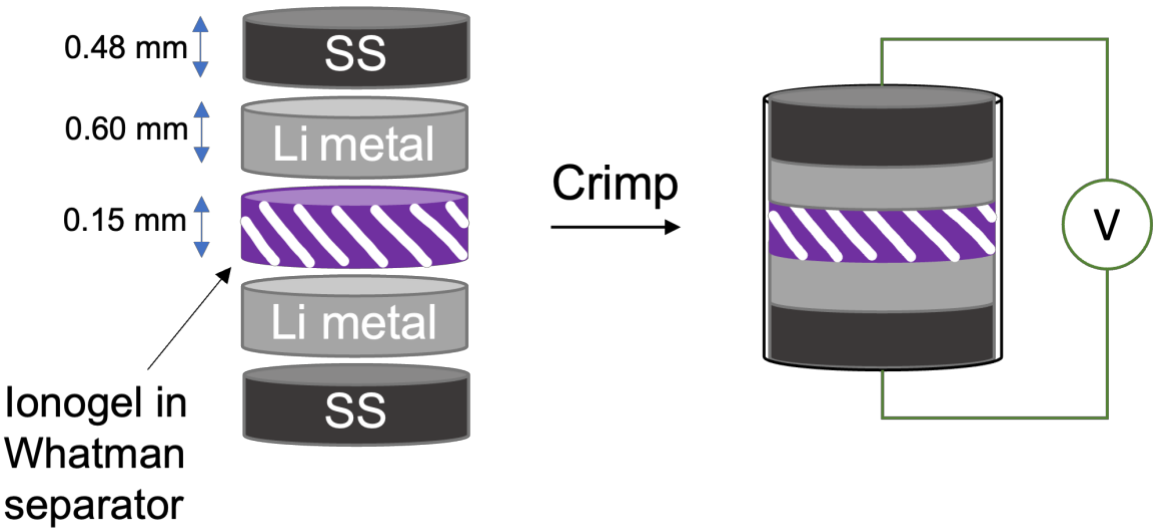


Figure 2.5. Coin cell assembly with the electrolyte in Whatman separator between lithium discs and stainless-steel current collectors.

2.3 Spectroscopic Characterization

2.3.1 Raman Spectroscopy

Raman spectroscopy is an analytical method where a laser is used to glean molecular information for samples. In a Raman spectrometer, photons scattered from the samples due to the incident laser are either scattered elastically (Rayleigh scattering) or inelastically (Raman scattering). The detector in a Raman spectrometer receives photons that result from inelastic scattering[7]. The change in frequency between the incident laser and the scattered photons is defined as Raman shift, and is the x-axis in a typical Raman spectrum, with the y-axis being the intensity of the scattered photons (Figure 2.6). The Raman shifts are indicative of specific vibrational modes for specific molecules. For example, as discussed in Chapter 4 of this dissertation, the vibrational modes for the molecule $TFSI^-$ are around ~742 and ~748 cm^{-1} depending on the molecules that surround it that produces this vibrational state within the $TFSI^-$ molecule[8,9].

In Chapter 4 of this dissertation, the Raman spectrometer used is a Renishaw InVia Raman Microscope. The Raman spectra in Chapter 4 were all baseline-corrected by using a 2^{nd} order polynomial fit and integrated between 730 and 760 cm^{-1}. The curves the peaks at ~742 and ~748 cm^{-1} were fit via non-linear regression between 720 and 770 cm^{-1}. Figure 2.7 shows an ionogel that was polymerized in a glass vial for Raman spectroscopy and figure 2.8 show the glass vial in the sample holder inside the Raman spectrometer. The height of the sample in the vial can be as low as 0.5 cm (figure 2.7).

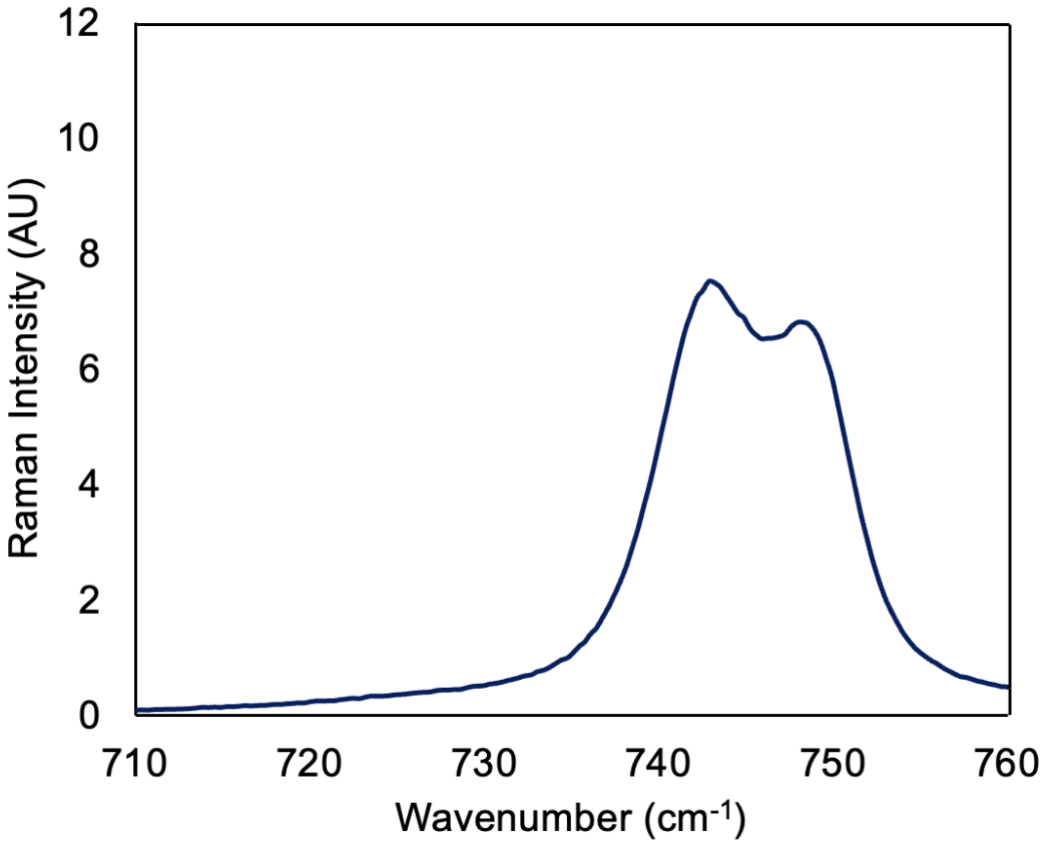


Figure 2.6. Raman spectrum for a Li^+-containing ionic liquid sample (from Chapter 4)



Figure 2.7. An ionogel in a glass vial for Raman spectroscopy.

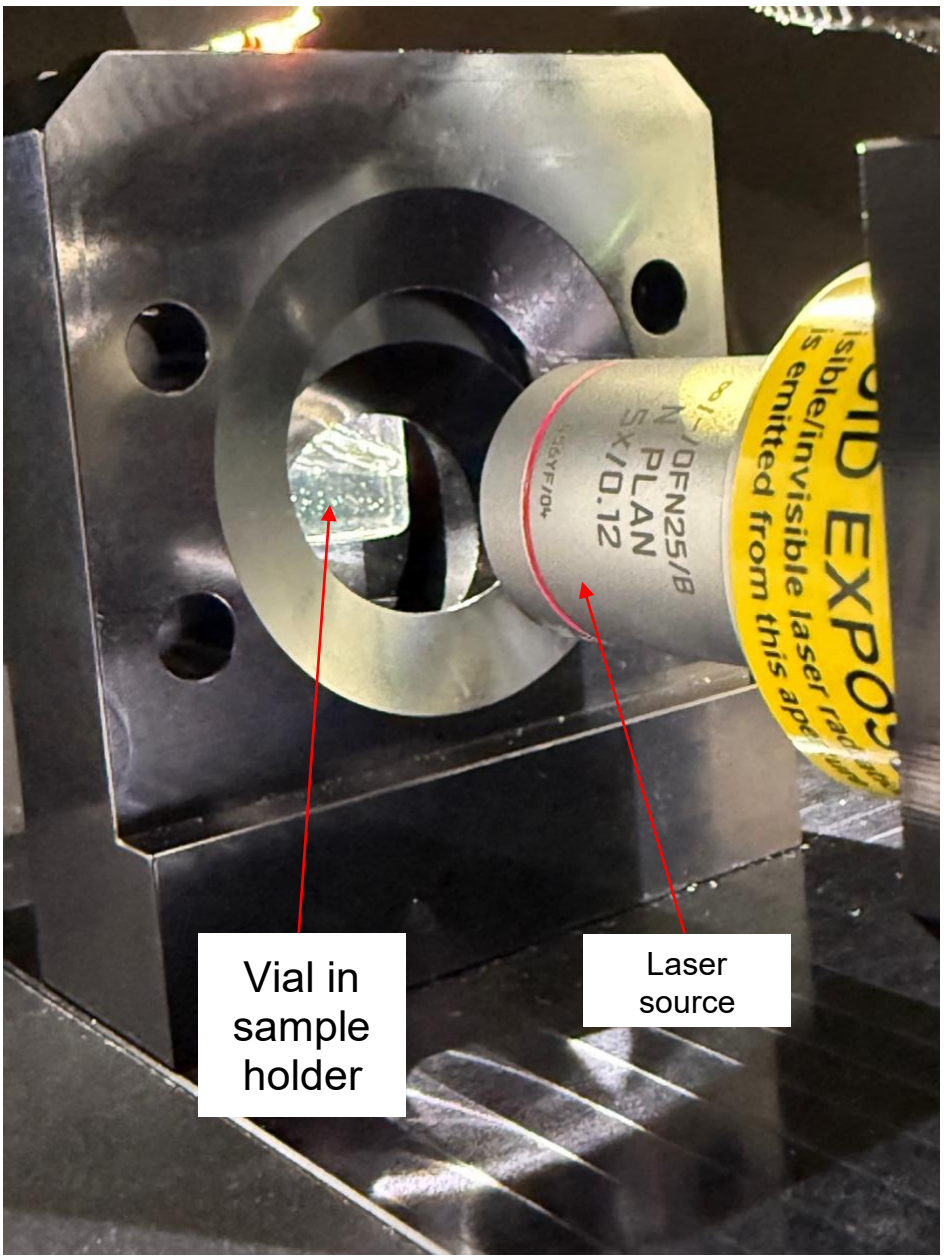


Figure 2.8. Vial containing ionogel in sample holder inside Raman spectrometer.

2.4 Mechanical Characterization

2.4.1 Compression Testing

In this dissertation, the mechanical properties of the ionogels were assessed by their elastic modulus values. Ionogels were placed between two parallel plates that compress the gels up to a certain pre-defined strain. In Chapters 3, 4, and 5, the gels were strained under compression from 0 to 15% strain. As an ionogel is compressed, it exerts stress onto one of the plates and the stress-strain relationship is plotted. A line is then fit through the stress-strain data between 4 and 10% strain for each gel. The slope of the line, which is the elastic modulus[10], is calculated (Eq. 2.4):

$$E = \frac{stress}{strain} \quad \text{(Eq. 2.4)}$$

where E is the elastic modulus.

The instruments used to compress gels are a Dynamic Mechanical Analyzer (DMA) in Chapter 3 and a Texture Analyzer in Chapters 4 and 5. Figure 2.9 shows what a typical stress-strain curve for the ionogels discussed in this dissertation looks like. The ionogel whose stress-strain curve is in figure 2.6 has an elastic modulus of ~2500 kPa.

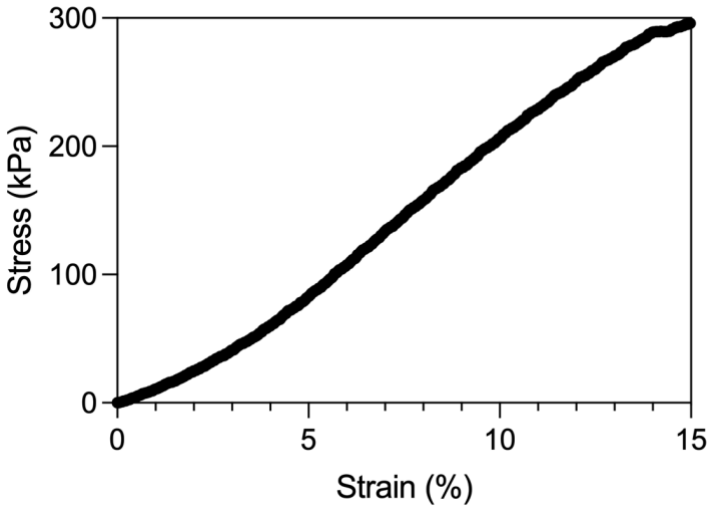


Figure 2.9. A typical stress-strain curve of an ionogel that is compressed to 15% strain. The elastic modulus of this ionogel is ~2500 kPa which was calculated by fitting a line through the curve from 4% to 10% strain.

2.5 References

(1) Young, R. J.; Lovell, P. A. *Introduction to Polymers*; CRC Press, 2011.

(2) Andrzejewska, E. Photoinitiated polymerization in ionic liquids and its application. *Polymer International* **2017**, *66* (3), 366-381. DOI: https://doi.org/10.1002/pi.5255 (acccessed 2025/09/30).

(3) Alsaedi, M. K.; Tadesse, M. Y.; Ganesan, V.; Panzer, M. J. Zwitterionic Polymer Ionogel Electrolytes Supported by Coulombic Cross-Links: Impacts of Alkali Metal Cation Identity. *The Journal of Physical Chemistry B* **2024**, *128* (13), 3273-3281. DOI: 10.1021/acs.jpcb.3c08144.

(4) Wieck, K. W.; Panzer, M. J. Ionogel Electrolytes Supported by Zwitterionic Copolymers Featuring Lithium Ion-Mediated, Noncovalent Cross-Links. *ACS Applied Polymer Materials* **2023**, *5* (4), 2887-2894. DOI: 10.1021/acsapm.3c00110.

(5) Ding, Y.; Zheng, Z. Stretchable ionics: How to measure the electrical resistance/impedance. *Matter* **2022**, *5* (9), 2570-2573. DOI: https://doi.org/10.1016/j.matt.2022.08.007.

(6) Lin, L.-Y.; Chen, C.-C. Accurate characterization of transference numbers in electrolyte systems. *Journal of Power Sources* **2024**, *603*, 234236. DOI: https://doi.org/10.1016/j.jpowsour.2024.234236.

(7) Das, R. S.; Agrawal, Y. K. Raman spectroscopy: Recent advancements, techniques and applications. *Vibrational Spectroscopy* **2011**, *57* (2), 163-176. DOI: https://doi.org/10.1016/j.vibspec.2011.08.003.

(8) Kerner, M.; Plylahan, N.; Scheers, J.; Johansson, P. Ionic liquid based lithium battery electrolytes: fundamental benefits of utilising both TFSI and FSI anions? *Physical Chemistry Chemical Physics* **2015**, *17* (29), 19569-19581, 10.1039/C5CP01891A. DOI: 10.1039/C5CP01891A.

(9) Umebayashi, Y.; Mitsugi, T.; Fukuda, S.; Fujimori, T.; Fujii, K.; Kanzaki, R.; Takeuchi, M.; Ishiguro, S.-I. Lithium Ion Solvation in Room-Temperature Ionic Liquids Involving Bis(trifluoromethanesulfonyl) Imide Anion Studied by Raman Spectroscopy and DFT Calculations. *The Journal of Physical Chemistry B* **2007**, *111* (45), 13028-13032. DOI: 10.1021/jp076869m.

(10) Brinson, H. F.; Brinson, L. C. Stress and Strain Analysis and Measurement. In *Polymer Engineering Science and Viscoelasticity: An Introduction*, Brinson, H. F., Brinson, L. C. Eds.; Springer US, 2015; pp 15-55.

Chapter 3: Zwitterionic Polymer Ionogel Electrolytes Supported by Coulombic Cross-links: Impacts of Alkali Metal Cation Identity

This chapter is reproduced from the following publication:

Alsaedi, M. K.; Tadesse, M. Y.; Ganesan, V.; Panzer, M. J. "Zwitterionic Polymer Ionogel Electrolytes Supported by Coulombic Cross-links: Impacts of Akali Metal Cation Identity." *J. Phys. Chem. B*. **2024**, 128 (13), 3273-3281

3.1 Abstract

Zwitterionic (ZI) polymers enable the formation of noncovalent cross-links within ionic liquid electrolytes (ILEs) to create nonflammable, mechanically robust, and highly conductive ionogel electrolytes. In this study, ZI homopolymer poly(2-methacryloyloxyethyl phosphorylcholine) (poly(MPC)) scaffolds are synthesized *in situ* within lithium and/or sodium salt-based ILEs to construct a series of ionogels that contain between 3-15 wt.% poly(MPC). Room temperature ionic conductivity values of these ionogels are found to vary between approximately 1.3 and 2.2 mS cm^{-1}. For sodium only and 1:1 lithium:sodium equimolar mixed salt ionogels containing 6 wt.% poly(MPC), the ionic conductivity is found to improve by 14% compared to the neat ILE due to the presence of the ZI scaffold. Moreover, comparing the elastic modulus values of lithium- versus sodium-containing ionogels revealed a difference of up to one order of magnitude (10.6 vs. 111 kPa, respectively, for 3 wt.% poly(MPC)). Molecular dynamics simulations of ionogel precursor solutions corroborate the experimental results by demonstrating differences in the lithium/ZI monomer and sodium/ZI monomer cluster size distributions formed, which is hypothesized to influence the scaffold network cross-link density obtained upon photopolymerization. This work provides insights as to why ZI polymer-supported ionogel properties that are relevant for the development of safer electrolytes for lithium-ion and sodium-ion batteries depend upon the chemical identity of the alkali metal cation.

3.2 Introduction

In order to address a growing global energy demand while minimizing carbon emissions, there is an increasing shift toward renewable energy generation sources, such as wind and solar power. Simultaneously, there is a push to electrify personal transportation through the continued

rollout of fully electric and hybrid vehicles. Thus, electrochemical energy storage devices such as batteries are also experiencing an increasing demand. Developing safer batteries for many applications is crucial, especially in the context of electric vehicles and/or small aircraft where ensuring passenger safety is of paramount concern.

Electrolytes, which are ion-conducting materials that provide a pathway for ion transport between the anode and cathode, are an integral component of every battery. Traditional lithium-ion battery electrolytes are based on flammable organic solvents such as propylene carbonate, and they can leak out of a compromised cell, which increases safety concerns regarding the battery.[1, 2] Despite many recent efforts toward developing solid-state electrolytes, there is usually a tradeoff between obtaining a more solid-like nature and maintaining high ionic conductivity.[3] Therefore, a need for electrolytes that have solid-like mechanical properties yet liquid-like ion transport levels brings gel electrolytes to the forefront of recent electrolyte development.[3-5] Gel electrolytes consist of a majority liquid electrolyte phase, which is supported by a volume-spanning solid network such as a cross-linked polymer. In general, gel electrolytes are stiff enough to not readily flow or leak, and they maintain a high level of ionic conductivity due to their substantial liquid fraction.

A unique class of liquid electrolytes that has been explored for safer battery operation is ionic liquids (ILs). ILs are molten salts at or near room temperature that are nonflammable and thermally stable, exhibiting ultralow volatility and high ionic conductivity.[6-9] When a gel electrolyte is created using an IL, the resulting material is typically referred to as an *ionogel*.[10-13] There are multiple ways by which a solid scaffold can be incorporated into the IL electrolyte to form an ionogel, such as polymerizing one of the IL ions[14-17] or introducing polymeric or inorganic nanoparticle-based scaffolds.[18-20] However, the presence of a solid scaffold reduces the liquid fraction of an ionogel by definition compared to a neat IL, which usually lowers the ionic

conductivity. Therefore, it is preferable to use a solid scaffold that can favorably interact with the IL in such a way that it mitigates any potential loss in conductivity.

A scaffold class that has recently been shown to achieve this balance between enhanced mechanical properties and favorable ion transport is zwitterionic (ZI) polymers.[21] ZI polymers contain repeat units featuring functional groups that have an equal number of positive and negative charges, resulting in a net zero overall charge. ZI molecules have been demonstrated to promote ion-pair dissociation,[22, 23] form physical cross-links that can increase electrolyte stiffness,[18, 24-27] improve ionic conductivity,[18, 22, 23, 26, 28-33] and enhance electrode/electrolyte interfacial stability and battery cycling.[21, 22, 28, 31, 34] Ionogels supported solely by noncovalent (Coulombic) Li^+ cation-mediated cross-links formed between the phosphorylcholine side groups of a ZI copolymer have also recently been reported.[35] Gaining a deeper understanding of the extent and mechanism of this alkali metal cation-mediated Coulombic cross-link formation in both lithium-ion and "beyond-lithium-ion" (*e.g.* sodium-ion) ionogel battery electrolytes is a key motivation for the present investigation.

In this study, a series of phosphorylcholine-type ZI homopolymer-supported ionogel electrolytes have been synthesized by *in situ* free radical polymerization and characterized in order to examine the impact of the alkali metal cation identity (Li^+ vs. Na^+) on Coulombic cross-link formation. These ionogels comprise a majority phase of ionic liquid electrolyte (ILE) supported by a ZI homopolymer, poly(2-methacryloyloxyethyl phosphorylcholine) (poly(MPC)). The components of the ILE are 1-butyl-1-methylpyrrolidinium bis(trifluoromethylsulfonyl)imide (BMP TFSI) and an alkali metal salt at a concentration of 0.5 M (either LiTFSI, NaTFSI, or an equimolar mixture of LiTFSI and NaTFSI). MPC monomers were fully polymerized *in situ* within the ILE via UV-photoinitiated free radical polymerization to create transparent, free-standing

ionogels that are supported via Coulombic cross-links mediated by the alkali metal cations of the ILE (illustrated in Figure 3.1). The ionic conductivities and mechanical properties of these ionogels were probed. Low ZI homopolymer contents were found to slightly improve the room temperature ionogel ionic conductivity (up to a 14% increase at 6 wt.% poly(MPC)). Changing the alkali metal cation identity resulted in ionogels that exhibited notably different elastic modulus values, with the Na^+-containing ionogels being consistently stiffer than their Li^+-containing counterparts (up to a tenfold difference at 3 wt.% poly(MPC) content). Furthermore, the mixed-salt ionogels, where the ILE contained both Li^+ and Na^+ cations in equal proportion, exhibited elastic modulus values similar to those of the Na^+ only ionogels. To help understand why this might be the case, molecular dynamics simulations were performed in order to explore the local environment around alkali metal cations within the ionogel precursor solutions. These simulations revealed that MPC monomers interact more strongly with Li^+ than Na^+ within the ILE, and that a greater number of MPC-alkali metal ion clusters having three or more constituents are formed for the Li^+ only ILE compared to the Na^+ only ILE. Based upon this finding, we hypothesize that the difference in the MPC-alkali metal ion cluster size distributions, which depends on the identity of the alkali metal cation (Li^+ vs. Na^+), leads to the formation of different network structures upon *in situ* photopolymerization, corroborating the difference in elastic modulus values observed for these ionogels.

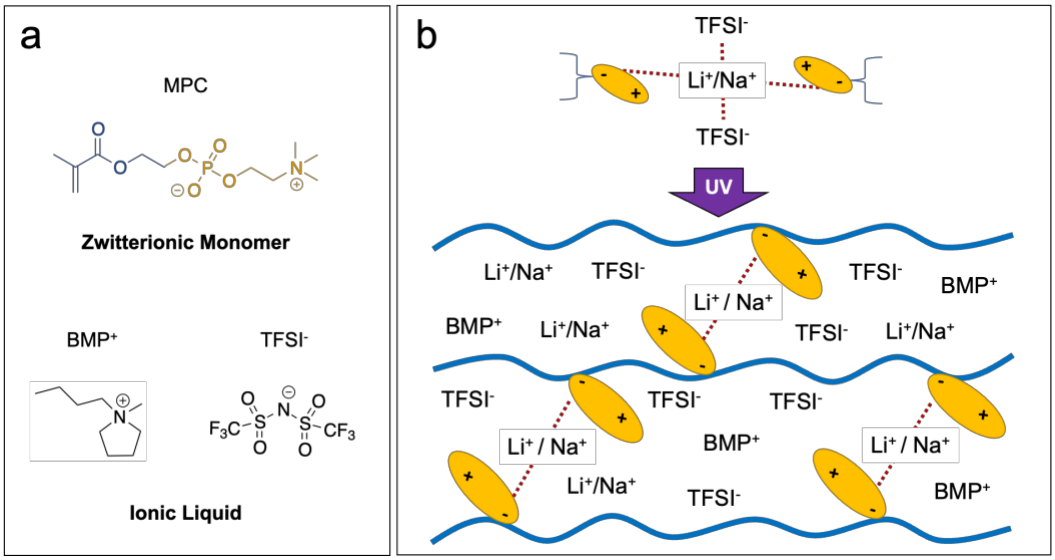


Figure 3.1. (a) Chemical structures of the zwitterionic monomer, 2-methacryloyloxyethyl phosphorylcholine (MPC), and the ionic liquid ions, 1-butyl-1-methylpyrrolidinium (BMP^+) and bis(trifluoromethylsulfonyl)imide ($TFSI^-$). (b) Schematic illustrations of: an MPC monomer/ionic liquid electrolyte ion cluster centered around an alkali metal cation (Li^+ or Na^+) within the ionogel precursor solution (top); the post-UV photopolymerization poly(MPC) ionogel scaffold that is supported by Coulombic, alkali metal cation-mediated cross-links between polymer chains (bottom).

3.3 Methods

3.3.1 Materials

1-butyl-1-methylpyrrolidinium bis(trifluoromethylsulfonyl)imide (BMP TFSI, 99%, Iolitech Ionic Liquids Technologies GmbH), lithium bis(trifluoromethylsulfonyl)imide (LiTFSI, 99.95% trace metals basis, Sigma Aldrich), sodium bis(trifluoromethylsulfonyl)imide (NaTFSI, 99.5%, Solvionic), and the photoinitiator, 2-hydroxy-2-methylpropiophenone (HOMPP, 97%, Sigma Aldrich), were stored in a nitrogen-filled glovebox (H_2O and O_2 < 0.1 ppm) until use. The zwitterionic monomer, 2-methacryloyloxyethyl phosphorylcholine (MPC, 97%, MilliporeSigma), was stored in a refrigerator until use. Stainless steel CR2032 coin cell parts (SS304 grade, MTI Corporation) were stored in an argon-filled glovebox (H_2O and O_2 < 0.5 ppm) until use. All materials were used as received.

3.3.2 Ionic Liquid Electrolyte (ILE) Preparation

LiTFSI and/or NaTFSI were mixed with BMP TFSI inside of a nitrogen-filled glovebox and stirred overnight at 400 rpm and 80 ^{o}C to produce three distinct, homogeneous ILE solutions: 0.5 M LiTFSI in BMP TFSI, 0.5 M NaTFSI in BMP TFSI, and a mixture of the two alkali metal salts, LiTFSI and NaTFSI, in BMP TFSI (total alkali metal cation concentration of 0.5 M, using a 1:1 Li^+:Na^+ molar ratio).

3.3.3 Ionogel Preparation

Inside of a nitrogen-filled glovebox, 0.1 g of MPC monomer is first added to a glass vial, followed by addition of the required amount of ILE to make up a 3-15 wt.% MPC "ionogel precursor" solution. The precursor solution is then stirred at 80 rpm at room temperature for 4 hours, until MPC is completely dissolved and the mixture is visually homogenous and transparent. The photoinitiator (HOMPP) is then added to the solution (2 mol% with respect to the MPC monomer) and stirred at 80 rpm for 10 seconds. The precursor solution is then used to fill the relevant mold, after which it is exposed to UV radiation (365 nm) from a handheld lamp (Spectronic Corp., 8 W) for 10 minutes to facilitate the *in situ* photopolymerization of the monomers. Ionogel samples were left overnight inside the glovebox prior to characterization. At least three replicate gels were prepared from each precursor for the characterization techniques described below.

For room temperature ionic conductivity measurements, ionogel precursor solution was pipetted inside a nitrogen-filled glovebox into cylindrical polytetrafluoroethylene (PTFE) wells of 125 μL volume that contained two gold-coated electrodes. To prepare samples for dynamic mechanical analysis (DMA), ionogel precursor solution was injected with a syringe into a PTFE washer (6.35 mm inner diameter and 3.15 mm thickness) sandwiched between two glass slides with a thin film of polyethylene separating the washer mold cavity from the glass on each side to prevent poly(MPC) from adhering to the glass surface. Samples for temperature-dependent ionic conductivity measurements were prepared in a similar manner using rubber O-ring molds (McMaster-Carr, BN70 SQ; 16 mm inner diameter and 1 mm thickness, square cross-section).

Prior to DMA characterization and temperature-dependent conductivity measurements, ionogels were removed from their molds.

In order to perform temperature-dependent ionic conductivity measurements, ionogels were sealed inside a CR2032 coin cell with symmetric stainless steel blocking electrodes (15.5 mm diameter, 0.5 mm thickness). A small amount of ILE (10 μL) was pipetted onto both sides of the ionogel to promote good contact at the gel/stainless-steel interface. For temperature-dependent conductivity measurements of neat ILEs, a Whatman separator (Cat. no. 1005070, Whatman Intl. Ltd.) with a diameter of 19 mm was soaked in neat ILE under vacuum for 10 minutes prior to being sealed inside a coin cell.

3.3.4 Dynamic Mechanical Analysis (DMA)

Elastic modulus values for ionogels were determined by compression testing using a dynamic mechanical analyzer (RSA3, TA Instruments) at room temperature. A parallel-plate geometry was used in free extension mode, with an applied strain rate of 0.5% s^{-1}. The elastic modulus was calculated as the slope of the linear region of the stress-strain data, approximately between 4% and 10% strain values.

3.3.5 Ionic Conductivity Measurements

Electrochemical impedance spectroscopy (EIS) was performed in order to determine electrolyte ionic conductivity values using a potentiostat with a built-in frequency response analyzer (VersaSTAT 3, Princeton Applied Research). EIS spectra were collected over a frequency range of 1-100 kHz with a sinusoidal voltage amplitude of 10 mV. Room temperature ionic conductivity measurements were performed using a custom PTFE well apparatus inside of a nitrogen-filled glovebox. The temperature dependence of ionic conductivity was measured using electrolytes sealed inside of CR2032 coin cells; these coin cells were placed on a temperature-controlled stage equipped with resistive heating and liquid nitrogen cooling (LTS 420, Linkam Scientific Instruments). Impedance spectra for the coin cell samples were collected at temperatures between 0 °C and 30 °C in 5 °C increments, with an isothermal hold of approximately 10 minutes at each temperature to allow the coin cell to thermally equilibrate. Apparent activation energy of ionic conductivity values were found by best-fit linear regression to the Arrhenius model.

3.3.6 Molecular Dynamics Simulations

In this study, atomistic molecular dynamics simulations were employed to understand the structural properties of the *ionogel precursor solutions.* Our model system for the precursor solution is comprised of ZI monomer (2-methacryloyloxyethyl phosphorylcholine, MPC) combined with 0.5 M X^+ $TFSI^-$/BMP TFSI ionic liquid electrolyte (where X^+ = Li^+, Na^+, or an

equimolar mixture of Li^+ and Na^+). Details regarding the simulation methodology and forcefield parameters are provided the Supporting Information.

3.3.7 Radial Distribution Functions

Ion-pair radial distribution functions, $g(r)$, were calculated using Equation 3.1 to describe the static interactions between species *i* and *j* in the precursor solutions and the corresponding base ILEs:

$$g_{ij}(r) = \frac{V}{4\pi r^2 N_i N_j} \sum_i \sum_j \langle \delta(r - r_{ij}) \rangle \qquad \text{(Eq. 3.1)}$$

Here, V is the volume of the simulation box, N_i and N_j are the number of molecules of species *i* and *j* respectively, and δ is the Dirac delta function. The $g(r)$ is used to define the association distance, r_{ij}, which is utilized to determine the average number of molecules, *j*, coordinated within the first coordination shell of species *i*. The association distance cutoff r_{ij} is determined by the position *r* where $g(r)$ is at its minimum after the first peak. For the MPC molecules, the phosphorus atom in the phosphonate group (PO_4^-) and the nitrogen atom in the quaternary amine group ($N^+(CH_3)_3$) were chosen to represent the anionic and cationic moieties in the ZI units, respectively. For the BMP^+ cation, the nitrogen atom in the pyrrolidinium ring is used to represent the IL cation; for $TFSI^-$, its nitrogen atom is selected to represent the common anion. Lastly, for the Li^+ ion, the Li^+ atom itself is used to obtain the $g(r)$.

3.4 Results and Discussion

Room temperature ionic conductivity values were obtained for ionogels containing 3-15 wt.% poly(MPC) in each of the three different ILEs at a 0.5 M total alkali metal ion concentration (Li^+ only, Na^+ only, or a 1:1 molar mixture of Li^+:Na^+). The results are displayed in Figure 3.2a. An alkali metal salt concentration of 0.5 M was used in this study due to the poor solubility of NaTFSI in BMP TFSI at 1 M (Appendix A, Figure A.1). For reference, the ionic conductivity of each neat ILE was also measured (*i.e.* 0 wt.% poly(MPC)). As the three ILEs possessed slightly different ionic conductivities (Li^+ only > 1:1 mixture > Na^+ only), *normalized* room temperature ionic conductivity values for each ionogel type (*i.e.* relative to its neat ILE value, σ/σ_{ILE}) are plotted in Figure 3.2b. For all three ILE systems, an initial boost in ionic conductivity was observed in the presence of a poly(MPC) network at low ZI contents (up to ~6 wt.%), beyond which the conductivity was found to decrease. The highest value of normalized ionic conductivity observed (~1.14, a 14% increase relative to neat ILE) was for 6 wt.% poly(MPC) in both the Na^+ only and the 1:1 mixed alkali metal ionogels. This boost in ionic conductivity realized at low ZI contents can be attributed to increased dissociation of ion pairs and ion clusters within the ILE due to Coulombic interaction with the ZI groups, which liberates a larger number of mobile ions.[21] For larger ZI polymer contents, the decrease in ionic conductivity seen with increasing ZI content reflects a reduction in the liquid electrolyte fraction within the ionogels (*i.e.* a reduced density of mobile ions). Temperature dependent ionic conductivity measurements performed over a moderate range (0-30 °C) yielded apparent activation energies of total ionic conductivity for the single-salt ionogels that were lower in the presence of both 5 wt.% and 10 wt.% poly(MPC) compared to those of their neat ILEs (Figure A.2). However, changing the identity of the alkali metal (Li^+ vs.

Na^+) in the ionogels was not observed to significantly affect the level by which the apparent activation energy of ionic conductivity was reduced.

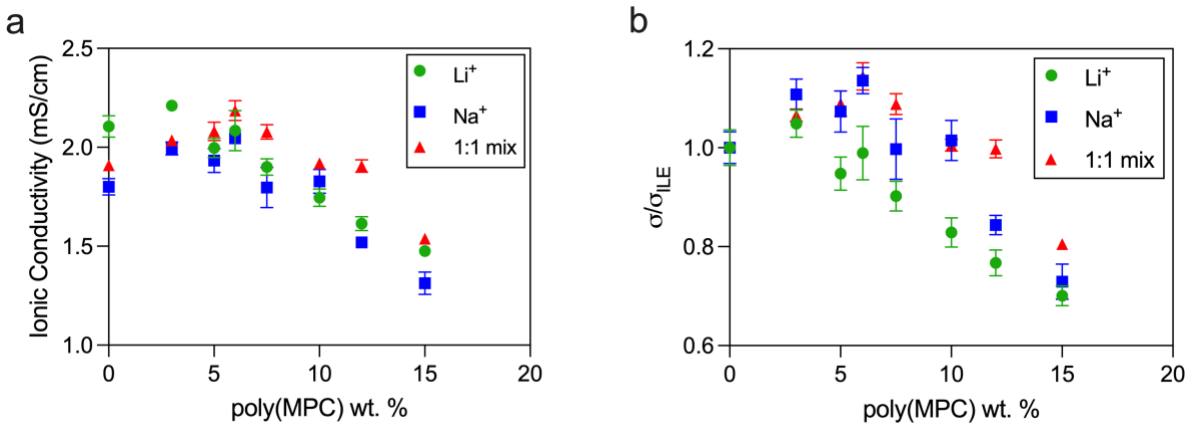


Figure 3.2. (a) Room temperature ionic conductivity values of poly(MPC)-supported ionogels synthesized *in situ* using 0.5 M LiTFSI in BMP TFSI ("Li^+"), 0.5 M NaTFSI in BMP TFSI ("Na^+"), or 0.5 M LiTFSI:NaTFSI (1:1 molar mixture) in BMP TFSI ("1:1 mix"). Neat ILE conductivity values for each electrolyte are shown at 0 wt.% poly(MPC) content. Values displayed are an average of 3 samples, with error bars indicating one standard deviation. (b) Normalized ionic conductivity values for the same ionogels (relative to the ionic conductivities of their base ILEs).

Ionogel elastic modulus values were determined using stress-strain data obtained via compression testing. Importantly, it was found that Na^+ only ionogels exhibited larger elastic moduli compared to those based on the Li^+ only ILE (Figure 3.3a), with the difference being especially notable at lower ZI polymer contents (3-7.5 wt.%). A larger elastic modulus value for a polymer-supported ionogel indicates a higher cross-link density within the polymer scaffold network. It is worth emphasizing that in these ionogels, all of the cross-links are noncovalent in nature and enabled by alkali metal cation interactions with ZI groups on neighboring polymer chains.[35] Indeed, the presence of the alkali metal salt is necessary both to sufficiently solubilize the MPC monomer in the ILE and to obtain visually homogeneous, transparent ionogels (Figure A.3). Therefore, these findings reveal that there are a greater number of alkali metal cation-mediated Coulombic cross-links formed per unit volume when Na^+ is present compared to Li^+ (for this ionogel system). The largest difference in elastic moduli between the two pure alkali metal cation ionogels was observed at the lowest polymer content studied here (3 wt.% poly(MPC)), where the elastic modulus of the Li^+ only ionogel is one order of magnitude lower than that of its Na^+ only counterpart (10.6 ± 2.1 kPa versus 111 ± 19 kPa, respectively). Elastic moduli of ionogels created using the 1:1 mixed alkali metal ILE at low poly(MPC) contents were also measured (Figure 3.3b). It was observed that the elastic moduli of the 1:1 mixed alkali metal ILE ionogels more closely resembled those of the Na^+ only ionogels, rather than those of the Li^+ only ionogels. This finding – that the 1:1 mixed alkali metal ILE ionogels are more similar to the Na^+ only ionogels (here, in terms of mechanical properties) – is also consistent with the normalized room temperature ionic conductivity trends for these materials, as well (see Fig. 3.2b).

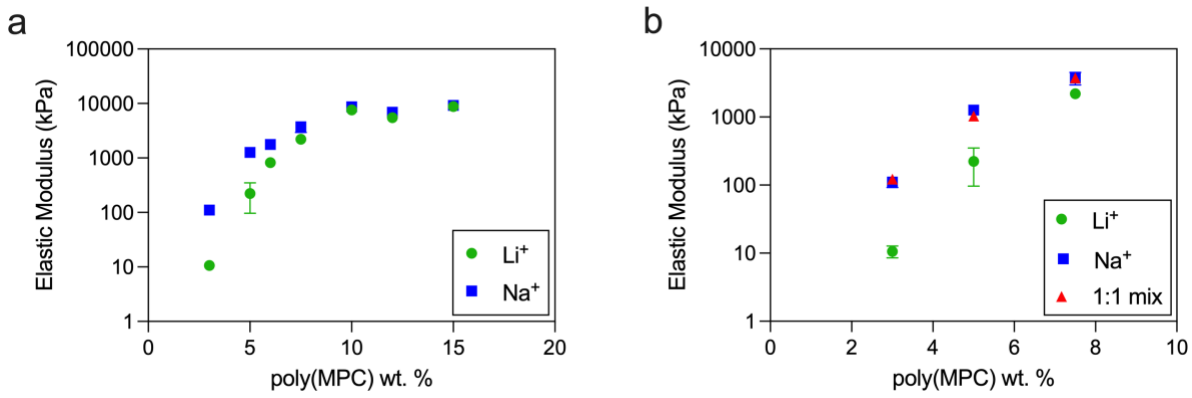


Figure 3.3. (a) Elastic modulus values of poly(MPC)-supported ionogels synthesized *in situ* using 0.5 M LiTFSI in BMP TFSI ("Li^+") or 0.5 M NaTFSI in BMP TFSI ("Na^+"). (b) Elastic modulus values of ionogels with low poly(MPC) contents for Li^+, Na^+, or 0.5 M LiTFSI:NaTFSI (1:1 molar mixture) in BMP TFSI ("1:1 mix") ILE. Values displayed are an average of 3 samples, with error bars indicating one standard deviation.

As noted previously, the ionogels studied here are supported by Coulombic cross-links that are hypothesized to originate from alkali metal cation/ZI monomer clusters that spontaneously assemble upon dissolution of the ZI monomers into the ILE.[35] Following *in situ* photopolymerization of the precursor solution, those clusters that bridge neighboring polymer chains can become cross-links within the resulting ionogel (Fig. 3.1b). Given this picture, it was deemed prudent to simulate the *ionogel precursor solutions*, in order to examine any potential differences in the alkali metal cation solvation environment (by ZI monomers and/or $TFSI^-$ anions) based on alkali metal cation identity (Li^+ vs. Na^+) and MPC content.

To gain insight into potential reasons why the ionic conductivity and mechanical properties of these ionogels were observed to depend on the chemical identity of the alkali metal cation, atomistic molecular dynamics simulations were performed to determine the structural properties of the ionogel precursor solutions. To understand the impact of ZI monomer content on the structure of the precursor solutions, the composition of the base ILE was held constant and the weight percentage of MPC monomers (W_{MPC}) was varied. Figures 3.4a and 3.4b display the radial distribution functions ($g(r)$) for Li^+–MPC and Na^+–MPC, respectively, as a function of the weight percentage of MPC (W_{MPC}) in the single-salt systems. In the context of equilibrium molecular dynamics, the intensity of the $g(r)$, especially the peak value, can be used to indirectly infer the relative interaction strengths between the two alkali metal cations with the anionic portion of MPC. By comparing the principal peaks of the $g(r)$, it can be observed that Li^+–MPC exhibits significantly higher interaction strength than Na^+–MPC, which is consistent with the smaller ionic radius and greater charge density of Li^+ compared to Na^+. The interaction strength between either alkali metal cation with the MPC monomer does not appear to change significantly with monomer content. Since ionogels were formed experimentally across this compositional range in both cases,

it is evident that the interaction strength of either alkali metal cation with the MPC monomer is of a sufficient magnitude to establish cation-mediated Coulombic cross-links. In addition, the ionogels did not display any self-healing behavior at room temperature, indicating the highly robust nature of the cross-links formed within the polymerized ionogel materials.

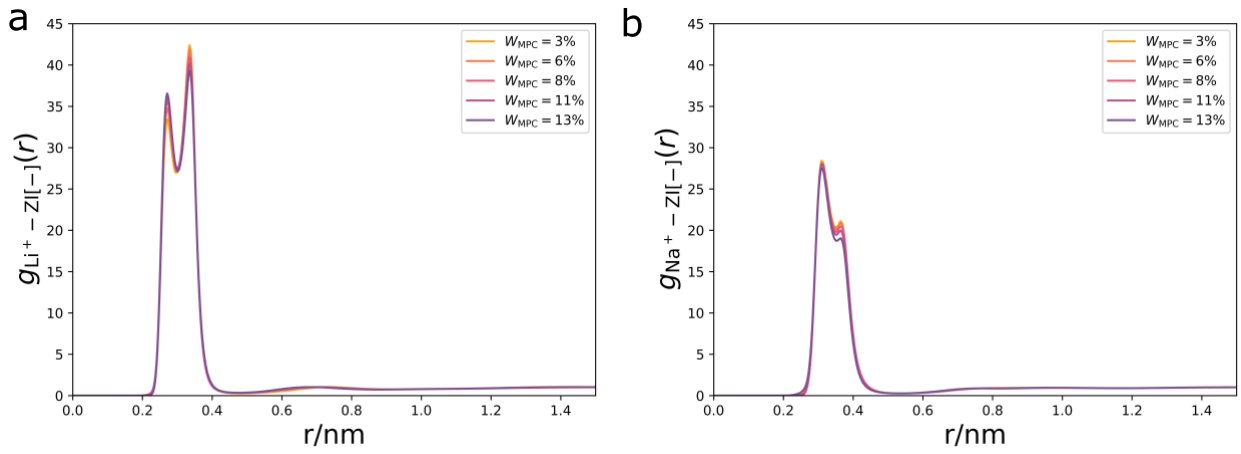


Figure 3.4. Radial distribution functions calculated for (a) Li^+ and ZI[-] and (b) Na^+ and ZI[-] at five different weight percentages of MPC monomer (W_{MPC}) in the single-salt ionogel precursor solutions. ZI[-] represents the anionic portion (PO_4^-) of the MPC molecule.

The effect of MPC concentration on the interaction of Li^+ or Na^+ with $TFSI^-$ in the single-salt precursor solutions was also investigated using the simulation results (Figure 3.5). Both the Li^+–$TFSI^-$ interaction and Na^+–$TFSI^-$ interaction strengths were found to decrease with increasing W_{MPC}. Overall, the preferential association of alkali metal ions with MPC and their decreasing interaction with $TFSI^-$ suggests the replacement of the $TFSI^-$ molecules from the solvation shell of Li^+ or Na^+.

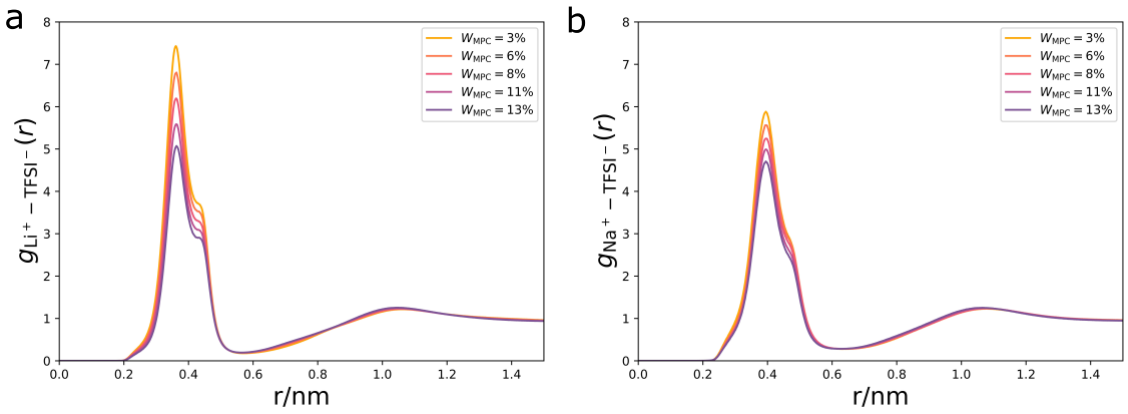


Figure 3.5. Radial distribution functions calculated for (a) Li^+ and $TFSI^-$, and (b) Na^+ and $TFSI^-$ at five different weight percentages of MPC monomer fraction (W_{MPC}) in the single-salt ionogel precursor solutions.

Simulations were further employed to examine the alkali metal cation/MPC coordination behavior within the precursor solutions in terms of the number of Li^+/Na^+–MPC "clusters" and cluster size distribution. A cluster was defined as a group of alkali metal cations/MPC monomers with overlapping coordination/solvation shells at a given time point in the simulation (*i.e.* direct associations). Figure 3.6 displays the number of Li^+/Na^+–MPC clusters as a function of cluster size for the simulated ionogel precursor solutions. For increasing $W_{MPC,}$ an increase in the overall number of clusters is observed in both single-salt and mixed-alkali metal cation precursor solutions (see also Figure A.5). This can be attributed to the increasing number of ZI molecules in the system with increasing W_{MPC}. Calculated alkali metal cation–MPC association lifetimes revealed approximately three times longer associations for Li^+–MPC compared to Na^+–MPC ion pairs, in both the single and mixed salt precursor solutions (Figure A.6).

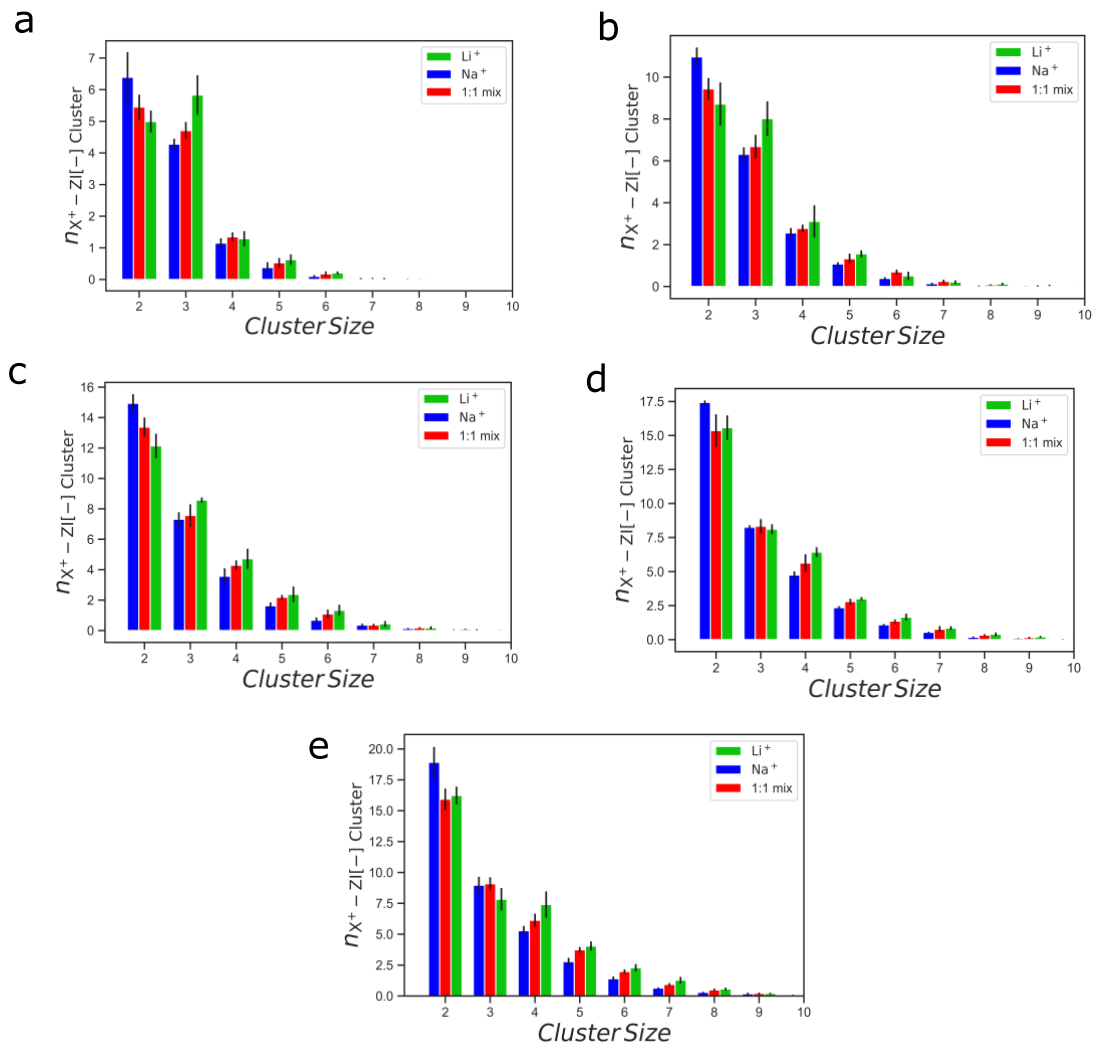


Figure 3.6. Number of clusters versus cluster size calculated for precursor solutions containing different weight percentages of MPC monomers (W_{MPC}): (a) 3 wt.%, (b) 6 wt.%, (c) 8 wt.%, (d), 11 wt.%, and (e) 13 wt.%. ZI[-] and X^+ represent the anionic portion (PO_4^-) of the MPC molecule and the alkali metal ion(s), respectively.

In Figure 3.6, it can be seen that for all W_{MPC} values simulated, a greater number of clusters of size three or larger were present for the Li^+ only systems compared to Na^+ only precursor solutions. We hypothesize that this leads to different Coulombically cross-linked network structures formed upon *in situ* polymerization within the Li^+ versus Na^+ ILE precursor solutions. One possibility is that the greater number of smaller clusters in the Na^+ only system may lead to more connections being formed between clusters upon polymerization, since smaller clusters would be expected to have higher mobility within the precursor solution compared to larger clusters. As these clusters can then become cross-links in the fully polymerized ionogel, this could explain the experimental observation of a higher elastic modulus for the Na^+ only ionogels compared to the Li^+ only ionogels (Figure 3.7). Moreover, larger clusters may be hypothesized to lead to a greater number of intramolecular cross-links (*i.e.* within a single polymer chain) upon polymerization, which would be expected to reduce the elastic modulus. For the 1:1 mixed alkali metal ILE precursors, the simulations also yielded cluster size distributions that were generally more similar to those of the Na^+ only precursors (Fig. 3.6). This agrees with the experimental observation that the elastic modulus values (and therefore the Coulombic cross-link densities) of the 1:1 mixed alkali metal ionogels were comparable to those of the Na^+ only ionogels (Fig. 3.3b).

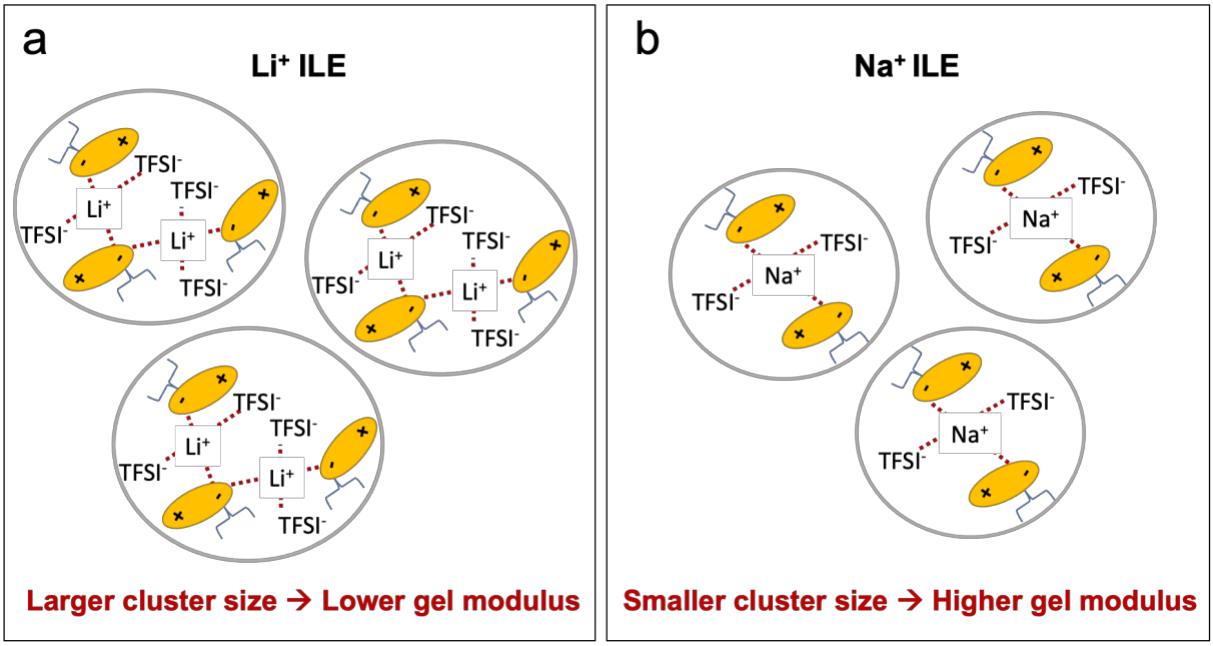


Figure 3.7. Schematic illustration showing the qualitative difference between the simulated alkali metal cation–MPC cluster sizes within ionogel precursor solutions, which lead to different experimentally-observed ionogel elastic modulus values: (a) Li^+ only ILE, (b) Na^+ only ILE.

3.5 Conclusions

This study has examined the ionic conductivity levels and mechanical properties of a series of ZI homopolymer-supported ionogels that were synthesized by *in situ* UV-initiated photopolymerization. A comparison of ionogels containing LiTFSI, NaTFSI, or a 1:1 equimolar mixture of these salts at a concentration of 0.5 M has illuminated some of the effects that alkali metal cation identity can yield on the properties of these electrolytes. Molecular dynamics simulations have revealed a difference in the alkali metal cation/MPC monomer cluster size distribution that forms within the ionogel precursor solutions, with the Na^+ ILE mixtures yielding somewhat smaller clusters compared to the Li^+ ILE mixtures. This may explain the experimental observation that Na^+ ionogels exhibited larger elastic modulus values (indicative of higher Coulombic cross-link densities) compared to their Li^+ counterparts, particularly at low ZI polymer contents. The simulations also suggested that the alkali metal cation/MPC cluster size distributions of the 1:1 mixed alkali metal precursor solutions were more similar to those of the Na^+ only precursors, which supports the good agreement found experimentally between the normalized ionic conductivity and elastic modulus values of these two groups of ionogel materials. Ionogels such as those examined in this work are nonflammable, highly conductive, and stiff enough to be free-standing, making them attractive alternatives to conventional battery electrolytes that are flammable and prone to leakage.

3.6 Author Contribution and Acknowledgements

M.K.A. performed the experimental work. M.Y.T. performed the molecular dynamics simulations. V.G. and M.J.P. supervised the work.

M.K.A. and M.J.P. gratefully acknowledge financial support from the National Science Foundation (CBET-2234243 and CBET-2217188). M.Y.T. and V.G. have been generously supported by the Robert A. Welch Foundation (F-1599) and National Science Foundation (DMR-2225167). M.Y.T. and V.G. acknowledge the Texas Advanced Computing Center (TACC) for the generous allocation of computing resources

3.7 References

1. Tang, X.; Lv, S.; Jiang, K.; Zhou, G.; Liu, X. Recent development of ionic liquid-based electrolytes in lithium-ion batteries. *J. Power Sources* **2022**, *542*, 231792.
2. Sasaki, Y. Organic Electrolytes of Secondary Lithium Batteries. *Electrochemistry* **2008**, *76*, 2-15.
3. Amanchukwu, C. V.; Chang, H.-H.; Gauthier, M.; Feng, S.; Batcho, T. P.; Hammond, P. T. One-Electron Mechanism in a Gel–Polymer Electrolyte Li–O_2 Battery. *Chem. Mater.* **2016**, *28*, 7167-7177.
4. Wu, F.; Zhang, K.; Liu, Y.; Gao, H.; Bai, Y.; Wang, X.; W, C. Polymer electrolytes and interfaces toward solid-state batteries: Recent advances and prospects. *Energy Storage Mater*. **2020**, *33*, 26-54.
5. Feuillade, G.; Perche, P. Ion-conductive macromolecular gels and membranes for solid lithium cells. *J. Appl. Electrochem*. **1975**, *5*, 63-69.
6. Rogers, R. D.; Seddon, K. R. Ionic Liquids--Solvents of the Future? *Science* **2003**, *302*, 792-793.

7. Armand, M.; Endres, F.; MacFarlane, D. R.; Ohno, H.; Scrosati, B. Ionic-liquid materials for the electrochemical challenges of the future. *Nat. Mater.* **2009**, *8*, 621-629.

8. MacFarlane, D. R; Forsyth, M.; Howlett, P. C.; Kar, M.; Passerini, S.; Pringle, J. M.; Ohno, H.; Watanabe, M.; Yan, F.; Zheng, W. et al. Ionic liquids and their solid-state analogues as materials for energy generation and storage. *Nat. Rev. Mater*. **2016**, *1*, 15005.

9. Kalhoff, J.; Eshetu, G. G.; Bresser, D.; Passerini, S. Safer Electrolytes for Lithium-Ion Batteries: State of the Art and Perspectives. *ChemSusChem* **2015,** *8*, 2154-2175.

10. Le Bideau, J.; Viau, L.; Vioux, A. Ionogels, ionic liquid based hybrid materials. *Chem. Soc. Rev*. **2011**, *40*, 907-925.

11. Chen, N.; Zhang, H.; Li, L.; Chen, R.; Guo, S. Ionogel Electrolytes for High-Performance Lithium Batteries: A Review. *Adv. Energy Mater*. **2018**, *8*, 1702675.

12. Néouze, M.-A.; Le Bideau, J.; Gaveau, P.; Bellayer, S.; Vioux, A. Ionogels, New Materials Arising from the Confinement of Ionic Liquids within Silica-Derived Networks. *Chem. Mater.* **2006**, *18*, 3931-3936.

13. Wang, M.; Zhang, P.; Shamsi, M.; Thelen, J. L.; Qian, W.; Truong, V. K.; Ma, J.; Hu, J.; Dickey, M. D. Tough and stretchable ionogels by in situ phase separation. *Nat. Mater.* **2022**, *21*, 359-365.

14. Osada, I.; de Vries, H.; Scrosati, B.; Passerini, S. Ionic-Liquid-Based Polymer Electrolytes for Battery Applications. *Angew. Chem. Int. Ed. Engl*. **2016**, *55*, 500-513.

15. Qian, W.; Texter, J.; Yan, F. Frontiers in poly(ionic liquid)s: syntheses and applications. *Chem. Soc. Rev*. **2017**, *46*, 1124-1159.

16. Zhang, S.-Y.; Zhuang, Q.; Zhang, M.; Wang, H.; Gao, Z.; Sun, J.-K.; Yuan, J. Poly(ionic liquid) composites. *Chem Soc. Rev*. **2020**, *49*, 1726-1755.

17. Tang, J.; Tang, H.; Sun, W.; Plancher, H.; Radosz, M.; Shen, Y. Poly(ionic liquid)s: a new material with enhanced and fast CO_2 absorption. *Chem. Commun.* **2005,** *26*, 3325-3327.

18. Taylor, M. E.; Panzer, M. J. Fully-Zwitterionic Polymer-Supported Ionogel Electrolytes Featuring a Hydrophobic Ionic Liquid. *J. Phys. Chem. B* **2018**, *122*, 8469-8476

19. Shaplov, A. S.; Marcilla, R.; Mecerreyes, D. Recent Advances in Innovative Polymer Electrolytes based on Poly(ionic liquid)s. *Electrochim. Acta* **2015**, *175*, 18-34.

20. Lin, D.; Liu, W.; Liu, Y.; Lee, H. R.; Hsu, P.-C.; Liu, K.; Cui, Y. High Ionic Conductivity of Composite Solid Polymer Electrolyte via In Situ Synthesis of Monodispersed SiO_2 Nanospheres in Poly(ethylene oxide). *Nano Lett*. **2016**, *16*, 459-465.

21. D'Angelo, A. J.; Panzer, M. J. Decoupling the Ionic Conductivity and Elastic Modulus of Gel Electrolytes: Fully Zwitterionic Copolymer Scaffolds in Lithium Salt/Ionic Liquid Solutions. *Adv. Energy Mater.* **2018**, *8*, 1801646.

22. Byrne, N.; Howlett, P. C.; MacFarlane, D. R.; Forsyth, M. The Zwitterion Effect in Ionic Liquids: Towards Practical Rechargeable Lithium-Metal Batteries. *Adv. Mater.* **2005**, *17*, 2497-2501.

23. Sun, J.; MacFarlane, D. R.; Bryne, N.; Forsyth, M. Zwitterion effect in polyelectrolyte gels based on lithium methacrylate-N,N-dimethyl acrylamide copolymer. *Electrochim. Acta* **2006**, *51*, 4033-4038.

24. Lind, F.; Rebollar, L.; Bengani-Lutz, P.; Asatekin, A.; Panzer, M. J. Zwitterion-Containing Ionogel Electrolytes. *Chem. Mater*. **2016**, *28*, 8480-8483.

25. D'Angelo, A.J.; Panzer, M. J. Design of Stretchable and Self-Healing Gel Electrolytes via Fully Zwitterionic Polymer Networks in Solvate Ionic Liquids for Li-Based Batteries. *Chem. Mater.* **2019**, *31*, 2913-2922.

26. Rebollar, L.; Panzer, M. J. Zwitterionic Copolymer-Supported Ionogel Electrolytes: Impacts of Varying the Zwitterionic Group and Ionic Liquid Identities. *ChemElectroChem* **2019**, *6*, 2482-2488.

27. Qin, H.; Panzer, M. J. Zwitterionic Copolymer-Supported Ionogel Electrolytes Featuring a Sodium Salt/Ionic Liquid Solution. *Chem. Mater.* **2020**, *32*, 7951-7957.

28. Woo, H.-S.; Son, H.; Min, J.-Y.; Rhee, J.; Lee, H.-T.; Kim, D.-W. Ionic liquid-based gel polymer electrolyte containing zwitterion for lithium-oxygen batteries. *Electrochim. Acta* **2020**, *345*, 136248.

29. Li, Z. H.; Xia, Q. L.; Liu, L. L.; Lei, G. T.; Xiao, Q. Z.; Gao, D. S.; Zhou, X. D. Effect of zwitterionic salt on the electrochemical properties of a solid polymer electrolyte with high temperature stability for lithium ion batteries. *Electrochim. Acta* **2010**, *56*, 804-809.

30. Zhang, Z.; Zhang, P.; Liu, Z.; Du, B.; Peng, Z. A Novel Zwitterionic Ionic Liquid-Based Electrolyte for More Efficient and Safer Lithium–Sulfur Batteries. *ACS Appl. Mater. Interfaces* **2020**, *12*, 11635-11642.

31. Lee, J. H.; Shin, J. C.; Kim, J.; Ho, J.-W.; Cho, W.-J.; Park, M. J.; Yi, G.-R.; Lee, Minjae; Yoo, P. J. Zwitterionic surfactant–stabilized ionogel electrolytes with high ionic conductivity for lithium secondary batteries. *J. Power Sources* **2023**, *557*, 232565.

32. Narita, A.; Shibayama, W.; Sakamoto, K.; Mizumo, T.; Matsumi, N.; Ohno, H. Lithium ion conduction in an organoborate zwitterion–LiTFSI mixture. *Chem. Commun*. **2006**, *18*, 1926-1928.

33. Wohde, F.; Bhandary, R.; Moldrickx, J. M.; Sundermeyer, J.; Schönhoff, M.; Roling, B. Li^+ ion transport in ionic liquid-based electrolytes and the influence of sulfonate-based zwitterion additives. *Solid State Ion*. **2016**, *284*, 37-44.

34. Yamaguchi, S.; Fujita-Yoshizawa, M.; Zhu, H.; Forsyth, M.; Takeoka, Y.; Rikukawa, M. Improvement of charge/discharge properties of oligoether electrolytes by zwitterions with an attached cyano group for use in lithium-ion secondary batteries. *Electrochim. Acta*. **2015**, *186*, 471-477.

35. Wieck, K. W.; Panzer, M. J. Ionogel Electrolytes Supported by Zwitterionic Copolymers Featuring Lithium Ion-Mediated, Noncovalent Cross-Links. *ACS Appl. Polym. Mater.* **2023**, *5*, 2887-2894.

Chapter 4: Understanding the Effects of Li^+ Salt Concentration and Zwitterion/Li^+ Stoichiometry on Ion Coordination in Zwitterionic Polymer-Supported Ionogel Electrolytes

This chapter is reproduced from the following manuscript:

Alsaedi, M. K.; Panzer, M. J. "Understanding the Effects of Li^+ Salt Concentration and Zwitterion/ Li^+ Stoichiometry on Ion Coordination in Zwitterionic Polymer-Supported Ionogel Electrolytes" *(submitted)*

4.1. Abstract

Ionogel electrolytes are nonflammable, non-leaking alternatives to conventional flammable organic solvent-based electrolytes. In this study, zwitterionic poly(2-methacryloxyethyl phosphorylcholine) (pMPC) homopolymer-supported ionogels were synthesized using solutions consisting of three different molarities of a lithium salt dissolved in an ionic liquid: 0.5 M, 1 M, and 2 M LiTFSI dissolved in 1-butyl-1-methylpyrrolidinium bis(trifluoromethyl sulfonyl)imide (BMP TFSI). The zwitterionic monomer (MPC) content was varied relative to the lithium ion concentration in order to realize ionogels containing molar ratios of 0.25, 0.5, and 0.75 mol MPC/mol Li^+ for each solution. All ionogels exhibited room temperature ionic conductivity values higher than those of their respective lithium salt solutions, with the greatest boost being ~50%. Elastic modulus values for ionogels created using the 0.5 M solution showed the widest range of tunability (0.5 kPa to 1750 kPa), corresponding to an estimated increase in the noncovalent cross-link density from approximately 9×10^{-6} nm^{-3} to 4×10^{-2} nm^{-3}. Deconvoluted Raman spectra revealed that the percentage of $TFSI^-$ anions coordinated with Li^+ increases from 24% to 71% as the concentration of Li^+ in the solution increases from 0.5 M to 2 M. Within the ionogels synthesized using these solutions, the percentage of $TFSI^-$ anions coordinated with Li^+ was observed to decrease with increasing MPC/Li^+ molar ratios. Calculated Li^+ coordination number (by $TFSI^-$) values, as well as the normalized ionic conductivity data, were both found to exhibit common behaviors across all three LiTFSI molarities when plotted versus the MPC/Li^+ molar ratio. These findings demonstrate that stoichiometry (*i.e.* zwitterionic unit/Li^+ molar ratio), rather than polymer mass fraction, plays a more fundamental role as a key parameter

in determining the properties of poly(MPC)-supported ionogel electrolytes, which are a promising safer alternative to traditional battery electrolyte materials.

4.2. Introduction

The demand for batteries has been increasing with a growing need for electrochemical energy storage devices. Ensuring the safe operation of batteries is crucial, especially when used in applications such as wearable electronics and electrical vehicles where the users would be at direct risk in the event of a catastrophic battery failure. Conventional battery electrolytes are composed of flammable organic solvents such as ethylene carbonate, which are not entirely safe due to the potential of leakage and combustion upon certain battery failure modes, such as thermal runaway.[1-4] Solid-state electrolytes offer a safer alternative to liquid ones. However, the solid nature of the electrolyte typically limits its room temperature ionic conductivity.[1, 5]

Gel electrolytes have been of interest due to their combination of both solid-like and liquid-like properties: liquid-like ionic conductivity due to the high liquid fraction and solid-like mechanical integrity due to a solid supporting network.[1, 5-7] Ionic liquids (ILs), which are nonflammable and highly conductive salts that are often liquid at room temperature, have been proposed as a safer option for preparing gel electrolytes (known as ionogels).[1, 8-11] The solid fraction of the ionogel electrolyte may be a polymerized IL,[12-15] a cross-linked polymer,[16-18] or an inorganic scaffold.[19-21]

Zwitterionic (ZI) polymers have recently shown promising benefits for supporting ionogel electrolytes due to their favorable interaction with the ILs. The large dipole moments inherent to many ZI functional groups can help to maintain a high ionic conductivity by facilitating the

dissociation of ion pairs/aggregates[1, 20, 22-30] while also realizing a high level of mechanical robustness.[1, 20, 24, 31-34] Polymeric phosphorylcholine-type ZI ionogel scaffolds have been previously shown to assemble via the formation of noncovalent cross-links that are mediated by alkali metal cations present in the ionogel (*e.g.* Li^+ or Na^+).[1, 35] Moreover, it has been demonstrated that the ZI monomer 2-methacryloxyethyl phosphorylcholine (MPC) cannot be dissolved to any significant extent in the ionic liquid 1-butyl-1-methylpyrrolidinium bis(trifluoromethyl sulfonyl)imide (BMP TFSI) in the absence of an alkali metal cation, suggesting that ZI monomer-alkali metal cation assemblies, which can later become noncovalent cross-linking points, are formed in solution prior to polymerization.[1]

Since the alkali metal cation (*e.g.* Li^+) is known to play a critical role in enabling the dissolution of MPC into a LiTFSI/BMP TFSI solution, its concentration in the ionic liquid is an important factor in the design of Li^+-containing, pMPC-supported ionogels. On the one hand, a lower LiTFSI concentration will minimize the viscosity increase of the solution and maintain a higher total ionic conductivity; however, low LiTFSI concentrations also limit the maximum amount of MPC monomer that can be dissolved in the LiTFSI/BMP TFSI solution, since Li^+ cations are necessary to solubilize the monomer in this particular ionic liquid. Therefore, in this study, we sought to gain a broader understanding of the MPC/Li^+ stoichiometric design space on the total ionic conductivity, stiffness, and ion coordination of pMPC-supported ionogels formed using three different ionic liquid/salt solutions: 0.5 M, 1 M, and 2 M LiTFSI in BMP TFSI. These particular lithium salt concentrations were selected to provide insights into the trade-offs of using both lower and higher LiTFSI molarities that center around the widely-used 1 M benchmark reported in the field. Homopolymer pMPC-supported ionogels were achieved by *in situ* UV photoinitiated free radical polymerization of MPC monomers dissolved in a LiTFSI/BMP TFSI solution. Depending

on the LiTFSI molarity used, visually transparent and free-standing ionogels could be realized using MPC contents as low as 2.5 wt.% and as high as 23 wt.%. However, given the envisioned ZI monomer/Li^+ assembly that enables MPC dissolution and results in noncovalent cross-link formation upon network polymerization, we conclude that the MPC/Li^+ molar ratio, rather than the polymer mass fraction, plays a more fundamental role in determining certain ionogel characteristics.

4.3. Experimental Methods

4.3.1. Materials

LiTFSI (99.5% Solvionic), BMP TFSI (99% Iolitec Ionic Liquids Technologies, GmbH), and 2-hydroxy-2-methypropiophenone (HOMPP) (97% Sigma-Aldrich) were stored in a nitrogen-filled glovebox. 2-methacryloxyethyl phosphorylcholine (MPC, 97%, MilliporeSigma) was stored in a refrigerator.

4.3.2. LiTFSI/BMP TFSI solution preparation

In a nitrogen-filled glovebox, LiTFSI was dissolved in BMP TFSI to make 0.5 M, 1 M, and 2 M salt solutions (approximately 9, 17, and 29 wt.% LiTFSI, respectively) by stirring at 70

°C and 400 rpm overnight. All salt solutions were cooled to room temperature (approximately 25 °C) before use.

4.3.3. Ionogel precursor solution preparation

In a nitrogen-filled glovebox, desired amounts of MPC were dissolved in 0.5 M, 1 M, or 2 M salt solution to make ionogel precursor solutions. The mixtures were stirred at 80 rpm at room temperature until the MPC was fully dissolved and the solution became visually transparent. HOMPP (photoinitiator) was then added to the precursor solution (20 μL HOMPP per 1 g MPC) and stirred at 80 rpm for ~20 s. Then, either salt solutions or HOMPP-containing ionogel precursor solutions were pipetted into ionic conductivity test molds, mechanical analysis test molds, or Raman spectroscopy vials. The ionogel precursor solutions were exposed to 365 nm UV light for 10 min (UV lamp Spectronic Corp., 8 W). The ionogels were rested overnight in the nitrogen-filled glovebox before any characterizations were performed.

4.3.4. Total ionic conductivity measurements

The molds into which the salt solutions were pipetted and the ionogel precursor gelled for ionic conductivity measurements were ~125 μL-internal volume polytetrafluoroethylene (PTFE) wells containing two gold-coated electrodes. Elechtrochemical impedance spectroscopy (EIS) was performed using a potentiostat (VersaSTAT 3, Princeton Applied Research) with a built-in frequency response analyzer. The frequency range was 1-100 kHz with 10 mV sinusoidal voltage

amplitude. Ionic conductivity values were calculated from the impedance measurements obtained at the phase angle values closest to zero degrees.

4.3.5. Ionogels for mechanical analysis

Ionogels for mechanical testing were cured in PTFE washers (6.35 mm inner diameter and 3.15 mm thickness), then demolded. Elastic modulus values for the ionogels were calculated from stress-strain measurements that were obtained by using a texture analyzer (TA.XTPlus 100 Connect, Texture Technologies Corp.). The ionogels were compressed at a rate of 0.01 mm/sec until 15% strain was achieved. The elastic modulus was calculated as the slope of the line between 4% and 10% strain for each ionogel.

To estimate the cross-link density (ρ_x) within ionogels, Eq. 4.1 was used,[36] where N_A is Avogadro's number, E is the ionogel elastic modulus, $\emptyset$ is the polymer volume fraction in the ionogel, R is the universal gas constant and T is room temperature (298 K). To estimate the polymer volume fraction in each ionogel (see Table B.1), Eq. 4.2 was used, where the density of the salt solution (ρ_{sol}) was determined by measuring the mass of 1 mL of solution and the density of the ionogel ($\rho_{ionogel}$) was found by measuring the weight of the gel and dividing by the approximate gel volume. ρ_{sol} values were 1.46, 1.49, and 1.55 g/mL for the 0.5 M, 1 M, and 2 M salt solutions, respectively. $\rho_{ionogel}$ values (1.35, 1.45, and 1.48 g/mL for ionogels synthesized using 0.5 M, 1 M, and 2 M salt solutions, respectively) were found to be essentially unchanged across the different pMPC contents examined in this study.

$$\rho_x = \frac{N_A E}{3\emptyset^{-\frac{2}{3}} RT} \qquad \text{(Eq. 4.1)}$$

$$\emptyset = 1 - \left(\frac{(100 - pMPC\ wt.\%)}{\rho_{sol}} \div \frac{100}{\rho_{ionogel}} \right) \quad \text{(Eq. 4.2)}$$

Using the calculated cross-link density values, the percentage of non-cross-linked lithium cations in each ionogel was determined using Eq. 4.3, which assumes that each lithium cation-mediated noncovalent cross-link formed between ZI groups on adjacent pMPC chains contains one Li^+ cation.[1]

$$\%\ \text{non} - \text{cross} - \text{linked}\ Li^+ = \left(\frac{\text{Overall}\ Li^+\ \text{molarity} - \rho_x \left(c\text{onverted to units of} \frac{mol}{L} \right)}{\text{Overall}\ Li^+\ \text{molarity}} \right) \times 100\% \quad \text{(Eq. 4.3)}$$

4.3.6. Raman spectroscopy

Vials (Fisherbrand, 1.5 mL Class A Clear Glass Threaded Vials) containing LiTFSI/BMP TFSI solutions or pMPC-supported ionogels were used in a Raman spectrometer (Renishaw inVia Raman Microscope, UK). The following Raman parameters were used for all samples: 700 cm^{-1} wavenumber centering, 785 nm laser, 1800 l/mm grating, 2 s exposure time, and 10 accumulations. Raman spectra baseline correction was performed using a 2nd order polynomial fit and integration was conducted between 730 and 760 cm^{-1}. Curve fitting for two deconvolution peaks, centered at ~742 and ~748 cm^{-1}, was performed via non-linear regression between 720 and 770 cm^{-1} to obtain the areas under the curves. The percentage of $TFSI^-$ ions coordinating with either BMP^+ (peak at ~742 cm^{-1}) or with Li^+ (peak at ~748 cm^{-1}) was estimated by dividing the area under each curve by the sum of areas under both curves and multiplying by 100. For each salt solution and ionogel, the average Li^+ solvation number by $TFSI^-$ values (Li^+ coordination number) were calculated by

dividing the moles of $TFSI^-$ coordinating with Li^+ by the moles of Li^+ in the system. The moles of $TFSI^-$ coordinating with Li^+ were calculated by multiplying the percentage of lithium-coordinated $TFSI^-$ ions by the total moles of $TFSI^-$ in the system. Tables B.2-B.5 summarize the calculated molar compositions and coordination number values of all samples.

4.4. Results and Discussion

The room temperature total ionic conductivity values for the ionogels and their parent salt solutions were determined using EIS measurements, and the results are displayed in Figure 4.1. Figure 4.1a shows the ionic conductivity values plotted as a function of ZI polymer mass fraction (pMPC wt.%), from which several observations can be made. First, the total conductivity values of the LiTFSI/BMP TFSI solutions and their corresponding ionogels are highest for the 0.5 M samples, and lowest for the 2 M samples. This is due to the well-known increase in viscosity with more LiTFSI salt added to BMP TFSI, due to the formation of a greater number of $Li(TFSI)_n$ complexes, which reduces overall ion mobility. Secondly, it is evident that the presence of pMPC in the ionogels increases their total ionic conductivities compared to those of the parent salt solutions. This can be attributed to the dissociative effect that substantial ZI dipoles inherent to the pMPC repeat units have on cation/anion aggregates within these extremely ion-dense mixtures, producing a larger fraction of higher mobility ions (Li^+, $TFSI^-$, and BMP^+) that contribute to a boost in the total ionic conductivity of the ionogel.[1, 31] This improvement in overall ionic conductivity across the different LiTFSI molarity solutions is easier to visualize by normalizing the ionic conductivity values with respect to those of the parent LiTFSI/BMP TFSI solutions (Fig. 4.1b). Importantly, since lithium cations are required in order to dissolve the MPC monomer into this ionic liquid,[1] high pMPC contents

can only be realized using larger LiTFSI molarities, which is why the accessible polymer mass fraction window is different for different LiTFSI concentration solutions.

For this reason, we chose to synthesize ionogels featuring three common MPC/Li^+ molar ratios (0.25, 0.5, and 0.75 mol MPC/mol Li^+) across the different LiTFSI molarity solutions, since this resulted in visually transparent, freestanding ionogels in all cases. Figure 4.1c shows the same room temperature ionic conductivity values for all samples plotted versus the MPC/Li^+ molar ratio. What is most notable, though, is the plot of the normalized ionic conductivity values versus the MPC/Li^+ molar ratio (Fig. 4.1d). Here, the relative boost in the total ionic conductivity across all three LiTFSI molarity solutions appears to show a common behavior, with the greatest increase in normalized ionic conductivity seen to occur for ionogels at the lower range of ZI content (0.25 mol MPC/mol Li^+). While the inclusion of a relatively low amount of ZI polymer increases the total ionic conductivity, the conductivity level is known to eventually decrease at higher polymer amounts due to the corresponding reduced volume fraction of ionic charge carriers in the ionogel (the polymer itself is not conductive).[1, 33] Here, the maximum relative increase in ionic conductivity achieved for the pMPC ionogels compared to their parent solution was approximately 50% the 2 M ionogels containing 0.25 or 0.5 mol MPC/mol Li^+, as seen in Fig. 4.1d. The similarity of the normalized ionic conductivity trend with increasing MPC/Li^+ molar ratio provides a first observation that the zwitterion/alkali metal cation stoichiometry, rather than the polymer mass fraction, may be a more insightful design parameter for understanding the behavior of these ionogel electrolytes.

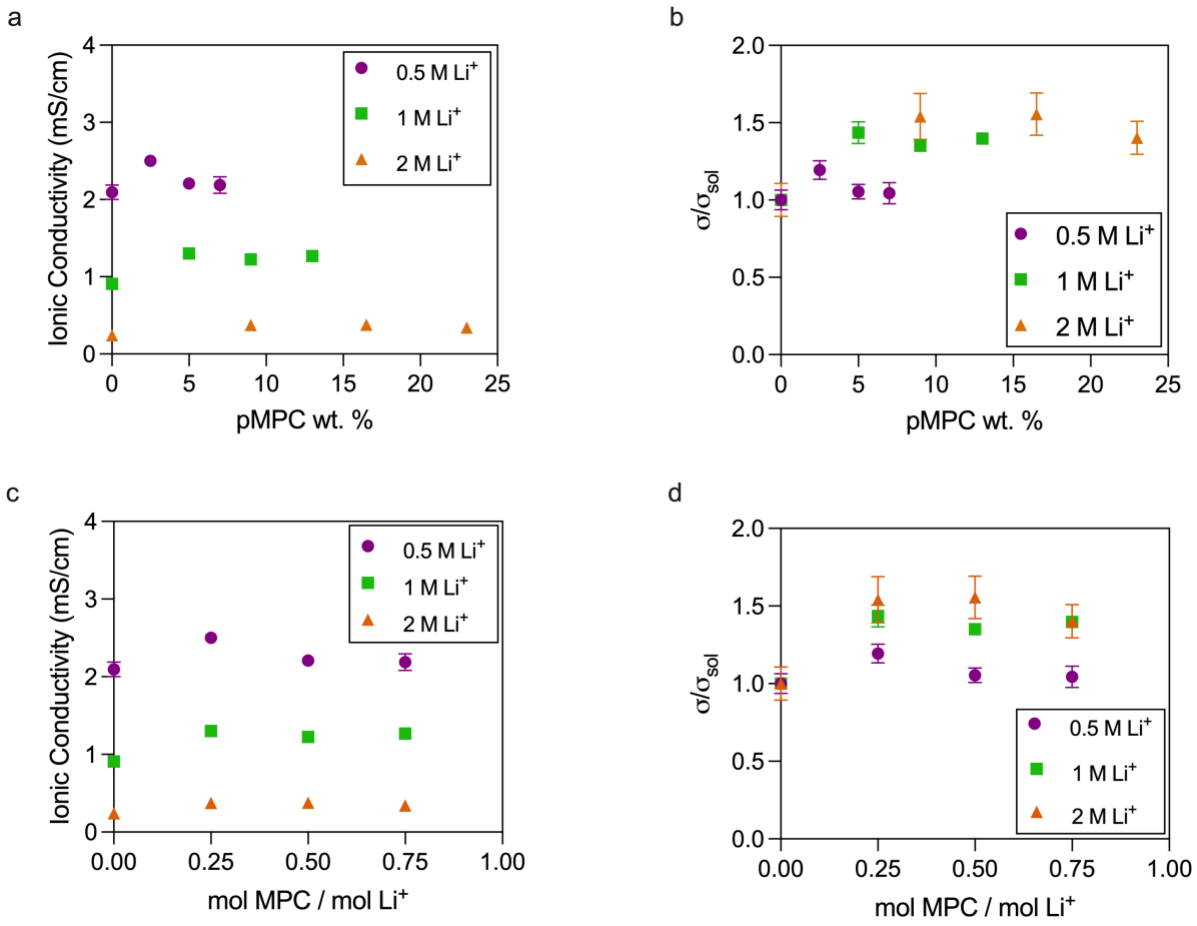


Figure 4.1. Room temperature (25 °C) total ionic conductivity values of 0.5 M, 1 M, and 2 M LiTFSI/BMP TFSI solutions and their pMPC-supported ionogels. **(a)** Total ionic conductivity plotted versus pMPC wt.%. **(b)** Normalized total ionic conductivity (with respect to the salt solution value) plotted versus pMPC wt.%. **(c)** Total ionic conductivity plotted versus the molar ratio of zwitterionic monomer repeat units to lithium cations (mol MPC/mol Li^+). **(d)** Normalized total ionic conductivity plotted versus the MPC/Li^+ molar ratio.

The dependence of ionogel stiffness and estimated noncovalent cross-link density values on MPC/Li^+ stoichiometry is shown in Figure 4.2. Ionogel elastic modulus values derived from compressive stress-strain measurements are displayed in Fig. 4.2a. It is evident that the elastic modulus values for ionogels of a given LiTFSI/BMP TFSI solution concentration increased with increasing pMPC content. In addition, elastic modulus values were also observed to increase with greater Li^+ molarity in the parent solution for all three fixed MPC/Li^+ molar ratios. This reinforces the notion that both ZI polymer functional groups and Li^+ cations are necessary components to form the noncovalently cross-linked networks that support these ionogels.[1, 35] Ionogel elastic modulus values were observed to vary by several orders of magnitude, depending on the stoichiometric composition. The softest ionogel corresponded to the 0.5 M LiTFSI sample prepared with 0.25 mol MPC/mol Li^+, which exhibited a modulus of 0.53 ± 0.02 kPa. The largest elastic modulus value (9.9 ± 0.2 MPa) was obtained for the 0.75 mol MPC/mol Li^+ ionogel created in 2 M LiTFSI solution, as it contained both the greatest concentration of Li^+ cations and the highest pMPC content (Fig. B.1).

Noncovalent cross-link density values (Fig. 4.2b) were estimated from the ionogel elastic modulus values via Eq. 4.1.[36] Cross-link densities were found to vary between 9 x 10^{-6} nm^{-3} and 0.33 nm^{-3} for the softest and stiffest ionogel formulations, respectively. Using these values, we also estimated the percentage of non-cross-linked Li^+ cations within each ionogel via Eq. 4.3, which assumes that each noncovalent cross-link contains one Li^+ cation. As shown in Fig. 4.2c, the percentage of non-cross-linked Li^+ cations within the ionogels created using a 0.25 MPC/Li^+ molar ratio was determined to be very high (>99.5% for all three LiTFSI solution molarities), which suggests that the vast majority of Li^+ cations are not immobilized in cross-links at this stoichiometric composition and contribute to a high normalized total ionic conductivity at this

composition (see Fig. 4.1d). Within the ionogel that exhibited the largest cross-link density (2 M LiTFSI solution, 0.75 MPC/ Li^+ molar ratio), the percentage of non-cross-linked Li^+ still remained quite high (73%), providing a large concentration of Li^+ cations (*i.e.* ~1.5 M) that should be able to contribute to the desired transport of Li^+ across the gel electrolyte, for example, within a lithium-ion battery.

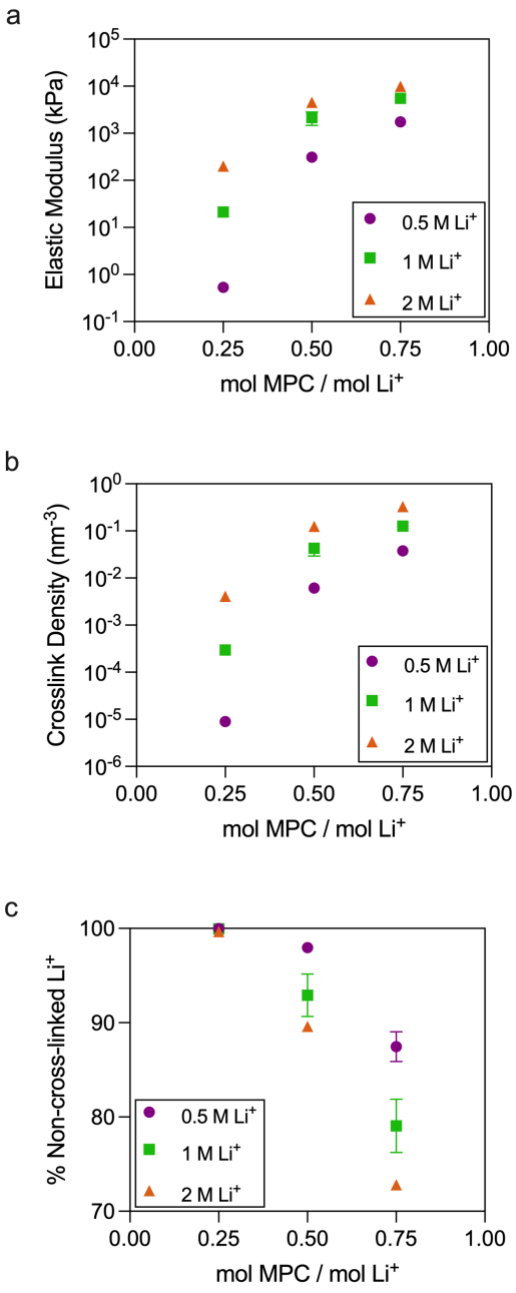


Figure 4.2. Characteristics of noncovalently cross-linked pMPC ionogel networks. (a) Elastic modulus, (b) cross-link density, and (c) estimated percentage of non-cross-linked Li^+ cation values.

The vibrational mode of $TFSI^-$ was probed by Raman spectroscopy performed on four liquid samples (neat BMP TFSI, as well as 0.5 M, 1 M, and 2 M LiTFSI/BMP TFSI solutions), and nine ionogels (0.25, 0.5, and 0.75 mol MPC/mol Li^+ prepared using 0.5 M, 1 M, and 2 M LiTFSI solutions) in order to examine the anion local coordination environment (Figure 4.3). As seen in Fig. 4.3a, the vibrational mode for $TFSI^-$ coordinating solely with BMP^+ corresponds to a single peak located at ~742 cm^{-1} (neat ionic liquid), while the appearance of a second peak located at ~748 cm^{-1} begins to appear with increasing LiTFSI concentration. This indicates the preferential coordination of $TFSI^-$ with Li^+ in this environment, corresponding to the formation of $Li(TFSI)_n$ complexes.[37, 38] Intensity changes of these two peaks within ionogels based on the 0.5 M, 1 M, and 2 M LiTFSI solutions that were created using different MPC/Li^+ molar ratios are shown in Fig. 4.3b-d. As the MPC content increases for a given LiTFSI solution molarity, the lower wavenumber peak increases and the higher wavenumber peak decreases, indicating that a greater fraction of $TFSI^-$ reverts to coordination with BMP^+ as ZI polymer content increases, which corroborates the idea that MPC can effectively outcompete $TFSI^-$ to coordinate with Li^+ when both anionic units are present (*i.e.* phosphate of MPC vs. $TFSI^-$). As discussed above, strong MPC-Li^+ coordination enables the formation of non-covalent cross-links that determine the ionogel mechanical properties (Fig. 4.2). The appearance of a small broad peak between 710 and 720 cm^{-1} seen in Fig. 4.3b-d is due to pMPC. It was confirmed that pMPC itself does not affect the vibrational mode of $TFSI^-$ in the absence of Li^+ (Fig. B.2).

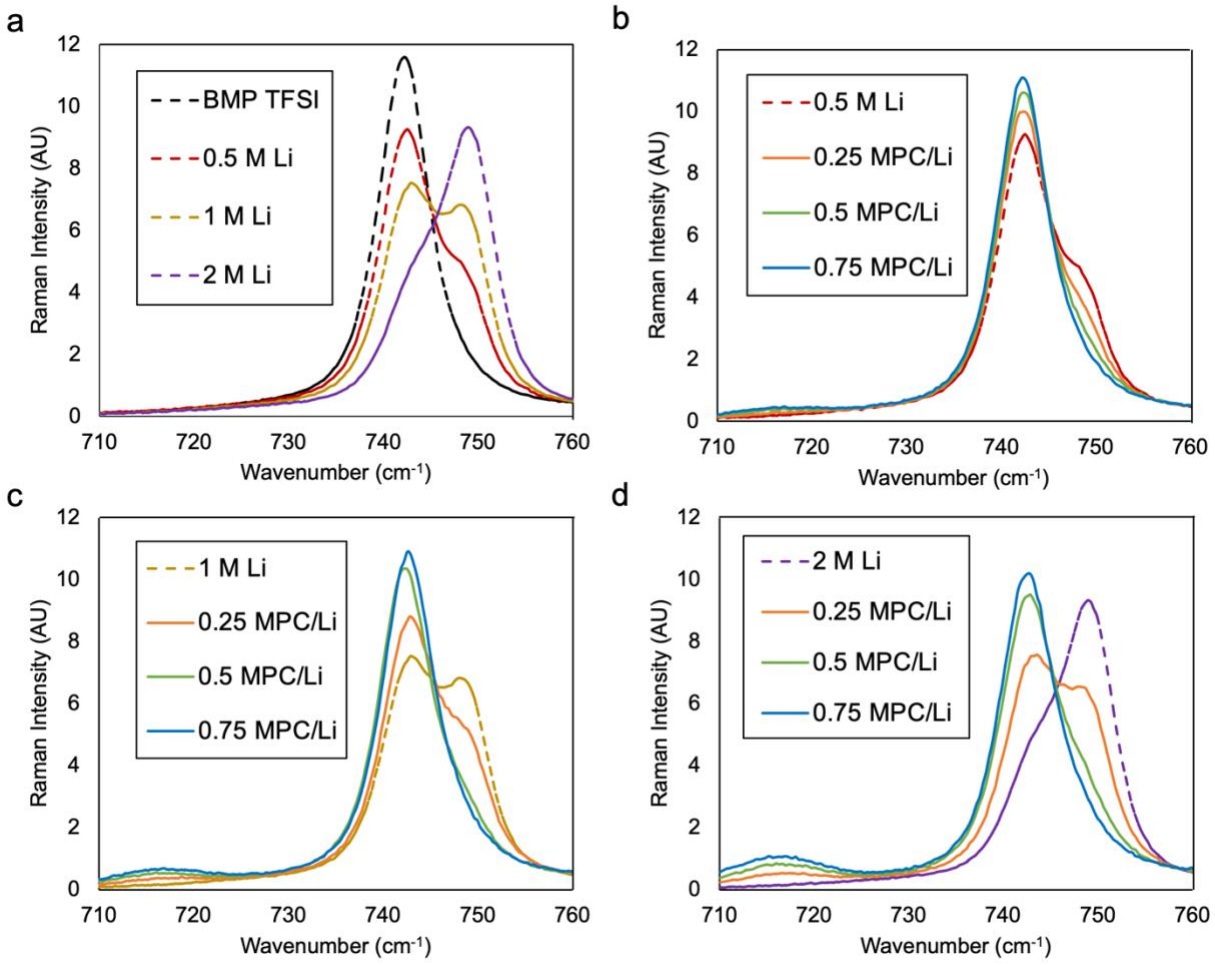


Figure 4.3. Raman spectra of liquid electrolyte and ionogel samples. (a) Neat BMP TFSI, 0.5 M, 1 M, and 2 M LiTFSI/BMP TFSI solutions. (b) 0.5 M LiTFSI solution and ionogels, (c) 1 M LiTFSI solution and ionogels, and (d) 2 M LiTFSI solution and ionogels. Ionogels were created from each LiTFSI solution at 0.25, 0.5, and 0.75 mol MPC/mol Li^+.

Spectral deconvolution and peak integration of the Raman data was performed in order to quantify the $TFSI^-$ population in each coordination state (*i.e.* primarily coordinating with BMP^+ or with Li^+). Figures B.3-B.6 show the deconvoluted and sum spectra for each sample. Figure 4.4 displays the calculated percentage of $TFSI^-$ anions present in each coordination state (with BMP^+ or Li^+) within the various liquid and ionogel environments. As seen in Fig. 4.4a, the percentage of $TFSI^-$ anions coordinating with Li^+ cations increases from 0% in neat BMP TFSI to 71% in 2 M LiTFSI/BMP TFSI solution. A linear regression to these values, in fact, suggests that $TFSI^-$ should be 100% coordinated with Li^+ at an extrapolated value of 2.7 M LiTFSI (Fig. B.7), which is reasonably close to the reported maximum room temperature solubility of LiTFSI in BMP TFSI.[39] With an increasing amount of ZI content in the ionogel samples, the percentage of Li^+-coordinating $TFSI^-$ anions decreases monotonically for each LiTFSI solution molarity (Fig. 4.4b-d), from approximately 24% to 7% for 0.5 M LiTFSI and from 71% to 16% in the case of 2 M LiTFSI as the MPC/Li^+ molar ratio increases from 0.25 to 0.75.

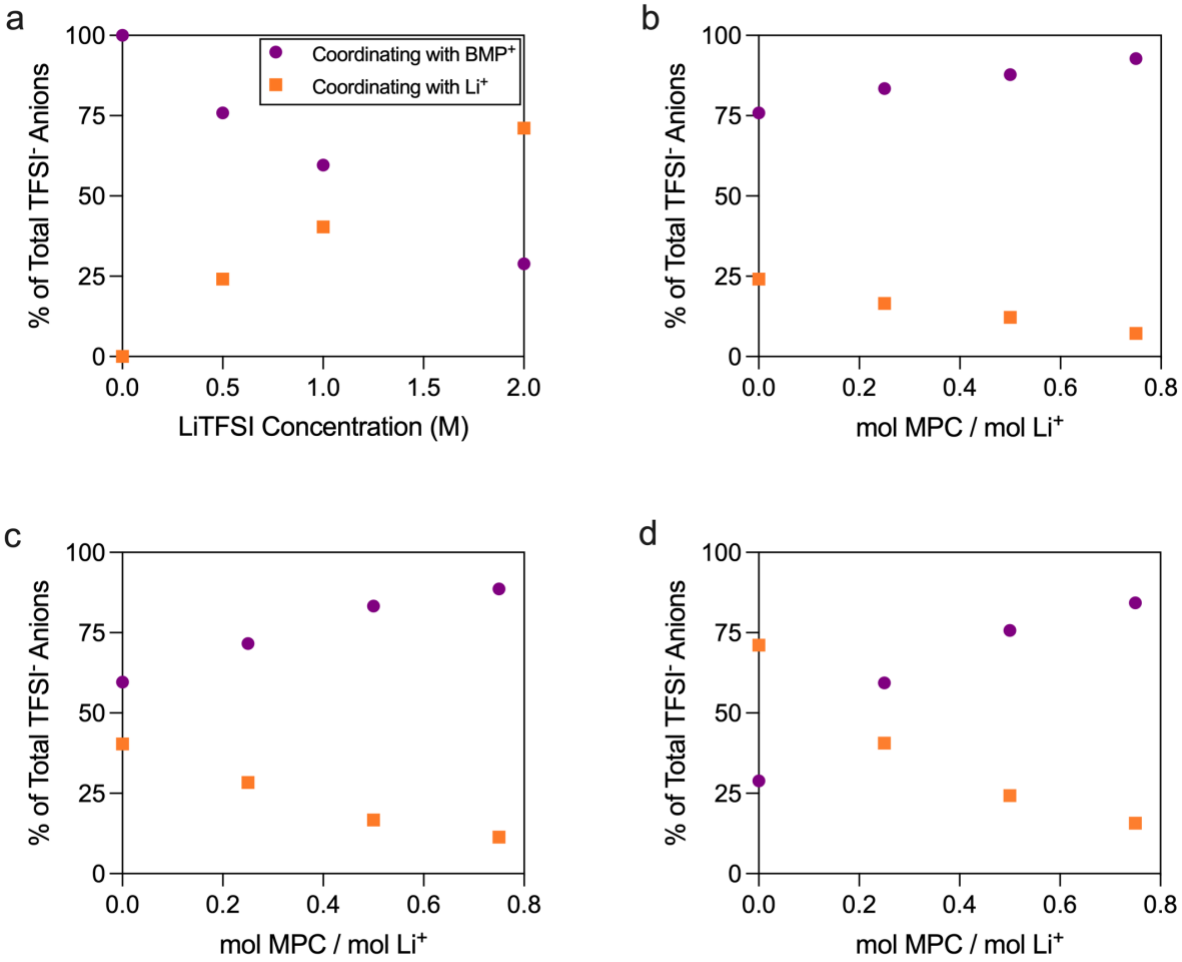


Figure 4.4. Percentage of total $TFSI^-$ anions coordinating with either BMP^+ or Li^+, calculated from deconvoluted Raman spectra. (a) Neat BMP TFSI, 0.5 M, 1 M, and 2 M LiTFSI/BMP TFSI solutions. (b) 0.5 M LiTFSI solution and ionogels, (c) 1 M LiTFSI solution and ionogels, and (d) 2 M LiTFSI solution and ionogels.

The number of $TFSI^-$ anions coordinating per Li^+ cation (Li^+ coordination number) was also calculated for each system using its molar composition and the values from Fig. 4.4 (Tables B.2-B.5). Figure 4.5 shows that the Li^+ coordination number is ~1.8 to 1.9 (about two $TFSI^-$ anions per Li^+ cation) in the LiTFSI/BMP TFSI solutions, in agreement with a previous report,[38] and is seen to decrease monotonically with greater pMPC content in the ionogels (down to ~0.4 to 0.5 for the 0.75 MPC/Li^+ molar ratio samples). When the Li^+ coordination number values are plotted versus the ZI polymer mass fraction (Fig. 4.5a), the greater maximum solubility of MPC with higher LiTFSI solution molarity is readily inferred. However, by plotting them versus the MPC/Li+ molar ratio (Fig. 4.5b), the data appear to once again collapse onto a common curve, reminiscent of a convergent trend observed when plotting the normalized ionic conductivity values on a similar x-axis (Fig. 4.1d). This finding supports the notion that ZI unit/Li^+ cation stoichiometry, rather than polymer mass fraction alone, is a more fundamental parameter to consider when designing this class of noncovalently cross-linked ionogel electrolytes.

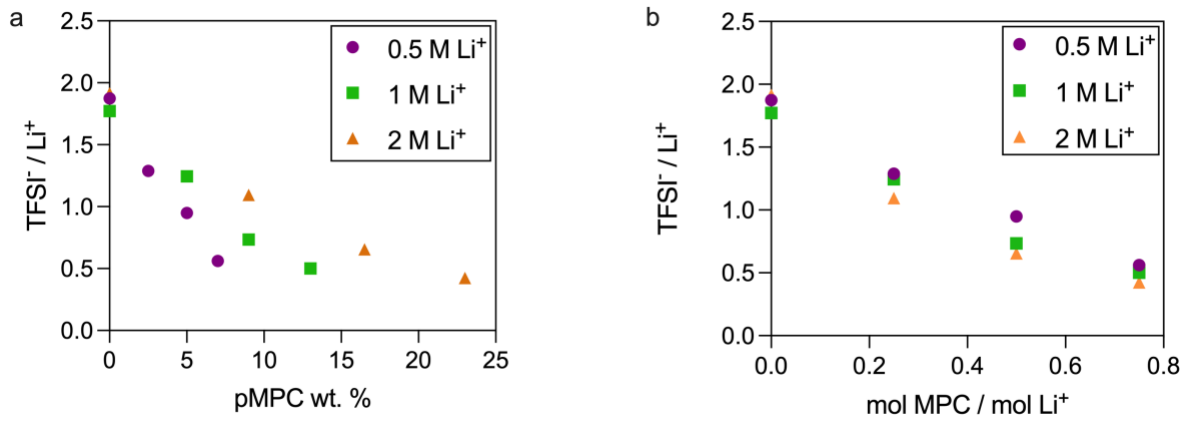


Figure 4.5. Number of $TFSI^-$ anions coordinating per Li^+ cation (Li^+ coordination number) calculated for LiTFSI solutions and ionogels, plotted as a function of either: (a) pMPC wt.%, or (b) MPC/Li^+ molar ratio.

4.5. Conclusions

In this study, zwitterionic pMPC-supported ionogels were synthesized via *in situ* UV-initiated polymerization across a wide range of polymer compositions and varying lithium salt concentrations. Room temperature ionic conductivity, elastic modulus, and the anion coordination environment within ionogels were all examined. The presence of the zwitterionic homopolymer network in these ionogels boosts the total ionic conductivity values compared to those of the polymer-free solutions. Since Li^+ cations are necessary for realizing the non-covalent cross-links that hold the polymer network together within the ionogels, both the zwitterionic unit/Li^+ molar ratio and the concentration of Li^+ present affect the elastic modulus and cross-link density values. Raman spectroscopy revealed that $TFSI^-$, which must coordinate with BMP^+ in the neat ionic liquid, coordinates preferentially with Li^+ when LiTFSI is present (dissolved to form an ionic liquid/salt solution). The population of $TFSI^-$ that coordinates with Li^+ increases as the concentration of Li^+ increases in the salt solution. However, when pMPC is synthesized within the salt solution to form an ionogel, $TFSI^-$ is found to coordinate less with Li^+ and more with BMP^+, which can be ascribed to the strong coordination of Li^+ by the negatively-charged phosphate group of MPC. The Li^+ coordination number by $TFSI^-$, which is found to be ~1.8-1.9 in the neat salt solution, decreases within all ionogels as the pMPC content increases. By comparing these trends of ionogel properties as a function of gel composition, this study demonstrates that the zwitterionic unit/Li^+ molar ratio is an important parameter that should be considered when designing pMPC-supported ionogel electrolytes.

4.6. Author Contribution and Acknowledgements

M.K.A. performed experimental investigation, data analysis, and writing. M.J.P. supervised and conceptualized the work, acquired the funding acquisition, and reviewed the writing. The authors would like to thank Professor David Kaplan in the Department of Biomedical Engineering at Tufts University for providing them with access to the texture analyzer used to obtain DMA data. The authors would also like to thank Professor Graham Leverick in the Department of Chemical and Biological Engineering at Tufts University for assisting them with the use of the Raman spectrometer. Financial support from the National Science Foundation (award numbers 2234243 and 2217188) is gratefully acknowledged.

4.7. References

(1) Alsaedi, M. K.; Tadesse, M. Y.; Ganesan, V.; Panzer, M. J. Zwitterionic Polymer Ionogel Electrolytes Supported by Coulombic Cross-Links: Impacts of Alkali Metal Cation Identity. *J. Phys. Chem. B* **2024**, *128* (13), 3273-3281. DOI: 10.1021/acs.jpcb.3c08144.

(2) Tang, X.; Lv, S.; Jiang, K.; Zhou, G.; Liu, X. Recent development of ionic liquid-based electrolytes in lithium-ion batteries. *J. Power Sources* **2022**, *542*, 231792. DOI: 10.1016/j.jpowsour.2022.231792.

(3) Sasaki, Y. Organic Electrolytes of Secondary Lithium Batteries. *Electrochem.* **2008**, *76* (1), 2-15. DOI: 10.5796/electrochemistry.76.2.

(4) Yamaguchi, M.; Sato, M.; Takeoka, Y.; Rikuakwa, M.; Yoshizawa-Fujita, M. Zwitterion-enhanced Performance of Pyrrolidinium-based Ionic Liquid Electrolytes as Sodium-ion Conductors. *Electrochim. Acta* **2025**, *527*, 146269. DOI: 10.1016/j.electacta.2025.146269.

(5) Amanchukwu, C. V.; Chang, H.-H.; Gauthier, M.; Feng, S.; Batcho, T. P.; Hammond, P. T. One-Electron Mechanism in a Gel–Polymer Electrolyte Li–O_2 Battery. *Chem. Mater.* **2016**, *28* (19), 7167-7177. DOI: 10.1021/acs.chemmater.6b03718.

(6) Wu, F.; Zhang, K.; Liu, Y.; Gao, H.; Bai, Y.; Wang, X.; Wu, C. Polymer Electrolytes and Interfaces Toward Solid-state Batteries: Recent Advances and Prospects. *Energy Storage Mater.* **2020**, *33*, 26-54. DOI: 10.1016/j.ensm.2020.08.002.

(7) Feuillade, G.; Perche, P. Ion-conductive Macromolecular Gels and Membranes for Solid Lithium Cells. *J. Appl. Electrochem.* **1975**, *5* (1), 63-69. DOI: 10.1007/BF00625960.

(8) Rogers, R. D.; Seddon, K. R. Ionic Liquids--Solvents of the Future? *Science* **2003**, *302* (5646), 792-793. DOI: 10.1126/science.1090313.

(9) Armand, M.; Endres, F.; Macfarlane, D. R.; Ohno, H.; Scrosati, B. Ionic-liquid Materials for the Electrochemical Challenges of the Future. *Nat. Mater.* **2009**, *8* (8), 621-629. DOI: 10.1038/nmat2448.

(10) MacFarlane, D. R.; Forsyth, M.; Howlett, P. C.; Kar, M.; Passerini, S.; Pringle, J. M.; Ohno, H.; Watanabe, M.; Yan, F.; Zheng, W.; et al. Ionic Liquids and Their Solid-state Analogues as Materials for Energy Generation and Storage. *Nat. Rev. Mater.* **2016**, *1* (2), 15005. DOI: 10.1038/natrevmats.2015.5.

(11) Kalhoff, J.; Eshetu, G. G.; Bresser, D.; Passerini, S. Safer Electrolytes for Lithium-Ion Batteries: State of the Art and Perspectives. *ChemSusChem* **2015**, *8* (13), 2154-2175. DOI: 10.1002/cssc.201500284.

(12) Osada, I.; de Vries, H.; Scrosati, B.; Passerini, S. Ionic-Liquid-Based Polymer Electrolytes for Battery Applications. *Angew. Chem. Int. Ed.* **2016**, *55* (2), 500-513. DOI: 10.1002/anie.201504971

(13) Qian, W.; Texter, J.; Yan, F. Frontiers in Poly(ionic liquid)s: Syntheses and Applications. *Chem. Soc. Rev.* **2017**, *46* (4), 1124-1159. DOI: 10.1039/C6CS00620E.

(14) Zhang, S.-Y.; Zhuang, Q.; Zhang, M.; Wang, H.; Gao, Z.; Sun, J.-K.; Yuan, J. Poly(ionic liquid) composites. *Chem. Soc. Rev.* **2020**, *49* (6), 1726-1755. DOI: 10.1039/C8CS00938D.

(15) Tang, J.; Tang, H.; Sun, W.; Plancher, H.; Radosz, M.; Shen, Y. Poly(ionic liquid)s: A New Material with Enhanced and Fast CO_2 Absorption. *Chem. Commun.* **2005**, (26), 3325-3327, 10.1039/B501940K. DOI: 10.1039/B501940K.

(16) Doyle, M.; Choi, S. K.; Proulx, G. High-Temperature Proton Conducting Membranes Based on Perfluorinated Ionomer Membrane-Ionic Liquid Composites. *J. Electrochem. Soc.* **2000**, *147* (1), 34. DOI: 10.1149/1.1393153.

(17) Mistry, M. K.; Subianto, S.; Choudhury, N. R.; Dutta, N. K. Interfacial Interactions in Aprotic Ionic Liquid Based Protonic Membrane and Its Correlation with High Temperature Conductivity and Thermal Properties. *Langmuir* **2009**, *25* (16), 9240-9251. DOI: 10.1021/la901330y.

(18) Ye, Y.-S.; Rick, J.; Hwang, B.-J. Ionic Liquid Polymer Electrolytes. *J. Mater. Chem. A* **2013**, *1* (8), 2719-2743, 10.1039/C2TA00126H. DOI: 10.1039/C2TA00126H.

(19) Shaplov, A. S.; Marcilla, R.; Mecerreyes, D. Recent Advances in Innovative Polymer Electrolytes based on Poly(ionic liquid)s. *Electrochim. Acta* **2015**, *175*, 18-34. DOI: 10.1016/j.electacta.2015.03.038.

(20) Lin, D.; Liu, W.; Liu, Y.; Lee, H. R.; Hsu, P.-C.; Liu, K.; Cui, Y. High Ionic Conductivity of Composite Solid Polymer Electrolyte via In Situ Synthesis of Monodispersed SiO_2 Nanospheres in Poly(ethylene oxide). *Nano Lett.* **2016**, *16* (1), 459-465. DOI: 10.1021/acs.nanolett.5b04117.

(21) Taylor, M. E.; Panzer, M. J. Fully-Zwitterionic Polymer-Supported Ionogel Electrolytes Featuring a Hydrophobic Ionic Liquid. *J. Phys. Chem. B* **2018**, *122* (35), 8469-8476. DOI: 10.1021/acs.jpcb.8b05985.

(22) Byrne, N.; Howlett, P. C.; Macfarlane, D. R.; Forsyth, M. The Zwitterion Effect in Ionic Liquids: Towards Practical Rechargeable Lithium-Metal Batteries. *Adv. Mater.* **2005**, *17* (20), 2497-2501. DOI: 10.1002/adma.200500595.

(23) Sun, J.; MacFarlane, D. R.; Byrne, N.; Forsyth, M. Zwitterion Effect in Polyelectrolyte Gels Based on Lithium Methacrylate-N,N-dimethyl Acrylamide Copolymer. *Electrochim. Acta* **2006**, *51* (19), 4033-4038. DOI: 10.1016/j.electacta.2005.11.017.

(24) Woo, H.-S.; Son, H.; Min, J.-Y.; Rhee, J.; Lee, H.-T.; Kim, D.-W. Ionic Liquid-based Gel Polymer Electrolyte Containing Zwitterion for Lithium-Oxygen Batteries. *Electrochim. Acta* **2020**, *345*, 136248. DOI: 10.1016/j.electacta.2020.136248.

(25) Li, Z. H.; Xia, Q. L.; Liu, L. L.; Lei, G. T.; Xiao, Q. Z.; Gao, D. S.; Zhou, X. D. Effect of Zwitterionic Salt on the Electrochemical Properties of a Solid Polymer Electrolyte with High Temperature Stability for Lithium Ion Batteries. *Electrochim. Acta* **2010**, *56* (2), 804-809. DOI: 10.1016/j.electacta.2010.09.068.

(26) Zhang, Z.; Zhang, P.; Liu, Z.; Du, B.; Peng, Z. A Novel Zwitterionic Ionic Liquid-Based Electrolyte for More Efficient and Safer Lithium–Sulfur Batteries. *ACS Appl. Mater. Interfaces* **2020**, *12* (10), 11635-11642. DOI: 10.1021/acsami.9b21655.

(27) Lee, J. H.; Shin, J. C.; Kim, J.; Ho, J.-W.; Cho, W. J.; Park, M. J.; Yi, G.-R.; Lee, M.; Yoo, P. J. Zwitterionic Surfactant–stabilized Ionogel Electrolytes with High Ionic Conductivity for Lithium Secondary Batteries. *J. Power Sources* **2023**, *557*, 232565. DOI: 10.1016/j.jpowsour.2022.232565.

(28) Narita, A.; Shibayama, W.; Sakamoto, K.; Mizumo, T.; Matsumi, N.; Ohno, H. Lithium Ion Conduction in an Organoborate Zwitterion–LiTFSI Mixture. *Chem. Commun.* **2006**, (18), 1926-1928. DOI: 10.1039/B517019B.

(29) Wohde, F.; Bhandary, R.; Moldrickx, J. M.; Sundermeyer, J.; Schönhoff, M.; Roling, B. Li^+ Ion Transport in Ionic Liquid-based Electrolytes and the Influence of Sulfonate-based Zwitterion Additives. *Solid State Ionics* **2016**, *284*, 37-44. DOI: 10.1016/j.ssi.2015.11.017.

(30) Rebollar, L.; Panzer, M. J. Zwitterionic Copolymer-Supported Ionogel Electrolytes: Impacts of Varying the Zwitterionic Group and Ionic Liquid Identities. *ChemElectroChem* **2019**, *6* (9), 2482-2488. DOI: 10.1002/celc.201900378.

(31) D'Angelo, A. J.; Panzer, M. J. Decoupling the Ionic Conductivity and Elastic Modulus of Gel Electrolytes: Fully Zwitterionic Copolymer Scaffolds in Lithium Salt/Ionic Liquid Solutions. *Adv. Energy Mater.* **2018**. DOI: 10.1002/aenm.201801646.

(32) Lind, F.; Rebollar, L.; Bengani-Lutz, P.; Asatekin, A.; Panzer, M. J. Zwitterion-Containing Ionogel Electrolytes. *Chem. Mater.* **2016**, *28* (23), 8480-8483. DOI: 10.1021/acs.chemmater.6b04456.

(33) Qin, H.; Panzer, M. J. Zwitterionic Copolymer-Supported Ionogel Electrolytes Featuring a Sodium Salt/Ionic Liquid Solution. *Chem. Mater.* **2020**, *32* (18), 7951-7957. DOI: 10.1021/acs.chemmater.0c02820.

(34) D'Angelo, A. J.; Panzer, M. J. Design of Stretchable and Self-Healing Gel Electrolytes via Fully Zwitterionic Polymer Networks in Solvate Ionic Liquids for Li-Based Batteries. *Chem. Mater.* **2019**, *31* (8), 2913-2922. DOI: 10.1021/acs.chemmater.9b00172.

(35) Wieck, K. W.; Panzer, M. J. Ionogel Electrolytes Supported by Zwitterionic Copolymers Featuring Lithium Ion-Mediated, Noncovalent Cross-Links. *ACS Appl. Polym. Mater.* **2023**, *5* (4), 2887-2894. DOI: 10.1021/acsapm.3c00110.

(36) Visentin, A. F.; Panzer, M. J. Poly(Ethylene Glycol) Diacrylate-Supported Ionogels with Consistent Capacitive Behavior and Tunable Elastic Response. *ACS Appl. Mater. Interfaces* **2012**, *4* (6), 2836-2839. DOI: 10.1021/am300372n.

(37) Umebayashi, Y.; Mitsugi, T.; Fukuda, S.; Fujimori, T.; Fujii, K.; Kanzaki, R.; Takeuchi, M.; Ishiguro, S.-I. Lithium Ion Solvation in Room-Temperature Ionic Liquids Involving Bis(trifluoromethanesulfonyl) Imide Anion Studied by Raman Spectroscopy and DFT Calculations. *J. Phys. Chem. B* **2007**, *111* (45), 13028-13032. DOI: 10.1021/jp076869m.

(38) Kerner, M.; Plylahan, N.; Scheers, J.; Johansson, P. Ionic Liquid Based Lithium Battery Electrolytes: Fundamental Benefits of Utilising Both TFSI and FSI Anions? *Phys. Chem. Chem. Phys.* **2015**, *17* (29), 19569-19581, 10.1039/C5CP01891A. DOI: 10.1039/C5CP01891A.

(39) Henderson, W. A.; Passerini, S. Phase Behavior of Ionic Liquid−LiX Mixtures: Pyrrolidinium Cations and $TFSI^-$ Anions. *Chem. Mater.* **2004**, *16* (15), 2881-2885. DOI: 10.1021/cm049942j

Chapter 5: The Role of Li^+ Ions in Polyzwitterionic Ionogels: a Gelator or Mobile Charge Carrier?

This chapter is reproduced from the following publication:

Arwish, S.; Alsaedi, M.K.; O'Hara, R. P.; Asatekin, A.; Panzer, M. J.; Schonhoff, M. "The Role of Li^+ Ions in Polyzwitterionic Ionogels: a Gelator or Mobile Charge Carrier?" *(accepted for publication in J. Phys. Chem. B)*

5.1 Abstract

Introducing zwitterionic (ZI) polymers to lithium-containing, ionic liquid-based electrolytes can change the dynamics and local environment of Li^+ ions. While Li^+ ions enable the formation of non-covalently cross-linked ionogels, they may also act as free charge carriers. Aiming at an understanding of these roles, we investigate Li^+ ion coordination and transport in ionogels consisting of 1-butyl-1-methyl pyrrolidinium bis(trifluoromethyl sulfonamide) (BMP TFSI), LiTFSI, and poly(2-(methacryloyloxyethyl phosphorylcholine)) p(MPC), obtained via *in situ* free radical polymerization. Ionic conductivity as well as self-diffusion of both IL ions benefit from increasing p(MPC) content, while Li^+ diffusion is reduced. Simultaneously, ^7Li spin relaxation documents Li^+ ion immobilization, attributed to a strong affinity of Li^+ to the negatively-charged phosphate group of p(MPC). Raman spectroscopy confirms decreasing TFSI-Li^+ coordination with increasing p(MPC) content. Mechanical analysis reveals a drastic increase in elastic modulus, suggesting noncovalent cross-link formation. Finally, the distribution of Li^+ on different sites, such as mobile and anion-coordinated, single chain-coordinated, or dual-chain cross-linking Li^+ is analyzed. The results allow for an in-depth discussion of the role of Li^+, partly acting as a cross-linker and partly as a mobile charge carrier, providing guidelines for optimizing the balance between ionic conductivity and mechanical strength.

5.2 Introduction

In modern society, the development and increasing use of electric vehicles and advanced portable electronics calls for the advancement of energy storage technologies. Supercapacitors and Li^+ ion-based batteries are widely used energy storage devices.[1] However, due to the nature of

their applications (airplanes, vehicles, wearable devices, etc.), it is crucial to ensure that they operate without posing any safety threats on their users. In currently employed batteries, a critical component concerning safety is the electrolyte.[2, 3] Its purpose is to provide high ionic conductivity, but no electronic conductivity. To this end, current electrolytes consist of a lithium salt in a carbonate mixture, with their flammability causing a severe risk.[4, 5] Therefore, in ongoing research, ionic liquids (ILs), which are salts that are liquid at room temperature, are being investigated as an alternative and promising class of thermally stable and nonvolatile solvents that could replace conventional liquid electrolytes.[6-11] Moreover, they also show broad electrochemical stability windows, making them suitable components for high voltage battery systems.[12-14] A further major advantage is their structural variety, which results in a plethora of combinations of different cation and anion motifs. This allows for significant tunability of physical and chemical properties,[13] and makes ILs highly versatile, allowing for their usage in hybrid electrolytes[15] as well as for beyond-Li battery technologies.[16]

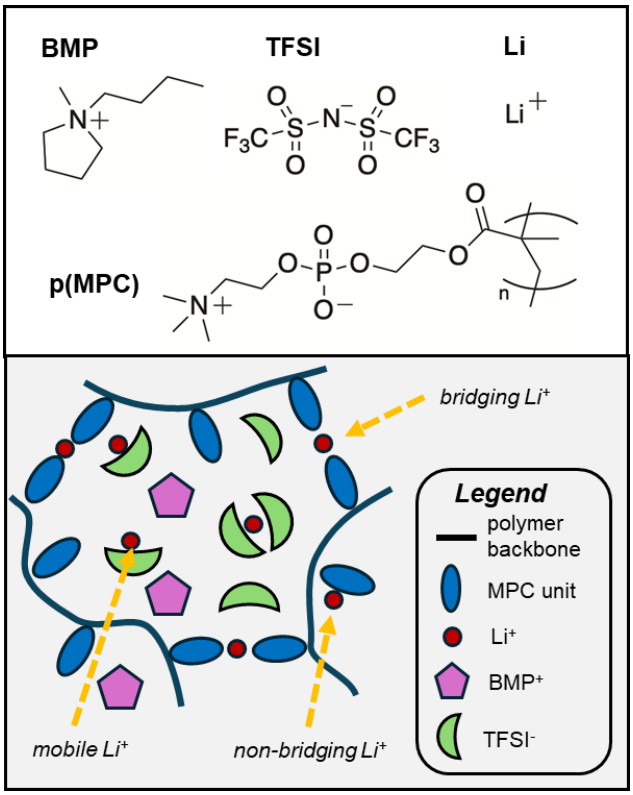
However, ILs often show strong Li^+ ion correlations and cluster formation, resulting in high viscosity and low Li^+ transference numbers.[17-21] Detailed studies based on MD simulations or Raman spectroscopy of the anion $TFSI^-$ could clarify the structural arrangement of Li^+-anion clusters, involving the determination of coordination numbers and the role of monodentate or bidentate coordinations.[22-26] Additionally, direct evidence of the role of such coordinated clusters in ion transport was given by electrophoretic NMR, when a vehicular transport of Li^+ ions in net negatively charged Li^+-anion clusters was identified in lithium salt-in-IL systems.[27, 28] This leads to an inverted Li^+ migration direction in an electric field and ultimately causes negative Li^+ transference numbers.[27, 29] Attempts to overcome the strong Li^+-anion coordination involved the use of asymmetric anions,[30, 31] or mixed anion compositions.[32] However, more successful

strategies were based on the addition of electrolyte constituents competing with the anions for Li^+ coordination. Following this concept, electrolyte compositions with either added cosolvents, polymer chains or coordinating cations, which provide Li^+ coordination, could finally revert the Li^+ ion drift direction.[33-35]

As an alternative approach to reduce Li^+-anion coordination, the introduction of zwitterionic (ZI) materials has proven to be beneficial.[36] ZI polymers have gained interest due to their ability to form three-dimensional solid scaffolds within a lithium salt/IL phase while maintaining ionic conductivity that is comparable to, and in some cases, higher than their fully liquid counterparts.[12, 37, 38] The presence of ZI moieties on the polymer chain can significantly affect Li^+ transport properties, with certain zwitterion chemistries promoting stronger interactions with Li^+, thereby reducing its mobility. Among various polyzwitterions, poly(2-methacryloyloxyethyl phosphorylcholine) (p(MPC)) in particular demonstrated excellent compatibility with a hydrophobic IL/lithium salt system.[39,] In these materials, Li^+ ions can assume different roles, on one hand behaving as a mobile species to facilitate Li^+ ion transport, and on the other hand acting as a gelator that can bridge p(MPC) chains, creating a nonflowing, IL phase-rich gel (ionogel). It is thus interesting to analyze the role of Li^+ in detail in order to identify the interplay of both roles, enabling further optimization of these electrolytes. A recent MD study has analysed Li coordination numbers and transport parameters in pMPC-based ionogels with different types of anions.[40]

Here, we investigate varying amounts of the ZI polymer p(MPC) prepared within a lithium salt-in-IL electrolyte, *i.e.* LiTFSI dissolved at a concentration of 1 mol/L in 1-butyl-1-methylpyrrolidinium bis(trifluoromethylsulfonyl)imide (BMP TFSI) mixed with the monomer MPC (see structures in Scheme 1). ZI p(MPC) (and consequently, above a certain minimum

polymer content, ionogels) are produced via photo-initiated in situ free radical polymerization. Ionic conductivity and pulsed field gradient NMR diffusion experiments elucidate overall charge transport as well as individual ionic constituent transport, and are complemented by Raman studies of anion coordination, dynamic mechanical analysis of the network, and spin relaxation of ^{7}Li. From these results, we analyze the coordination and mobility of Li^{+} ions, identifying three different proposed Li^{+} populations (see Scheme 5.1) that help to clarify the various roles that Li^{+} ions may play (*e.g.* mobile charge carrier versus immobilized cross-linker) within these materials for different ZI polymer contents.



Scheme 5.1. Structures of the main electrolyte components (top) and illustration of different Li^+ species within a p(MPC)-supported ionogel: bridging Li^+ that acts as noncovalent cross-linker between ZI units, non-bridging Li^+ coordinated to a single ZI unit, and mobile Li^+ in solution (bottom).

5.3 Materials and Methods

5.3.1. Materials

BMP TFSI (99%, Iolitec Ionic Liquids Technologies GmbH, or 99.9%, Solvionic), LiTFSI (99.95% trace metals basis, Sigma-Aldrich), and 2-hydroxy-2-methylpropiophenone (HOMPP, 97%, Sigma-Aldrich) were stored in a nitrogen-filled glovebox (Mbraun Inc., MBRAUN Unilab) or argon-filled glovebox (GS Glovebox Systemtechnik) until used. 2- methacryloyloxyethyl phosphorylcholine (MPC, 97%, Millipore Sigma, and Sigma-Aldrich) was stored in a refrigerator until used. Stainless-steel CR2032 coin-cell parts (SS304, MTI Corporation) and lithium discs (LIB-LIC60, MTI Corp.) were stored in an argon-filled glovebox (H_2O and O_2 < 0.5 ppm) until used. The LiTFSI salt was dried for 24 h at 100 ºC and 10^{-7} bar. All materials were used as received.

5.3.2. Ionogel preparation

As the basis for the ionogels, a stock lithium salt-in-IL solution was prepared by dissolving LiTFSI into the ionic liquid BMP TFSI at a concentration of 1 mol/L. All sample preparation and handling was performed in a glove box due the hygroscopic nature of LiTFSI and the MPC monomer. MPC monomer was first added to a glass vial, then the required amount of LiTFSI/IL solution was added to realize 2−14 wt % MPC “ionogel precursor” solutions. The resulting precursor solutions were stirred at 80 rpm at room temperature until MPC was completely dissolved and the mixture was transparent. The photoinitiator (HOMPP) was then added to the solutions (6 mol% with respect to the amount of MPC). The HOMPP-containing precursor solutions were then stirred at 80 rpm for 15 s. Molds or tubes relevant to the respective

characterization method were filled with precursor solution. They were then exposed to UV radiation (365 nm) from a hand-held lamp (Spectronic Corp., 8 W, or Winger Electronics., 3 W) in the containers for 10 min to initiate the in situ photopolymerization of the MPC. Ionogel samples cured overnight inside the glovebox prior to carrying out any characterization. Three replicate gels were prepared for each sample composition.

Samples for Pulsed Field Gradient NMR and Raman spectroscopy were directly prepared in 5 mm outer diameter NMR tubes. Ionogels for room temperature ionic conductivity measurements were prepared in cylindrical polytetrafluoroethylene (PTFE) 125 μL wells with gold-coated electrodes. For dynamic mechanical analysis (DMA), ionogel precursor solutions were injected with a needle and syringe into cylindrical PTFE washers (6.35 mm inner diameter and 3.15 mm thickness). PTFE washers were sandwiched between two glass slides and two thin films of polyethylene separating the washer mold cavity from the glass on each side to prevent the adherence of p(MPC) to the glass slides. Prior to DMA characterization, ionogels were removed from their PTFE washer molds.

5.3.3. Dynamic Light Scattering (DLS)

p(MPC) synthesized *in situ* in ionogels were analyzed by dynamic light scattering (Nano Brook 90Plus PALS particle sizer, Brookhaven Instruments, Holtsville, NY) to determine their Stokes' diameters in solution as an indicator of chain length. The instrument light source was a helium-neon laser with a fixed wavelength of 659 nm and an entrance aperture of 1 mm. Ionogels were mixed with ultra-pure deionized water inside a 15 mL centrifuge tube at a concentration according to the monomer content of each ionogel (2 mg monomer / 1 mL of solvent). BMP TFSI is insoluble in water, causing it to readily form a separate phase. However, p(MPC) is soluble in

water, allowing us to perform a simple liquid-liquid extraction. The Stokes diameter of the polymer contained in the water phase of the dissolved ionogel was measured at 25 °C using a scattering angle of 90°. Three gels were measured through three consecutive runs to obtain average Stokes diameter and polydispersity index values.

5.3.4. Ionic conductivity

Electrochemical impedance spectroscopy (EIS) was performed to determine ionogel ionic conductivities using a potentiostat with a built-in frequency response analyzer (VersaSTAT 3, Princeton Applied Research). EIS spectra were collected over a frequency range from 1 kHz to 100 kHz with a sinusoidal voltage amplitude of 10 mV. The values of ionic conductivity for each ionogel were calculated from the impedance values obtained at phase angle closest to zero (real impedance).

5.3.5. NMR spectroscopy and Pulsed-Field Gradient NMR (PFG NMR)

NMR spectra and diffusion experiments were performed on a Bruker AVANCE Neo 400 MHz or AVANCE III HD 400 MHz NMR spectrometer equipped with gradient amplifiers, using either a gradient probe head with selective radiofrequency inserts for ^{1}H or ^{19}F, (Bruker Diff50 with maximum gradient strength of 28.73 T/m) or a broad band diffusion probe head (Bruker, DIFF BBO, with maximum gradient strength of 17 T/m). Measurements were performed at room temperature (25°C), or in the range up to 65°C, respectively. Temperature control was provided by an air stream and an internal temperature sensor, which was calibrated prior to experiments using a Pt100 thermocouple (Greisinger electronics) inserted in an oil-filled NMR tube. The self-diffusion coefficients for the nuclei ^{1}H, ^{7}Li and ^{19}F were measured by PFG-NMR using a

stimulated echo pulse sequence and recording a series of spectra varying the gradient strength, g. The diffusion coefficients for distinct resonances were obtained from the decay of the signal intensity I with g employing the Stejskal-Tanner equation (Equation 5.1).[41]

$$I = I_0 \exp\left(-\gamma^2 \delta^2 g^2 D \left(\Delta - \frac{\delta}{3}\right)\right) \quad \text{(Eq. 5.1)}$$

Here, γ represents the gyromagnetic ratio of the observed nucleus, and I_0 indicates the signal intensity without gradient influence. The gradient pulse length duration δ was set to a fixed value between 1 and 2 ms, while the gradient strength g was incremented in a series of spectra up to a maximum value of 16 T/m, depending on the nature of the observed nucleus and sample. Spin relaxation rates R_1 and R_2 were determined by inversion recovery and a CPMG (Carr, Purcell, Meiboom, Gill)[42, 43] pulse sequence, respectively, and fitted with corresponding exponential functions.

5.3.6. Raman Spectroscopy

The same samples sealed in NMR tubes were inserted into a Raman spectrometer (MultiRAM, Bruker, Rheinstetten) equipped with a laser providing 263 mW at 1064 nm. The Raman spectra were recorded at room temperature in a range of (30 – 3600) cm^{-1} with a minimum resolution of 0.5 cm^{-1}. The spectra were baseline corrected and normalized to the integral of the Raman band region from 700 cm^{-1} to 800 cm^{-1}. Spectral decomposition was carried out using Voigt profiles fitting in OPUS software (Bruker, Rheinstetten). For the region a fixed contribution of 60% Lorentzian and 40% Gaussian is used. The peak position, intensity, and width were treated as free parameters during the fitting process.

5.3.7. Dynamic mechanical analysis

Elastic modulus values for ionogels were obtained by compressing the gels using a texture analyzer (TA.XT Plus 100, Texture Technologies Corp.) at room temperature. Compression was performed at 0.01 mm/sec to achieve 15% strain with respect to the ionogel thickness. Elastic moduli values were calculated as the slopes of the linear regions on the stress−strain curves between 4% and 10% strain values.

5.4. Results and Discussion

5.4.1. In situ polymerization and molecular weight

In order to characterize the molecular weight of p(MPC) produced by in situ polymerization and examine any potential effects of monomer concentration on average polymer size, as-prepared samples were immersed in ultra-pure deionized water to extract the ZI polymer. As a selective solvent, water dissolves p(MPC). The ionic liquid, BMP TFSI, has minimal solubility in water and thus creates a separate phase. The resulting aqueous solution likely also contains some LiTFSI (not quantified), though studies have shown that the Stokes diameter of p(MPC) is not significantly affected by salt concentration.[44, 45] This aqueous phase containing p(MPC) chains was analyzed with DLS to estimate the Stokes diameter, which is correlated with the molar mass of the polymer. Table 5.1 shows that as the p(MPC) wt % in the ionogel increases, the extracted p(MPC) Stokes diameter in aqueous solution was observed to decrease, which indicates a decrease in polymer molecular weight. The large Stokes diameter found in the 2 wt % samples, ~42 nm, implies a very high molar mass. In comparison, past studies have reported the Stokes diameter for a p(MPC) sample with an M_n of 234,000 g/mol to be ~22 nm in aqueous

solution.[44, 45] The high molar mass could be explained by the Trommsdorf effect, where the high viscosity of the reaction mixture in the ionic liquid decreases the ability of chain ends to meet each other and terminate the polymerization reaction, resulting in longer chains.[46] In other reaction media, increasing monomer concentrations tend to lead to higher molar mass due to increasing propagation rates compared with chain initiation and termination. The trend of decreasing Stokes diameter, and thus molar mass, with increasing monomer concentration appears to be linked with this specific polymerization environment. At higher MPC concentrations, the noncovalent cross-link density of p(MPC) is higher (presented below). These non-covalent interactions are also likely present between monomers in solution. As a result, the mobilities of both polymer chains and monomer molecules are much lower at higher MPC contents. This may have led to a decrease in the probability of active chain ends meeting and reacting with monomer molecules, decreasing polymerization rate compared with initiation rate and resulting in shorter chains. It should be noted that the 2 wt % p(MPC) sample was a highly viscous solution (insufficient polymer content to form a gel), while the 4 wt % p(MPC) and higher polymer content samples were all free-standing ionogels. The *in situ* synthesized polymers all displayed full conversion according to the ^{1}H NMR spectra of the dissolved material (see Appendix C, Fig. C.1), most likely due to the high initiator concentration used. This indicates that in situ synthesized p(MPC) ionogels are able to achieve full conversion for a wide range of compositions, and that the molecular weight of the polymer is inversely correlated with the p(MPC) content.

Table 5.1. Stokes diameter and polydispersity index measured by dynamic light scattering for dissolved p(MPC) extracted from polymer/LiTFSI-in-IL samples of varying composition.

p(MPC) content (wt %)	Stokes diameter (nm)	Polydispersity index
2	42 ± 2	0.15 ± 0.04
4	39 ± 3	0.16 ± 0.02
6	38 ± 1	0.14 ± 0.01
8	35 ± 3	0.15 ± 0.04
10	29 ± 2	0.15 ± 0.03
12	25 ± 0.2	0.14 ± 0.02
14	21 ± 0.8	0.16 ± 0.02

5.4.2. Ionic conductivity

Room temperature (25 °C) ionic conductivities for neat 1M LiTFSI/BMP TFSI solution (0 wt % p(MPC)) and samples containing 2-14 wt % p(MPC) are displayed in Figure 5.1. Comparing the ionic conductivity values of the p(MPC) ionogels (4 wt% p(MPC) and above) to that of the 1M LiTFSI/BMP TFSI solution, all ionogels exhibited a higher ionic conductivity. The introduction of p(MPC) through *in situ* photopolymerization therefore results in a boost in total ionic conductivity (up to 50% increase in the case of the 8 wt % p(MPC) ionogel). This is attributed to the dissociative effect that the charges on the zwitterion have on the surrounding ion clusters reported previously,[37, 38] *i.e.* $TFSI^-$ is liberated from both Li^+ and BMP^+, which results in less anion-cation coordination and creates more mobile ions. The presence of the ZI polymer at a weight percent as low as 2 wt % resulted in an increase in ionic conductivity by ~25%. In the higher range of 10-14 wt % p(MPC), the ionic conductivity starts to decrease, which can be attributed to the decrease in the liquid fraction of the ionogels and an increase in their solid (polymer) fraction.

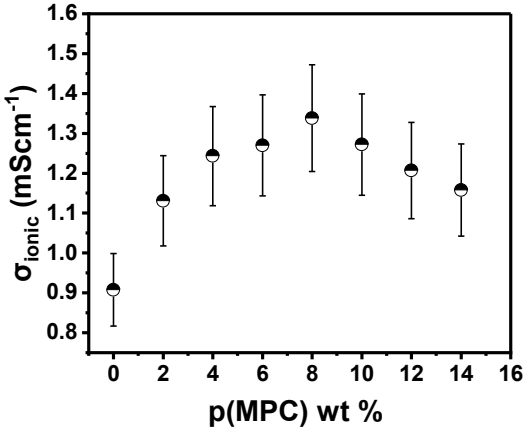


Figure 5.1. Total ionic conductivity at room temperature (25 °C) as a function of p(MPC) wt %.

5.4.3. Diffusion coefficients of the constituents

The room temperature self-diffusion coefficients of each nucleus (^{1}H, ^{19}F, and ^{7}Li) for neat LiTFSI/BMP TFSI solution and 2-14 wt % p(MPC) samples are displayed in Figure 5.2a, representing the diffusion of the BMP^{+} cation, $TFSI^{-}$ anion, and Li^{+} ion, respectively. In the neat LiTFSI/BMP TFSI solution, the order of the diffusion coefficients is IL cation > IL anion > Li^{+}, which is typical for Li salt-containing ILs, since Li strongly complexes with the anions. With increasing p(MPC) content, the samples exhibited an increase in self-diffusion coefficients for the ^{1}H and ^{19}F nuclei. In contrast, the trend for ^{7}Li is different, as there is a monotonic decrease of self-diffusivity observed with increasing p(MPC) content. The decreasing trend can be attributed to the binding of Li^{+} to the p(MPC) units, hence decreasing the number of free Li^{+} ions. On the other hand, the increase in diffusion of the other ionic constituents, both the IL cation and anion, is reminiscent of a dilution of Li^{+} ions in the IL, since an increase of Li^{+} concentration typically enhances viscosity and lowers the diffusion coefficients of all ionic constituents.[18, 20, 21, 47] The increase in the BMP^{+} cation and $TFSI^{-}$ anion self-diffusivities likely stems from enhanced IL ion pair/cluster dissociation by the ZI group of p(MPC), while a portion of the increased anion diffusion is also due to liberation of $TFSI^{-}$ resulting from the strong p(MPC)-Li^{+} coordination.

We note that ^{7}Li diffusion measurements at p(MPC) contents above 8 wt % were not feasible due to T_2 relaxation times that were too rapid.

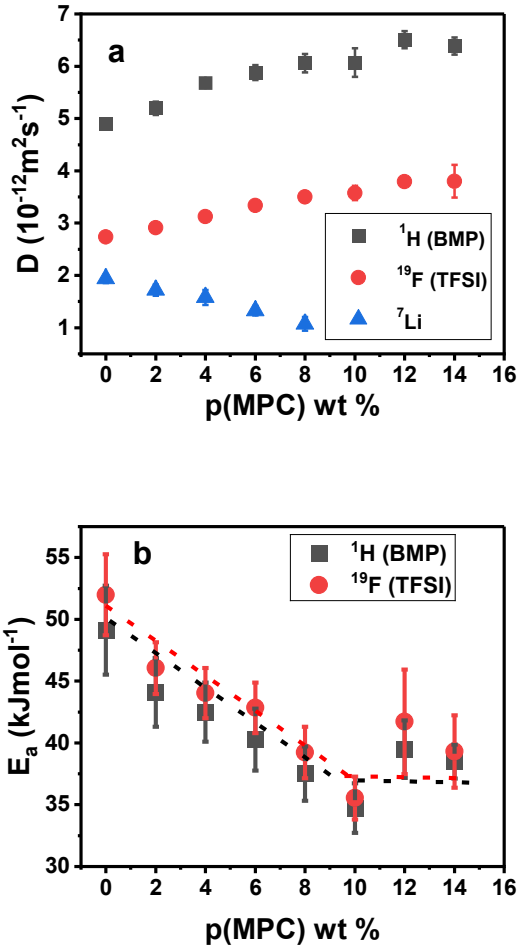


Figure 5.2. (a) Self-diffusion coefficients of the nuclei (^{1}H, ^{19}F, ^{7}Li) obtained from PFG-NMR at room temperature (25°C) as function of p(MPC) content. (b) Activation energies of diffusion as a function of p(MPC) content measured over a temperature range of 25-65°C. The dotted lines are merely guides to the eye.

Temperature dependent diffusion coefficient data are shown in Figure C.2 for the ^{1}H and ^{19}F nuclei over the range of 25 ºC to 65 ºC. To estimate the activation energy of diffusion, the data is fitted by an Arrhenius equation (details in Appendix C). The resulting activation energies are displayed in Figure 5.2b. The decrease in activation energy observed for both the BMP^{+} and $TFSI^{-}$ ions with increasing p(MPC) content (up to 10 wt %) indicates a higher mobility within the polymer matrix and an improved ion transport mechanism. It can be concluded that the facilitated transport of these two constituents contributes to the improved ionic conductivity of the ionogel as compared to the neat LiTFSI/BMP TFSI solution (see Figure 5.1). The findings corroborate the idea that p(MPC) can enhance the dissociation of the LiTFSI and BMP TFSI anion-cation pairs/clusters, hence BMP^{+} and $TFSI^{-}$ are becoming more freely available in an uncoordinated form, enhancing their contribution to the total ionic conductivity. On the other hand, a beneficial influence of MPC groups is not visible for Li^{+}, as its diffusivity is decreasing with greater p(MPC) content. In line with arguments from previous work,[38, 39] we can conclude that Li^{+} ions are strongly interacting with the zwitterionic MPC groups. While this has a beneficial effect in terms of dissolving Li^{+}-anion clusters, thus enhancing overall conductivity, the effect on transport of the Li^{+} ion species is rather unfavorable. In the following sections, we will therefore focus on the Li^{+} ions and further elucidate their dynamics.

5.4.4. Li^{+} ion apparent transference number

In concentrated electrolytes, ion correlations generally cause invalidity of the Nernst-Einstein equation. Therefore, a transference number obtained from diffusion coefficients is a mere estimate under the assumption that correlations are negligible.[48] In this case, the Li^{+} apparent

transference number (t_{Li}^{*}) is calculated using Equation 5.2, where c_i and D_i represent the molar concentration and self-diffusion coefficients of each ionic constituent, i.

$$t_{Li}^{*} = \frac{c_{Li}D_{Li}}{c_{BMP}D_{BMP}+c_{Li}D_{Li}+c_{TFSI}D_{TFSI}} \quad \text{(Eq. 5.2)}$$

Figure 5.3 shows that the contribution of Li^+ to overall charge transport is decreasing with increasing p(MPC) content up to 8 wt %, which is again an indication of a strong Li^+ interaction with the zwitterionic units. This behavior favors the liberation of anions from Li^+ cations. The decrease of the Li^+ apparent transference number is therefore due to two trends, namely an increase of the partial conductivity of the anions, and a decrease of the partial conductivity of Li^+ ions. Thus, the increase in total ionic conductivity is dominated by the more mobile species (BMP^+, $TFSI^-$), which was also evident in the diffusion data (Figure 5.2a).

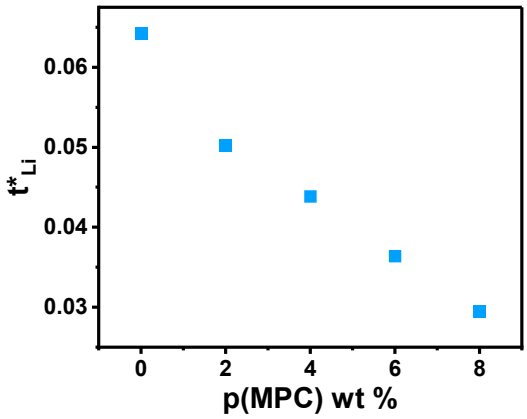


Figure 5.3. Li^+ ion apparent transference number as function of p(MPC) content.

5.4.5. ^{7}Li NMR spectra and spin-spin relaxation rates

A directly evident influence of the p(MPC) content in the ionogels on the Li^+ ions is seen in 1D ^{7}Li spectra of the samples. Figure 5.4a shows ^{7}Li spectra for compositions from 2 wt % to 8 wt % p(MPC), where the decrease of the ^{7}Li peak intensity, accompanied by broadening of the peak, indicates a decrease in the Li^+ ion mobility at higher compositions, while above 8 wt % p(MPC) no ^{7}Li signal was detectable.

Generally, line broadening may arise due to an increased heterogeneity of the local environment of nuclei ("heterogeneous broadening"), or due to motional constraints, which lead to a reduced lifetime of the excited state and thus to line broadening ("homogeneous broadening"). For an analysis of the contributions of either broadening mechanism, we analyzed the ^{7}Li peak integral (Figure 5.4b) and the line width (full width at half maximum, FWHM) (Figure 5.4c). In case of homogeneous broadening, the line width is connected to the spin-spin relaxation rate R_2. Figure 5.4d presents R_2 values of ^{7}Li in the samples, as measured by a CPMG experiment, in comparison to R_2^*, which is extracted from the linewidth as $R_2^* = \pi \cdot \mathrm{FWHM}$. These values are in good agreement with each other, indicating that the broadening can be fully attributed to homogeneous broadening, which is induced by an immobilization of Li^+ that enhances the spin-spin relaxation rate R_2.

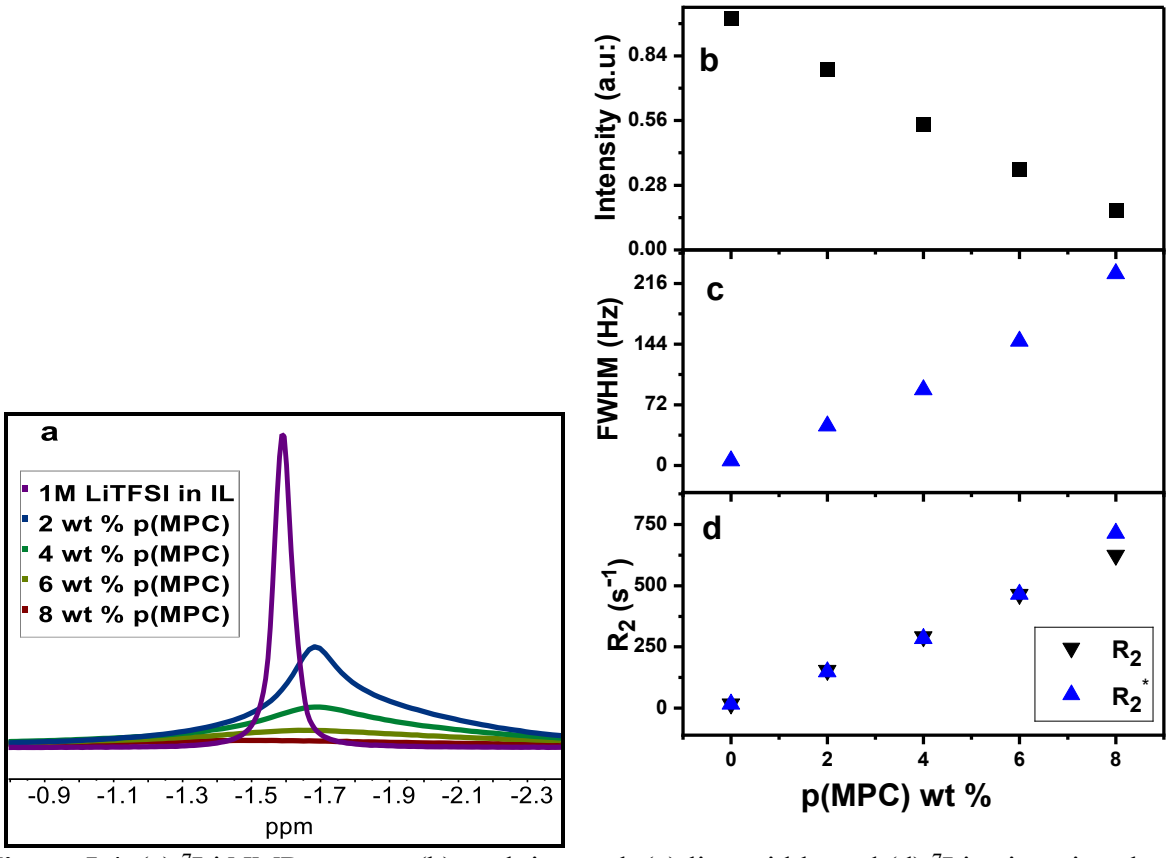


Figure 5.4. (a) ^{7}Li NMR spectra, (b) peak integral, (c) line width, and (d) ^{7}Li spin-spin relaxation rate R_2 determined by a stimulated echo sequence (black) and R_2^* determined by linewidth analysis (red star) for 1M LiTFSI/BMP TFSI solution (0 wt % p(MPC)), 2 wt % p(MPC) solution, and 4-8 wt % p(MPC) free-standing ionogels.

The increase in relaxation rates with increasing p(MPC) content is strongly pronounced and suggests an immobilization of Li^+ ions within the ionogels, which most probably is due to a stronger affinity of Li^+ ions to the phosphate group of the MPC units. Since the echo decays of the CPMG experiment are exponential, a single relaxation rate describes the data. From this we conclude that bound and free Li^+ ions are in fast exchange, such that the experiment yields an averaged relaxation rate over both sites. Higher polymer concentrations lead to more MPC repeat units around each Li^+ ion, thus immobilizing a larger number of Li^+ ions, contributing to the

increase of R_2. Additional evidence for the restriction of local Li^+ dynamics with increasing MPC content is provided by spin-lattice relaxation rates, R_1, as these show a strong decrease with increasing polymer content (see Fig. C.3a). Moreover, the ratio of R_2/R_1, which serves as an indicator for motional restriction, strongly increases with p(MPC) content, achieving values up to 500 (Fig. C.3b), which is far from the value of 1 expected for motional narrowing. Similar to the spin-spin relaxation enhancement, the loss of signal intensity can be attributed to Li^+ ion immobilization. At 2 wt % p(MPC), for example, the molar ratio of Li^+ to MPC is 8.5, thus the ^7Li signal is dominated by free Li^+ ions (including Li^+ ions in Li^+-anion clusters). In contrast, at 8 wt % p(MPC), the Li^+ to MPC molar ratio is approximately 2, and the ^7Li signal vanishes above this p(MPC) concentration. We thus conclude that an average coordination number of 0.5 MPC units per Li^+ ion immobilizes the latter sufficiently to impede the observation of any liquid state NMR signal. Thus, from the ^7Li NMR data, the presence of two different localizations of the Li^+ ions can be concluded. As the ^7Li spectra in Fig. 5.4b are showing, these Li sites do not occur as a superposition, but as an averaged single resonance, which is shifting and broadening with increasing fraction of MPC-coordinated Li. In conclusion, the exchange time τ between the Li sites is fast compared to the inverse spectral spacing, such that an upper limit can be given as $\tau < 80$ ms. In relation to this time scale, the Li coordinations are transient. The relevance of these mobile and immobile Li^+ species for network formation and charge transport will be discussed further below in context of the results of the other characterization methods.

5.4.6. Raman Spectroscopy

Since with greater p(MPC) content the Li^+ coordination environment appears to shift from coordination with $TFSI^-$ anions to coordination with p(MPC), it is worthwhile to study the

coordination state of the anions, which is feasible by Raman spectroscopy. The Raman peaks observed for neat 1M LiTFSI/BMP TFSI solution occur at 742 cm^{-1} for free $TFSI^-$ ions and at 748 cm^{-1} for $TFSI^-$ ions coordinated to Li^+.[25, 49] Figure 5.5a shows the Raman spectra for the IL itself (see black curve), the LiTFSI/IL solution (red curve), and for samples with increasing amounts of p(MPC). Upon addition of LiTFSI to the IL, a peak of Li^+-coordinated anions appears (see green dotted line), which then becomes weakened with increasing p(MPC) content. In order to quantify the fractions of free and Li^+-coordinated anions, Raman spectra were deconvoluted by Voigt profiles (Fig. C.4)**.** From the integrals of the ‘‘free’’ $TFSI^-$ species (A_f) and the coordinated $TFSI^-$ species (A_c) the integral ratio $A_c/(A_c + A_f)$ is determined. According to a procedure introduced by Lassegues et al.[50] the Li^+ coordination number, *i.e.* the number of anions coordinated per Li^+ ion (*n*) is evaluated, taking the known LiTFSI salt fraction for each composition into account. This method requires equal Raman scattering cross-sections of either $TFSI^-$ species, however, the validity of this assumption has been shown in literature.[25, 51] Details of the procedure and the relevant equations are given in Appendix C. The resulting Li^+ coordination number is plotted against the p(MPC) composition and shown in Figure 5.5b. A decrease in coordination number of $TFSI^-$ to Li^+ is observed with increasing p(MPC) content, which is in line with the high binding affinity of Li^+ ions to MPC units as compared to $TFSI^-$, as discussed above. Interestingly, however, the coordination number of anions to Li^+ does not reduce to zero, even in the composition range where the molar ratio of MPC to Li^+ is 0.5 (at 8 wt % p(MPC), see Table C.1) or higher. At 14 wt % p(MPC) the molar ratio of MPC to Li^+ is close to 1, and the average coordination environment of Li^+ consists of 0.72 anions (Table C.2), and one MPC group, if all MPC is coordinating . This shows that Li^+ is still coordinated with some fraction of anions while coordinating to an MPC group. While in the 1M LiTFSI/BMP TFSI solution a coordination of 2 $TFSI^-$ anions per Li^+ is

found, consistent with a previous study,[27] the lower contribution of anions to Li^+ coordination in the samples with larger p(MPC) contents may suggest a replacement of more than one coordinating anion by MPC groups in the Li^+ ion coordination environment, such that Li^+ acts as a cross-linker between polymer segments. However, the stoichiometry of the molar ratio of MPC to Li^+ being close to 1 (at 14 wt % p(MPC)) would then equally require several Li^+ ions coordinated to the same MPC group. Such a stoichiometry can occur if Li^+-MPC clusters are formed. This scenario is in line with theoretical predictions of the same system, where MD simulations at high MPC content of 13% showed that 35% of the Li ions are coordinated to two MPC monomers, and 25% even coordinate to three MPC units.[40]

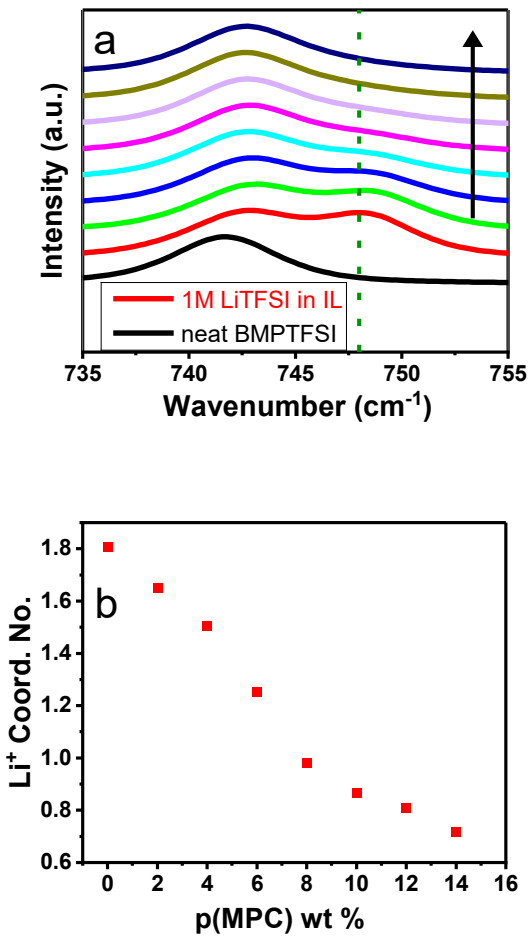


Figure 5.5. (a) Raman spectra and (b) Li^+ coordination number (coordinated anions per Li^+) as extracted from the fraction of coordinated anions in dependence on p(MPC) content. The green dotted line in a) marks the position of the band of coordinated $TFSI^-$ and the black arrow represents the increase in p(MPC) content from 2 wt % (green spectrum) to 14 wt % (dark blue).

5.4.7. Dynamic Mechanical Analysis (DMA)

In order to elucidate the role of Li^+ as a cross-linker in a p(MPC) network, dynamic mechanical properties of the samples were probed. Using stress-strain curves from compression tests, elastic modulus values were obtained for the ionogel compositions with 4, 6, 8, 10, 12, and 14 wt % p(MPC). As shown in Figure 5.6a, the elastic modulus values increased drastically (by three orders of magnitude) upon a 6 wt % increment in polymer content (3.80 ± 0.35 kPa and 3000 ± 330 kPa for 4 wt % and 10 wt % p(MPC) ionogels, respectively). This is an indication of a similarly drastic increase in the cross-link density of the gels, which is directly proportional to elastic modulus. This finding corroborates the decrease in Li^+ diffusivity observed with increasing p(MPC) content. More Li^+ cations are noncovalently coordinating with increasing p(MPC), which reduces the number of mobile Li^+ cations and increases the Li^+ ion-mediated cross-link density of the gels.

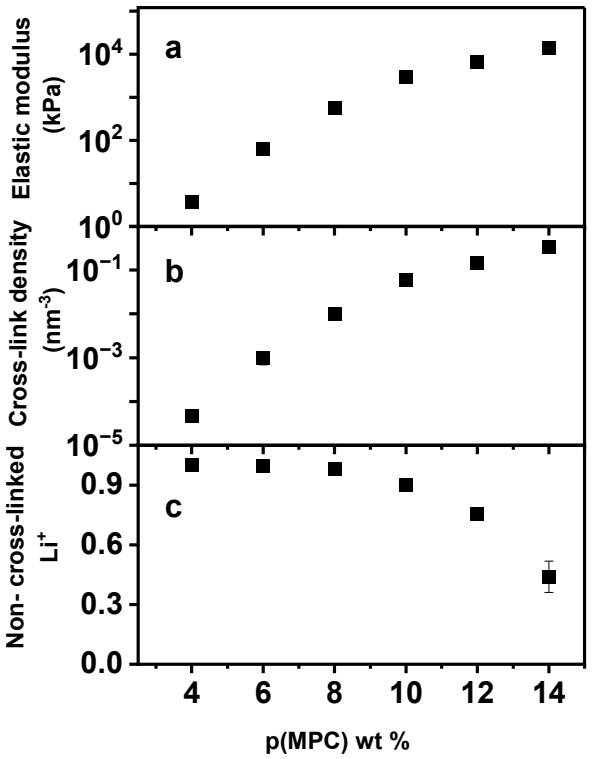


Figure 5.6. (a) Elastic modulus values for ionogels containing 4 to 14 wt % p(MPC). (b) Calculated cross-link density within the ionogels, representing the number of Li^+ ion-mediated noncovalent cross-links per nm^3, and (c) the corresponding fraction of Li^+ that is not participating in noncovalent cross-links.

Since the increasing modulus might include contributions from direct MPC-MPC-cross-links in addition to Li-mediated cross-links, it would be instructive to analyze a reference with MPC in IL without any Li salt. Unfortunately, MPC is not soluble in BMP TFSI,[38] however, previous preparation of an MPC-containing copolymer was performed in a similar IL, EMI TFSI. This yielded a transparent viscous polymer solution instead of a gel, apparently lacking cross-links.[52] Thus, direct MPC-MPC cross-links are unlikely to occur in BMP TFSI.

To gain more information from the elastic modulus values of the p(MPC) ionogels, the cross-link density and the concentration of non-cross-linked Li^+ were calculated (details in Appendix C). Figures 5.6b and 5.6c show the cross-link density and the fraction of non-cross-linked Li^+ in the ionogels, respectively. As the p(MPC) content increases from 4 to 10 wt %, the cross-link density increases from 4.8 $\times 10^{-5}$ nm^{-3} to 0.06 nm^{-3}, which is around a three-order-of-magnitude increase, with only a slight decrease in the fraction of non-cross-linked Li^+ (0.99 and 0.90 fraction of non-cross-linked Li^+ for 4 wt % and 10 wt % p(MPC) ionogels, respectively). This demonstrates the importance of Li^+ in the formation of the noncovalent cross-links that bridge p(MPC) chains and hold these gels together, as well as the ability to obtain relatively stiff gels (3000 ± 330 kPa for 10 wt % p(MPC) ionogels) by using only ~10% of the available Li^+ ions in the system, leaving the remaining ~90% of Li^+ ions not in cross-links.

5.4.8. Discussion of Li^+ sites

The above results show that the introduction of polymerized ZI units within the 1M LiTFSI/BMP TFSI solution has two different effects: On the one hand, the Li^+ ion local mobility is severely hindered, on the other hand, mechanical stability is introduced by Li^+ acting as a cross-linker for the polymeric network. In the following discussion, we draw conclusions from the

combination of the above findings, in order to describe the nature of Li^+ sites and the respective Li^+ dynamics in these sites for different regimes of p(MPC) content. It is important to note that with the different characterization methods we monitor different properties of Li^+ ions. First, the ^7Li NMR intensity provides the fraction of Li^+ ions detectable in liquid state spectra, which we designate as the "mobile" Li^+ fraction, *m*. The fraction *m* is given in Table 5.2, and it decreases drastically with greater p(MPC) content, see Figure 5.7a**.** Any Li^+ ions with liquid-like dynamics are included in this site, irrespective of their coordination environment. We define *r* to be the molar ratio of MPC to Li^+ present in each sample. Assuming that all immobilized Li^+ ions are coordinated to MPC groups, the immobilized fraction of Li^+ (1-*m*) can be related to the MPC amount by calculating $b = (1-m)/r$ as the number of Li^+ ions immobilized per MPC group, see Table 5.2. Furthermore, the Raman spectra of the $TFSI^-$ anions provide information about the anion-related average coordination number of Li^+. Finally, the DMA analysis provides the fraction of non-cross-linked Li^+ ions, f_{Li}, which are not involved in network formation, see Figure 5.7a. This allows a further distinction of the MPC-coordinated Li^+ into cross-linking or non-cross-linking species. With these data, the different Li^+ sites and the role of Li^+ in cross-linking and charge transport can be discussed for the different concentration regimes of polymer in the ionogel. From Figure 5.7a it is clear that at *no or low MPC content* there are no Li^+ species involved in network formation, *i.e.* $f_{Li} = 1$, and all Li^+ species are mobile, $m \sim 1$. In the neat LiTFSI/BMP TFSI solution, the coordination number *n* is almost two, suggesting a predominant coordination of Li^+ by two $TFSI^-$ anions, in accordance with literature.[27, 51] This scenario is schematically depicted in Figure 5.7b, where Li^+ is coordinated by anions and freely mobile.

With increasing MPC content the coordination number of anions per Li^+ ion (*n*) decreases, see Table 5.2. This is accompanied by a decrease of *m*, and both trends mark the shift of Li^+

coordination from anions to MPC, where apparently polymer-coordinated Li^+ does not yield a narrow liquid state NMR signal. Interestingly, in the low polymer concentration range, the number of immobilized Li^+ ions per MPC group, *b*, increases with polymer content, in spite of an enhanced availability of MPC groups. The increase could be a signature of a cooperative effect, where ionic clusters are formed by Li^+ and MPC, which increase with MPC content, attracting an increasing number of Li^+ ions per MPC group. At the same time, the fraction of non-cross-linking Li^+, as extracted from the DMA analysis, remains equal to one, showing that virtually no cross-links are formed in the low concentration regime. Therefore, Li^+-MPC coordinations remain local without providing inter-chain links.

At intermediate polymer content (r = 0.5 at 8 wt % p(MPC)), the coordination number is reduced to one anion per Li^+, while ~1.5 Li^+ ions are immobilized per MPC group. Interestingly, while the Li^+ coordination is further shifting from anions to MPC, the $TFSI^-$ ions are still playing a role in Li^+ coordination, forming a heterogeneous environment, as illustrated in Figure 5.7c. Here, Li^+ is shared by MPC and anions in a mixed coordination. This regime also marks the onset of cross-linking, *i.e.* the decrease of f_{Li}. It is also evident from NMR that the immobilized Li^+ fraction is increasing, reaching a plateau of 1-m = 1 at higher MPC content. Here, we can conclude that all Li^+ is coordinated by MPC and consequently immobilized. While anions still contribute to the average coordination environment, there is virtually no Li^+ which is exclusively coordinated by anions, as this species would appear as a liquid state signal in ^{7}Li NMR.

Table 5.2. Collection of resulting parameters, detailing the distribution of Li^+ on different sites as a function of p(MPC) content.

Composition wt % p(MPC) (target value)	*r* MPC:Li^+ molar ratio (actual)	*m* mobile fraction of Li^+ (^{7}Li NMR)	*b* Immobilized Li^+ per MPC	*n* Coord. no. $TFSI^-$ per Li^+ (Raman)	f_{Li} non-cross-linked Li^+ (DMA)
0	0	1	0	1.81	1
2	0.13	0.96	0.31	1.65	1
4	0.24	0.73	1.13	1.51	1
6	0.34	0.47	1.55	1.25	1
8	0.50	0.24	1.52	0.98	0.98
10	0.62	0	1.60	0.88	0.90
12	0.69	0	1.40	0.81	0.75
14	0.92	0	1.10	0.72	0.44

Finally, *at the highest polymer content* of 14 % wt p(MPC), more than 50 % of the Li^+ ions are forming cross-links. This agrees well predictions from MD simulations at high polymer content.[40] The remaining Li^+ ions are not contributing to the network, but since they are immobile, they are likely strongly bound to the phosphate group of zwitterionic MPC, as evident from the mobile fraction of Li^+ ions being zero. Figure 5.7d shows this scenario, where anions are still playing a major role in a mixed coordination environment of Li^+, with a coordination number of n = 0.72 (at 14 wt % p(MPC)). In this concentration regime, Li^+ is predominantly acting as a cross-linker in providing a stiff ionogel, and as even the non-cross-linking Li^+ ions are coordinated to the network, it is questionable whether Li^+ contributes at all to the total ionic conductivity.

We note here that while we discuss the distribution of Li^+ on different sites as a static picture, there is continuous exchange between these sites. This is evident from observing only a single spectral line and single exponential in all diffusion as well as spin relaxation data, instead of two or more superimposed contributions. Since the time scale of exchange is rapid as compared to the experimental time scale, the resulting diffusion coefficients and spin relaxation rates are weighted averages over Li^+ in different sites.

The role of the anion is interesting, as it provides some seemingly opposing trends with increasing MPC content: On the one hand the anion diffusion coefficient is increasing (see Figure 5.2a), while on the other hand the anion is contributing to the heterogeneous coordination environment of Li^+, implying its immobilization close to MPC groups. Here, the Raman data shed some light on different anion fractions: The anion coordination number n per Li ion is decreasing from 1.81 to 0.72 (see Table 5.2). Thus, 60 % of the anions previously contained in Li-anion clusters become liberated by Li-MPC interaction and contribute to anion diffusion enhancement. In contrast, 40 % of anions remain coordinated to Li and become indirectly immobilized by MPC

groups. These anions limit the diffusion enhancement, as the measured diffusion coefficient is a fast exchange average over both sites. Interestingly, the diffusion enhancement is rather similar for cation and anion (see Figure C.5), demonstrating their mutual correlations. However, a slightly stronger enhancement of anion diffusion is observed, which is a signature of the partial cluster dissociation.

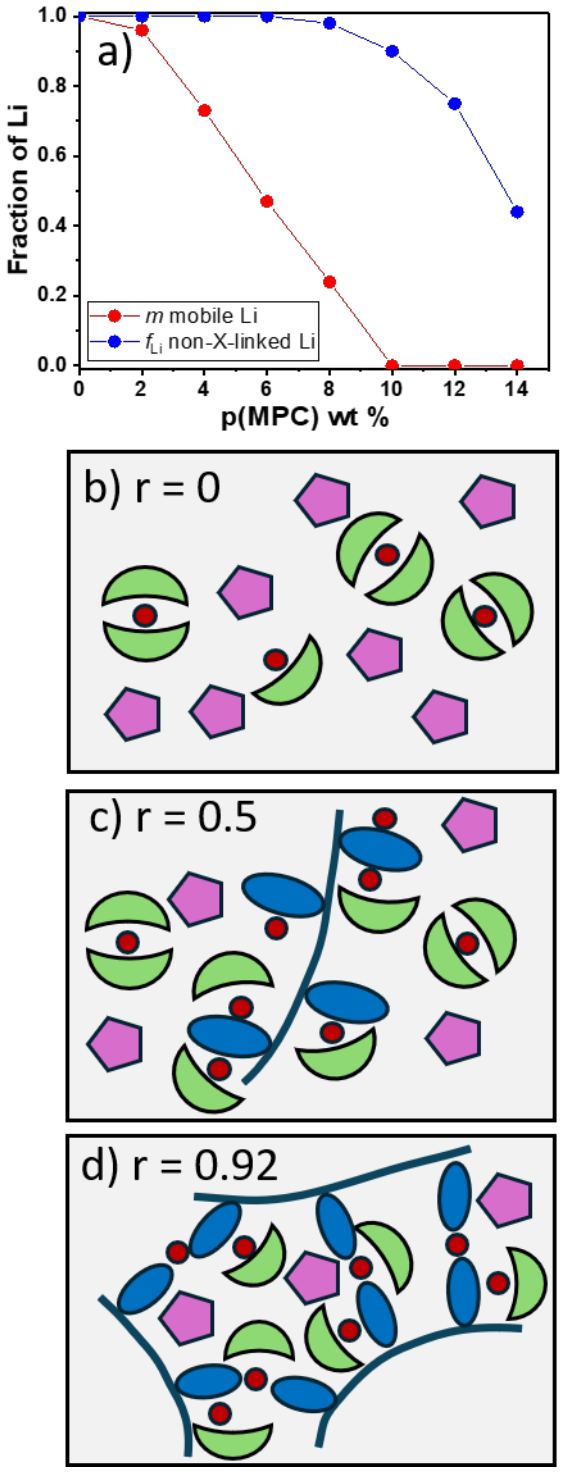


Figure 5.7. (a) Distribution of Li^+ in different sites; (b) – (d) Li^+ coordination scenarios at 0, 8, and 14 wt % p(MPC), showing free, immobilized, and cross-linking Li^+ ions. For a legend of the symbols, see Scheme 1. Note that the MPC:Li^+ molar ratio and number of coordinating anions are

shown according to scale, while the total number of IL cations and anions is not to scale to enhance clarity.

5.4.9. Implications for transport

In summary, three distinct fractions of Li^+ with different dynamic properties could be identified and their contributions estimated from different methods. The present system provides some interesting beneficial features, as the interactions of the p(MPC) polymer with Li^+ can on the one hand enhance overall conductivity and can on the other hand provide mechanical stability by generating noncovalent cross-links. However, the interaction of Li^+ with MPC units is so strong that it leads to immobilization and ultimately to a reduction of Li^+ transport, as evidenced by the reduced Li^+ diffusion coefficients and the resulting apparent transference numbers. While we cannot quantify the lifetime of the Li^+-MPC coordination or assess potential contributions of Li^+ transport along p(MPC) chain pathways, the enhancement of total ionic conductivity in the low p(MPC) content range is mostly due to the anions, which are liberated from their coordination to Li^+ ions.

For a more beneficial ionogel system, it is desirable that the onset of ionic cross-linking would occur at a lower polymer content, where Li^+ immobilization by MPC is not yet as detrimental. A strategy for improvement may lie in the architecture of the polymer: the present p(MPC) homopolymer bears a very high density of ZI units, and, according to the above discussion, this may favor local ionic clusters. Improved polymer architectures might involve copolymers with a reduced p(MPC) density along the chain.[52] This would reduce the fraction of Li^+ being immobilized, while longer spacers between the MPC groups may enhance the

accessibility of MPC groups for cross-linking, due to a more even distribution in space, which could shift the curve of f_{Li} to lower MPC content. Work along these lines is currently in progress.

5.5. Conclusions

Our findings reveal that the incorporation of p(MPC) into the ionogel matrix significantly reduces the diffusivity of Li^+ ions. This decrease suggests that Li^+ ions are being partially immobilized due to complexation or physical cross-linking with the negatively-charged phosphate groups of p(MPC). This Li^+-MPC coordination is strong, and its relevance increases with p(MPC) content, at the cost of Li^+-anion coordination, which is reduced. This liberates the anions, and probably reduces local viscosity within the IL/salt liquid phase, such that for both the IL cation and anion, an enhanced mobility contributes to a boost in total ionic conductivity. Interestingly, up to a medium p(MPC) content of 6 wt %, the number of immobilized Li^+ ions per MPC group increases, indicating a cooperative effect. At this p(MPC) content, the fraction of Li^+ ions acting as cross-linkers remains low, and a far larger MPC content is required for effective crosslinking. Considering the large number of immobilized Li^+ per MPC at a still rather low fraction of cross-linking Li^+ ions, it appears likely that a large fraction of Li^+ undergoes a local coordination, possibly between neighboring MPC groups, which causes immobilization, while efficient crosslinking requires a larger MPC density with a beneficial spatial distribution. Thus, a guideline for promoting the role of Li^+ ions as structural gelators is to dilute the ZI units on the chains in order to avoid local crosslinking and clustering. With this strategy, the strong immobilization of Li^+ at the high charge density of the chain might be overcome, paving the way towards developing systems with a defined fraction of Li^+ ions acting as crosslinkers, while still a sufficient fraction remains to ensure effective ion transport by mobile Li^+ ions. This study highlights the significance

of optimizing the composition and architecture of polyzwitterion-supported ionogels to achieve a good balance between mechanical integrity, Li^+ ion transport, and ionic conductivity.

5.6. Author Contribution and Acknowledgements

S.A. synthesized gels and performed NMR and Raman spectroscopy. M.K.A. synthesized gels and performed room temperature ionic conductivity measurements and dynamic mechanical analysis. R.P.O. performed dynamic light scattering. A.A., M.J.P., and M.S. supervised the work.

The authors would like to thank Professor David Kaplan in the Department of Biomedical Engineering at Tufts University for providing them with access to the texture analyzer used to obtain dynamic mechanical analysis (DMA) results. This project is funded by the DFG-NFS (German Science Foundation-US National Science Foundation) joint program CONFINE, project no. 509154483 (NSF award 2234243). The NMR spectrometer is funded by the DFG via proposal INST 211/999-1 FUGG, project ID 452849940.

5.7. References

1. Kim, T.; Song, W.; Son, D.-Y.; Ono, L. K.; Qi, Y., Lithium-ion batteries: outlook on present, future, and hybridized technologies. *J. Mater. Chem. A* **2019,** *7* (7), 2942-2964.

2. Lu, L.; Han, X.; Li, J.; Hua, J.; Ouyang, M., A review on the key issues for lithium-ion battery management in electric vehicles. *J. Power Sources* **2013,** *226*, 272-288.

3. Wang, Y.; Zhong, W.-H., Development of Electrolytes towards Achieving Safe and High-Performance Energy-Storage Devices: A Review. *ChemElectroChem* **2015,** *2* (1), 22-36.

4. Wang, Q.; Ping, P.; Zhao, X.; Chu, G.; Sun, J.; Chen, C., Thermal runaway caused fire and explosion of lithium ion battery. *J. Power Sources* **2012,** *208*, 210-224.

5. Goodenough, J. B.; Kim, Y., Challenges for Rechargeable Li Batteries. *Chem. Mater.* **2010,** *22* (3), 587-603.

6. Balducci, A., Ionic Liquids in Lithium-Ion Batteries. *Top. Curr. Chem.* **2017,** *375* (2).

7. Francis, C. F. J.; Kyratzis, I. L.; Best, A. S., Lithium-Ion Battery Separators for Ionic-Liquid Electrolytes: A Review. *Adv. Mater.* **2020,** *32* (18), 1904205.

8. Tang, X.; Lv, S. Y.; Jiang, K.; Zhou, G. H.; Liu, X. M., Recent development of ionic liquid-based electrolytes in lithium-ion batteries. *J. Power Sources* **2022,** *542*, 231792.

9. Liu, J.; Yao, Y. C.; Zhang, S. Z.; Zhang, K. Y.; Peng, C. J.; Liu, H. L., Application of Ionic Liquids in Lithium Metal Batteries. *Prog. Chem.* **2025,** *37* (5), 788-800.

10. Watanabe, M.; Thomas, M. L.; Zhang, S. G.; Ueno, K.; Yasuda, T.; Dokko, K., Application of Ionic Liquids to Energy Storage and Conversion Materials and Devices. *Chem. Rev.* **2017,** *117* (10), 7190-7239.

11. Armand, M.; Endres, F.; MacFarlane, D. R.; Ohno, H.; Scrosati, B., Ionic-liquid materials for the electrochemical challenges of the future. *Nat. Mater.* **2009,** *8* (8), 621-629.

12. Lewandowski, A.; Świderska-Mocek, A., Ionic liquids as electrolytes for Li-ion batteries—An overview of electrochemical studies. *J. Power Sources* **2009,** *194* (2), 601-609.

13. Piatti, E.; Guglielmero, L.; Tofani, G.; Mezzetta, A.; Guazzelli, L.; D'Andrea, F.; Roddaro, S.; Pomelli, C. S., Ionic liquids for electrochemical applications: Correlation between molecular structure and electrochemical stability window. *J. Mol. Liq.* **2022,** *364*, 120001.

14. Hayyan, M.; Mjalli, F. S.; Hashim, M. A.; AlNashef, I. M.; Mei, T. X., Investigating the electrochemical windows of ionic liquids. *J. Ind. Eng. Chem.* **2013,** *19* (1), 106-112.

15. Le Bideau, J.; Viau, L.; Vioux, A., Ionogels, ionic liquid based hybrid materials. *Chem. Soc. Rev.* **2011,** *40* (2), 907-925.

16. Giffin, G. A., Ionic liquid-based electrolytes for "beyond lithium" battery technologies. *J. Mater. Chem. A* **2016,** *4* (35), 13378-13389.

17. Galiński, M.; Lewandowski, A.; Stępniak, I., Ionic liquids as electrolytes. *Electrochim. Acta* **2006,** *51* (26), 5567-5580.

18. Hayamizu, K.; Aihara, Y.; Nakagawa, H.; Nukuda, T.; Price, W. S., Ionic conduction and ion diffusion in binary room-temperature ionic liquids composed of emim BF4 and LiBF4. *J. Phys. Chem. B* **2004,** *108* (50), 19527-19532.

19. Saito, Y.; Umecky, T.; Niwa, J.; Sakai, T.; Maeda, S., Existing condition and migration property of ions in lithium electrolytes with ionic liquid solvent. *J. Phys. Chem. B* **2007,** *111* (40), 11794-11802.

20. Nicotera, I.; Oliviero, C.; Henderson, W. A.; Appetecchi, G. B.; Passerini, S., NMR investigation of ionic liquid-LiX mixtures: Pyrrolidinium cations and TFSI- anions. *J. Phys. Chem. B* **2005,** *109* (48), 22814-22819.

21. Castiglione, F.; Famulari, A.; Raos, G.; Meille, S. V.; Mele, A.; Appetecchi, G. B.; Passerini, S., Pyrrolidinium-Based Ionic Liquids Doped with Lithium Salts: How Does Li+ Coordination Affect Its Diffusivity? *J. Phys. Chem. B* **2014,** *118* (47), 13679-13688.

22. Tong, J. H.; Wu, S. L.; von Solms, N.; Liang, X. D.; Huo, F.; Zhou, Q.; He, H. Y.; Zhang, S. J., The Effect of Concentration of Lithium Salt on the Structural and Transport Properties of Ionic Liquid-Based Electrolytes. *Front. Chem.* **2020,** *7*, 945.

23. Umebayashi, Y.; Mori, S.; Fujii, K.; Tsuzuki, S.; Seki, S.; Hayamizu, K.; Ishiguro, S., Raman Spectroscopic Studies and Ab Initio Calculations on Conformational Isomerism of 1-

Butyl-3-methylimidazolium Bis-(trifluoromethanesulfonyl)amide Solvated to a Lithium Ion in Ionic Liquids: Effects of the Second Solvation Sphere of the Lithium Ion. *J. Phys. Chem. B* **2010,** *114* (19), 6513-6521.

24. Méndez-Morales, T.; Carrete, J.; Bouzón-Capelo, S.; Pérez-Rodríguez, M.; Cabeza, O.; Gallego, L. J.; Varela, L. M., MD Simulations of the Formation of Stable Clusters in Mixtures of Alkaline Salts and Imidazolium-Based Ionic Liquids. *J. Phys. Chem. B* **2013,** *117* (11), 3207-3220.

25. Umebayashi, Y.; Mitsugi, T.; Fukuda, S.; Fujimori, T.; Fujii, K.; Kanzaki, R.; Takeuchi, M.; Ishiguro, S. I., Lithium ion solvation in room-temperature ionic liquids involving bis(trifluoromethanesulfonyl) imide anion studied by Raman Spectroscopy and DFT calculations. *J. Phys. Chem. B* **2007,** *111* (45), 13028-13032.

26. Pitawala, J.; Martinelli, A.; Johansson, P.; Jacobsson, P.; Matic, A., Coordination and interactions in a Li-salt doped ionic liquid. *J. Non-Cryst. Solids* **2015,** *407*, 318-323.

27. Gouverneur, M.; Schmidt, F.; Schönhoff, M., Negative effective Li transference numbers in Li salt/ionic liquid mixtures: does Li drift in the "Wrong" direction? *Phys. Chem. Chem. Phys.* **2018,** *20* (11), 7470-7478.

28. Brinkkötter, M.; Giffin, G. A.; Moretti, A.; Jeong, S.; Passerini, S.; Schönhoff, M., Relevance of ion clusters for Li transport at elevated salt concentrations in [Pyr(12O1)][FTFSI] ionic liquid-based electrolytes. *Chem. Commun.* **2018,** *54* (34), 4278-4281.

29. Molinari, N.; Mailoa, J. P.; Kozinsky, B., General Trend of a Negative Li Effective Charge in Ionic Liquid Electrolytes. *J. Phys. Chem. Lett.* **2019,** *10* (10), 2313-2319.

30. Brinkkötter, M.; Mariani, A.; Jeong, S.; Passerini, S.; Schönhoff, M., Ionic Liquid in Li Salt Electrolyte: Modifying the Li+ Transport Mechanism by Coordination to an Asymmetric Anion. *Adv. Energy Sustainability Res.* **2021,** *2* (2), 2000078.

31. Nürnberg, P.; Lozinskaya, E. I.; Shaplov, A. S.; Schönhoff, M., Li Coordination of a Novel Asymmetric Anion in Ionic Liquid-in-Li Salt Electrolytes. *J. Phys. Chem. B* **2020,** *124* (5), 861-870.

32. Lorenz, M.; Schönhoff, M., Evaluating Strategies to Enhance Li Transference in Salt-in-Ionic Liquid Electrolytes: Mixed Anions, Coordinating Cations, and High Salt Concentration. *J. Phys. Chem. B* **2024,** *128* (11), 2782-2791.

33. Rosenwinkel, M. P.; Schönhoff, M., Polymer-Induced Inversion of the Li+ Drift Direction in Ionic Liquid-Based Ternary Polymer Electrolytes. *Macromol. Chem. Phys.* **2022,** *223* (8).

34. Ackermann, F.; Schönhoff, M., Chelating Additives Reversing the Lithium Migration Direction in Ionic Liquid Electrolytes. *J. Phys. Chem. C* **2020,** *125* (1), 266-274.

35. Nürnberg, P.; Atik, J.; Borodin, O.; Winter, M.; Paillard, E.; Schönhoff, M., Superionicity in Ionic-Liquid-Based Electrolytes Induced by Positive Ion-Ion Correlations. *J. Am. Chem. Soc.* **2022,** *144* (10), 4657-4666.

36. Li, Z. H.; Xia, Q. L.; Liu, L. L.; Lei, G. T.; Xiao, Q. Z.; Gao, D. S.; Zhou, X. D., Effect of zwitterionic salt on the electrochemical properties of a solid polymer electrolyte with high temperature stability for lithium ion batteries. *Electrochim. Acta* **2010,** *56* (2), 804-809.

37. D'Angelo, A. J.; Panzer, M. J., Decoupling the Ionic Conductivity and Elastic Modulus of Gel Electrolytes: Fully Zwitterionic Copolymer Scaffolds in Lithium Salt/Ionic Liquid Solutions. *Adv. Energy Mater.* **2018,** *8* (26), 1801646.

38. Alsaedi, M. K.; Tadesse, M. Y.; Ganesan, V.; Panzer, M. J., Zwitterionic Polymer Ionogel Electrolytes Supported by Coulombic Cross-Links: Impacts of Alkali Metal Cation Identity. *J. Phys. Chem. B* **2024,** *128* (13), 3273-3281.

39. Taylor, M. E.; Clarkson, D.; Greenbaum, S. G.; Panzer, M. J., Examining the Impact of Polyzwitterion Chemistry on Lithium Ion Transport in Ionogel Electrolytes. *ACS Appl. Polym. Mater.* **2021,** *3* (5), 2635-2645.

40. Tadesse, M. Y.; Marioni, N.; Zhang, Z. D.; Ganesan, V., Influence of Cation and Anion Chemistry on the Ionic Conductivity and Transference Number of Zwitterionic Polymer-Supported Ionic Liquid Electrolytes. *ACS Appl. Energy Mater.* **2025,** *8* (6), 3314-3326.

41. Stejskal, E. O.; Tanner, J. E., Spin Diffusion Measurements: Spin Echoes in the Presence of a Time-Dependent Field Gradient. *J. Phys. Chem.* **1965,** *42* (1), 288-292.

42. Carr, H. Y.; Purcell, E. M., Effects of diffusion on free precession in nuclear magnetic resonance experiments. *Phys. Rev.* **1954,** *94* (3), 630-638.

43. Meiboom, S.; Gill, D., Modified spin-echo method for measuring nuclear relaxation times. *Rev. Sci. Instrum.* **1958,** *29* (8), 688-691.

44. Kikuchi, M.; Terayama, Y.; Ishikawa, T.; Hoshino, T.; Kobayashi, M.; Ogawa, H.; Masunaga, H.; Koike, J.; Horigome, M.; Ishihara, K.; *et al.,* Chain dimension of polyampholytes in solution and immobilized brush states. *Polym. J.* **2012,** *44* (1), 121-130.

45. Kobayashi, M.; Terayama, Y.; Kikuchi, M.; Takahara, A., Chain dimensions and surface characterization of superhydrophilic polymer brushes with zwitterion side groups. *Soft Matter* **2013,** *9* (21), 5138-5148.

46. Kubisa, P., Kinetics of radical polymerization in ionic liquids. *Eur. Polym. J.* **2020,** *133*, 109778.

47. Tokuda, H.; Hayamizu, K.; Ishii, K.; Abu Bin Hasan Susan, M.; Watanabe, M., Physicochemical properties and structures of room temperature ionic liquids. 1. Variation of anionic species. *J. Phys. Chem. B* **2004,** *108* (42), 16593-16600.

48. Stolwijk, N. A.; Kösters, J.; Wiencierz, M.; Schönhoff, M., On the extraction of ion association data and transference numbers from ionic diffusivity and conductivity data in polymer electrolytes. *Electrochim. Acta* **2013,** *102*, 451-458.

49. Alía, J. M.; Edwards, H. G. M., Ion solvation and ion association in lithium trifluoromethanesulfonate solutions in three aprotic solvents. An FT-Raman spectroscopic study. *Vib. Spectrosc.* **2000,** *24* (2), 185-200.

50. Lassegues, J. C.; Grondin, J.; Talaga, D., Lithium solvation in bis(trifluoromethane-sulfonyl)imide-based ionic liquids. *Phys. Chem. Chem. Phys.* **2006,** *8* (48), 5629-5632.

51. Lassègues, J.-C.; Grondin, J.; Aupetit, C.; Johansson, P., Spectroscopic Identification of the Lithium Ion Transporting Species in LiTFSI-Doped Ionic Liquids. *J. Phys. Chem. A* **2009,** *113* (1), 305-314.

52. Wieck, K. W.; Panzer, M. J., Ionogel Electrolytes Supported by Zwitterionic Copolymers Featuring Lithium Ion-Mediated, Noncovalent Cross-Links. *ACS Appl. Polym. Mater.* **2023,** *5* (4), 2887-2894.

Chapter 6: Future Work

The previous chapters of this dissertation all look at a system that involved one type of possible species that makes up the liquid component of the electrolytes: an ionic liquid. They also do not discuss the implications of using ionogel electrolytes on the electrodes they are in contact with. This chapter will discuss the potential directions that the chapters of this thesis could point to, but were outside the scope of this dissertation.

6.1. Characterizing the Solid-Electrolyte Interphase (SEI) Layer

One essential aspect of electrolyte development is characterizing the solid-electrolyte interphase (SEI) layer. The SEI is a layer that forms due to reactions at the interface between the electrolyte and the electrode, which, in the case of lithium metal batteries, is lithium. The SEI reduces the conductivity across the electrochemical cell as it introduces more resistance the more it grows. Chronoamperometric data for the ionogels discussed in Chapter 4 suggest the SEI is worth characterizing.

The ionogels in Chapter 4 were electrochemically tested as described in Chapter 2 section 2.2.2. The ionogels were sealed in a symmetrical coin cell with lithium metal on either side of the electrolyte. After preconditioning (described in Chapter 2 section 2.2.2), the coin cells were polarized at 80 mV for four hours. The initial current (I_0) is the current due to the motion of all ions and is measured at 1 second from starting the polarization. The steady-state current (I_{ss}), which is measured at four hours from starting the polarization, is the current due to the motion of Li^+ across the electrolyte as it is being oxidized and reduced at both ends of the electrolyte. The current

fraction (I_{ss}/I_0) represents the fraction of current carries across by lithium out of all mobile ions combined. The values for I_0, I_{ss}, and I_{ss}/I_0 are tabulated in table 6.1 and the values for I_{ss}/I_0 are plotted in figure 6.1 as a function of mol MPC / mol Li^+ for 0.5 M, 1 M, and 2 M salt solution concentration.

The ionogels in table 6.1 and figure 6.1 are identical in composition to those in figure 4.1 in Chapter 4. In figure 4.1, the ionic conductivity increases with the addition of the zwitterionic polymer, up to a certain point, for any given salt solution concentration. Conductivity is inversely proportional to resistance at a fixed voltage according to the following equation:

$$\sigma = \frac{t}{RA} \qquad \text{Eq. 6.1}$$

where σ is the conductivity, t is the thickness, A is the cross-sectional area, and R is the resistance. Since the conductivity is increasing, the resistance should be decreasing. At a fixed voltage, a decrease in resistance indicates an increase in current according to the following equation:

$$R = \frac{V}{I} \qquad \text{Eq. 6.2}$$

where V is the voltage and I is the current. However, table 6.1 shows that the initial current I_0 does not increase with increasing mol MPC / mol Li^+, which is counter intuitive. An increase in ionic conductivity should result in an increase in current. Therefore, this increase in ionic conductivity (and decrease in resistance) with increasing polymer content is being countered by an increase in resistance somewhere within the coin cell. This resistance is primarily due to the SEI layer forming between the electrodes and the electrolyte.

One way to characterize the SEI is to investigate the thickness of the SEI as a function of polymer content. An increasing thickness would correspond to an increase in resistance. SEI thickness can be visually characterized using microscopy such as scanning electron microscopy (SEM). Specifically, extreme high resolution SEM (XHR-SEM) can be used to visually

investigate SEI thickness[1]. Compared to SEM, XHR-SEM allows for resolutions that are < 1 nm and scanning at low accelerating voltages[2]. While electrolytes can be imaged using SEM[3], SEI layers are usually 30-100 Å[4] in thickness, making XHR-SEM more suitable for SEI imaging than regular SEM.

Another way to characterize the SEI is through focused ion beam (FIB) imaging[5]. FIB is a technique that is similar to SEM, but instead of using electrons, it uses ions. Zhang *et al*.[6] were the first to report using FIB to investigate SEI, including its thickness. In their study, they use FIB to characterize graphite spheres in a $LiPF_6$-containing EC/DMC electrolyte.

Given that the ionogels could form intimate contact with the lithium discs, which could also be more difficult to separate after the formation of the SEI, the lithium-SEI-ionogel-SEI-lithium assembly can be imaged as-is by cutting through it with a sharp metallic blade and exposing the layers from a cross-sectional point of view for imaging.

Table 6.1: I_0, I_{ss}, and I_{ss}/I_0 as a function of mol MPC / mol Li^+ for 0.5 M, 1 M, and 2 M salt concentration ionogels.

Mol MPC / Mol Li^+	Salt solution concentration (M)	I_0 (µA)	I_{ss} (µA)	I_{ss}/I_0
0	0.5	423 ± 24.0	171 ± 4.041	0.404 ± 0.0171
0.25	0.5	210 ± 13.9	91.3 ± 8.34	0.434 ± 0.0243
0.5	0.5	134 ± 11.9	28.1 ± 4.47	0.210 ± 0.0279
0.75	0.5	96.3 ± 4.97	12.7 ± 2.05	0.131 ± 0.0193
0	1	378 ± 30.5	111 ± 14.4	0.293 ± 0.0144
0.25	1	238 ± 33.1	66.5 ± 7.07	0.281 ± 0.0102
0.5	1	146 ± 8.72	17.3 ± 0.755	0.119 ± 0.00492
0.75	1	95.0 ± 23.1	7.88 ± 1.43	0.0838 ± 0.00655
0	2	288 ± 7.55	5.2 ± 2.11	0.0180 ± 0.007
0.25	2	185 ± 29.3	32.3 ± 0.764	0.178 ± 0.0295
0.5	2	141 ± 4.04	12.9 ± 3.29	0.0914 ± 0.0238
0.75	2	121 ± 15.4	7.22 ± 1.65	0.0590 ± 0.00621

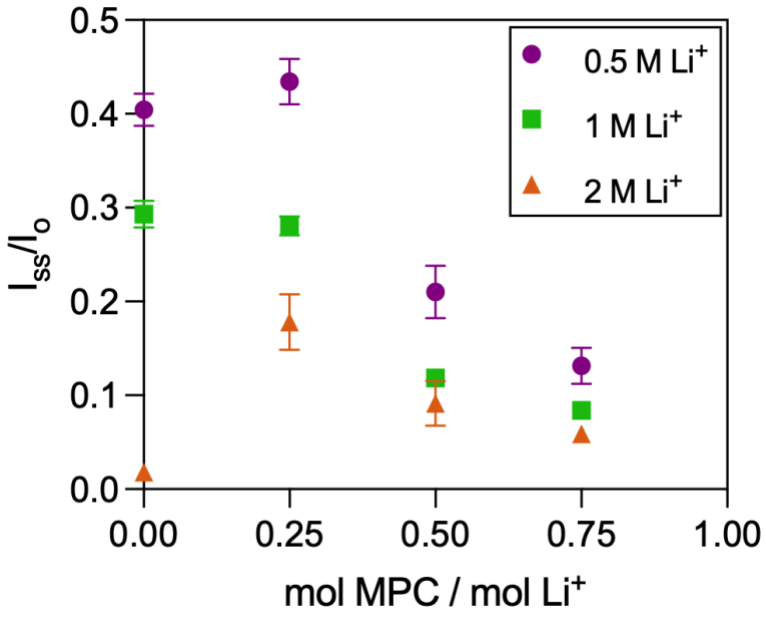


Figure 6.1. I_{ss}/I_0 for 0, 0.25, 0.5, and 0.75 mol MPC / mol Li^+ in 0.5 M, 1 M, and 2 M LiTFSI in BMP TFSI salt solution.

6.2. Non-Ionic Liquid-Based Polyzwitterion-Containing Gel Electrolytes

Even though ionic liquids (ILs) have advantages over other solvents used in electrolytes, such as being nonvolatile, thermally stable, and inherently ionic, other solvents, such as molecular solvents, could be used to form the liquid fraction of the polymer-supported gel electrolytes. Molecular solvents, such as propylene carbonate (PC), are already being used as electrolytes in conventional batteries. However, they are flammable, and therefore could be harmful in the case of leakage from a compromised battery pack[7,8].

A molecular solvent of interest that could be used in battery electrolytes is gamma-valerolactone (GVL). The chemical structure of GVL is similar to that of PC, except PC has an additional oxygen in its ring (figure 6.2). GVL is biodegradable, has low toxicity, and can be produced from biomass sources[9]. Such properties make it safer, cheaper to produce, and more environmentally friendly than ILs and other potential solvents for electrolytes. This section will demonstrate preliminary results showing the possibility of fabricating GVL-based, zwitterionic polymer-supported gels as potential battery electrolytes.

LiTFSI was dissolved in GVL at different molalities (1, 2, and 4 m). The total ionic conductivity of those three lithium salt-GVL solutions were calculated as described in Chapter 2 section 2.2.1. Figure 6.3 shows the ionic conductivities as a function of LiTFSI molality in GVL. 1, 2, and 4 m LiTFSI in GVL had ionic conductivity values of 6.90 ± 0.08 mS/cm, 4.57 ± 0.29 mS/cm, and 1.18 ± 0.02 mS/cm, respectively. The decrease in ionic conductivity with increasing molality can be attributed to the increase in viscosity due to the increase of LiTFSI amount dissolved in GVL. Even though the ionic conductivity decreases, these values are relatively high compared to those obtained from dissolving LiTFSI in BMP TFSI (at 0.5 M, 1 M, and 2 M

concentrations) shown in Chapter 4 (2.1 ± 0.094 mS/cm, 0.91 ± 0.013 mS/cm, and 0.24 ± 0.018 mS/cm for 0.5 M, 1 M, and 2 M LiTFSI in BMP TFSI, respectively). For a given amount of LiTFSI in GVL and in BMP TFSI, the increase in ionic conductivity going from BMP TFSI to GVL is attributed to the inherent higher viscosity of BMP TFSI compared to GVL.

MPC was also dissolved in LiTFSI/GVL to prepare gel precursor solutions for *in situ* UV-initiated polymerization (as described in Chapter 2 section 2.2.1). Similar to the case with BMP TFSI, MPC does not dissolve in GVL without the presence of LiTFSI. A 30 wt. % pMPC gel was successfully prepared using 2 m LiTFSI/GVL as the liquid component of the gel. The gel had an ionic conductivity value of 0.86 ± 0.01 mS/cm and an elastic modulus value of 6200 ± 850 kPa. This 30 wt. % gel is stiffer and more ionically conductive than a 16.5 wt. % pMPC ionogel (from Chapter 4). Furthermore, pMPC was able to dissolve in 2 m LiTFSI/GVL at 30 wt. %, whereas pMPC was not able to dissolve at higher than 23 wt. % in 2 M LiTFSI/BMP TFSI. This demonstrates the higher solubility of pMPC in LiTFSI/GVL compared to LiTFSI/BMP TFSI.

Moving forward, more gels with varying pMPC content in LiTFSI/GVL at different salt concentrations can be fabricated and tested (e.g. ionic conductivity and mechanical properties). This could elucidate and help better understand the difference in the nature of interaction between the zwitterionic parts of MPC and the LiTFSI ion clusters when in GVL compared to when in BMP TFSI.

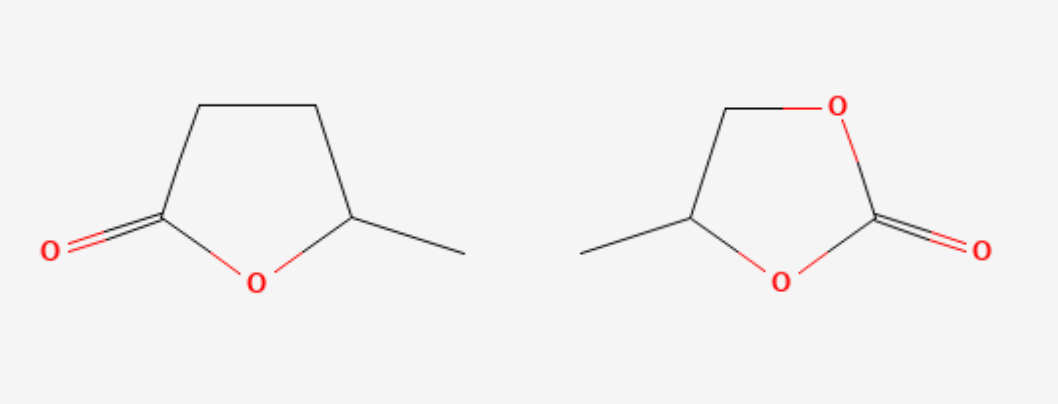


Figure 6.2. Chemical structure of gamma-valerolactone (GVL) (left) and propylene carbonate (PC) (right).

Image of GVL structure obtained from PubChem: https://pubchem.ncbi.nlm.nih.gov/compound/Gamma-Valerolactone.

Image of PC obtained from PubChem: https://pubchem.ncbi.nlm.nih.gov/compound/7924.

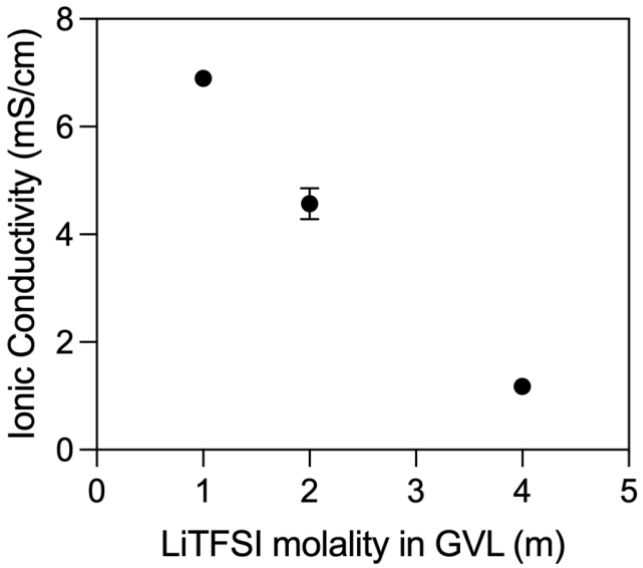


Figure 6.3. Total ionic conductivity for 1, 2, and 4 m LiTFSI/GVL solutions.

6.3. Non-Polymerizable Zwitterionic Phosphorylcholine Molecules in Lithium-Containing Ionic Liquid-Based Electrolytes

Chapters 3, 4, and 5 of this dissertation all discuss using the polymerizable zwitterion MPC. However, it would be interesting to examine the properties of the electrolyte that would be made using the same components of the ionogels but with a non-polymerizable zwitterionic component instead of a polymerizable one. This would elucidate the effect of the presence and absence of polymer chains on the properties of the electrolytes.

L-alpha-Glycerylphosphorylcholine (α-GPC) (chemical structure in figure 6.4) is a non-polymerizable analogue to MPC. This section will discuss preliminary results for electrolyes comprised of α-GPC, LiTFSI, and BMP TFSI at different LiTFSI/BMP TFSI concentrations (0.5, 1, and 2 M). Figure 6.5 shows the total ionic conductivity (6.5a) and normalized ionic conductivity with resoect to the LiTFSI/BMP TFSI solution (6.5b). At any given mol ratio of α-GPC to Li^+, the ionic conductivity is higher when the LiTFSI molarity is lower due to the lower viscosity with lower molarity. However, the highest boost in ionic conductivity from going from pure LiTFSI/BMP TFSI solutions to α-GPC-containing ones is seen in the higher LiTFSI concentration systems (at a fixed mol ratio of α-GPC to Li^+). Due to solubility limits, α-GPC in 1 M and 2 M LiTFSI/BMP TFSI was not able to dissolve at 0.75 and 0.5 mol α-GPC / mol Li^+, respectively.

Comparing the ionic conductivity values between α-GPC and pMPC ionogels at a given LiTFSI/BMP TFSI concentration helps understand the effect of the polymer chains, and therefore chain-bridging noncovalent cross-links, on the ion cluster dissociation and ion mobility. Figure 6.6 shows the ionic conductivity of α-GPC and pMPC electrolytes in 0.5 M (6.6a), 1 M (6.6b), and 2 M (6.6c) LiTFSI/BMP TFSI. It is evident that the ionic conductivity value increases by adding

ZIs, but, at a certain point, plateaus and/or decreases for pMPC but not for α-GPC. This could be attributed to the presence of the polymer chains at higher pMPC content that hinder the ion mobility.

Moving forward from these preliminary results, investigating the effect of the presence and absence of the polymer chains on the selective mobility of lithium ions would be interesting. The incorporation of zwitterionic polymer has been reported to increase alkali ion mobility by facilitating chain-hopping transport, which is faster than vehicular transport[10,11]. Comparing Li^+ current fraction (I_{ss}/I_0) of pMPC ionogels and α-GPC-containing LiTFSI/BMP TFSI solutions would give an idea if the polymer chains do play a role in selective lithium mobility. This can be done by preparing the electrolytes in porous separators (e.g. Whatman), sealing them in symmetric coin cells of the Li | electrolyte-in-separator | Li configuration, polarizing them (Chapter 2 section 2.2.2), and calculating the current fraction values.

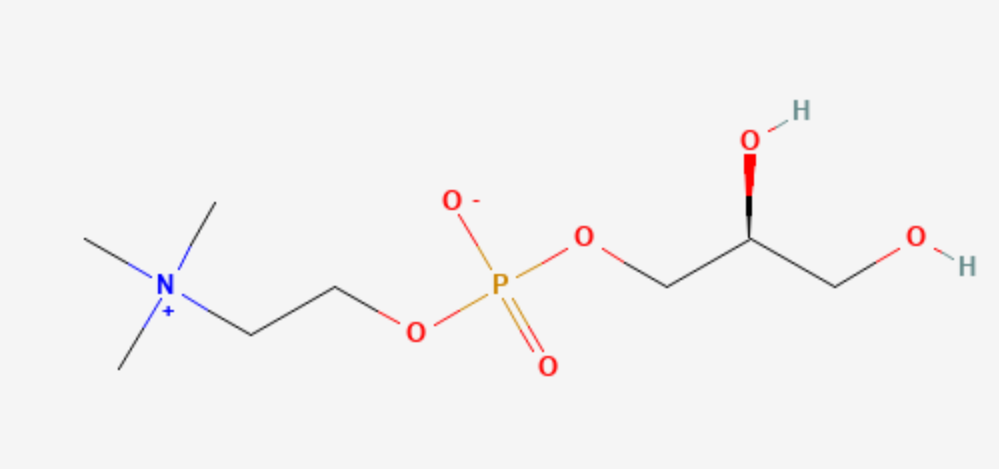


Figure 6.4. Chemical structure of L-alpha-Glycerylphosphorylcholine (α-GPC).

Image of α-GPC obtained from PubChem: https://pubchem.ncbi.nlm.nih.gov/compound/71920

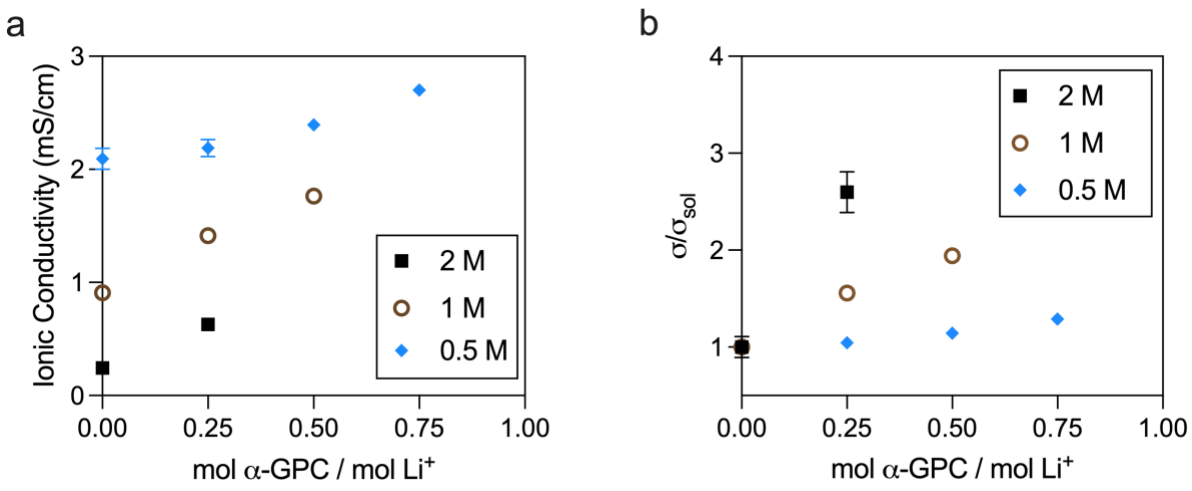


Figure 6.5. a) Ionic conductivity and b) normalized ionic conductivity of α-GPC-containing electrolytes with different LiTFSI/BMP TFSI concentrations (0.5 M, 1 M, and 2 M).

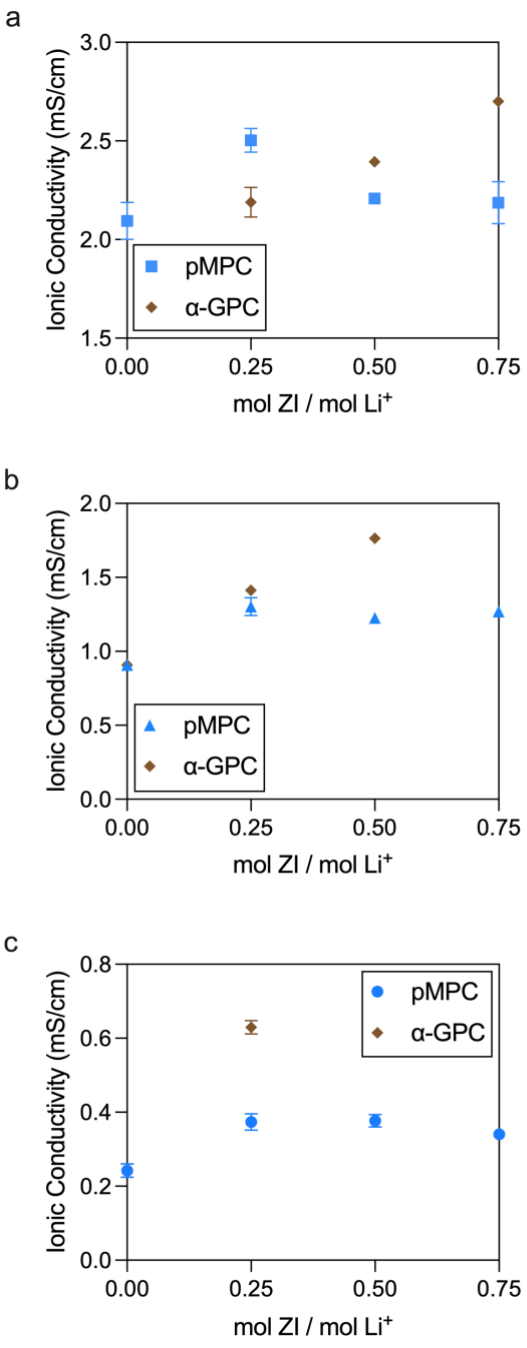


Figure 6.6. The ionic conductivity of pMPC ionogels and α-GPC-containing LiTFSI/BMP TFSI solutions in a) 0.5 M, b) 1 M, and c) 2 M LiTFSI/BMP TFSI solution concentrations.

6.4. References

(1) Lee, S.-H.; You, H.-G.; Han, K.-S.; Kim, J.; Jung, I.-H.; Song, J.-H. A new approach to surface properties of solid electrolyte interphase on a graphite negative electrode. *Journal of Power Sources* **2014**, *247*, 307-313.

(2) Young, R.; Templeton, T.; Roussel, L.; Gestmann, I.; van Veen, G.; Dingle, T.; Henstra, S. Extreme High-Resolution SEM: A Paradigm Shift. *Microscopy Today* **2008**, *16* (4), 24-29.

(3) Woo, H.-S.; Son, H.; Min, J.-Y.; Rhee, J.; Lee, H.-T.; Kim, D.-W. Ionic liquid-based gel polymer electrolyte containing zwitterion for lithium-oxygen batteries. *Electrochimica Acta* **2020**, *345*, 136248.

(4) Malmgren, S.; Ciosek, K.; Hahlin, M.; Gustafsson, T.; Gorgoi, M.; Rensmo, H.; Edström, K. Comparing anode and cathode electrode/electrolyte interface composition and morphology using soft and hard X-ray photoelectron spectroscopy. *Electrochimica Acta* **2013**, *97*, 23-32.

(5) Chu, Y.; Shen, Y.; Guo, F.; Zhao, X.; Dong, Q.; Zhang, Q.; Li, W.; Chen, H.; Luo, Z.; Chen, L. Advanced Characterizations of Solid Electrolyte Interphases in Lithium-Ion Batteries. *Electrochemical Energy Reviews* **2020**, *3* (1), 187-219.

(6) Zhang, H.-L.; Li, F.; Liu, C.; Tan, J.; Cheng, H.-M. New Insight into the Solid Electrolyte Interphase with Use of a Focused Ion Beam. *The Journal of Physical Chemistry B* **2005**, *109* (47), 22205-22211.

(7) Tang, X.; Lv, S.; Jiang, K.; Zhou, G.; Liu, X. Recent development of ionic liquid-based electrolytes in lithium-ion batteries. *Journal of Power Sources* **2022**, *542*, 231792.

(8) Sasaki, Y. Organic Electrolytes of Secondary Lithium Batteries. *Electrochemistry* **2008**, *76* (1), 2-15.

(9) Pierini, A.; Migliorati, V.; Gómez-Urbano, J. L.; Balducci, A.; Brutti, S.; Bodo, E. Simulations of γ-Valerolactone Solvents and Electrolytes for Lithium Batteries Using Polarizable Molecular Dynamics. In *Molecules*, 2025; Vol. 30.

(10) Li, Z. H.; Xia, Q. L.; Liu, L. L.; Lei, G. T.; Xiao, Q. Z.; Gao, D. S.; Zhou, X. D. Effect of zwitterionic salt on the electrochemical properties of a solid polymer electrolyte with high temperature stability for lithium ion batteries. *Electrochimica Acta* **2010**, *56* (2), 804-809.

(11) D'Angelo, A. J.; Panzer, M. J. Decoupling the Ionic Conductivity and Elastic Modulus of Gel Electrolytes: Fully Zwitterionic Copolymer Scaffolds in Lithium Salt/Ionic Liquid Solutions. **2018**.

Appendix A: Supplementary Information Concerning Chapter 3

This appendix is reproduced from the following publication:

Alsaedi, M. K.; Tadesse, M. Y.; Ganesan, V.; Panzer, M. J. "Zwitterionic Polymer Ionogel Electrolytes Supported by Coulombic Cross-links: Impacts of Akali Metal Cation Identity." *J. Phys. Chem. B*. **2024**, 128 (13), 3273-3281

A.1 Additional Experimental Results

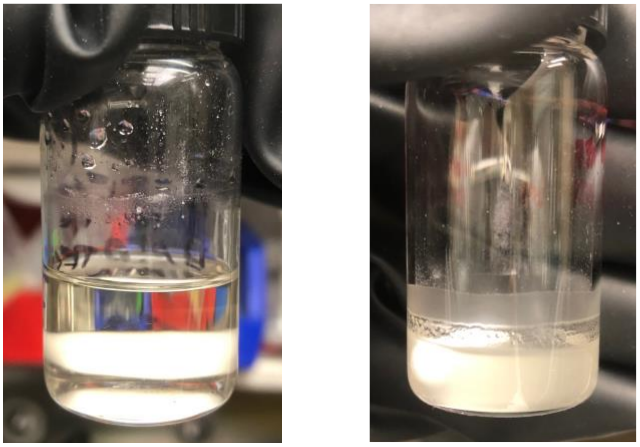


Figure A.1. Photographs of NaTFSI solutions prepared in BMP TFSI at 0.5 M (left) and 1 M (right). White oblong object is a stir bar.

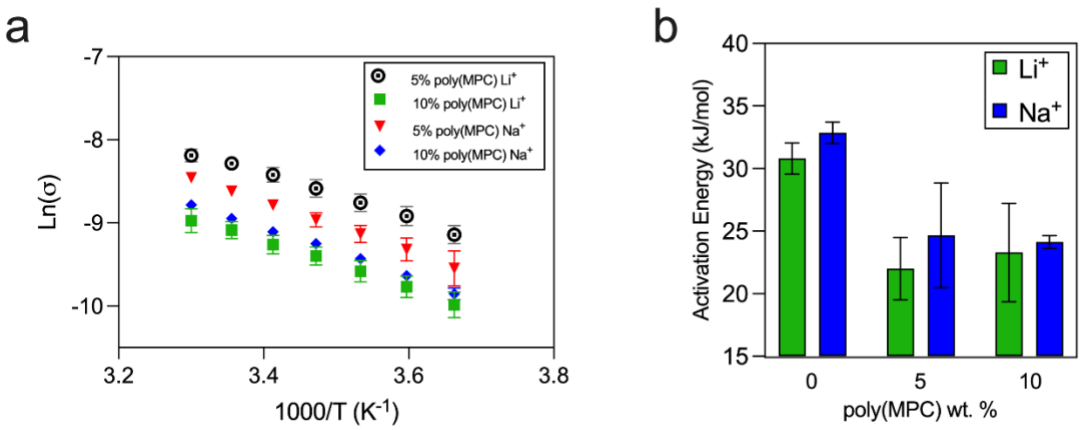


Figure A.2. (a) Natural logarithm of ionic conductivity plotted as a function of inverse absolute temperature for 5 wt.% and 10 wt.% poly(MPC) single salt ionogels. (b) Apparent activation energy of ionic conductivity values measured for Li^+ and Na^+ ILEs (0 wt.% poly(MPC)), as well as the 5 wt.% poly(MPC) and 10 wt.% poly(MPC) single salt ionogels.

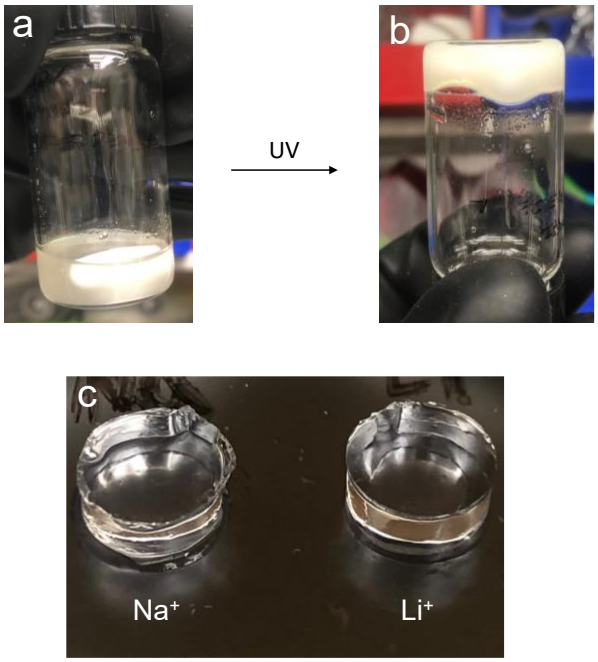


Figure A.3. Top series: photographs showing (a) 3 wt.% MPC monomer in neat BMP TFSI (white oblong object is a stir bar), and (b) post-photopolymerization specimen of the same 3 wt.% MPC in neat BMP TFSI, vial inverted. The opacity of both samples indicates the poor solubility of MPC and poly(MPC) in neat ionic liquid, in the absence of alkali metal salt. Bottom image: (c) photograph of representative 5 wt.% poly(MPC)-supported ionogels containing 0.5 M NaTFSI (left, Na^+) or 0.5 M LiTFSI (right, Li^+). The freestanding, transparent ionogels were synthesized in cylindrical-shaped molds, then removed.

A.2 Computational Methods and Details

In this study, we used atomistic molecular dynamic simulations to understand the structural and dynamic properties of the ionogel precursor solutions of ZI monomer MPC in 0.5M X^+ $TFSI^-$ /BMP TFSI ionic liquid electrolyte (where X^+ = Li^+, Na^+, or Li^+ and Na^+). To understand the impact of ZI content on the MPC ionogel precursor, the content of the base ionic liquid was held constant and the weight percentages of MPC units (W_{MPC}) were varied in both single- and mixed-salt monomeric MPC precursor solutions. The simulation details for the LiTFSI single-salt precursors, the NaTFSI single-salt precursors, and the LiTFSI and NaTFSI (equimolar) mixed-salt precursors are shown in Tables A.1, A.2, and A.3, respectively.

Table A.1. Simulation details for LiTFSI single-salt ionogel precursor solutions at different MPC weight percentage values (W_{MPC}).

System	BMP^+	$TFSI^-$	Li^+	MPC	Box Length (nm)	Conc. Li^+ (M)
W_{MPC} = 3%	300	380	80	15	6.03	0.61
W_{MPC} = 6%	300	380	80	30	6.10	0.59
W_{MPC} = 8%	300	380	80	45	6.16	0.57
W_{MPC} = 11%	300	380	80	60	6.23	0.55
W_{MPC} = 13%	300	380	80	75	6.31	0.53

Table A.2. Simulation details for NaTFSI single-salt ionogel precursor solutions at different MPC weight percentage values (W_{MPC}).

System	BMP^+	$TFSI^-$	Na^+	MPC	Box Length (nm)	Conc. Li^+ (M)
W_{MPC} = 3%	300	380	80	15	6.03	0.61
W_{MPC} = 6%	300	380	80	30	6.10	0.59
W_{MPC} = 8%	300	380	80	45	6.16	0.57
W_{MPC} = 11%	300	380	80	60	6.23	0.55
W_{MPC} = 13%	300	380	80	75	6.31	0.53

Table A.3. Simulation details for NaTFSI and LiTFSI (equimolar) mixed-salt ionogel precursor solutions at different MPC weight percentage values (W_{MPC}).

System	BMP^+	$TFSI^-$	Li^+	Na^+	MPC	Box Length (nm)	Conc. Li^++Na^+ (M)
W_{MPC} = 3%	300	380	40	40	15	6.03	0.61
W_{MPC} = 6%	300	380	40	40	30	6.10	0.59
W_{MPC} = 8%	300	380	40	40	45	6.16	0.57
W_{MPC} = 11%	300	380	40	40	60	6.23	0.55
W_{MPC} = 13%	300	380	40	40	75	6.31	0.53

The molecular dynamics simulations were performed using the Gromacs 2020.5 package.[1,2] The all-atom optimized potential for liquid simulations (OPLS-AA) was used for modeling the MPC molecules, Li^+ and Na^+ ions.[3,4] The CL&P force field[5] was chosen to model the IL (BMP^+–$TFSI^-$) interactions. The total potential energy of the system in terms of its bonded and nonbonded potential interactions are displayed below in Equations A.1 and A.2 respectively:[6]

$$U_b = \sum_b \frac{1}{2} k_b (b - b_0)^2 + \sum_\theta \frac{1}{2} k_\theta (\theta - \theta_0)^2 + \sum_\phi \sum_{m=1}^{5} (-1)^m C_m (\cos \phi)^m + \sum_\psi \frac{1}{2} k_\psi (1 - \cos (2\psi))$$

(Eq. A.1)

$$U_{nb} = f_{ij} \sum_{i<j} \frac{e^2 z_i z_j}{4\pi\epsilon_0 r_{ij}} + 4\epsilon_{ij} \left[\left(\frac{\sigma_{ij}}{r_{ij}} \right)^{12} - \left(\frac{\sigma_{ij}}{r_{ij}} \right)^{6} \right]$$

(Eq. A.2)

In Equation A.1, the bonded potential is modeled as the sum of the intermolecular bond, angle, dihedral, and improper torsions, where k_b, k_θ, and C_m denote bond length spring constants, bond angle spring constants, and Ryckaert-Bellemans potential constants, respectively. Further, b are bond lengths, θ are bond angles, ϕ are the dihedral angles, and ψ is the improper dihedral angle. b_0, θ_0, and ψ_0 are the equilibrium bond lengths, angles, and improper dihedral angles, respectively.

Equation A.2 displays the functional form of the nonbonded interactions which are modeled as the sum of the electrostatic and Lennard-Jones (LJ) interactions scaled by f_{ij} , where f_{ij} = 0 for 1,2 and 1,3 interactions, f_{ij} = 0.5 for 1,4 interactions and f_{ij} = 1 for interactions beyond 1-4 interactions. The geometric combining rule was used to generate the LJ parameters for cross terms.[6] The partial charges of the MPC molecules were obtained by optimizing MPC trimers by applying B3LYP/6-311 g** theory using Gaussian 16 Rev. C.01.[7] The restrained electrostatic

potential (RESP)[8] was post-processed through the Multiwfn package.[9, 10] The topology files of the MPC molecules were obtained using MKTOP[11] and in-house code was used to assemble the molecular structure and topology file. A factor of 0.8 was used to scale the atomic partial charges of the MPC molecules, lithium, sodium, and IL ions in the system to mimic polarizability.[12]

Inspired by the 21-step decompression method proposed by Colina and co-workers,[13] the following loop of multi-step equilibration procedure was used to prepare the equilibrated configuration:

1. 0.1 ns NVT simulation at 1000 K,

2. 0.1 ns NPT simulation at 600 K and 100 bar, and

3. 0.1 ns NPT simulation at 600 K and 1 bar.

This three-step loop was repeated eight times in our study to prepare the initial configuration for the production run. A 110 ns NPT ensemble was employed for the production run. The initial 10 ns was used for equilibration whereas the last 100 ns were used for analyzing the static and dynamic properties. The leapfrog integration scheme was used to integrate Newton's equations of motion.[14] A timestep of δt = 1 fs was used to update the simulations' force, velocity, and position. The Lennard−Jones (LJ) potential was set to 1.3 nm along with long-range electrostatic interactions calculated with the particle mesh method.[15] The v−rescale thermostat[16] was used for temperature coupling at 600 K with coupling parameters of τ_T = 1.0 ps. The Parrinello−Rahman barostat[17, 18] was used for pressure control at 1 bar with coupling parameters

of τ_P = 1.0 ps. All simulations were run at 600 K, and the average of five samples with different initial configurations was used to obtain the static results presented in this work.

A.2.1 Forcefield Parameters

Figure A.2 shows the atom naming scheme of MPC, BMP^+, and $TFSI^-$. The atom names associated with their GROMACS atom types and their corresponding LJ interaction parameters and atomic partial charges are listed in Tables A.4-A.7. The GROMACS atom types are associated with their corresponding bond lengths, spring constants, bond angles, dihedral, and improper dihedral forcefield parameters in Tables A.8-A.16.

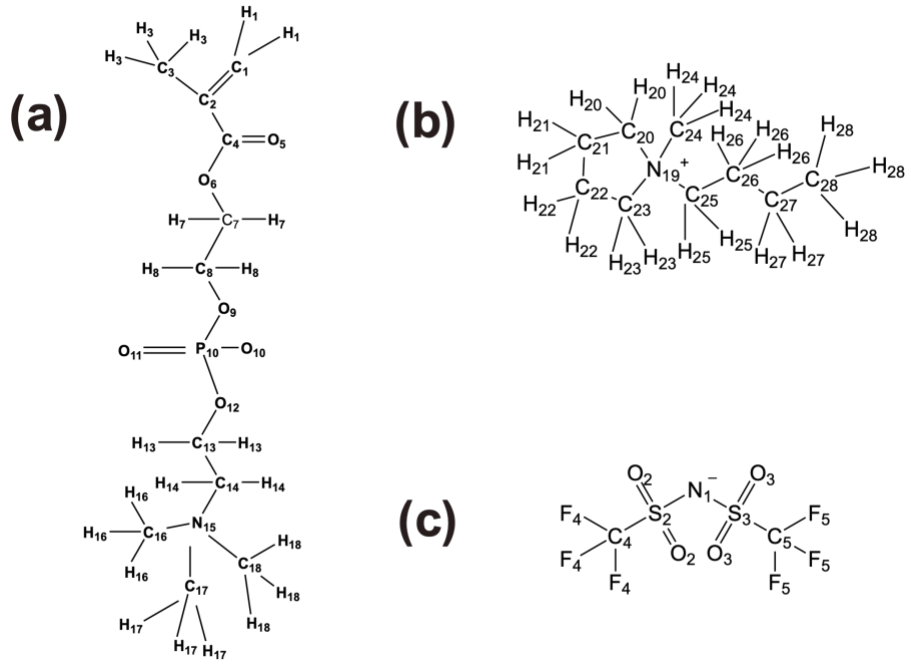


Figure A.4. Atom naming scheme for (a) MPC, (b) BMP^{+} and (c) $TFSI^{-}$ molecules.

A.2.2 Atom types, LJ parameters, and partial charges

Table A.4. Atom type, Lennard-Jones parameters, and partial charges for MPC. Dashes indicate that the value from the previous line is repeated.

Atom	Atom Type	σ (nm)	ϵ (kJ/mol)	q
C1	CT	0.350	0.276	-0.300
C2	CT	-	-	0.122
C3	C1	-	-	-0.157
C4	CO	0.355	0.293	0.597
C7	C1	0.350	0.276	0.322
C8	C1	-	-	0.091
C13	C1	-	-	0.121
C14	C1	-	-	-0.027
C16	CT	-	-	-0.348
C17	CT	-	-	-
C18	CT	-	-	-
H1	HC	0.250	0.126	0.074
H3	HC	-	-	0.042
H7	HC	-	-	0.000
H8	HC	-	-	0.037
H13	HC	-	-	0.038
H14	HC	-	-	0.079
H16	HT	-	-	0.157
H17	HT	-	-	-

H18	HT	-	-	-
N15	N3	0.325	0.711	0.079
O5	O2	0.296	0.879	-0.446
O6	OC	0.290	0.586	-0.468
O9	OC	-	-	-0.366
O11	OP	0.296	0.879	-0.545
O10	OP	-	-	-0.558
O12	OC	0.290	0.586	-0.351
P10	P	0.374	0.837	0.864

Table A.5. Atom type, Lennard-Jones parameters, and partial charges[19, 20] for $TFSI^-$. Dashes indicate that the value from the previous line is repeated.

Atom	Atom Type	σ (nm)	ϵ (kJ/mol)	q
N1	NI	0.325	0.711	-0.400
S2	SO	0.355	1.046	0.600
O2	OS	0.296	0.879	-0.400
O3	OS	0.296	0.879	-0.400
C4	CF	0.350	0.276	0.300
C5	CF	0.350	0.276	0.300
F4	FC	0.295	0.222	-0.100
F5	FC	0.295	0.222	-0.100

Table A.6. Atom type, Lennard-Jones parameters, and partial charges[19, 20] for BMP^+. Dashes indicate that the value from the previous line is repeated.

Atom	Atom Type	σ (nm)	ϵ (kJ/mol)	q
N19	NT	0.325	0.711	0.096
C20	CT	0.350	0.276	-0.136
C21	CT	-	-	-
C22	CT	-	-	0.008
C23	CT	-	-	-
C24	CT	-	-	-0.136
C25	CT	-	-	-
C26	CT	-	-	0.008
C27	CT	-	-	-0.120
C28	CT	-	-	-0.180
H20	HC	0.250	0.126	0.104
H21	HC	-	-	-
H22	HC	-	-	0.048
H23	HC	-	-	-
H24	HC	-	-	0.104
H25	HC	-	-	-
H26	HC	-	-	0.048
H27	HC	-	-	0.060
H28	HC	-	-	-

Table A.7. Atom type, Lennard-Jones parameters, and partial charge for Li^+.

Atom	Atom Type	σ (nm)	ϵ (kJ/mol)	q
Li^+	-	0.2126	0.0765	0.8

A.2.3 Equilibrium bond lengths and spring constants

Table A.8. Equilibrium bond lengths and spring constants for MPC. Dashes indicate that the value from the previous line is repeated.

Atom Types	b_0 (nm)	k_b (kJ/mol/nm^2)
HC – CT	0.1090	284512
CT – CT	0.1529	224262
C1 – CT	-	-
HC – C1	0.1090	284512
CO – CT	0.1522	265265
O2 – CO	0.1229	476976
OC – CO	0.1327	179075
C1 – OC	0.1410	267776
C1 – C1	0.1529	224262
OC – C1	0.1410	267776
P – OC	0.1610	192464
OP – P	0.1480	439320
OC – P	0.1610	192464
N3 – C1	0.1471	307105
CT – N3	-	307105
HT – CT	0.1090	284512

Table A.9. Equilibrium bond lengths and spring constants[19, 20] for $TFSI^-$.

Atom Types	b_0 (nm)	k_b (kJ/mol/nm^2)
CF – FC	0.1323	369700
CF – SO	0.1818	197000
SO – OS	0.1442	533100
NI – SO	0.1570	311300

Table A.10. Equilibrium bond lengths and spring constants[19, 20] for BMP^+.

Atom Types	b_0 (nm)	k_b (kJ/mol/nm^2)
HC – CT	0.1090	-284500
CT – CT	0.1529	224200
NT – CT	0.1471	307100

A.2.4 Equilibrium bond angles and spring constants

Table A.11. Equilibrium bond angles and spring constants for MPC.

Atom Types	θ_0 (°)	k_θ (kJ/mol/rad^2)
HC – CT – HC	107.8	276.144
HC – CT – CT	110.7	313.800
CT – CT – C1	112.7	488.273
CT – C1 – HC	110.7	313.800
CT – CT – CO	111.1	527.184
CT – CO – O2	120.4	669.440
CT – CO – OC	111.4	677.808
CO – OC – C1	116.9	694.544
OC – C1 – HC	109.5	292.880
OC – C1 – C1	109.5	418.400
C1 – C1 – HC	110.7	313.800
C1 – C1 – OC	109.5	418.400
C1 – OC – P	120.5	836.800
OC – P – OP	108.23	836.800
OC – P – OC	102.6	376.560
P – OC – C1	120.5	836.800
C1 – C1 – N3	111.2	669.440
C1 – N3 – CT	113.0	418.400
N3 – CT – HT	109.5	292.880

HC – CT – HT	107.8	276.144
OP – P – OP	108.4	531.954
HC – C1 – HC	107.8	276.144
HC – C1 – N3	109.5	292.880
HT – CT – HT	107.8	276.144
HC – C1 – C1	110.7	313.800
CT – CT – HT	110.7	313.800
OP – P – OC	108.23	836.800
HC – C1 – OC	109.5	292.880
C1 – CT – CO	111.1	527.184
CT – N3 – CT	113.0	418.400
O2 – CO – OC	123.4	694.544
CT – CT – CT	112.7	488.273
CT – CT – HC	110.7	313.800
CO – CT – CT	111.1	527.184
C1 – CT – CT	112.7	488.273
C1 – CT – HT	110.7	313.800
CO – CT – HT	109.5	292.880

Table A.12. Equilibrium bond angles and spring constants[19, 20] for $TFSI^-$.

Atom Types	θ_0 (°)	k_θ (kJ/mol/rad^2)
OS – SO – OS	118.5	969
OS – SO – NI	113.6	789
CF – SO – NI	100.2	816
SO – NI – SO	125.6	671
FC – CF – FC	107.1	781
FC – CF – SO	111.7	694
CF – SO – OS	102.6	870

Table A.13. Equilibrium bond angles and spring constants[19, 20] for BMP^+.

Atom Types	θ_0 (°)	k_θ (kJ/mol/rad^2)
CT – CT – CT	112.7	488.3
CT – CT – HC	110.7	313.8
HC – CT – HC	107.8	276.1
NT – CT – CT	109.5	669.4
CT – NT – CT	109.5	418.4
HC – CT – NT	109.5	209.2

A.2.5 Dihedral potential constants

Table A.14. Ryckaert-Bellemans dihedral potential constants for MPC. Dashes indicate that the value from the previous line is repeated.

Atom Types	C_0 (kJ/mol)	C_1 (kJ/mol)	C_2 (kJ/mol)	C_3 (kJ/mol)	C_4 (kJ/mol)	C_5 (kJ/mol)
C1 – CT – CT – HC	0.628	1.883	0	-2.51	0	0
C1 – C1 – OC – CO	-2.197	5.201	0.527	-3.531	-	-
C1 – C1 – OC – P	-5.356	3.598	2.594	-0.837	-	-
C1 – OC – CO – CT	31.206	-9.768	21.439	0	-	-
C1 – OC – CO – O2	21.439	0	-	-	-	-
C1 – OC – P – OP	0	-	0	-	-	-
C1 – OC – P – OC	-	-	-	-	-	-
C1 – CT – CT – CT	2.301	-1.464	0.837	-1.674	-	-
CO – CT – C1 – HC	-0.209	-0.628	0	0.837	-	-
CO – CT – CT – HC	-	-	-	-	-	-
CO – CT – CT – CT	-4.96	6.286	1.31	-2.636	-	-
CT – N3 – C1 – C1	3.042	-1.351	0.519	-2.209	-	-
CT – N3 – C1 – HC	0.632	1.895	0	-2.527	-	-
CT – N3 – C1 – HT	-	-	-	-	-	-
CT – CT – CO – O2	0	0	-	0	-	-
CT – CT – CO – OC	-1.157	-3.471	-	4.628	-	-
CT – CT – CT – CO	-4.96	6.286	1.31	-2.636	-	-
CT – CT – CT – CT	2.301	-1.464	0.837	-1.674	-	-

CT – CT – CT – C1	-	-	-	-	-	-
CT – CT – CT – HC	0.628	1.883	0	-2.51	-	-
CT – CT – C1 – HC	-	-	-	-	-	-
CT – CT – CT – HT	-	-	-	-	-	-
HC – C1 – CT – CT	-	-	-	-	-	-
HC – C1 – C1 – HC	-	-	-	-	-	-
HC – C1 – C1 – OC	0.979	2.937	-	-3.916	-	-
HC – C1 – OC – CO	0.414	1.243	-	-1.657	-	-
HC – C1 – OC – P	0.628	1.883	-	-2.51	-	-
HC – CT – CT – CO	-0.209	-0.628	-	0.837	-	-
HC – CT – CT – C1	0.628	1.883	-	-2.51	-	-
HC – CT – CT – CT	-	-	-	-	-	-
HT – CT – CT – CO	-0.209	-0.628	-	0.837	-	-
HT – CT – CT – C1	0.628	1.883	-	-2.51	-	-
HT – CT – N3 – CT	0.632	1.895	-	-2.527	-	-
HT – CT – N3 – C1	-	-	-	-	-	-
HT – CT – CO – O2	0	0	-	0	-	-
HT – CT – CO – OC	0.276	0.828	-	-1.105	-	-
HT – CT – CT – HC	0.628	1.883	-	-2.51	-	-
HT – CT – C1 – HC	-	-	-	-	-	-
HT – CT – CT – CT	-	-	-	-	-	-
N3 – C1 – C1 – HC	0.803	2.41	-	-3.213	-	-
N3 – C1 – C1 – OC	16.736	16.736	-	0	-	-
O2 – CO – CT – C1	0	0	-	-	-	-
O2 – CO – CT – CT	-	-	-	-	-	-

Table A.15. Fourier dihedral potential[19, 20] constants for BMP^+ and $TFSI^-$. Dashes indicate that the value from the previous line is repeated.

Atom Types	C_1 (kJ/mol)	C_2 (kJ/mol)	C_3 (kJ/mol)	C_4 (kJ/mol)
CT – CT – CT – CT	0.0000	0.0000	1.3305	0.0000
CT – CT – CT – HC	-	-	1.5313	-
CT – CT – CT – CT	7.2800	-0.6569	1.1673	-
HC – CT – CT – NT	-4.2384	-2.9665	1.9790	-
CT – CT – CT – NT	10.0081	-2.8200	2.3012	-
CT – NT – CT – CT	1.7405	-0.5356	2.9079	-
HC – CT – NT – CT	0.0000	0.0000	2.3430	-
OS – SO – CF – FC	0.0000	0.0000	1.4510	0.0000
NI – SO – CF – FC	-	-	1.3220	-
OS – SO – NI – SO	-	-	-0.0150	-
SO – NI – SO – CF	32.7730	-10.4200	-3.1950	-

Table A.16. Improper dihedral constants.

Atom Types	ψ_0 (°)	k_ψ (kJ/mol/rad^2)	n
OC – CO – CT – O2	180.0	43.932	2

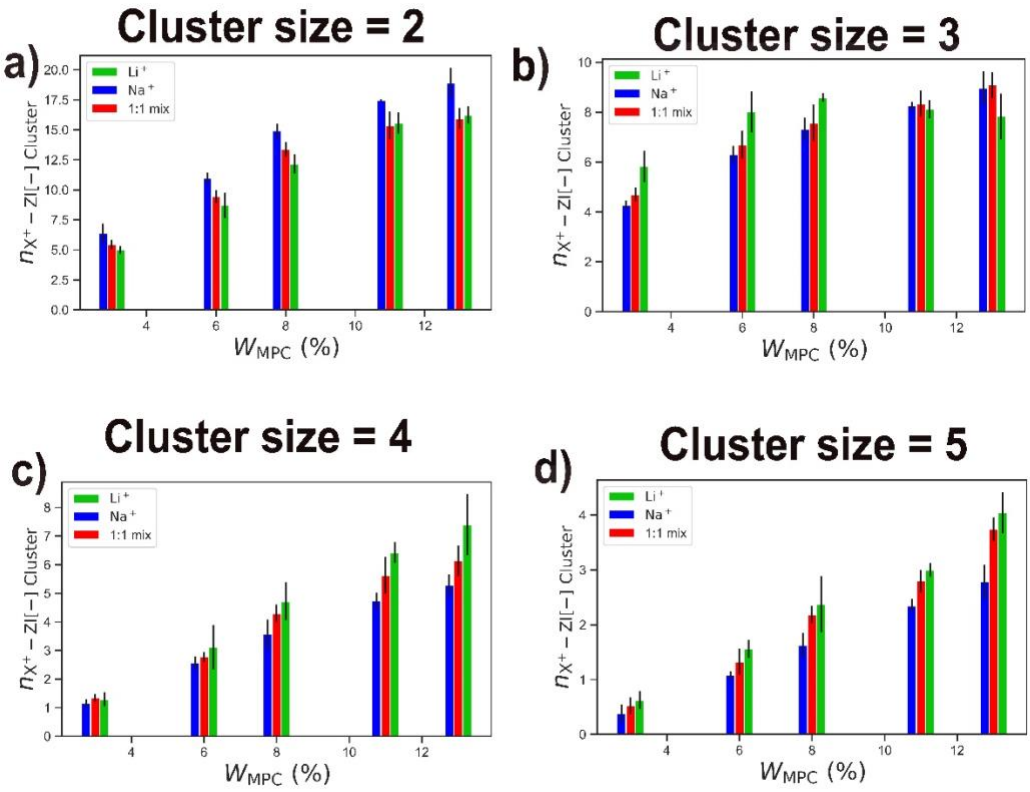


Figure A.5. Number of clusters in ionogel precursor solutions as a function of weight percentages of MPC monomers (W_{MPC}) for cluster sizes of (a) 2, (b) 3, (c) 4 and (d) 5. ZI[-] and X^+ represent the anionic portion of the MPC molecule and the alkali metal ion(s), respectively.

In Figure A.6, we present the ion pair relaxation timescale (τ_c) characterizing the intermittent residence time of a given ion pair, *i.e.* the alkali metal cation and MPC ion pair. τ_c can be calculated using the following equation:

$$C(t) = \frac{< h(t_0) \cdot h(t_0 + t) >}{< h^2 >}$$

where $h(t)$ equals 1 for an existing pair of ions and 0 otherwise. The $C(t)$ is fitted to the Kohlrausch-Williams-Watts (KWW) stretched exponential form shown below:

$$C(t) = exp\left(-\left(\frac{t}{\alpha}\right)^{\beta}\right)$$

The relaxation timescale τ_c was calculated using the following equation:

$$\tau_c = \alpha\, \Gamma\left(1 + \frac{1}{\beta}\right)$$

where Γ denotes the Gamma function.

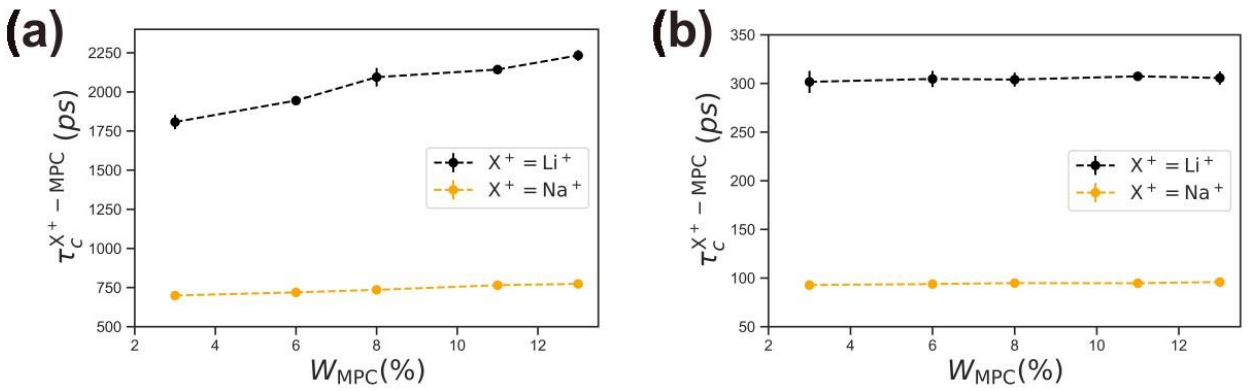


Figure A.6. The alkali metal cation-MPC intermittent association lifetimes, $\tau_c^{X^+ - MPC}$ in (a) single- and (b) 1:1 mixed-salt ionogel precursor solutions.

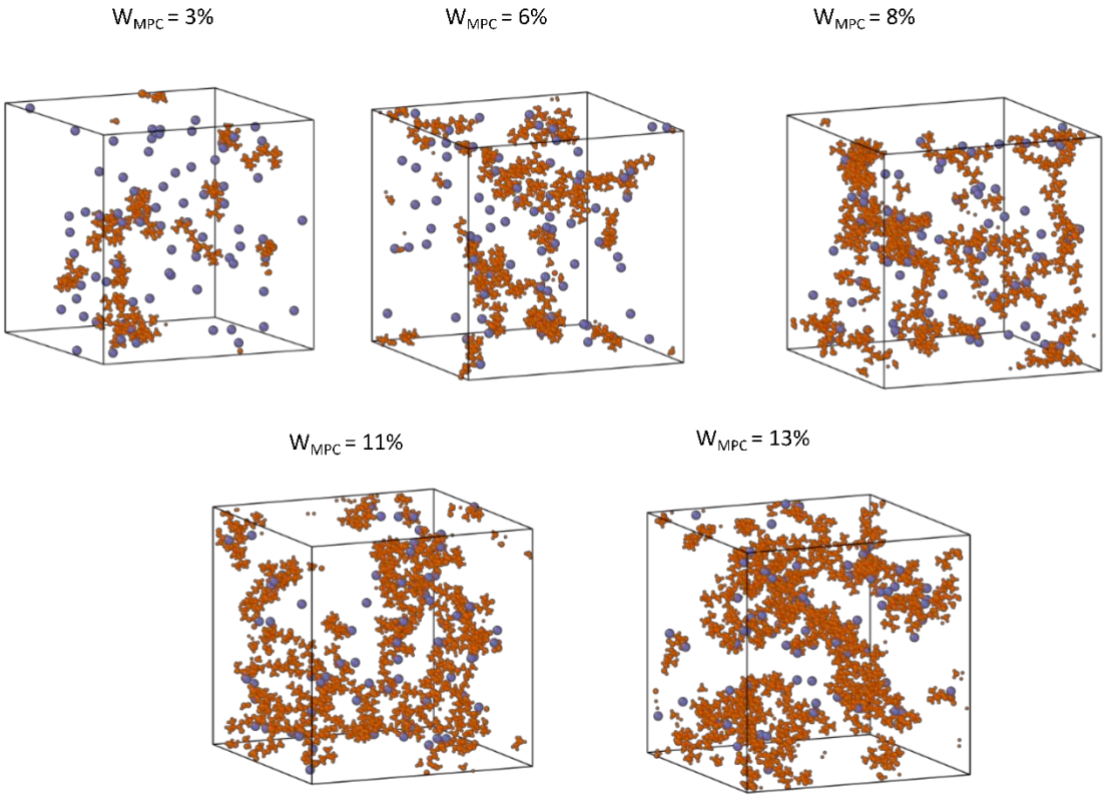


Figure A.7. Molecular dynamics (MD) snapshots of Li^+ only system simulation boxes with increasing mass fraction of MPC monomer, W_{MPC}. MPC molecules (orange) and Li^+ ions (purple) are displayed in the simulation snapshots. The ionic liquid ions, BMP^+ and $TFSI^-$, have been removed from the snapshots for ease of viewing MPC and Li^+.

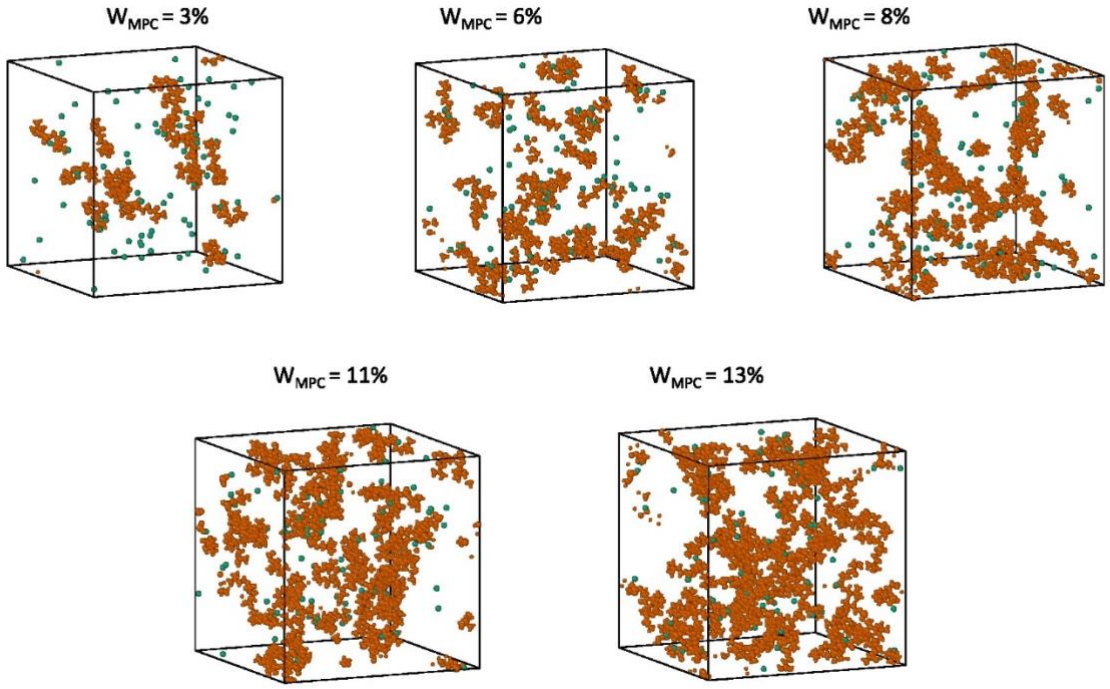


Figure A.8. Molecular dynamics (MD) snapshots of Li^+ only system simulation boxes with increasing mass fraction of MPC monomer, W_{MPC}. MPC molecules (orange) and Na^+ ions (green) are displayed in the simulation snapshots. The ionic liquid ions, BMP^+ and $TFSI^-$, have been removed from the snapshots for ease of viewing MPC and Na^+.

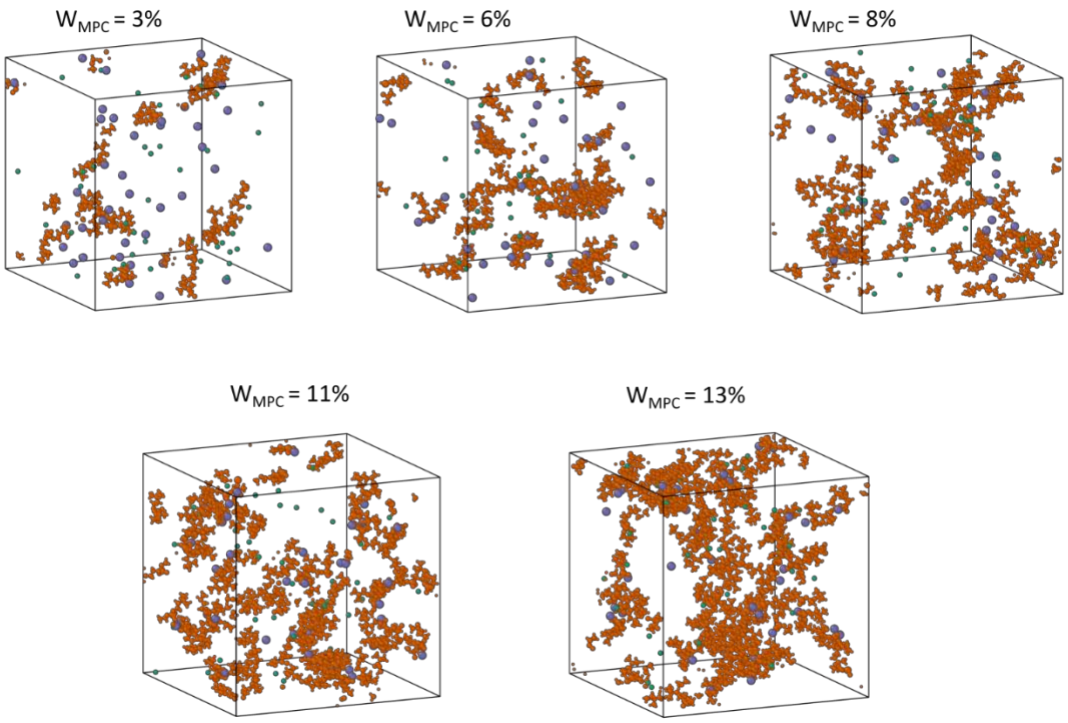


Figure A.9. Molecular dynamics (MD) snapshots of 1:1 mixed Li^+/Na^+ system simulation boxes with increasing mass fraction of MPC monomer, W_{MPC}. MPC molecules (orange), Li^+ ions (purple), and Na^+ ions (green) are displayed in the simulation snapshots. The ionic liquid ions, BMP^+ and $TFSI^-$, have been removed from the snapshots for ease of viewing MPC, Li^+, and Na^+.

Supporting References

1. Abraham, M. J.; Murtola, T.; Schulz, R.; Pall, S.; Smith, J. C.; Hess, B.; Lindahl, E. GROMACS: High performance molecular simulations through multi-level parallelism from laptops to supercomputers. *SoftwareX* **2015**, *1*, 19–25.

2. Spoel, V. D.; others GROMACS 2020.5 Source code. *Zenodo*

3. Jorgensen, W. L.; Maxwell, D. S.; Tirado-Rives, J. Development and testing of the OPLS all-atom force field on conformational energetics and properties of organic liquids. *J. Am. Chem. Soc.* **1996**, *118*, 11225–11236.

4. Jorgensen, W. L.; Tirado-Rives, J. Potential energy functions for atomic-level simulations of water and organic and biomolecular systems. Proc. Nat. Acad. Sci. **2005**, *102*, 6665–6670.

5. Canongia Lopes, J. N.; Padua, A. A. CL&P: A generic and systematic force field for ionic liquids modeling. *Theoretical Chemistry Accounts* **2012**, *131*, 1–11.

6. Bauer, P.; Hess, B.; Lindahl, E. GROMACS 2022.1 Manual. Preprint at https://doi. org/10.5281/zenodo.6103567 **2022**.

7. Frisch, M. e.; Trucks, G.; Schlegel, H.; Scuseria, G.; Robb, M.; Cheeseman, J.; Scalmani, G.; Barone, V.; Petersson, G.; Nakatsuji, H.; others Gaussian 16, revision C. 01.

2016.

8. Bayly, C. I.; Cieplak, P.; Cornell, W.; Kollman, P. A. A well-behaved electrostatic potential based method using charge restraints for deriving atomic charges: the RESP model. *J. Phys. Chem.* **1993**, *97*, 10269–10280.

9. Lu, T.; Chen, F. Multiwfn: A multifunctional wavefunction analyzer. *J. Comp. Chem.* **2012**, *33*, 580–592.

10. Lu, T.; Chen, F.-W. Comparison of computational methods for atomic charges. *Acta Physico-Chimica Sinica* **2012**, *28*, 1–18.

11. Ribeiro, A. A.; Horta, B. A.; Alencastro, R. B. d. MKTOP: a program for automatic construction of molecular topologies. *Journal of the Brazilian Chemical Society* **2008**, *19*, 1433–1435.

12. Zhang, Z.; Nasrabadi, A. T.; Aryal, D.; Ganesan, V. Mechanisms of ion transport in lithium salt-doped polymeric ionic liquid electrolytes. *Macromolecules* **2020**, *53*, 6995–7008.

13. Larsen, G. S.; Lin, P.; Hart, K. E.; Colina, C. M. Molecular simulations of PIM-1-like polymers of intrinsic microporosity. *Macromolecules* **2011**, *44*, 6944–6951.

14. Hockney, R. W.; Goel, S.; Eastwood, J. Quiet high-resolution computer models of a plasma. *J. Comp. Phys.* **1974**, *14*, 148–158.

15. Darden, T.; York, D.; Pedersen, L. Particle mesh Ewald: An N-log (N) method for Ewald sums in large systems. *J. Chem. Phys.* **1993**, *98*, 10089–10092.

16. Bussi, G.; Donadio, D.; Parrinello, M. Canonical sampling through velocity rescaling. *J. Chem. Phys.* **2007**, *126*, 014101.

17. Parrinello, M.; Rahman, A. Polymorphic transitions in single crystals: A new molecular dynamics method. *J. Appl. Phys.* **1981**, *52*, 7182–7190.

18. Nose, S.; Klein, M. Constant pressure molecular dynamics for molecular systems. *Molecular Physics* **1983**, *50*, 1055–1076.

19. Voroshylova, I. V.; Chaban, V. V. Atomistic force field for pyridinium-based ionic liquids: reliable transport properties. *J. Phys. Chem. B* **2014**, *118*, 10716–10724.

20. Chaban, V. V.; Voroshylova, I. V. Systematic refinement of canongia Lopes–Padua force field for pyrrolidinium-based ionic liquids. *J. Phys. Chem. B* **2015**, *119*, 6242–6249.

Appendix B: Supplementary Information Concerning Chapter 4

This appendix is reproduced from the following manuscript:

Alsaedi, M. K.; Panzer, M. J. "Understanding the Effects of Li^+ Salt Concentration and Zwitterion/ Li^+ Stoichiometry on Ion Coordination in Zwitterionic Polymer-Supported Ionogel Electrolytes" (submitted)

Table B.1. Calculated polymer volume fraction values based on experimental measurements of salt solution and ionogel densities via Eq. 4.2.

	Polymer Volume Fraction (ø)		
mol MPC / mol Li^+	**0.5 M Li^+**	**1 M Li^+**	**2 M Li^+**
0.25	0.096	0.072	0.13
0.5	0.12	0.12	0.19
0.75	0.14	0.15	0.26

Table B.2. Molar compositions of ionic species in LiTFSI/BMP TFSI salt solutions (1 L basis) and calculated Li^+ coordination numbers (with $TFSI^-$).

	Mol from ionic liquid		**Mol from lithium salt**		**Total Mol**				
LiTFSI (M)	**Mol $TFSI^-$**	**Mol BMP^+**	**Mol $TFSI^-$**	**Mol Li^+**	**Mol BMP^+**	**Mol $TFSI^-$**	**Mol Li^+**	**Total number of $TFSI^-$ coordinating with Li^+**	**Coordination number ($TFSI^-/Li^+$)**
0	3.39	3.39	0	0	3.39	3.39	0	0	0
0.5	3.39	3.39	0.5	0.5	3.39	3.89	0.5	0.94	1.87
1	3.39	3.39	1	1	3.39	4.39	1	1.77	1.77
2	3.39	3.39	2	2	3.39	5.39	2	3.83	1.92

Table B.3. Molar compositions of ionic species in 0.5 M LiTFSI/BMP TFSI salt solution and ionogels (1 L solution basis) and calculated Li^+ coordination numbers (with $TFSI^-$).

	From ionic liquid		**From lithium salt**		**Total Mol**				
Mol MPC^+ / mol Li^+	**Mol $TFSI^-$**	**Mol BMP^+**	**Mol $TFSI^-$**	**Mol Li^+**	**Mol BMP^+**	**Mol $TFSI^-$**	**Mol Li^+**	**Total number of $TFSI^-$ coordinating with Li^+**	**Coordination number ($TFSI^-/Li^+$)**
0	3.39	3.39	0.5	0.5	3.39	3.89	0.5	0.94	1.87
0.25	3.39	3.39	0.5	0.5	3.39	3.89	0.5	0.64	1.29
0.5	3.39	3.39	0.5	0.5	3.39	3.89	0.5	0.47	0.95
0.75	3.39	3.39	0.5	0.5	3.39	3.89	0.5	0.28	0.56

Table B.4. Molar compositions of ionic species in 1 M LiTFSI/BMP TFSI salt solution and ionogels (1 L solution basis) and calculated Li^+ coordination numbers (with $TFSI^-$).

	Mol from ionic liquid		**Mol from lithium salt**		**Total Mol**				
Mol MPC^+ / mol Li^+	**Mol $TFSI^-$**	**Mol BMP^+**	**Mol $TFSI^-$**	**Mol Li^+**	**Mol BMP^+**	**Mol $TFSI^-$**	**Mol Li^+**	**Total number of $TFSI^-$ coordinating with Li^+**	**Coordination number ($TFSI^-/Li^+$)**
0	3.39	3.39	1	1	3.39	4.39	1	1.77	1.77
0.25	3.39	3.39	1	1	3.39	4.39	1	1.25	1.25
0.5	3.39	3.39	1	1	3.39	4.39	1	0.73	0.73
0.75	3.39	3.39	1	1	3.39	4.39	1	0.5	0.5

Table B.5. Molar compositions of ionic species in 2 M LiTFSI/BMP TFSI salt solution and ionogels (1 L solution basis) and calculated Li^+ coordination numbers (with $TFSI^-$).

	Mol from ionic liquid		**Mol from lithium salt**		**Total Mol**				
Mol MPC^+ / mol Li^+	**Mol $TFSI^-$**	**Mol BMP^+**	**Mol $TFSI^-$**	**Mol Li^+**	**Mol BMP^+**	**Mol $TFSI^-$**	**Mol Li^+**	**Total number of $TFSI^-$ coordinating with Li^+**	**Coordination number ($TFSI^-/Li^+$)**
0	3.39	3.39	2	2	3.39	5.39	2	3.83	1.92
0.25	3.39	3.39	2	2	3.39	5.39	2	2.19	1.09
0.5	3.39	3.39	2	2	3.39	5.39	2	1.31	0.66
0.75	3.39	3.39	2	2	3.39	5.39	2	0.85	0.42

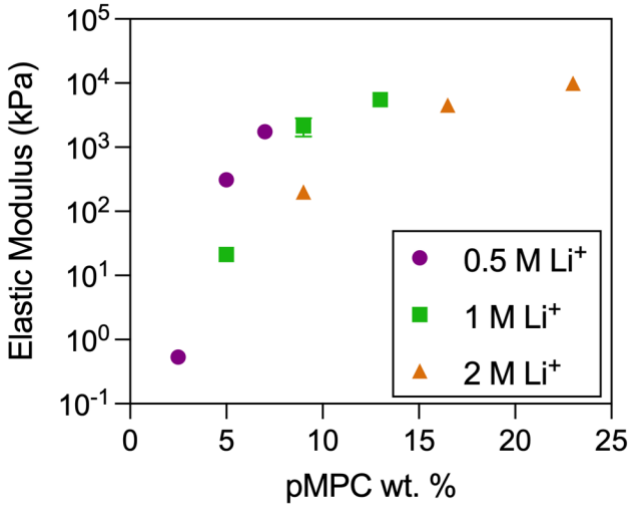


Figure B.1. Elastic modulus values of ionogels prepared using 0.5 M, 1 M, and 2 M LiTFSI/BMP TFSI solutions plotted versus pMPC wt.%.

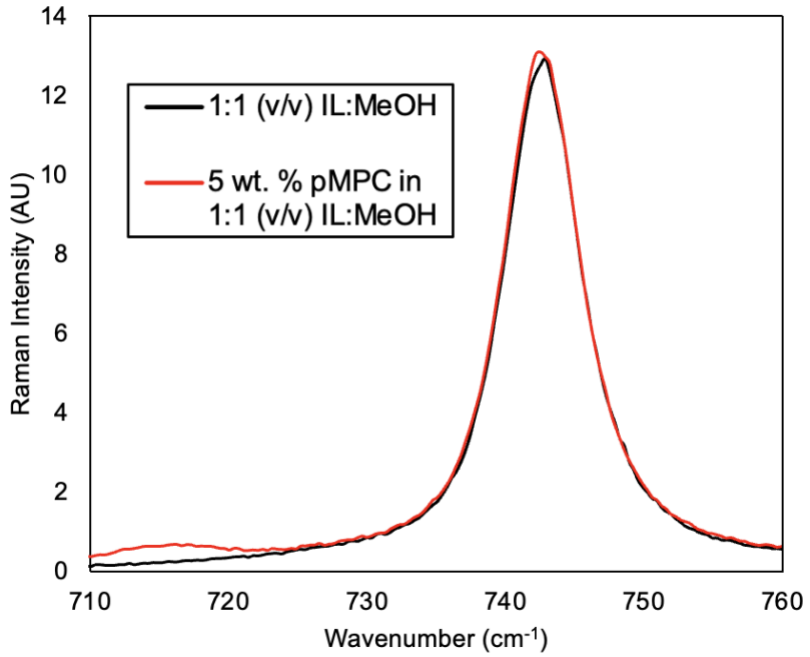


Figure B.2. Raman spectra for an equivolume mixture of IL (BMP TFSI) with methanol (MeOH) (black curve) and for a 5 wt. % pMPC solution prepared in the same equimolar mixture via UV-initiated *in situ* free radical polymerization (red curve). Methanol was used here to adjust the solvent quality in order to dissolve the MPC monomer, which is not soluble in the neat BMP TFSI ionic liquid.

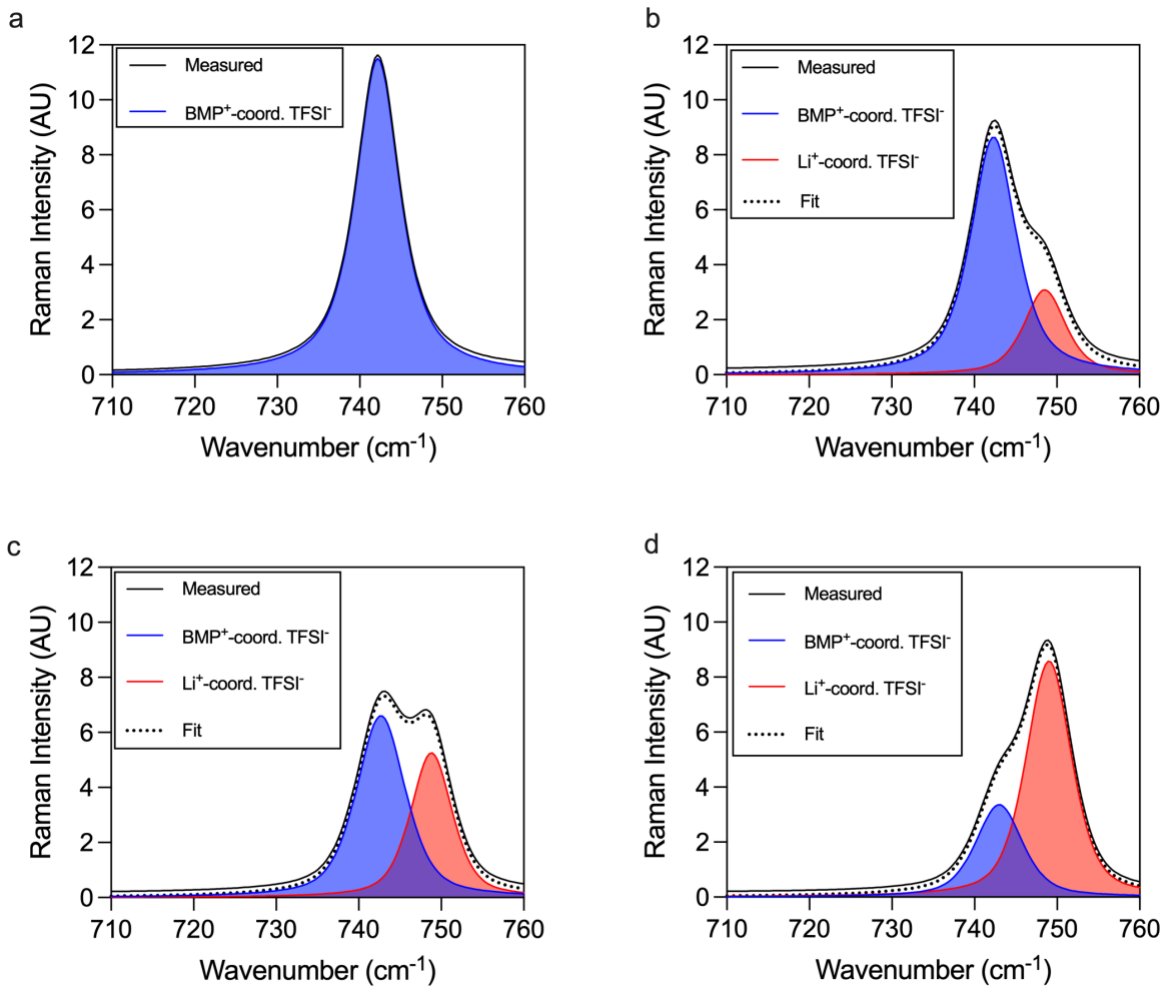


Figure B.3. Deconvoluted Raman spectra showing the BMP^+-coordinated $TFSI^-$ and Li^+-coordinated $TFSI^-$ sub-peaks for: **a)** BMP TFSI, **b)** 0.5 M LiTFSI/BMP TFSI solution, **c)** 1 M LiTFSI/BMP TFSI solution, and **d)** 2 M LiTFSI/BMP TFSI solution.

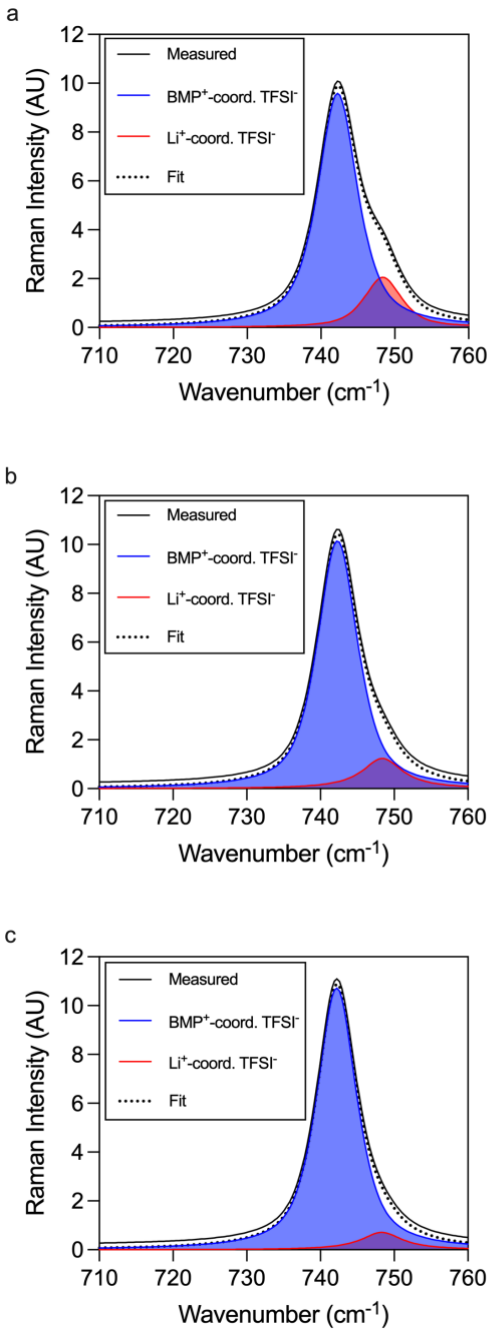


Figure B.4. Deconvoluted Raman spectra showing the BMP^+-coordinated $TFSI^-$ and Li^+-coordinated $TFSI^-$ sub-peaks for ionogels prepared from a 0.5 M LiTFSI/BMP TFSI solution containing: **a)** 0.25 mol MPC/mol Li^+ , **b)** 0.5 mol MPC/mol Li^+, and **c)** 0.75 mol MPC/mol Li^+.

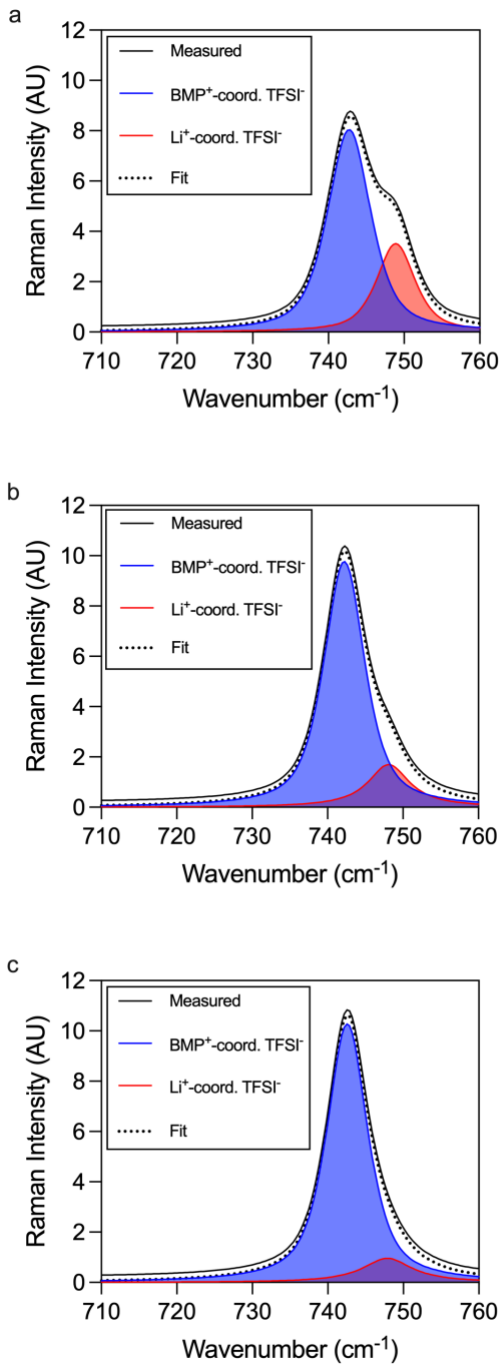


Figure B.5. Deconvoluted Raman spectra showing the BMP^+-coordinated $TFSI^-$ and Li^+-coordinated $TFSI^-$ sub-peaks for ionogels prepared from a 1 M LiTFSI/BMP TFSI solution containing: **a)** 0.25 mol MPC/mol Li^+ , **b)** 0.5 mol MPC/mol Li^+, and **c)** 0.75 mol MPC/mol Li^+.

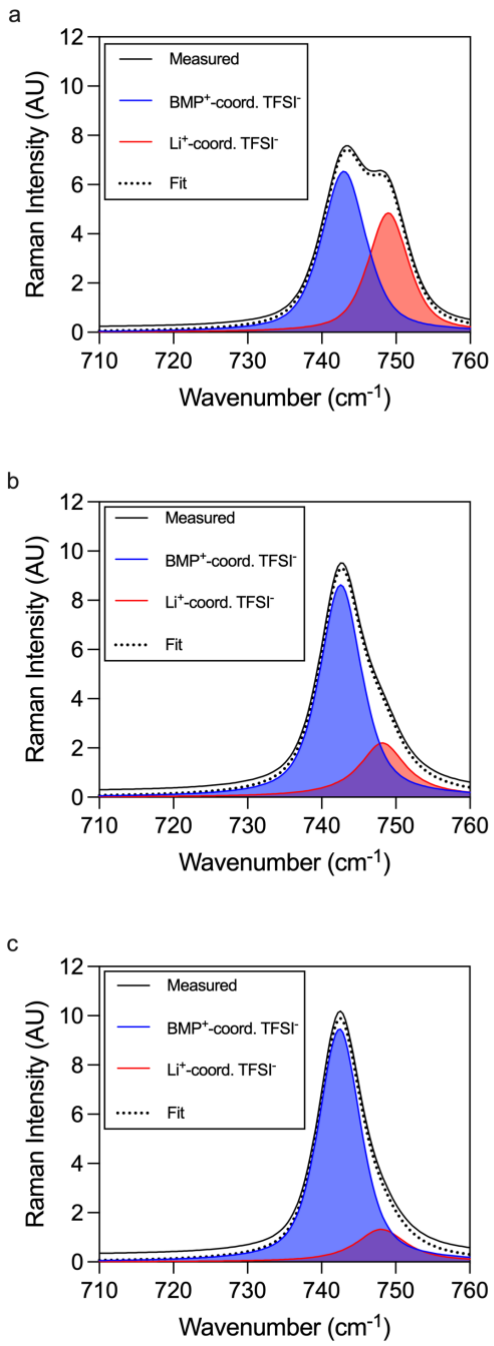


Figure B.6. Deconvoluted Raman spectra showing the BMP^+-coordinated $TFSI^-$ and Li^+-coordinated $TFSI^-$ sub-peaks for ionogels prepared from a 2 M LiTFSI/BMP TFSI solution containing: **a)** 0.25 mol MPC/mol Li^+ , **b)** 0.5 mol MPC/mol Li^+, and **c)** 0.75 mol MPC/mol Li^+.

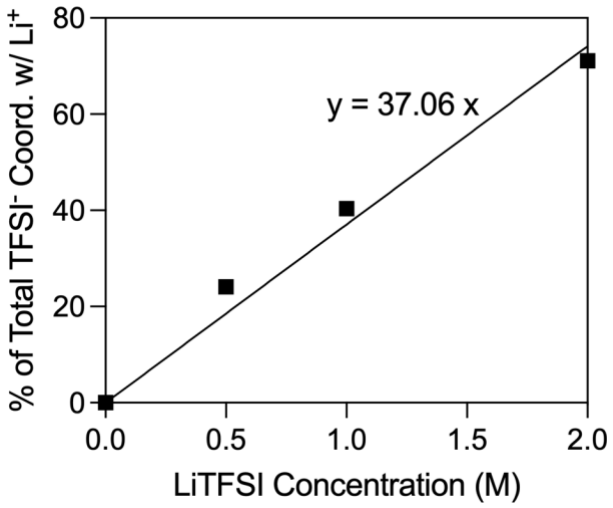


Figure B.7. Percentage of total $TFSI^-$ anions that are coordinating with Li^+ cations in the LiTFSI/BMP TFSI solutions plotted versus Li^+ concentration. Extrapolation of the best-fit linear regression to the data through the origin (equation shown) predicts 100% of the $TFSI^-$ anions will be Li^+-coordinated for a LiTFSI concentration of approximately 2.7 M.

Appendix C: Supplementary Information Concerning Chapter 5

This appendix is reproduced from the following publication:

Arwish, S.; Alsaedi, M. K.; O'Hara, R. P.; Asatekin, A.; Panzer, M. J.; Schonhoff, M. "The Role of Li^+ Ions in Polyzwitterionic Ionogels: a Gelator or Mobile Charge Carrier?" *(accepted for publication in J. Phys. Chem. B)*

C.1. Sample compositions:

Table C.1: Molar ratios of different constituents (MPC, Li^+, and $TFSI^-$) for varying weight percent of p(MPC).

Composition wt % p(MPC)	**MPC:Li^+**	**Li^+:$TFSI^-$**	**MPC:$TFSI^-$**
0	0	0.23	0
2	0.13	0.23	0.03
4	0.24	0.23	0.05
6	0.34	0.23	0.08
8	0.50	0.23	0.12
10	0.62	0.23	0.15
12	0.69	0.23	0.18
14	0.92	0.23	0.21

C.2. ^{1}H NMR of the dissolved ionogels:

To determine the conversion of the in situ photopolymerization reaction, 40-80 mg of each ionogel was dissolved in D_2O at a ratio of 2 mg of initial monomer/ 1 mL of solvent. Similar to the DLS measurements, the BMP TFSI phase separated from the solvent while the MPC, p(MPC), and LiTFSI dissolved readily. After dissolution, ^{1}H NMR was performed on the majority solvent phase using a Bruker AVANCE III 500 MHz spectrometer with 32 scans and a 10s relaxation delay.

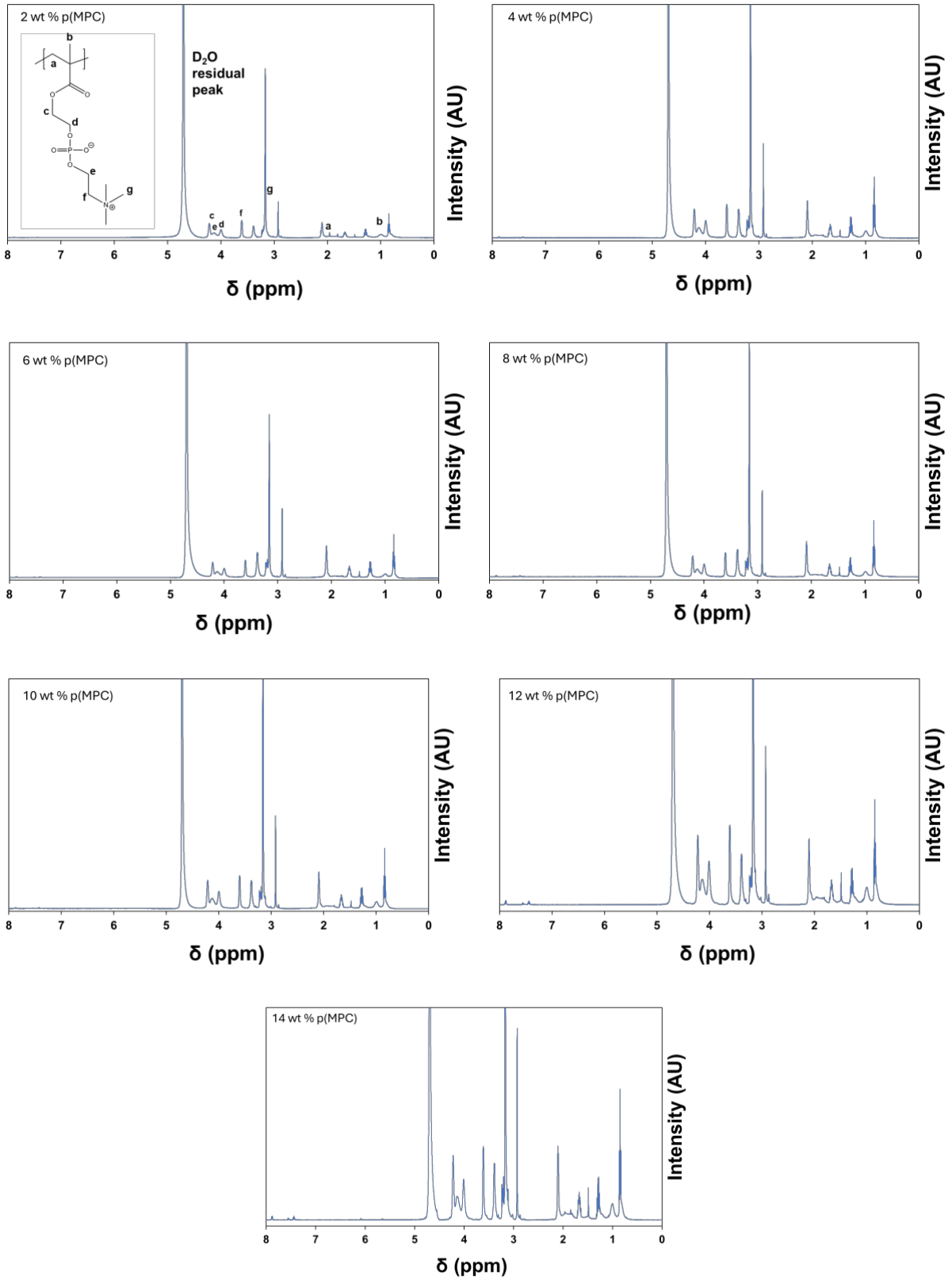
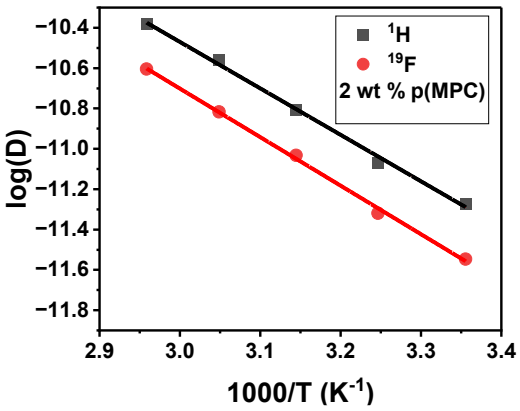


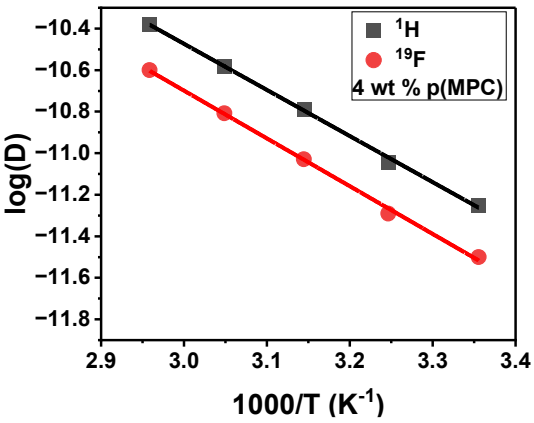
Figure C.1. ^{1}H NMR spectra of the dissolved p(MPC) ionogels in D_2O. The lack of peaks related to the CH_2=CH- bonds between 5-6 ppm indicates the full conversion of p(MPC).

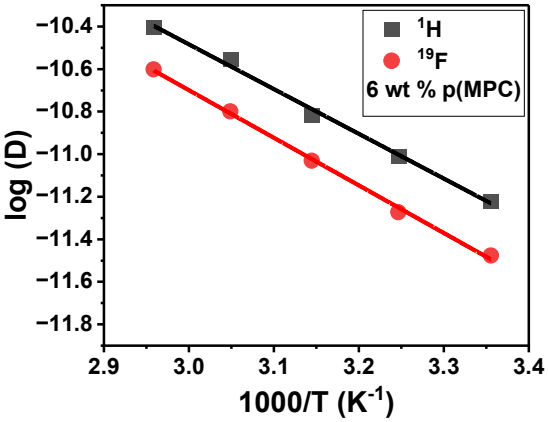
C.3. Temperature-dependent diffusion coefficients:

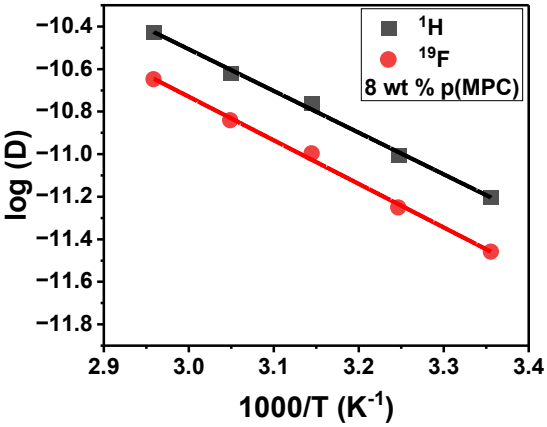
Diffusion data are fitted with the Arrhenius equation, (Eq. C.1), for ionogels with varying content of p(MPC). The fitted plots are shown in Figure C.2.

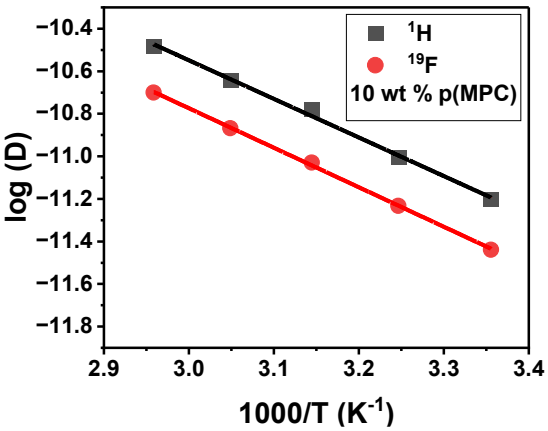
$$D = Do \exp\left(\frac{-E_a}{k_b T}\right) \quad \text{(Eq. C.1)}$$

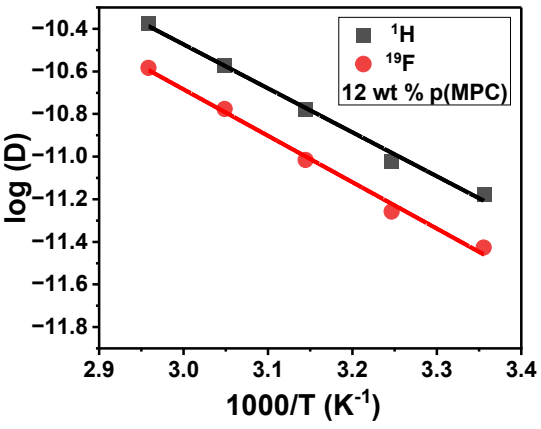

log(D)
1000/T (K-1)
1H
19F
2 wt % p(MPC)


log(D)
1000/T (K-1)
1H
19F
4 wt % p(MPC)


log (D)
1000/T (K-1)
1H
19F
6 wt % p(MPC)


log (D)
1000/T (K-1)
1H
19F
8 wt % p(MPC)


log (D)
1000/T (K-1)
1H
19F
10 wt % p(MPC)


log (D)
1000/T (K-1)
1H
19F
12 wt % p(MPC)

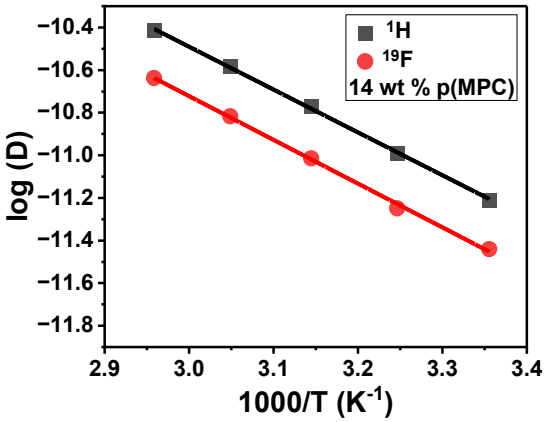


Figure C.2. Temperature dependent diffusion coefficients for ^{1}H and ^{19}F for the different compositions of p(MPC) varying from 2 wt % p(MPC) to 14 wt % p(MPC). Data points: Experimental values, solid lines: Arrhenius fits.

C.4. ^{7}Li Spin Lattice Relaxation Rates and Relaxation Rate Ratios:

The longitudinal relaxation times T_1 were determined by employing an inversion recovery pulse sequence to find the relaxation rate ratios within ionogels (Fig. S3a). The increase in relaxation rate ratios with higher content of p(MPC) is strongly pronounced (Fig. S3b) and suggests a strong Li^+ ion-polymer interaction and thus reduced mobility of Li^+ ions within the ionogels, which is most probably due to a stronger affinity of Li^+ ions to the phosphate group of the MPC units.

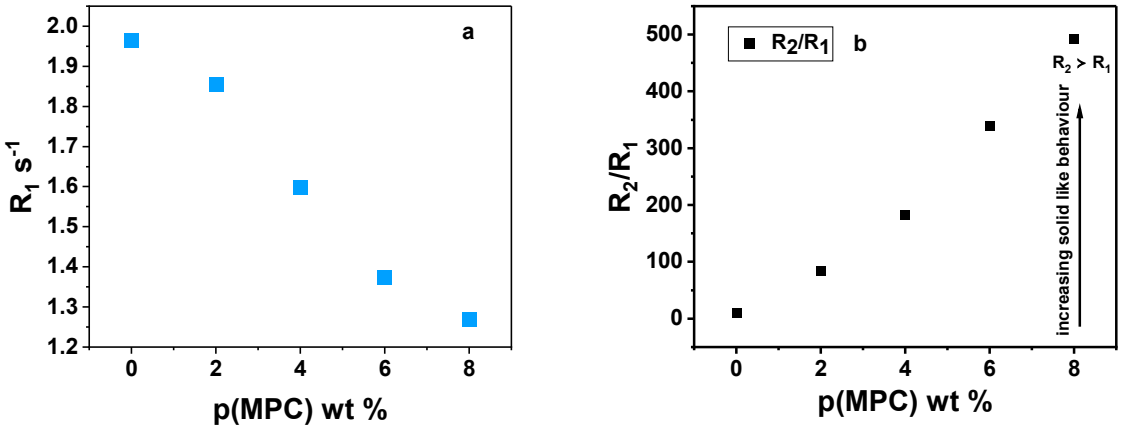
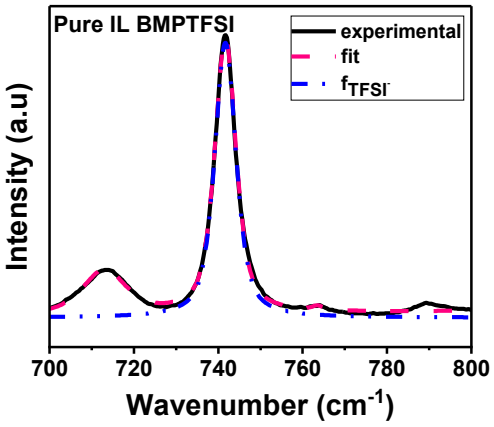
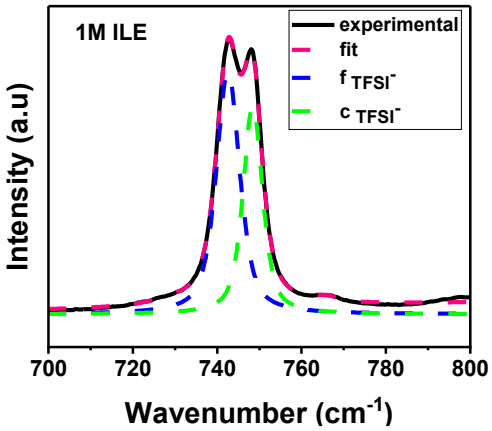


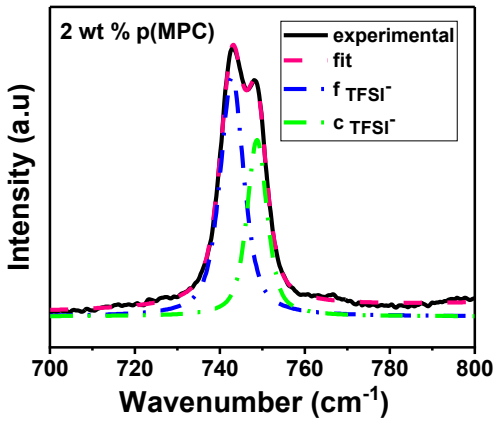
Figure C.3. (a) ^{7}Li spin-lattice relaxation rate R_1 determined by inversion recovery pulse sequence (b) Relaxation rate ratios for 1M LiTFSI/BMP TFSI solution (0 wt % p(MPC)), 2 wt % p(MPC) solution, and 4-8 wt % p(MPC) ionogels.

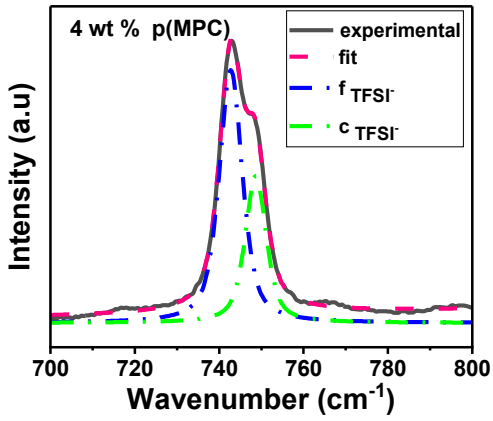
C.5. Raman Spectra and their Deconvolution:

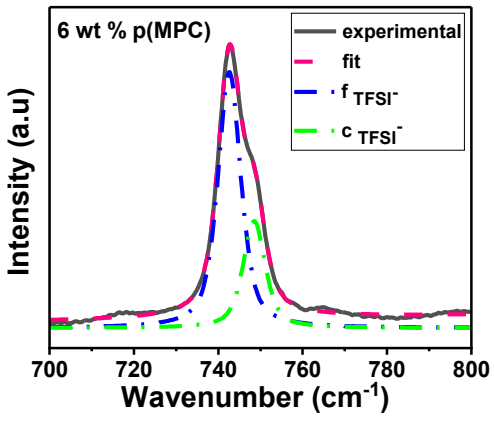
The Raman spectra were deconvoluted by performing fits with the Voigt profiles in specific software OPUS 8.5 (Bruker, Rheinstetten) using 40% Gaussian and 60% Lorentzian for the region in range of 700 to 800 cm^{-1}. The intensity, peak position, and width for each band were varied as free parameters. The deconvoluted Raman spectra are shown in Figure C.4.

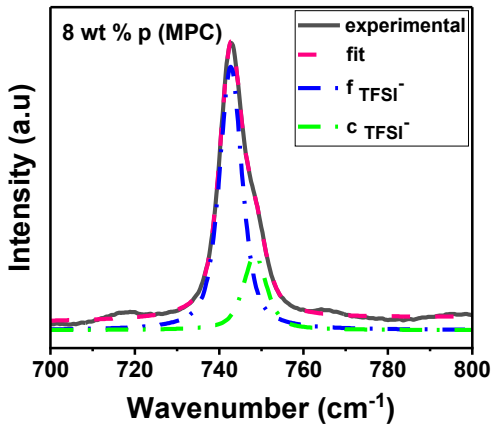

Pure IL BMPTFSI
experimental
fit
f TFSI-
Intensity (a.u)
Wavenumber (cm-1)
700
720
740
760
780
800


1M ILE
experimental
fit
f TFSI-
c TFSI-
Intensity (a.u)
Wavenumber (cm-1)
700
720
740
760
780
800


2 wt % p(MPC)
experimental
fit
f TFSI-
c TFSI-
Intensity (a.u)
Wavenumber (cm-1)
700
720
740
760
780
800


4 wt % p(MPC)
experimental
fit
f TFSI-
c TFSI-
Intensity (a.u)
Wavenumber (cm-1)
700
720
740
760
780
800


6 wt % p(MPC)
experimental
fit
f TFSI-
c TFSI-
Intensity (a.u)
Wavenumber (cm-1)
700
720
740
760
780
800


8 wt % p (MPC)
experimental
fit
f TFSI-
c TFSI-
Intensity (a.u)
Wavenumber (cm-1)
700
720
740
760
780
800

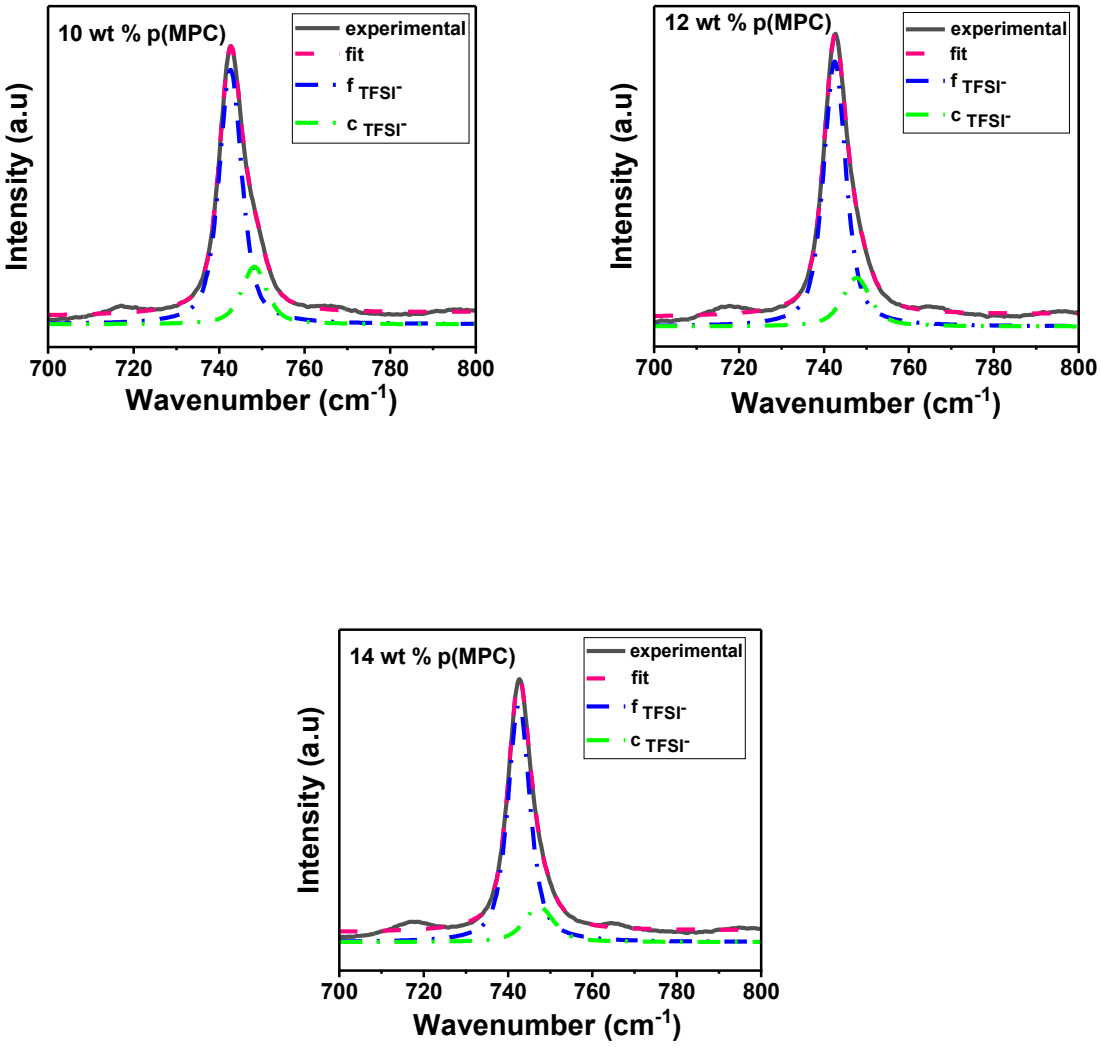


Figure C.4. Raman spectra of BMP TFSI, neat 1M LiTFSI/BMPTFSI solution, and ionogels containing varying wt % of p(MPC) in the spectral region between 700 cm^{-1} and 800 cm^{-1}. The blue and green lines are obtained by deconvolution by Voigt profiles where f_{TFSI^-} represents free $TFSI^-$ ions and c_{TFSI^-} represents the coordinated $TFSI^-$ ions.

To obtain deeper insight to the local environment of $TFSI^-$ ions, the integrals of free (A_f) and coordinated (A_c) $TFSI^-$ ions were estimated from deconvoluted Raman peaks. Following a protocol introduced by Lassegues *et al.*,[1] the integral ratio $A_c/(A_c+A_f)$ was evaluated (see data in Table C.2) and used to determine the coordination number n of anions per Li^+ in each composition. It is:

$$\frac{A_c}{A_c + A_f} = \frac{Snx}{(Snx - nx + 1)} \quad \text{(Eq. C.2)}$$

where S is the molar Raman scattering coefficient ratio, $S = s_c/s_f$, (s_c represents the coordinated $TFSI^-$ ions and s_f represents the free $TFSI^-$ ions), and x is the Li salt fraction in the LiTFSI/BMP TFSI solution. With the assumption of S=1, which was previously validated,[2, 3] eq. C.2 reduces to[1]:

$$\frac{A_c}{A_c + A_f} = nx \quad \text{(Eq. C.3)}$$

This simplified equation allows one to estimate the coordination number of anions per Li^+ (n) in each composition with known lithium salt fraction (x= 0.23); see results in Table C.2.

Table C.2: Integral ratios of the Raman peaks obtained through spectral deconvolution, quantifying the coordinated fraction of anions and coordination numbers resulting from Eq. (C.3).

Composition wt % p(MPC)	$A_c/(A_c+A_f)$	n
0	0.42	1.81
2	0.38	1.65
4	0.35	1.51
6	0.29	1.25
8	0.23	0.98
10	0.20	0.88
12	0.19	0.81
14	0.17	0.72

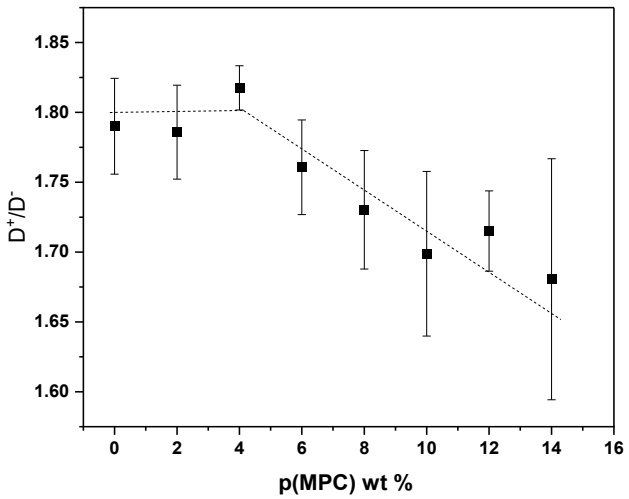


Figure C.5. Ratio of diffusion coefficients D_+ of BMP versus D_- of TFSI, showing a slight loss of their coupling with increasing p(MPC) content.

C.6. Crosslink Density and Non-cross-linked Li^+ Concentration:

To calculate the crosslink density, Eq. C.4 was used[4, 5] in which ρ_x is the crosslink density, N_A is Avogadro's number, E is the elastic modulus of the ionogel, ϕ is the volume fraction of the polymer in the ionogel (Eq. C.5), R is the universal gas constant, T is the temperature (298 K). The LiTFSI/BMP TFSI solution density is ρ_{ILE} = 1.489 g/mL, and the ionogel density is $\rho_{ionogel}$ = 1.454 g/mL.

$$\rho_x = \frac{N_A E}{3\emptyset^{-2/3} RT} \tag{C.4}$$

$$\emptyset = 1 - \left(\frac{(100 - p(MPC)\ wt.\%)}{\rho_{ILE}} \div \frac{100}{\rho_{ionogel}}\right) \tag{C.5}$$

The concentration of cross-linked lithium was calculated by dividing the cross-link density by Avogadro's number, assuming one Li^+ ion per cross-link. The molar concentration of non-cross-linked lithium was calculated by subtracting the concentration of cross-linked lithium from the total concentration of the LiTFSI/BMP TFSI solution (1M), which is also the fraction of non-cross-linked lithium.

C.7. References:

1. Lassegues, J. C.; Grondin, J.; Talaga, D., Lithium solvation in bis(trifluoromethane-sulfonyl)imide-based ionic liquids. *Phys. Chem. Chem. Phys.* **2006,** *8* (48), 5629-5632.

2. Lassègues, J.-C.; Grondin, J.; Aupetit, C.; Johansson, P., Spectroscopic Identification of the Lithium Ion Transporting Species in LiTFSI-Doped Ionic Liquids. *J. Phys. Chem. A* **2009,** *113* (1), 305-314.

3. Umebayashi, Y.; Mitsugi, T.; Fukuda, S.; Fujimori, T.; Fujii, K.; Kanzaki, R.; Takeuchi, M.; Ishiguro, S. I., Lithium ion solvation in room-temperature ionic liquids involving bis(trifluoromethanesulfonyl) imide anion studied by Raman Spectroscopy and DFT calculations. *J. Phys. Chem. B* **2007,** *111* (45), 13028-13032.

4. Visentin, A. F.; Panzer, M. J., Poly(Ethylene Glycol) Diacrylate-Supported lonogels with Consistent Capacitive Behavior and Tunable Elastic Response. *ACS Appl. Mater. Interfaces* **2012,** *4* (6), 2836-2839.

5. Hiemenz , P. C.; Lodge, T. P., *Polymer Chemistry, 2nd edition*. CRC Press: 2007.

Appendix D: Smart Sensing Flexible Sutures for Glucose Monitoring in House Sparrows

This appendix is reproduced from the following publication:

Alsaedi, M. K.; Riccio, R. E.; Sharma, A.; Xia, J.; Owyeung, R. E.; Romero, L. M.; Sonkusale S. Smart Sensing Flexible Sutures for Glucose Monitoring in House Sparrows. *Analyst.* **2023**, 148 (22), 5714-5723

D.1. Abstract

There is a need for flexible chemical sensors for the ecological and physiological research of avian species such as house sparrows (*Passer domesticus*). Current methods in this field are invasive and require multiple physical interactions with the birds. Emerging research in flexible bioelectronics can enable realization of implantable devices that are mechanically compliant with the underlying tissues for continuous real-time sensing *in situ*. However, challenges still remain in forming an intimate flexible interface. One of the promising flexible bioelectronic platforms for tissue-embedded sensing is based on functionalizing surgical sutures or threads. Threads have three-dimensional flexibility, high surface-area-to-volume ratio, inherent wicking properties, and are easily functionalizable using reel-to-reel dip coating. Threads are ideal as they are lightweight, therefore, would not interfere with flight motion and would only require minimal interaction with the bird. However, the challenge remains in achieving a highly conductive yet flexible electrode for electrochemical sensing using materials such as gold. In this study, we address this issue through novel gold deposition directly on thread substrate followed by enzyme immobilization to realize flexible electrochemical glucose biosensors on medical-grade sutures. These sensors were calibrated and tested in a range that is wide enough to include the expected range of glucose concentration in house sparrows (0-8.55 mM). Glucose monitoring in house sparrows will provide insights into energy metabolism and regulation during stress responses. In addition, the stability, repeatability, and selectivity of the sensor were tested with final validation in a real bird. Our innovative gold-coated, thread-based flexible electrochemical glucose sensor can also be used in other small and large animals. This can also be extended to monitoring other metabolites in future.

D.2. Introduction

Flexible bioelectronics have become popular in precision health and medicine as they offer seamless electronic-tissue physical contact and comparable mechanical properties (elastic moduli) [1]. Threads have previously been utilized in biomedical applications to realize thread-based sensors, transistors, and even drug-delivery platforms [1-6]. Their three-dimensional flexibility ensures seamless integration with underlying tissues and organs and intimate contact with tissue/organ surfaces [1]. Threads are also favorable because of their cleanroom-free and low-cost fabrication processes, mechanical stability and durability, large surface area, and inherent wicking properties [1, 7-11]. The ability to select different types of fibers that make up threads also provides flexibility in terms of the application and the desired properties of the thread-based device [7]. Choosing biocompatible fibers, such as silk and polylactic-co-glycolic acid (PLGA), can tailor their use towards biomedical applications.

One application of thread-based biosensors is continuous glucose monitoring (CGM). CGM systems measure glucose levels in interstitial fluid (ISF) and convert those measurements to blood glucose concentration [12]. Compared to other flexible bioelectronic platforms that are realized on two dimensional planar polymeric substrates, threads are one dimensional and thus capable of three-dimensional tissue embedded sensing, which is ideal for small animals such as house sparrows [1-6, 11, 13-25]. Although CGM has been implemented in a range of laboratory and captive animals for studies on diabetes [26-29], real-time monitoring in free-living species extends beyond medical research. However, CGM has yet to be explored in free-living species due to difficulties of measuring and transmitting data over the long distances travelled in flying or

diving animals [30, 31]. Moreover, current methods for monitoring glucose levels in free-living small animal species are invasive and require multiple interactions with the animal (e.g., collecting blood samples at a few time points using a point-of-care device). Capturing and handling the animals to perform sampling restrict natural behaviour, produce stress artifacts, and may miss the fluctuation in glucose response. Therefore, a less invasive and continuous monitoring method to improve animal welfare and accuracy of glucose measurements is a needed ideal alternative. It is for this reason we propose a thread-based sensor for flexible tissue-embedded sensing in captive live birds such as house sparrows.

House sparrows are relatively small birds that weight 24-39.4 g with a total length of ~16 cm. So, any flexible bioelectronic platform to be implanted in such small species should not be bulky (less than 5% of bodyweight). In addition, these sensors are meant to be implanted transdermally to achieve high signal-to-noise ratio and continuous real-time monitoring, which adds more constraints. For example, implantation should not cause harm or injury to the bird and should not alter its natural behaviour. We believe lightweight functionalized threads would address these challenges. Compared to microneedles, which would be an alternate approach, there will be less motion artifact and no chance for it to be displaced or peeled off from the body [32, 33]. Different animals have different skin thicknesses, and birds have relatively thin skin compared to mammals (humans, mice, etc.). Therefore, microneedles could penetrate through all the bird's skin layers, eliminating the non-invasiveness aspect of microneedles. However, it is incredibly challenging to realize flexible conductive coating on threads for realization of sensors and interconnects. Prior work relied on carbon coating using dip and dry approach, which compromised the flexibility of the treads [2, 34-37]. Therefore, it is more desirable to realize metallic conductive electrodes using noble metals such as gold. Furthermore, dealing with rough

and intricate curved surfaces, such as threads, presents an additional challenge because of the significant likelihood of uneven coating and the potential for the active coating to flake off. This manuscript attempts to address these challenges by realizing an innovative process for gold-coated glucose-sensing flexible threads for tissue-embedded sensing in birds.

We chose to realize glucose sensing threads/sutures in this paper. Glucose regulation is a key indicator of various biological processes, nutritional state, and energy usage in free-living flying wildlife species [30, 38-40]. CGM in free-flying species would provide valuable insights into the complex energy dynamics of the high energetic demands of their internal and external state. CGM provides ample data for individual repeatability and allows for individuals to act as their own controls. Monitoring glucose levels in individuals, and therefore their energy usage, links behaviour to individual fitness. For example, monitoring glucose in well-characterized avian species (e.g. house sparrows) offers insights into energy mobilization and regulation during a stress response, which has implications for both ecological and physiological research [41]. Understanding how individual animals respond to natural or unpredictable stressors could indicate how animals are coping in their environments, and become a valuable tool for conservation, rehabilitation, and translocation of endangered or threatened species.

In this study, we realize lightweight, flexible sensing sutures for glucose monitoring using electrochemical principles. The conductive layer on the working and counter electrodes is gold that is achieved via solution-based electroless deposition and plating [42] of colloidal gold [43], which produces a more uniform and cohesive coating layer of gold on a thread's rough, uneven surface. Compared to other conductive coatings, such as carbon which requires multiple coatings for adequate conductivity, electroless deposition of gold produces a more flexible conductive suture. In addition to the conductive layer, an electron-mediating layer (Prussian blue) is

electrically deposited, and enzyme-chitosan bilayers are coated [44]. Glucose oxidase, which is the enzyme immobilized in the enzyme-chitosan matrix, catalyzes the oxidation of glucose in the presence of oxygen and, as a result, alters the current in the system [44], which is then measured using electronic circuitry and communicated wirelessly if needed.

We demonstrate the functionality of sensors by obtaining calibration curves and test data for real-time glucose monitoring, sensor stability, sensor repeatability, and analyte interference. The sensing sutures had a sensitivity value of 36.23 nA/mM within a range from 0.62 mM to 36.4 mM glucose and a limit of detection (LOD) of 0.62 mM. The sensors were able to successfully monitor changes in glucose concentration over a period of 40 minutes and remain stable for at least five days. In addition, the sensors showed selectivity towards glucose, even in the presence of other molecules. Tests on euthanized house sparrows were performed to validate sensor function in an ex-vivo environment and small animal species. While glucose monitoring has been reported in this manuscript, sensing sutures can be expanded to the monitoring of other analytes, such as lactate, electrolytes, chemokines, and metabolites. Future efforts will integrate these sensing sutures with miniaturized wireless electronics for real-time monitoring in birds.

D.3. Materials and Methods

3-Aminopropyltriethoxysaline (APTES), potassium chloride (KCl), Hydrochloric acid (HCl, ACS reagent 37%), potassium ferricyanide [$K_3Fe(CN)_6$], iron chloride hexahydrate ($FeCl_3$), chitosan (high molecular weight), glutaraldehyde solution (50 wt. % in water), hydroxylamine hydrochloride, sodium citrate tribasic dihydrate, tetrachloroauric (III) acid trihydrate (HAuCl4 .

$3H_2O$), and acetic acid were all purchased from Sigma Aldrich and used as received. Isopropyl alcohol 99% (IPA) was purchased from Florida Laboratories and used as received. Methanol was purchased from Fischer Chemical and used as received. Dulbecco's Phosphate Buffered Saline (1X, PBS) was purchased from Gibco and used as received. Glucose oxidase (GOD) was purchased from Toyobo and used as received.

Polysorb^{TM} 5-0 braided absorbable sutures were purchased from Covidien (Medtronic, USA). The heated ultrasonic cleaner (sonicator) was purchased from Sharpertek. The potentiostat used (Electrochemical Workstation) and the commercial Ag/AgCl reference electrode used were both purchased from CH Instruments, Inc. Anton Paar Litesizer 500 Particle Analyzer was used for dynamic light scattering (DLS). Oxygen plasma treatment was done in a plasma chamber from Plasma Etch, Inc. The laboratory rotator oscillator used was a TYZD-IIIA Oscillator model. The ultraviolet-visible spectrometer used was an Evolution 220 UV-Visible Spectrometer and was purchased from Thermo Scientific. Fourier transform infrared (FTIR) spectroscopy were performed using a Nicolet 6700 FTIR with an iTX attachment (Thermo Scientific).

D.3.1. Synthesis of gold nanoparticles (Au NPs)

1.0 wt% sodium citrate trihydrate is added to boiling 2.5 x 10^{-4} M hydrogen tetrachloroaurate (III) acid trihydrate to make a 3.0 vol% solution. The solution is then heated until the color changes to a deep red color, then stirred for an additional 30 minutes. The synthesized Au NP solution is stored at 4 °C when not in use.

D.3.2. Coating sutures with gold (electroless deposition of gold)

Sutures (5-0) were first submerged in IPA and sonicated for 10 minutes. Then, the sutures were transferred for oxygen plasma treatment for 10 minutes. Once plasma treatment was done, the sutures were then submerged in a 0.20 M APTES in methanol solution and stirred overnight (not more than 24 hours).

The sutures are then taken out of the methanol/APTES solution and rinsed three times with methanol, then three times with DI water. This step is crucial to ensure the removal of unbound APTES from the surface of the suture. Then, the sutures are transferred to a petri dish where 4.0 mL of Au NP solution is added (volume is dependent on the size of the petri dish). The petri dish is then transferred onto a rotator oscillator for 25 minutes.

Once the 25-minute shaking step is over, the sutures are transferred to a new petri dish for the gold-plating step. In this step, 3.95 mL of DI water and 1.0 mL of 5.0 mM $H_7AuCl_4O_3$ is added to the fresh petri dish with the sutures. This step is followed by the addition of 50 mL of 40.0 mM hydroxylamine hydrochloride to the same petri dish. The petri dish is then transferred onto the rotator oscillator to stir for 25 minutes. This gold plating step (adding DI water, $H_7AuCl_4O_3$, hydroxylamine hydrochloride, then oscillating for 25 minutes) is repeated two more times (a total of three times). The absorbance of gold layer as a function of time is shown in Figure E.1 (one cycle). The sutures are eventually rinsed with DI water and dried off with nitrogen gas.

D.3.3. Coating sutures with Prussian Blue

Prussian blue (PB) is deposited onto the gold-coated sutures via an electro-assisted process where Prussian blue is reduced onto the surface of the sutures. In a 0.10 M KCl/0.010 M HCl solution, potassium ferricyanide and iron trichloride are added (to achieve a 2.0 mM concentration of each of the solutes in the KCl/HCl solution). This solution is used as the medium in a 3-electrode system where one gold-coated suture is the working electrode, another gold-coated suture is the counter electrode, and an Ag/AgCl is the reference electrode. For the electrodeposition of PB, a cyclic voltammetry (CV) measurement is carried out onto the gold-coated suture (working electrode) by sweeping the voltage from -0.10 V to 0.40 V at a scan rate of 50.0 mV/s in 0.010 V intervals and 7.0 sweep cycles. The suture is then rinsed with DI water and dried off with nitrogen gas.

D.3.4. Chitosan-glucose oxidase bi-layer coating

The PB -coated suture is then dipped in a 1.0% chitosan in acetic acid and water solution for 5 minutes, rinsed in 1X PBS, dipped in 20.0 mg/mL solution of glucose oxidase (GOD) in 1X PBS for 5 minutes, then rinsed in 1X PBS again. This creates one bi-layer of chitosan-glucose oxidase on the suture. This step is repeated 5 times (6 bilayers in total). Once the bilayers are coated, the suture is dipped in a 2.5% solution of glutaraldehyde (GA) in water for 5 minutes, rinsed in 1X PBS, then dried with nitrogen gas. The suture is stored in a 4 °C refrigerator to preserve the enzyme layers for later use.

D.3.5. Flexibility studies

To assess the range of flexibility in which the conductivity of the thread remains intact and does not deviate from the starting resistance, we measured the change in resistance after flexing 3-cm long gold coated thread around 2.0 cm, 1.5 cm, and 1.0 cm radii of curvature. Eutectic Gallium-Indium (EgaIn) contacts were added on to the ends of threads and connected to multimeter. The baseline, non-flexed 3.0 cm thread resistance was first measured. The thread was flexed at 2.0 cm radius of curvature for 10 seconds then returned to a straight position for remeasurement of resistance. These steps were repeated for 1.5 cm and 1.0 cm radii of curvature on three different threads. The resistance was compared pre- and post-flexing to determine the maximum flexibility affordable to maintain reliability of the threads' conductivity.

To assess the range of flexibility of glucose detection and effect of flexibility on the immobilized enzyme layering, the above process was repeated on a glucose sensing suture taking chronoamperometric measurements with a benchtop potentiostat with known concentration of glucose instead of taking resistance measurements. Measures of glucose concentrations were taken prior to flexing and post flexing and the change in current at baseline and at known glucose concentration was measured and compared pre-and post-flexing.

D.3.6. Chronoamperometric measurements

Sensor calibration, interference, stability, and repeatability tests as well as real-time glucose monitoring were all conducted using chronoamperometry. All these tests were conducted

in a beaker containing 1X PBS with a stir bar and a conventional three-electrode system using a potentiostat. The three-electrode system is comprised of a GA/chitosan/GOD/PB/Au-coated suture as the working electrode (WE), and Ag/AgCl as a reference electrode (RE), and an Au-coated suture as a counter electrode (CE). In each test, volumes of known analyte concentration in 1X PBS were pipetted into the beaker to achieve the desired concentration, then chronoamperometry is run for 90 seconds with -0.20 V applied voltage. For each analyte concentration, the average current last 10 seconds of the run is calculated and reported except for the real-time glucose monitoring and the interference tests. In the real-time glucose monitoring test, the glucose concentration is increased every 10 minutes for 40 minutes. In the interference test, a different analyte is introduced every five minutes for 25 minutes.

D.3.7. Glucose monitoring in euthanized house sparrows

To validate sensor function in small animal species, the sensor performance was evaluated in euthanized house sparrows by infusing known glucose concentrations. Herein, a two-electrode set-up was used with the sensor (GA/chitosan/GOD/PB/Au-coated suture) as a WE and an Ag/AgCl suture as a CE/RE. These Ag/AgCl sutures were fabricated using methods previously described [2]. For implantation, we made a small incision (~2.0 mm) near the base of the neck within the dorsal featherless tract of the euthanized bird and implanted two 2.0 cm-long silastic tubes subcutaneously. Each electrode was inserted into a silastic tube to keep them separated. The incision was sutured to secure the sensing threads in place. Then, sterile saline was injected near the incision site. A baseline signal was recorded 30 minutes after saline was injected by connecting

the sensor to the potentiostat. Then, known glucose concentrations were injected and measured the response as described above.

D.4. Results and discussion

D.4.1. Characterization of gold nanoparticles (Au NPs)

The smaller the size of Au NPs, the more the surface coverage, that will in turn result in faster and uniform electroless deposition of gold on rough thread surface, to be carried out in next step, for improved conductivity. Dynamic light scattering (DLS) measurement confirmed that the synthesized Au NPs have a hydrodynamic diameter of 43.36 ± 1.11 nm with a polydispersity index (PDI) of 24.90 ± 0.70%. This confirms that the size of Au NPs was less than 50.0 nm, resulting in a uniform surface coverage as depicted in Figure D.1c,e.

D.4.2. Gold coating and Prussian Blue deposition

The layers coating the suture were deposited in the following order: gold, PB, and six bilayers of chitosan-glucose oxidase (illustrated in Figure D.1a). Figure D.1b-d show optical microscope images of the suture and the gold and PB layers. Figure D.1e shows an SEM image of the gold-coated suture. This suture was not sputter coated with gold or any other conductive metal before imaging. Instead, the electroless deposition of gold formed a layer that was conductive enough to

result in an SEM image. The light parts of the suture represent the areas covered with gold, and the dark parts represent ones where gold was not deposited or peeled off before taking the image. Additionally, an EDS measurement was taken on the same spot. The resulting EDS spectrum, shown in Figure E.2, confirms the presence of carbon (0.25 keV), oxygen (0.50 keV), and gold (0.21 keV) on the gold-coated suture. The parameters used for PB deposition can be found in the Appendix E. Figure E.3 shows the corresponding cyclic voltammetry plot, which also shows the corresponding redox signal at 0.165 V and 0.145 V of PB on the gold-coated suture surface. The redox behavior is similar to what has been previously reported [44].

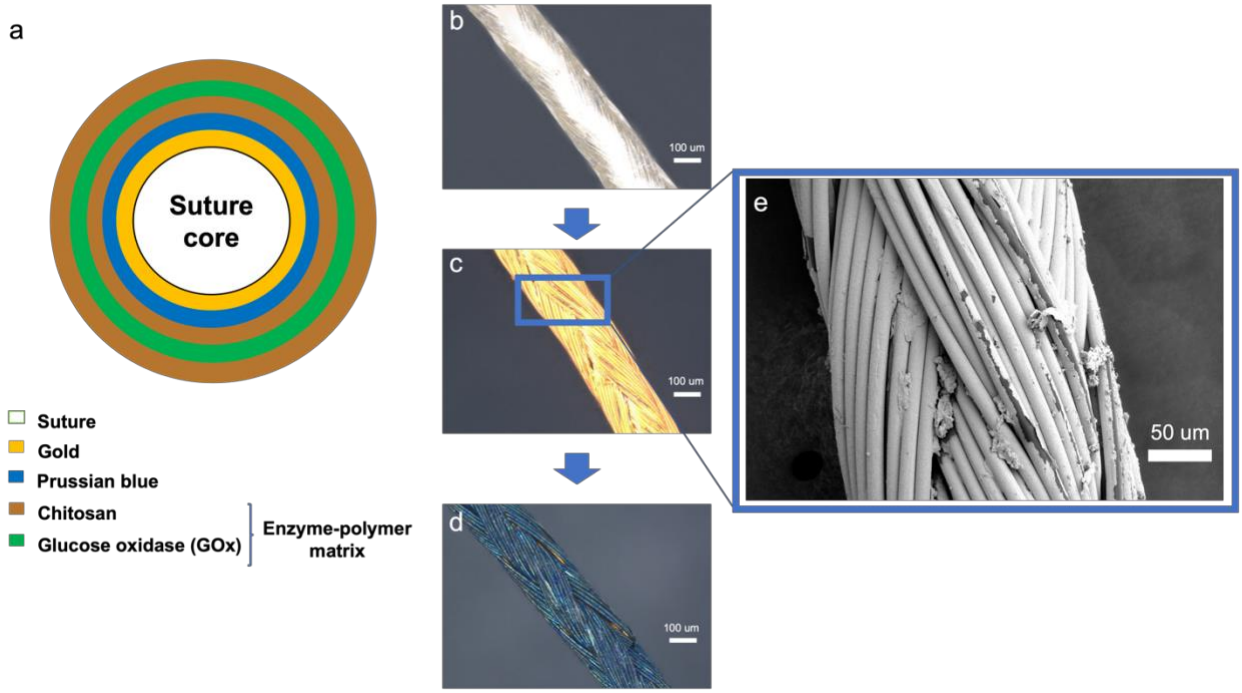


Figure D.1. Sensor layers and characterization. a) A schematic showing a sensor's cross-section with conductive layers (gold and Prussian blue) and enzyme-immobilization layers (chitosan and glucose oxidase). Microscopic images of **b)** pristine Polysorb^{TM} suture (COVIDIEN 5-0), **c)** the suture coated with gold, and **d)** the suture coated with Prussian blue (blue arrows represent an order of coating sequence). **e)** A scanning electron microscopy (SEM) image of the gold-coated suture.

D.4.3. Fourier transform infrared (FTIR) spectroscopy

The step-by-step surface modification of suture was verified by FTIR. The FTIR spectrum of the gold-coated suture (Au-NP) in Figure D.2a shows absorption bands at 597, 1292, 1416, and 1749 cm^{-1} which correspond to the citrate capped gold nanoparticles on the suture. Figure D.2b shows a vibrational band at 2066 cm^{-1} which corresponds to the C≡N stretching with a weak, broad band around 3292 cm^{-1} that confirm the presence of Prussian blue on the suture. In Figure D.2c, vibrational bands at 1520, 1630, 2841, and 2910 cm^{-1} correspond to the presence of amide (NH), C=C double bonds, and the stretching of CH2 which confirm the presence of glucose oxidase [45]. The additional peaks at 1390 cm^{-1} (bend., imide) further confirms the successful modification of surface. The suppression of the C≡N vibration band with a small shift to 2073 cm^{-1} confirms that surface has been completely modified with the enzyme layer [45].

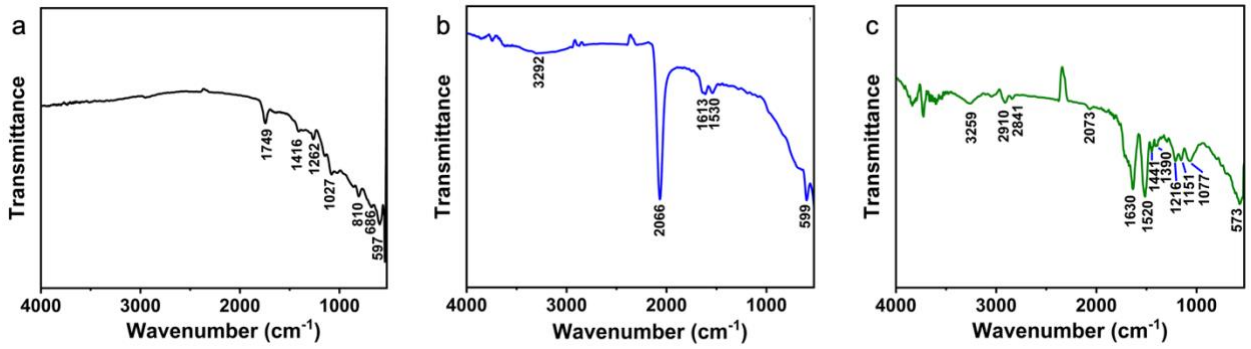


Figure D.2. FTIR spectra for **a)** gold-coated suture, **b)** Prussian blue-coated suture, and **c)** enzyme-polymer matrix-coated suture.

D.4.4. Flexibility studies

Figure D.3a-d shows the gold-coated suture being flexed to 2.0, 1.5, and 1.0 cm. Figure D.3e shows the normalized change in resistance as a function of radius of curvature (extent of bending). The length of the suture was 3.0 cm, hence the normalized change in resistance is at 0 when the radius is 3.0 cm (initial point). As the suture is bent, the resistance increases, and the normalized change in resistance increases. The increase in resistance due to bending is due to the creation of gaps within the gold layer of the surface of the suture, which decreases the conductivity.

Figure D.3f-i shows the enzyme-immobilized suture being flexed to 2.0, 1.5, and 1.0 cm. Figure D.3j shows the current measured at known glucose concentrations (0.10 and 0.30 mM). It is evident that the performance of the sensor is not disrupted by flexion down to 1.5 cm but begins to change past that flexion point. These results show that the suture is reliable in conductivity and glucose detection while flexed up to 67% flexion. When implanted in birds, the flexion is expected to be less than 10% and hence this level of performance is more than adequate.

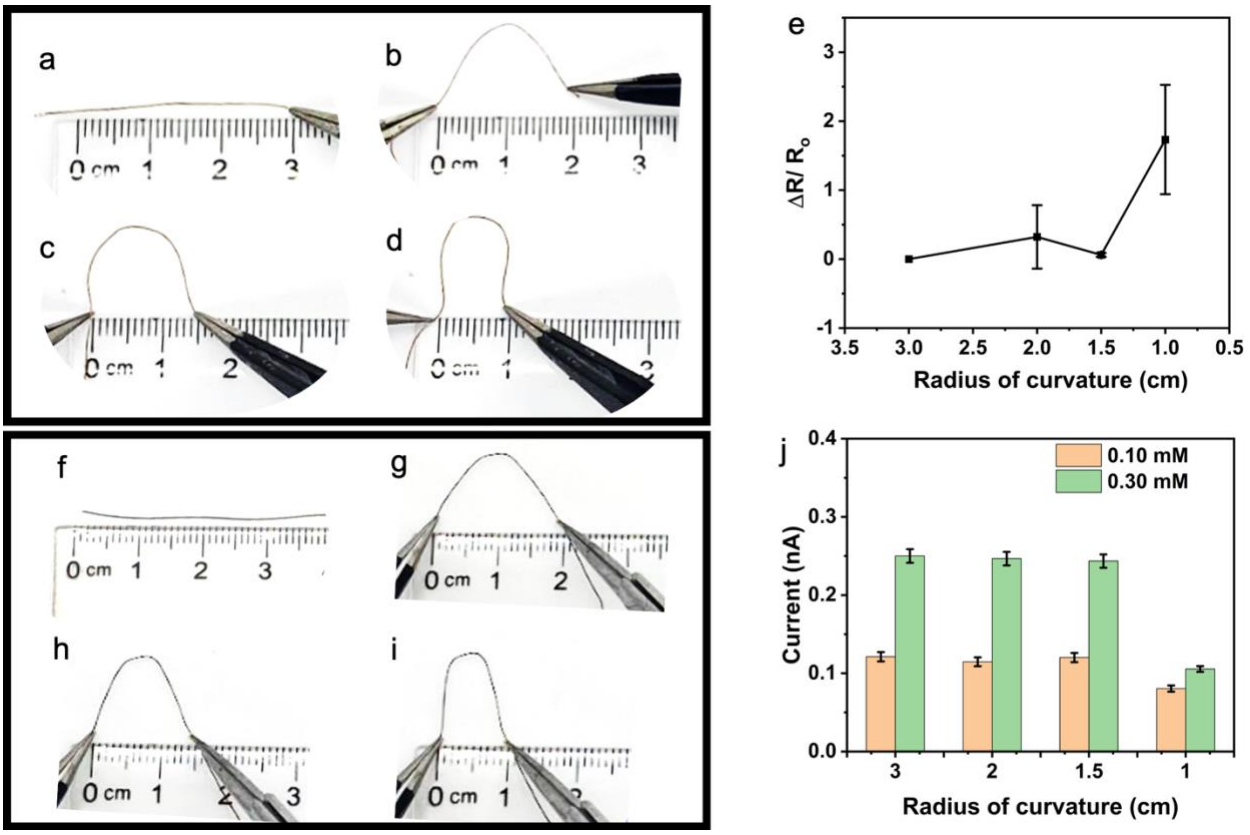


Figure D.3. a-d) bending a gold-coated suture to radii of curvature of 2.0, 1.5, and 1.0 cm from its original 3 cm length. **e)** normalized change in resistance as a function of radius of curvature. **f-i)** bending a glucose sensing suture (fully functionalized) to radii of curvature of 2.0, 1.5, and 1.0 cm from its original 3.0 cm length. **e)** Normalized change in resistance as a function of radii of curvature (n=3, multiple sensors) **j)** Current readout for two different glucose concentrations (0.10 mM and 0.30 mM) as a function of radius of curvature (n=3, multiple sensors).

D.4.5. Sensor calibration and real-time glucose monitoring

The sensor performance was evaluated in an in-vitro environment. The sensor calibration was obtained by changing the concentration of glucose in 1X PBS from 0 to 36.4 mM and recording the current for each glucose concentration. Figure D.4a shows the calibration curve for the glucose sensor. The sensor showed a linear range from 0.62 to 36.4 mM glucose with a correlation coefficient (R^2) of 0.9978 (n = 4). Based on the obtained calibration curve, limit of detection (LOD) for the sensor is 0.62 mM glucose in 1X PBS. The sensor's sensitivity within the 0.62-36.4 mM concentration range is 36.23 nA/mM. The blank concentration (0 mM) was assumed to be 1 order of magnitude lower than the next lowest concentration to be included on the x-axis of Figure D.4a.

For continuous glucose measurements, the concentration of glucose was changed from 0 to 0.30 mM in intervals of 0.10 mM per 10 minutes while the potentiostat was continuously recording the current (shown in Figure D.4b). The current for 1X PBS before the addition of any glucose was 2.15 nA (blank). The current then increased to ~2.48 nA, ~2.81 nA, and ~2.98 nA when the glucose concentration increased to 0.10 mM, 0.20 mM, and 0.30 mM, respectively.

D.4.6. Interference test

To test the selectivity of the sensor to glucose in the presence of structural and non-structural co-contaminants, a sensor interference test was run to test the interference of lactate,

NaCl, and KCl on the sensor (shown in Figure D.5a). The sensor gave a current readout of 3.29 nA as a baseline signal. After five minutes of incubation in 1X PBS, glucose was added to the solution to achieve 0.10 mM total glucose concentration. At 0.10 mM total concentration of glucose, the current read by the sensor increased to ~3.75 nA and stayed constant until the next analyte was added. At the 10-minute mark, lactate was added to the solution to achieve a total concentration of 18.0 mM lactate. With the addition of lactate, the sensor current readout increased to 3.83 nA. Adding NaCl (18.0 mM total NaCl concentration) at the 15-minute mark increased the current to 3.92 nA. And adding KCl (18.0 mM total KCl concentration) at the 20-minute mark did not change the current readout. The selectivity studies demonstrates that even though the sensor current readout changed with the addition of lactate and NaCl, the change in current due to glucose (4.6 nA/mM glucose) is about three orders of magnitude higher than the change in current due to lactate (0.00444 nA/mM lactate) and to NaCl (0.005 nA/mM NaCl).

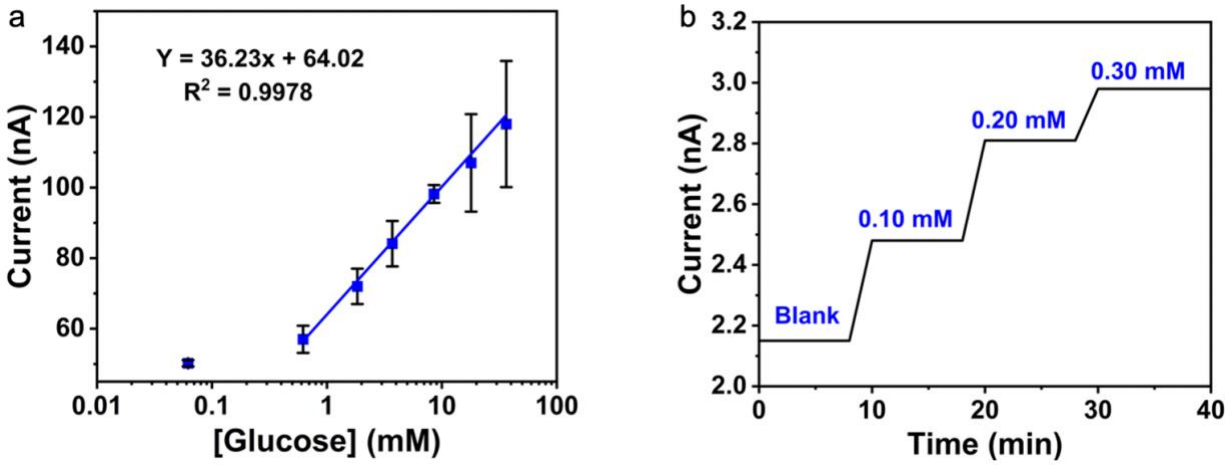


Figure D.4. Sensor calibration and real-time glucose monitoring: a) Sensor calibration curve showing the change in current with changing glucose concentration in 1X PBS-based solution (n = 4, one sensor). b) Real-time glucose sensing by monitoring the current as the glucose concentration was increased every ~10 minutes (0, 0.10, 0.20, then 0.30 mM glucose in 1X PBS).

D.4.7. Sensor repeatability and stability

As depicted in Figure D.5b, the sensor precision was verified by testing at two different glucose concentrations (0.62 mM and 36.4 mM) in the following order: 0.62 mM, 36.4 mM, 0.62 mM (second test), then 36.4 mM (second test). The first and second 0.62 mM chronoamperometry tests gave current readouts of 59.2 nA and 58.3 nA, respectively. The percentage difference between both measurements is a 1.50% drop in the current. This pair of tests suggest that the change in concentration from 0.62 mM to 36.4 mM and then back to 0.62 mM does not affect the performance of the sensor. The first and second 36.4 mM tests gave current readouts of 126 nA and 124 nA, respectively. The percent difference between both measurements is a 1.60% drop in the current. This pair of tests also suggest that the change in concentration from 36.4 mM to 0.62 mM and then back to 36.4 mM does not affect the performance of the sensor. Such a test is important to ensure consistency in the sensor's performance in environments with fluctuating glucose concentrations. The sensor's stability was tested within a span of five days from fabrication (Figure D.5c). On day one, the chronoamperometry measurement of PBS-glucose solutions resulted in current readouts of 9.34 nA and 30.3 nA for 0.62 mM and 3.71 mM, respectively. Day five tests resulted in current readouts of 9.82 nA and 27.5 nA for 0.62 mM and 3.71 mM, respectively. The percent change in the current readout between the first and fifth day was a 5.1% increase and a 9.0% drop for 0.62 mM and 3.71 mM, respectively. This drop in signal over 5 days is less than 10.0%, which is under statistically significant acceptable limit.

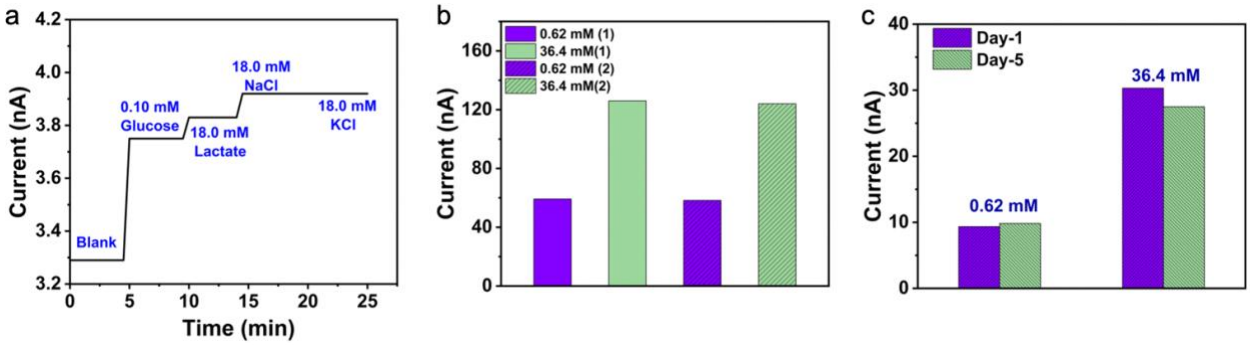


Figure D.5. Sensor interference, repeatability, and stability tests. a) Sensor interference/selectivity test showing the change in current in 1X PBS and after the addition of 0.10 M glucose, 18.0 mM lactate, 18.0 mM NaCl, and 18 mM KCl (added sequentially with five-minute intervals). **b)** Sensor repeatability test showing the current read by the sensor in 0.62 mM glucose (first measurement), 36.4 mM glucose (first measurement), 0.62 mM glucose (second measurement), then 36.4 mM glucose (second measurement). (1) and (2) in the legend of **b** represent the first and the second measurement, respectively, obtained for each of the two glucose concentrations. **c)** Sensor stability showed as a comparison between the current read by the sensor for two glucose concentrations (0.62 and 3.71 mM glucose) on days one and five from sensor fabrication.

D.4.8. Glucose monitoring in euthanized house sparrows

The procedure of implanting the sensor in euthanized house sparrows and the glucose sensing test results are shown in Figure D.6. Figure D.6 shows the increases in current that correspond to the spikes of glucose in the house sparrows. The changes were detected from baseline (0 mM) to the addition of 8.55 mM of glucose total, with an overall increase of current from 2.25 to 2.81 nA. In house sparrows and similar bird species, such as the European starling, this range of change is typical of the change in blood glucose levels birds experience throughout the day or in baseline to stress-induced levels [46, 47]. Figure D.6 also shows an R^2 of 0.9567, and a slope of 0.29 nA/mM, which corresponds to the sensor's sensitivity in the euthanized bird. Similar to Figure D.4a, the blank concentration (0 mM) was assumed to be 1 order of magnitude lower than the next lowest concentration to be included on the x-axis of Figure D.6. These results reveal that these sensors function as expected and detect changes in glucose concentrations in the tissue environment of house sparrows.

These results overall prove the possibility of fabricating gold-coated sutures that could be further functionalized to produce flexible electrochemical sensors for detecting biomarkers other than glucose, such as lactate. The results also prove the viability of such sensors *ex vivo*. Moving to *in-vivo* studies will need parallel effort to miniaturize the size and weight of the electronics module for readout, which will be basis of future work. After which, further studies can be done on *in-vivo* animal models and possibly freely moving/flying house sparrows in natural habitat.

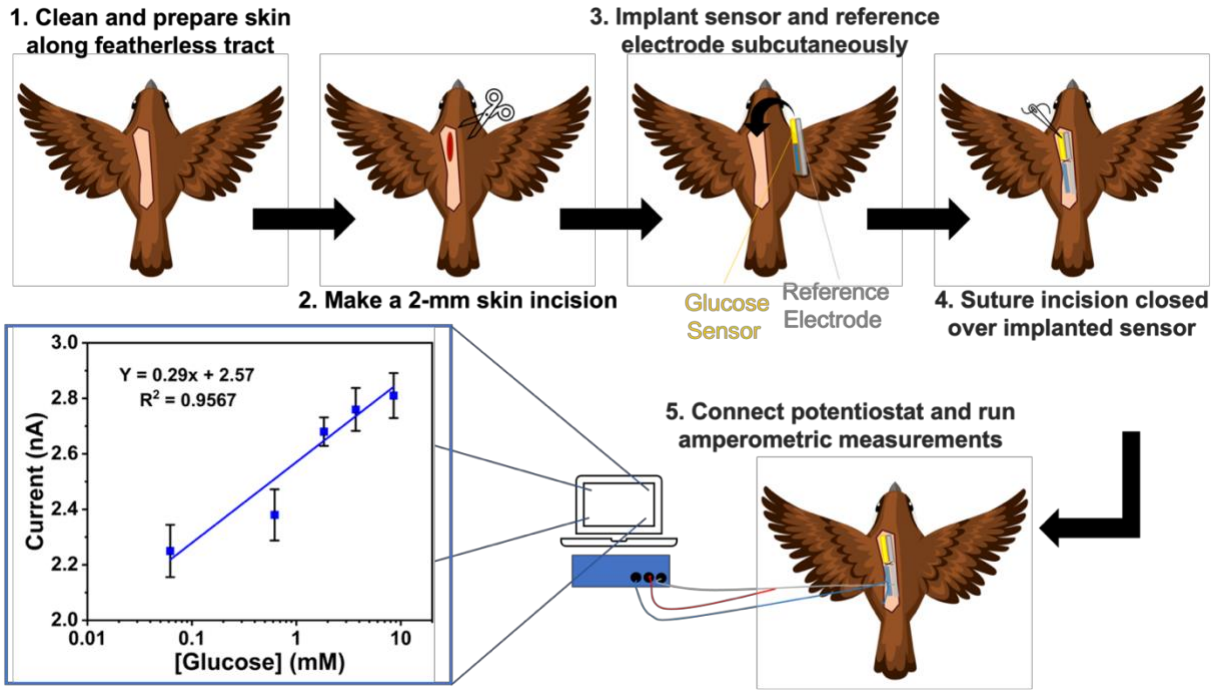


Figure D.6. Glucose monitoring in euthanized house sparrows (*Passer domesticus*) (n = 3, multiple sensors). Chronoamperometric measurements were obtained by a two-electrode system implanted in house sparrows for monitoring glucose. The concentration of glucose around the sensing region was changed by infusing 1X PBS-glucose solutions of known concentrations (x-axis) and the current was recorded after each infusion.

D.5. Conclusions

Thread-based biosensors are a promising alternative to rigid, bulky implantable sensors. Specifically, they offer a less invasive alternative for the continuous monitoring of biomarkers in small animal species, such as avian species, by simply stitching smart sutures transdermally into the skin tissue. Transdermal, stitched-in-place smart sensing sutures are expected to perform better in live birds than say microneedles which are prone to be misplaced due to motion. In this study, we demonstrate fabricating gold-coated, enzyme-immobilized, electrochemical glucose biosensors for transdermal implantation. We test their stability, repeatability, and selectivity. We also test them ex vivo in euthanized house sparrows (*Passer domesticus*). The sensors demonstrated glucose sensitivity of 5.0 nA/mM and were calibrated and tested within the expected blood glucose level in house sparrows (0-8.55 mM). Future studies include characterizing thread-based sensors in live animals, exploring other relevant biomarkers (e.g., lactate), and developing lightweight wearable-electronic systems that have the potential to revolutionize ecological and physiological research and assist in the conservation and management of free-living species.

D.6. References

1. Xia, J. and Sonkusale, S. *Flexible thread-based electrochemical sensors for oxygen monitoring.* Analyst, 2021. **146**(9): p. 2983-2990.
2. Terse-Thakoor, T., et al., *Thread-based multiplexed sensor patch for real-time sweat monitoring.* npj Flexible Electronics, 2020. **4**(1): p. 1-10.

3. Punjiya, M., et al., *PH sensing threads with CMOS readout for Smart Bandages.* Proceedings - IEEE International Symposium on Circuits and Systems, 2017: p. 10-13.

4. Mostafalu, P., et al., *A Textile Dressing for Temporal and Dosage Controlled Drug Delivery.* Advanced Functional Materials, 2017. **27**(41): p. 1-10.

5. Nejad, H.R., Sadeqi, A., and Sonkusale, S. *Thread as a Precise Sampling and Delivery Platform for Implantable or Ingestible Applications*. 2020. The 24th International Conference on Miniaturized Systems for Chemistry and Life Sciences (μTAS 2020).

6. Owyeung, R.E., et al., *Highly Flexible Transistor Threads for All-Thread Based Integrated Circuits and Multiplexed Diagnostics.* ACS Applied Materials and Interfaces, 2019. **11**(34): p. 31096-31104.

7. Tan, W., et al., *Go with the capillary flow. Simple thread-based microfluidics.* Sensors and Actuators, B: Chemical, 2021. **334**: p. 129670-129670.

8. Acar, G., et al., *Wearable and Flexible Textile Electrodes for Biopotential Signal Monitoring: A review.* Electronics, 2019. **8**(5): p. 479.

9. Hatamie, A., et al., *Review—Textile Based Chemical and Physical Sensors for Healthcare Monitoring.* Journal of The Electrochemical Society, 2020. **167**(3): p. 037546.

10. Stoppa, M. and Chiolerio. A., *Wearable electronics and smart textiles: A critical review.* sensors, 2014. **14**(7): p. 11957-11992.

11. Mostafalu, P., et al., *A toolkit of thread-based microfluidics, sensors, and electronics for 3D tissue embedding for medical diagnostics.* Microsystems and Nanoengineering, 2016. **2**.

12. Lee, I., et al., *Continuous glucose monitoring systems - Current status and future perspectives of the flagship technologies in biosensor research.* Biosens Bioelectron, 2021. **181**: p. 113054.

13. Kumar, T., Owyeung, R.E., and Sonkusale. S.R., *Rapid cleanroom-free fabrication of thread based transistors using three-dimensional stencil-based patterning.* Flexible and Printed Electronics, 2021. **6**(1): p. 015007.

14. Owyeung, R.E., Sonkusale, S., and Panzer, M.J., *Opportunities for ionic liquid/ionogel gating of emerging transistor architectures.* Journal of Vacuum Science & Technology B, 2020. **39**(1): p. 011001.

15. Punjiya, M., Mostafalu, P., and Sonkusale, S., *Smart bandages for chronic wound monitoring and on-demand drug delivery.* Midwest Symposium on Circuits and Systems, 2017: p. 495-498.

16. Owyeung, R., et al., *Free form three dimensional integrated circuits and wearables on a thread using organic eutectogel gated electrochemical transistors.* arXiv pre-print server, 2023.

17. Sonkusale, S. and Mostafalu, P., *Thread-based integrated functional devices*, in *U.S. Patent Application No. 15/749,207*.

18. Matsuhisa, N., et al., *Materials and structural designs of stretchable conductors.* Chemical Society Reviews, 2019. **48**(11): p. 2946-2966.

19. Yang, J.C., et al., *Electronic Skin: Recent Progress and Future Prospects for Skin-Attachable Devices for Health Monitoring, Robotics, and Prosthetics.* Advanced Materials, 2019. **31**(48): p. 1904765.

20. Chortos, A., Liu, J., and Bao, Z., *Pursuing prosthetic electronic skin.* Nature Materials, 2016. **15**(9): p. 937-950.

21. Park, S., Vosguerichian, M., and Bao, Z., *A review of fabrication and applications of carbon nanotube film-based flexible electronics.* Nanoscale, 2013. **5**(5): p. 1727-1752.

22. Rogers, J.A., Someya, T., and Huang, Y., *Materials and Mechanics for Stretchable Electronics.* Science, 2010. **327**(5973): p. 1603-1607.

23. Kim, D.H., et al., *Epidermal Electronics.* Science, 2011. **333**(6044): p. 838-843.

24. Asci, C., et al. *Ingestible pH Sensing Capsule with Thread-Based Electrochemical Sensors*. *2022 IEEE Sensors*. 2022.

25. Liu, M., et al. *Preliminary Results on Sensing Pillow to Monitor Head Movement using strain sensing threads*. *2022 IEEE Sensors*. 2022.

26. Klueh, U., et al., *Continuous Glucose Monitoring in Normal Mice and Mice with Prediabetes and Diabetes.* Diabetes Technology & Therapeutics, 2006. **8**(3): p. 402-412.

27. King, A.J.F., Kennard, M.R., and Nandi, M., *Continuous Glucose Monitoring in Conscious Unrestrained Mice*, in *Animal Models of Diabetes: Methods and Protocols*. 2020, Springer US: New York, NY. p. 225-239.

28. Korstanje, R., et al., *Continuous Glucose Monitoring in Female NOD Mice Reveals Daily Rhythms and a Negative Correlation With Body Temperature.* Endocrinology, 2017. **158**(9): p. 2707-2712.

29. Wuyts, C., et al., *Continuous glucose monitoring during pregnancy in healthy mice.* Scientific Reports, 2021. **11**(1): p. 4450.

30. Elliott, K.H., *Measurement of flying and diving metabolic rate in wild animals: review and recommendations.* Comparative Biochemistry and Physiology Part A: Molecular & Integrative Physiology, 2016. **202**: p. 63-77.

31. Morales, A., et al., *Point-of-care blood analyzers measure the nutritional state of eighteen free-living bird species.* Comparative Biochemistry and Physiology Part A: Molecular & Integrative Physiology, 2020. **240**: p. 110594.

32. Wang, Y., Wu, Y., and Lei, Y., *Microneedle-based glucose monitoring: a review from sampling methods to wearable biosensors.* Biomaterials Science, 2023. **11**(17): p. 5727-5757.

33. Saifullah, K.M. and Faraji Rad, Z., *Sampling Dermal Interstitial Fluid Using Microneedles: A Review of Recent Developments in Sampling Methods and Microneedle-Based Biosensors.* Advanced Materials Interfaces, 2023. **10**(10): p. 2201763.

34. Jiang, Y., et al., *Head motion classification using thread-based sensor and machine learning algorithm.* Scientific Reports, 2021. **11**(1): p. 2646.

35. Alaimo, F., et al., *Reel-to-reel fabrication of strain sensing threads and realization of smart insole.* Sensors and Actuators A: Physical, 2020. **301**: p. 111741.

36. Alaimo, F., et al. *Wearable Flexible Touch Interface Using Smart Threads*. *2018 IEEE SENSORS*. 2018.

37. Sadeqi, A., et al., *Washable Smart Threads for Strain Sensing Fabrics.* IEEE Sensors Journal, 2018. **18**(22): p. 9137-9144.

38. McGuire, L.P., et al., *Determining feeding state and rate of mass change in insectivorous bats using plasma metabolite analysis.* Physiological and Biochemical Zoology, 2009. **82**(6): p. 812-818.

39. Gerson, A.R. and Guglielmo, C.G., *Energetics and metabolite profiles during early flight in American robins (Turdus Migratorius).* Journal of Comparative Physiology B, 2013. **183**: p. 983-991.

40. Alonso-Alvarez, C. and Ferrer, M., *A biochemical study of fasting, subfeeding, and recovery processes in yellow-legged gulls.* Physiological and biochemical zoology, 2001. **74**(5): p. 703-713.

41. Romero, L.M. and Wingfield, J.C., *Tempests, poxes, predators, and people: stress in wild animals and how they cope*. 2015: Oxford University Press.

42. Monk, D.J. and Walt, D.R., *Fabrication of gold microtubes and microwires in high aspect ratio capillary arrays.* Journal of the American Chemical Society, 2004. **126**(37): p. 11416-11417.

43. Grabar, K.C., et al., *Preparation and Characterization of Au Colloid Monolayers.* Analytical Chemistry, 1995. **67**(4): p. 735-743.

44. Yin, B., et al., *Amperometric glucose biosensors based on layer-by-layer assembly of chitosan and glucose oxidase on the Prussian blue-modified gold electrode.* Biotechnol Lett, 2008. **30**(2): p. 317-22.

45. Khan, N.I., et al., *An integrated microfluidic platform for selective and real-time detection of thrombin biomarkers using a graphene FET.* Analyst, 2020. **145**(13): p. 4494-4503.

46. Beattie, U.K., et al., *The Effect of a Combined Fast and Chronic Stress on Body Mass, Blood Metabolites, Corticosterone, and Behavior in House Sparrows (Passer domesticus).* Yale J Biol Med, 2022. **95**(1): p. 19-31.

47. Romero, L.M. and Remage-Healey, L., *Daily and seasonal variation in response to stress in captive starlings (Sturnus vulgaris): corticosterone.* Gen Comp Endocrinol, 2000. **119**(1): p. 52-9.

Appendix E: Supplementary Information Concerning Appendix D

This appendix is reproduced from the following publication:

Alsaedi, M. K.; Riccio, R. E.; Sharma, A.; Xia, J.; Owyeung, R. E.; Romero, L. M.; Sonkusale S. Smart Sensing Flexible Sutures for Glucose Monitoring in House Sparrows. *Analyst.* **2023**, 148 (22), 5714-5723

E.1. Electroless deposition of gold on suture:

Figure E.1 shows the absorbance of a glass slide that was coated with gold in the same procedure described in the main text that was used to coat the sutures with gold (electroless deposition). This absorbance data was obtained using a UV-Vis spectrometer. The longer the glass slide is submerged in the plating solution, the higher the absorbance becomes, which corresponds to more reduction of gold nanoparticles on the surface and formation of gold layer. However, the absorbance plateaus, which is why the deposition process was repeated three times with fresh plating solution every time. This process is also reported in another work that was published from our group by Owyeung, R. et al [16].

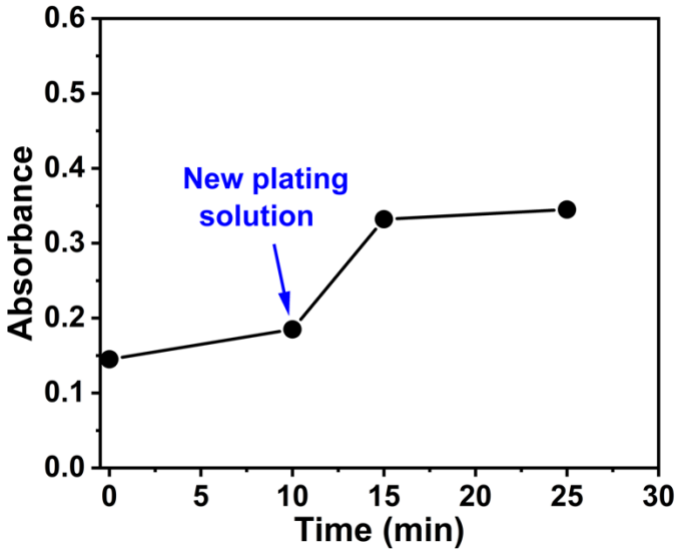


Figure E.1. Absorbance as a function of time for the electrodeposition of gold on a glass slide (one cycle) using the same procedure used to deposit gold on sutures.

E.2. Energy dispersive spectroscopy (EDS) on gold-coated suture:

Figure E.2 shows an EDS graph obtained using SEM of the gold-coated suture by scanning the region imaged in Figure D.1e. Figure E.2 shows the presence of carbon at ~0.25 keV and oxygen at 0.5 keV (from polymer backbone) and gold at ~2.1 keV (from the outer coat).

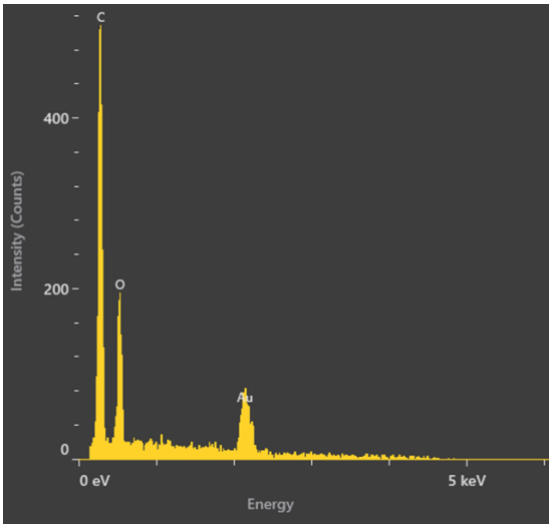


Figure E.2. Energy dispersive spectroscopy (EDS) on gold-coated suture showing the presence of carbon, oxygen, and gold.

E.3. Cyclic voltammetry (CV) for electro-assisted Prussian blue deposition onto gold-coated sutures:

The following parameters were set for CV: -0.1 V initial voltage, 0.4 V high voltage, 50 mV/s scan rate, 0.01 V intervals, and 7 sweeps. The suture is then rinsed with DI water and dried off with nitrogen gas. CV curve is shown in Figure E.3.

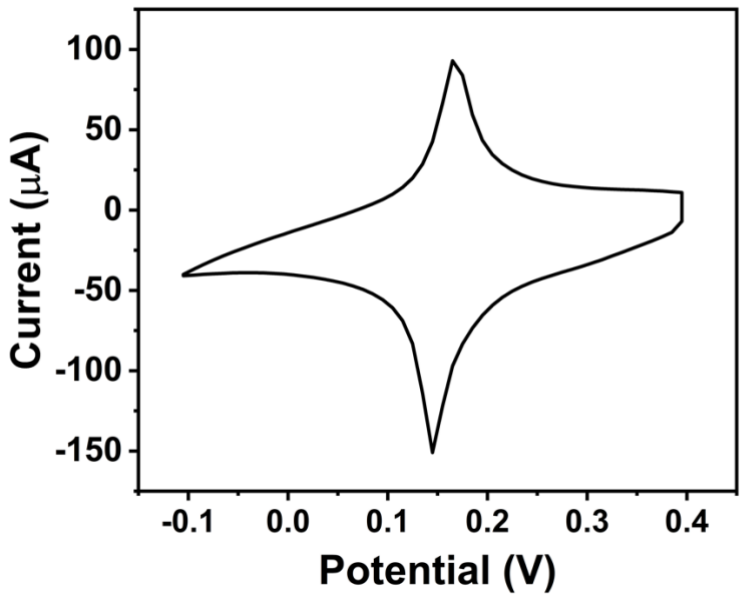


Figure E.3. Cyclic voltammetry (CV) plot for the deposition of Prussian blue onto the gold-coated suture. The redox peaks for Prussian blue are at 0.165 V and 0.145 V.

Appendix F: Soft Injectable Sutures for Dose-Controlled and Continuous Drug Delivery

This appendix is reproduced form the following publication:

Alsaedi, M. K., Lone, O., Nejad, H. R., Das, R., Owyeung, R. E., Del-Rio-Ruiz, R., Sonkusale, S., Soft Injectable Sutures for Dose-Controlled and Continuous Drug Delivery, *Macromolecular Bioscience*, **2024**, *24*(3), 2300365

F.1 Abstract

Transdermal drug delivery offers a promising alternative to traditional methods like oral ingestion and hypodermic injection. Hypodermic injections are painful, while oral ingestion requires higher doses due to enzymatic degradation and poor absorption. While microneedles address the pain issue, they are limited to delivering small amounts of drugs and can be impractical due to peeling off with motion and sweat. Herein, we propose soft injectables using drug-carrying sutures for painless and localized sustained delivery in the dermis. These sutures can remain in place during delivery and are suitable for all skin types. Surgical sutures can also serve as open capillary microfluidic channels carrying drug from a wearable drug reservoir to enable long-term (weeks to months) transdermal drug delivery. Our experiments focus on delivering 5-fluorouracil, a cancer drug, and rhodamine B, a drug model. A fixed-length suture of 60 cm delivers 0.43 mg of 5-flurouracil in 15 minutes. Our experiments also demonstrate a continuous drug delivery of rhodamine B for over 8 weeks at a rate of 0.0195 mL per hour. Our results highlight that soft injectable sutures are promising candidates for long-term sustained delivery of varying quantities of drugs over weeks period compared to hypodermic injection, oral ingestion, or microneedles.

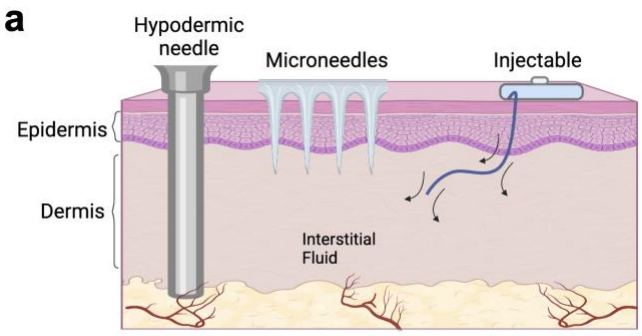
F.2 Introduction

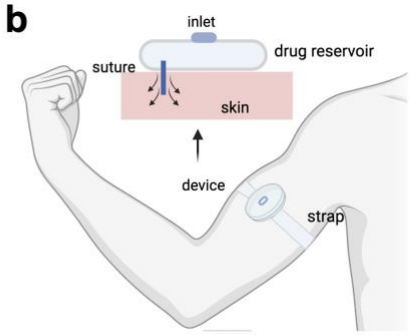
Only a fraction of the total amount of an administered drug is eventually delivered to the location in the body where its therapeutic effect is most needed. Therefore, it is of great importance to minimize the amount of drug lost in the drug-delivery process. Reasons for drugs not reaching their intended target locations are numerous. Drugs that are being delivered can undergo degradation due to enzymes, such as degradation in the liver or the GI tract, especially when administered orally. Also, the pharmacokinetics and pharmacodynamics of the drugs

limit their absorption to less than 100%.[1-3] Therefore, drugs are always administered in quantities much higher than needed in order to compensate for these losses from drug degradation or non-targeting.[4] To resolve the issue of drug degradation, patients get painful injections using hypodermic needles. Such reduction in drug efficacy and pain endurance that patients go through could be avoided by localizing drug delivery. Localizing drug delivery could also decrease the drug's side effects and the overall frequency of administration, increase patient compliance, and ensure that exposure to drugs is limited to the targeted regions in the body, which is important when administering potent drugs, such as chemotherapeutics.[1, 5]

One of the methods for localized sustained drug delivery is transdermal. Transdermal drug delivery using microneedles, for example, offers a relatively painless route of drug delivery through interstitial fluid, where the release of drugs can be sustained over long periods of time and tuned through size, number, and matrix composition of microneedles.[2, 6-20] However, microneedles can still cause skin inflammation, may not penetrate reliably in all skin types, are prone to breakage, and can peel off due to sweating or motion, which makes them highly unreliable for drug delivery. One of the new classes of drug-delivery systems that is being studied is injectable hydrogels, which allow for painless delivery of therapeutics to desired delivery sites.[21] Delivery using such type of injectables, however, is limited to the dermis layer to ensure painless injection. Drugs can be mixed with the gel precursor solution and injected with a hypodermic needle before undergoing a solution-gel transition (e.g. in-situ gelation). The tunable biodegradation rate of the gel controls the drug's release profile. In this paper, we propose *soft injectables,* a complementary platform which utilizes drug-loaded surgical sutures for long-term delivery with weeks-to-months release profiles (illustrated in Figure F.1). The drugs are loaded onto the suture or delivered from a wearable reservoir using natural capillary transport along the length of the suture into the skin. Like microneedles, they are painless, as they are injected in the dermis layer of the skin. However, unlike microneedles and like injectable hydrogels, they are not prone to being peeled off with motion or by sweating

and do not cause inflammation as they are realized using medical-grade sutures as substrates and fixed into the skin like any suture. The use of threads for drug delivery in the context of wound healing[1] and as sutures[22, 23] was investigated by our group, and by others[5], however they are yet to be used as injectables. Soft injectables using sutures provide precise control over drug quantity and delivery rate either by simply controlling their lengths and thickness, when used as an implant, and/or adjusting the amount of drug in an optional wearable reservoir connected to it when used as a continuous drug-delivery system. While transdermal applications have been proposed, sutures can also be implanted in deeper organs/tissues, which are locations that cannot be accessed by microneedle patches. In this study, we report on the fabrication and validation of suture-based injectables for dose-controlled drug delivery both as a drug-loaded injectables capable of delivering a fixed payload over long term, or as a drug-carrying injectable from a drug reservoir for unlimited payload over weeks/months of release. We demonstrate these suture-based injectables by using rhodamine B (model drug) and *in-vitro* experiments with 5-fluorouracil (5-FU), which is a cancer drug, and studying its release in cultured cancer cells.





c

	Hypodermic needles	Microneedles	Soft injectable sutures
Drug Release Profile	Burst	Sustained	Sustained
Drug Quantity	Single large dose	Small	Continuous large dose
Duration of Delivery	Seconds	Days	Weeks/months
Region of delivery	Dermis, subcutaneous layer, and muscle layer	Dermis	Any organ and tissue depth allowed by a surgical needle
Pain of injection	High	Moderate, may cause skin sensitivity over large area	Low due to use of suture and single site of skin penetration
Reliability	High	Low, due too unreliable penetration or peeling from motion or sweat	High, due to suturing in skin
Mechanical compatibility	Not applicable	Moderate due to hard needles	High due to soft and flexible sutures

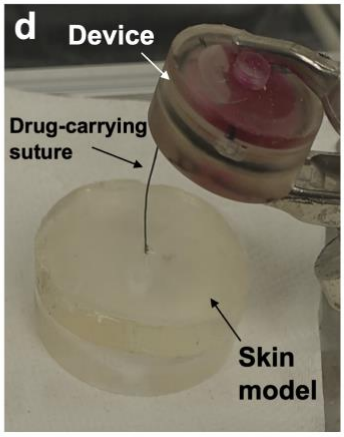


Figure F.1. a) Illustration and comparison of transdermal (microneedles and injectable) and dermal drug delivery platforms. Soft injectables are smart surgical sutures that are either loaded with the drug (method 1) or carry drug from a wearable reservoir into the skin (method 2). **b)** Illustration of suture-based drug-delivery wearable device. **c)** Table comparing hypodermic needles, microneedles, and soft injectable sutures. **d)** Wearable device delivering dye (rhodamine B) from drug reservoir to a skin model gel through a surgical suture.

Delivery via sutures uses natural wetting (capillary action) of surgical grade threads to carry the drug from the drug reservoir into the dermis, or to load the drugs onto them. Sutures are made of multiple fibers that are combined and woven together. These fibers can be natural fibers, such as silk and cotton, or synthetic ones, such as polyester and nylon.[24] Hydrophilicity and wettability are two important properties of sutures when it comes to drug loading. Different surface chemistries and structural morphologies of sutures result in their varying wettability degrees.[24] Therefore, surface plasma treatment (surface oxidation) is used to increase sutures' wettability and hydrophilicity.[24] Furthermore, the uniformity of a suture's surface allows for more precise wetting.[25] In addition to selecting the suture with the appropriate surface uniformity and wettability, the length of the suture can be controlled. When used as a drug-loaded injectable without an external drug reservoir, the length/width of the suture allows one to precisely control the amount of drug being loaded and released.

Drug-loaded injectables: A suture-based soft drug-loaded injectable (without the drug reservoir) can be administered in different ways. It can either be inserted through a catheter tube after the tube reaches the depth or internal organ where delivery is desired. In such cases, the underlying sutures are bioresorbable, so they do not need to be recovered. Thread injectables can also be sutured in through the skin using a fine surgical needle or a cannula, keeping part of it on the surface of the skin to hold the injectable in place while the rest of it penetrates to the desired depth or internal organ. This injectable can be made from coating drug on either a bioresorbable or a non-resorbable suture, the latter removed after delivery is complete. Because these injectables are soft and flexible, they would be less painful and more stable when kept in place during drug delivery compared to rigid microneedles. The microneedles, being rigid to enable their penetration, do not conform to the soft and flexible nature of the underlying tissue cause some skin inflammation, and may also cause them to come off the skin if not properly secured.

We showcase these suture-based soft injectables for the delivery of chemotherapeutics. More specifically, we demonstrate the delivery of 5-fluorouracil (5-FU), which is a common drug that is administered intravenously and is used to treat a wide range of cancers including breast cancer and aerodigestive-tract cancers.[26] It is converted to active metabolites upon entering a cell which hinder ribonucleic acid (RNA) synthesis and inhibit thymidylate synthase enzymes in cancer cells.[26] In our case, 5-FU can be delivered to cancer tumors, such as skin cancer, through drug-loaded injectable sutures rather than microneedles or the more invasive intravenous approach, which exposes other parts of the body to this potent chemotherapeutic drug.

Drug-carrying injectables: We also demonstrate the potential of using the same sutures as drug-carrying channels for long-term (weeks long) transdermal drug delivery from a drug reservoir into the skin. The natural capillary action of appropriately treated sutures enable continuous delivery of the drug into the skin over long term. In this report, Rhodamine B (drug model) was delivered from a wearable drug reservoir via a polyester suture to a deep eutectic solvent (DES) based gelatin gel (tissue model) in a linear fashion for a record-setting period of 2 months and more. One such design of a 3-D printed wearable and refillable drug-delivery reservoir for transdermal drug delivery is also presented in this paper (Figure F.1b,d). In Appendix G, we also discuss a suture-insertion assist device (Appendix G figures G.10-G.14) to help caregivers to administer the suture-based injectable into the skin at any desired depth. This will eliminate the need for a skilled expertise to perform administration of the platform.

F.3 Materials

F.3.1 Sutures

Polysorb™ sutures (5-0, braided, absorbable) were obtained from Covidien. Polyester sutures (3-0, braided, green) were purchased from CynaMed. Polyester thread (#50/3-ply, So Fine™) were purchased from Superior Threads.

F.3.2 Devices

The plasma treatment device was purchased from Plasma Etch, Inc (Carson City, NV). The scanning electron microscope (SEM) used was an Axia model from Thermo Scientific. The ultraviolet visible spectrometer used was an Evolution 220 UV-Visible Spectrometer and was purchased from Thermo Scientific. Cell viability data were obtained using a Sunergy 4 (BioTek) plate reader. A Form 3B+ printer, purchased from Formlabs (Somerville, MA), was used to print the drug delivery reservoir.

F.3.3 Chemicals

Rhodamine B, cresol red, 5-fluoruouracil, gelatin (porcine gelatin, 175 g bloom type A), ethylene glycol, choline chloride, and agarose were all bought from Sigma Aldrich and used as received. Gibco Dulbecco's Phosphate-Buffered Saline (DPBS) 1X was bought from Thermo Fisher Scientific and used as received. High Temp V2 Resin and Dental LT Clear V2 Resin were bought from Formlabs.

F.4 Results and Discussion

F.4.1 Injectable sutures' uptake

We compare different sutures serving as substrates for injectables for their drug loading capacities by assessing their water uptake in a sealed environment to prevent evaporation. Figure F.2 shows results using non-resorbable polyester, cotton threads, and polyester sutures, and resorbable Polysorb™ sutures. Loading capacities are attributed to the threads' surface properties. Cotton consists of less organized fibers with more open pockets that can take up more fluid, but random topography results in less control over amount (error bars in Figure F.2e). Polysorb™ sutures also exhibit less uniform uptake (error bars in Figure F.2e). For purpose of demonstration, we chose polyester sutures for their uniform drug loading capacity. Water uptake (and hence the drug loading capacity) of polyester thread, polyester suture, cotton thread, and Polysorb™ suture are 28.1±4.66 μg mm^{-1}, 57.9±10.3 μg mm^{-1}, 229±18.4 μg mm^{-1}, and 506±288 μg mm^{-1}, respectively (n=7). When sutures are used for carrying drug from the reservoir into the skin, the total drug delivered is dependent on the flow rate which is primarily diffusion limited in the dermis layer of the skin.

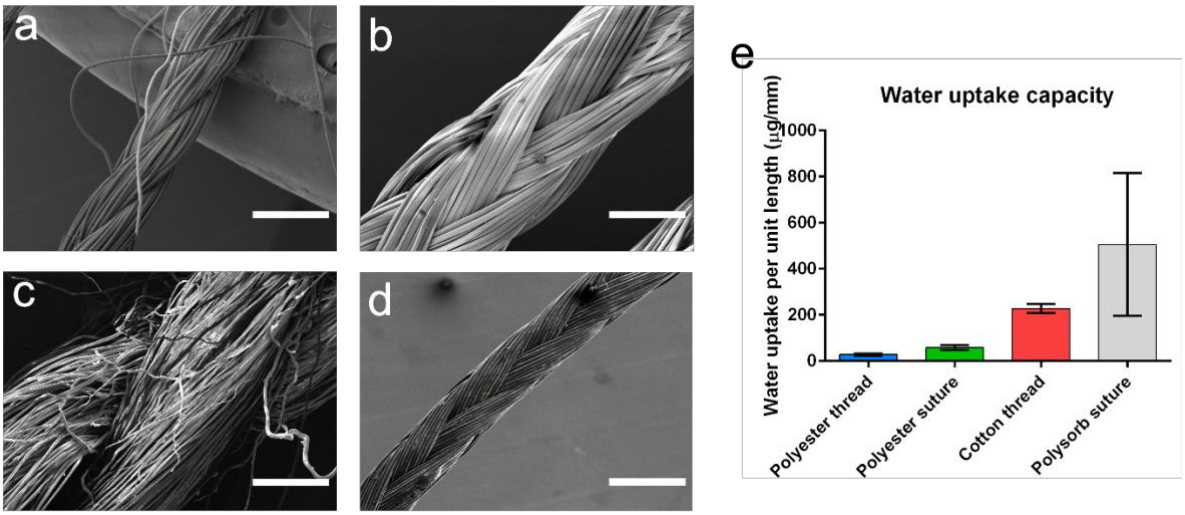


Figure F.2. SEM images of **a)** polyester thread, **b)** polyester suture, **c)** cotton thread, and **d)** Polysorb^{TM} suture (scale bars = 300 µm). **e)** Water uptake of polyester thread, polyester suture, cotton thread, and Polysorb^{TM} suture (n=7).

If transport is not diffusion limited, in highly perfused and vascularized tissues, the drug delivery will be proportional to the water uptake capacity of the thread discussed above, which indicates that the Polysorb^{TM} suture would be capable of delivering almost twice the amount of drug as that of cotton sutures, and ten times that of polyester sutures.

F.4.2 Visual monitoring of dye diffusion from polyester suture-based injectable

Figure G.1 in Appendix G shows the release of cresol red dye off of a polyester suture as injectable in water bath.[25] The cresol-red-loaded suture, which is yellow after initially being white in color, becomes white again after the complete release of the yellow-colored dye. Similarly, Figure F.3a-c show an initially green polyester suture retaining its original color after releasing the purple rhodamine B dye that was loaded onto it. These images show that no residual dye is retained by the sutures, which is an appropriate feature to have in dye- and drug-release scenarios.

The diffusion of a model drug, rhodamine B dye, from soft injectable sutures was monitored to help visualize the drug-release mechanism into biological tissue. Figure F.3d shows a time lapse of the dye's release profile into an agarose gel, which is the artificial skin model in this study. All the dye that was loaded on the suture, diffused from the suture into the surrounding agarose gel within 10 minutes.

Release of rhodamine B was also demonstrated in biological tissue: porcine skin. In Figure F.3e and f, a 1-cm dye-loaded polyester suture was used. The suture was simply in physical contact with the surface of the skin. But in Figure F.3g and h, the suture was inserted into a 1-cm, horizontal incision that was made in the center of the porcine skin patch. More dye was released from the suture as more time went by (in both scenarios). Since the length of the suture was constant, it is evident, when comparing images from both scenarios of identical timestamps, that having the suture in an incision allows for the release of more dye than having

it only in surface contact with the skin. This sheds light on another parameter that can be investigated with respect to controlling amount of drug released: the area of overlap between the soft injectable and the surrounding tissue. The more overlap area there is, the most drug can be released after a certain amount of time.

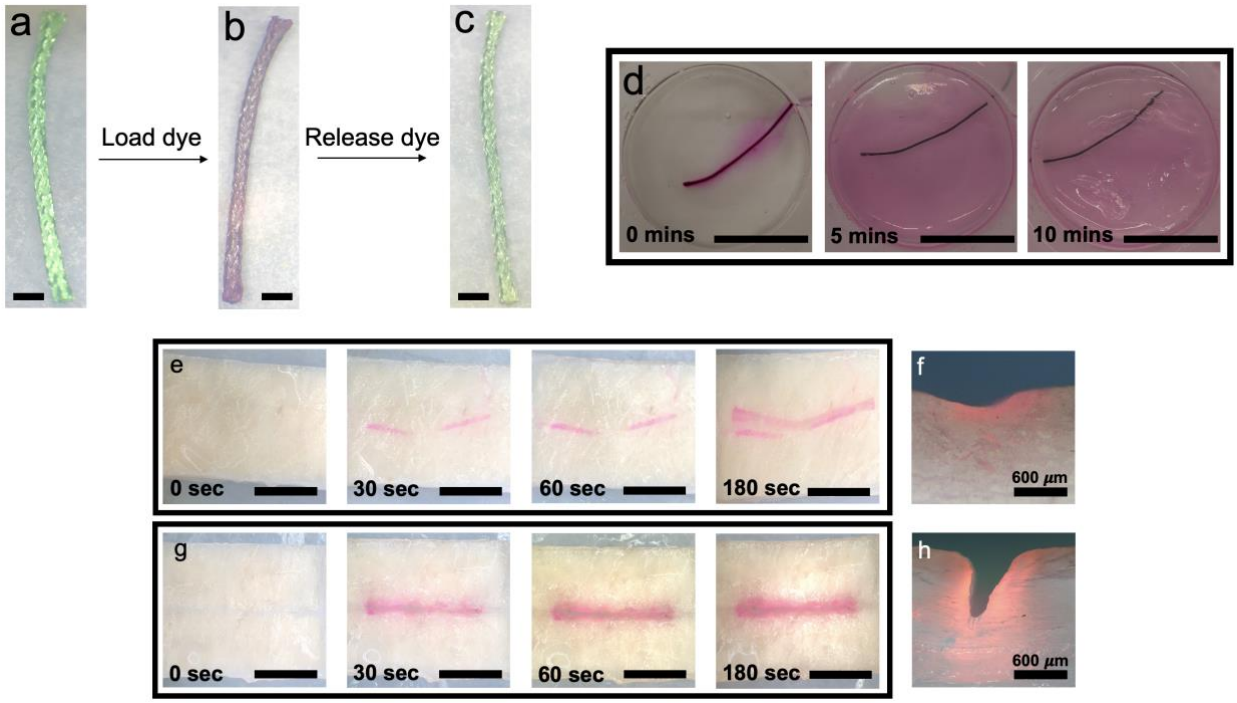


Figure F.3. Qualitative assessment of drug release: release of rhodamine B dye (drug model) from polyester suture into agarose gel (skin model) and porcine skin. Pictured is a polyester suture **a)** before dye loading, **b)** after dye loading, and **c)** after complete release of dye (a-b scale bars = 0.4 mm). Images in **d** show the release of dye from a polyester suture in an agarose gel at different time points (scale bars = 2.5 cm). Images **g** and **f** pertain to the release of dye from a polyester suture that was brought to contact with the surface of the skin patch: images in **g** (scale bars = 0.5 cm) are top view images of the porcine skin patch at different time points and **f** is the cross-sectional image (UV-illuminated sideview) of the same porcine skin patch after 180 seconds. Images **g** and **h** pertain to the release of dye from a polyester suture that was inserted in a horizontal incision made in the center of the skin patch: images in **g** (scale bars = 0.5 cm) are top view images of the porcine skin patch at different time points and **h** is the cross-sectional image (UV-illuminated sideview) of the same porcine skin patch after 180 seconds.

F.4.3 Dose-controlled release of 5-fluorouracil from injectable, drug-loaded sutures

To show control over quantity of drug released by controlling suture length, 5-FU was released in 1X DPBS from sutures of different lengths. Sutures of lengths 0.6 cm, 6 cm, and 60 cm each released different quantities of 5-FU. These lengths were chosen for characterization and to correlate suture's length with amount of drug released. The longer the suture is, the more 5-FU it released, which is attributed to the increase in drug loading with increasing suture length. Figure F.4a shows the release profile of 5-FU from drug-loaded sutures of different lengths in the first 240 minutes after the suture was submerged in 1X DPBS. Total amount of drug released after 240 minutes from 0.6 cm, 6 cm, and 60 cm long sutures is 0.0193±0.000438 mg, 0.0470±0.0148 mg, and 0.431±0.0543 mg, respectively (n=3). Figure F.4b shows the same release profile as in F.4a, but in terms of percent release (n=3). It is inferred from Figure F.4b that all the loaded drug is released within the first 15 minutes from 6 and 60 cm sutures. (100% release). The 0.6 cm sutures required 240 minutes to reach 100% release. Releasing 5-FU from microneedles, on the contrary, achieves less than 5% cumulative permeability in the first 10 hours.[27]

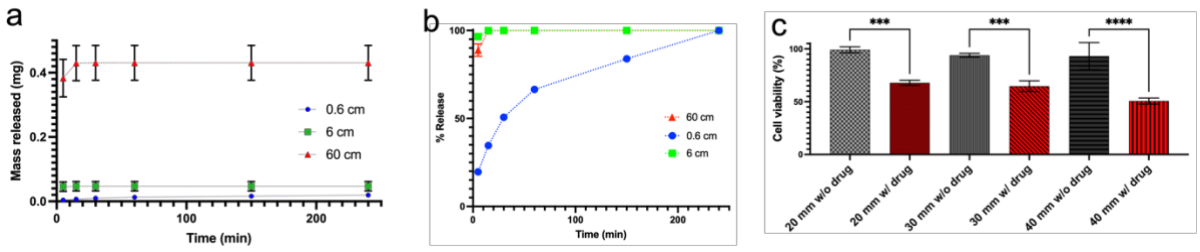


Figure F.4. Chemotherapeutic soft injectables. a) Release of 5-fluorouracil from polyester sutures of different lengths into 1X PBS (n=3). **b)** 5-FU release as percent of total amount of loaded onto 0.6, 6, and 60 into 1X PBS (n=3). **c)** Cell viability of HeLa cells 48 hours after incubating with bare and cancer-drug-loaded polyester sutures of different lengths. Ordinary one-way ANOVA was used for **c** (*** p value < 0.001, **** p value < 0.0001).

HeLa cells were chosen as a cancer-cell model to study *in-vitro* drug release. 5-FU-loaded injectable sutures showed considerable reduction in cell viability compared to bare sutures, demonstrating successful drug delivery from polyester sutures (Figure F.4c). Furthermore, polyester-suture injectables demonstrated excellent biocompatibility. Cell viability after 48 hours of being in contact with bare sutures was 99.1±2.83%, 93.9±1.87%, and 93.1±12.8% for bare 20 mm, 30 mm, and 40 mm long sutures, respectively. The 5-FU-loaded soft injectables demonstrated lower cell viability compared to bare ones due to the presence of the cancer drug. They also demonstrated lower cell viability with higher suture length, which is attributed to the increase in amount of drug released with increasing suture length. The cell viability after 48 hours of being in contact with drug-loaded injectables was 67.9±2.46%, 64.7±5.09%, and 50.6±2.90% for 20 mm, 30 mm, and 40 mm long sutures, respectively. The number of dead HeLa cells after 48 hours of being in contact with a bare suture and a drug-loaded suture can also be visually compared under the microscope (Figure G.2 in Appendix G). These results demonstrate the potential of utilizing the suture based injectables for drug delivery.

F.4.4 Long-term continuous drug delivery using drug-carrying sutures from a drug reservoir

The polyester suture based injectable also reliably delivered fluids over a record-breaking period of 63 days when connected to a drug reservoir. One end of a suture was submerged in a "drug reservoir," which was a vial filled with a known amount of rhodamine B (drug model). The other end of the suture was in a gel serving as a skin mimic. Figure F.5a and G.3 shows the experimental setup in more detail. Figure F.5d shows the volume of dye delivered from the reservoir to the gel over a period of 63 days. It can be inferred from Figure F.5d that the wicking occurred in a linear fashion throughout the entire 2-month period with a rate of 0.0195 mL per day and $R^2 = 0.998$. The loss of dye volume in the control vials is attributed to the evaporation of the dye solution in the vials, not to wicking, as the sutures in the control vials

were not in contact with the dye solution. Figure F.5b show the evident change in color of the gel due to the increasing volume of dye in the gel over time (0, 30, and 63 days, respectively).

To study the effect of interfacial surface area on total volume wicked, the surface area of the suture that is interfacing with the gel on the inside was varied. Two conformations of the sutures inside the gels were formed: a suture going straight from the bottom of the gel to the top, and a U-shaped suture that curves down (Figure F.5c). The U-shaped suture forms a higher interfacial surface area when in contact with the gel and, therefore, wicked more dye to the gel in 6 days (0.197±0.0123 mL) compared to the straight suture (0.156±0.0124 mL). There is no apparent limit to the amount of the drug that can be delivered. Our experiments were stopped on day 63.

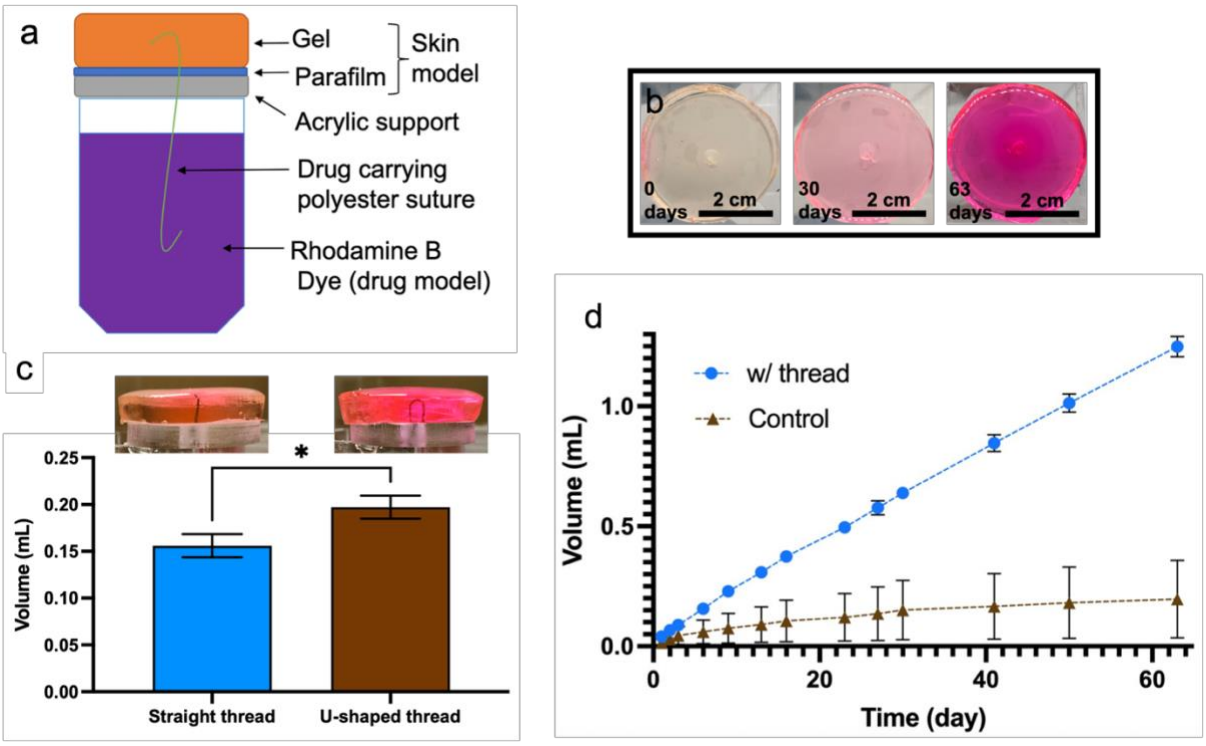


Figure F.5. Long-term continuous delivery. a) Schematic of experimental setup used to obtain results. Parafilm and deep eutectic solvent or DES based gelatin gel constitute the skin model. **b)** Images of gel on day 0, after 30 days, and after 63 days. **c)** Volume of rhodamine B delivered to gel by sutures of different conformations in the gel (straight and U-shaped, n=3) after 6 days. Unpaired t-test was used in **c** (* p value < 0.1). **d)** Volume of rhodamine B dye delivered from reservoir to gel by sutures in the span of 63 days (n=3).

F.4.5 Wearable drug-delivery reservoir

An example 3D-printed, refillable drug reservoir was also developed and characterized. The weight of the DES gelatin gel serving as a skin mimic was monitored for 66 hours since the insertion of the suture coming out of the drug reservoir. Figure F.6b shows that the increase in gel mass showed an almost linear behavior from hour 0 up to hour 49 then started to plateau thereafter (R^2 = 0.9428 and slope of 0.015 gram of dye per hour). Figure F.6c and F.6d show the 3-D printed rhodamine B reservoir and the DES gelatin gel connected by the injectable sutures at different timepoints (initial and after 2 hours had elapsed). Delivery of dye to the gel is not only confirmed by the increase in gel weight, but also by the visible appearance and gradual increase of dye in the gel.

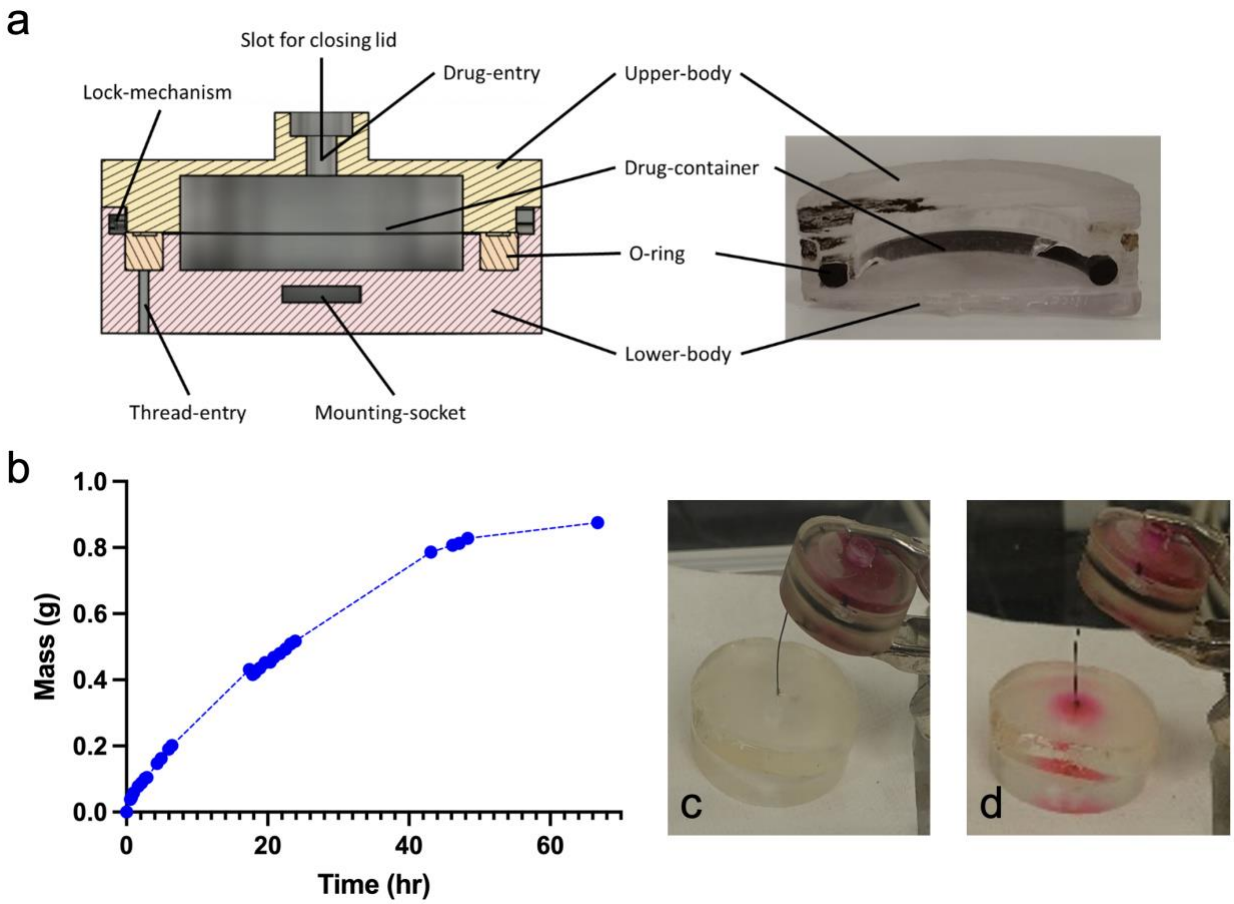


Figure F.6. a) Cross-sectional view of the drug-delivery wearable device showing the upper and lower parts of the device, the O-ring, and the screw-lock assembly. **b)** Increase in mass of DES gelatin gel connected to delivery reservoir via polyester suture over a period of 66 hours. Images of DES gelatin gel connected to delivery reservoir via polyester suture at **c)** 0 hours and **d)** after 2 hours.

F.5 Conclusion

Soft injectables can substitute conventional and painful drug delivery methods, such as using hypodermic needles, or unreliable methods, such as using microneedles. In this study we explored medical-grade polyester sutures as soft injectables for transdermal drug delivery. Two unique and complementary drug delivery formats were presented. In the first platform, drug loaded sutures provided long term drug release. In the second platform, sutures were used as drug carriers to deliver drug in the skin using a wearable drug-reservoir device. In the first platform, polyester sutures showed appropriate and uniform loading capacity. Controlling the injectables' length allowed for the control of the drug dose released. Also, increasing the area of overlap between the suture and surrounding tissue allowed for the release of more drugs. In the second platform, sutures showed continuous drug delivery using open microfluidic transport of the drug due to capillary action on sutures from the wearable reservoir. The release of rhodamine B dye (model drug) was qualitatively analyzed, and the release of a cancer drug (5-fluorouracil) was quantitatively analyzed. Furthermore, chemotherapeutic soft injectables were explored. They demonstrated biocompatible properties and successful release of 5-fluorouracil within cultured cancer cells environment, resulting in lower cancer cell viability, as expected with increasing injectables' lengths. This study not only showcases a new class of suture-based injectables for dose-controlled drug delivery, but also a new class of long-term continuous drug delivery platforms. Polyester sutures were able to deliver a model drug (rhodamine B dye) continuously for over 2 months. We also demonstrated the integration of drug-carrying sutures with a compact wearable drug reservoir to facilitate long-term, continuous drug delivery. This paper discussed delivery of hydrophillic drugs. In future studies, one could chemically treat the threads to make them hydrophobic, or start with hydrophobic threads, which will enable them to load or carry hydrophobic drugs. This could be basis for future work. Drug carrying sutures can be inserted conveniently using curved surgical needles in a standard stitching procedure.

One could also employ the specialized needle used in thread-lift cosmetic surgeries developed for face-lifts, which literally involve placing a barbed absorbable thread under the skin using a specialized needle or cannula attached to a thread.[28] To improve administration of the drug-delivering sutures into the skin by untrained professionals, we also included a preliminary design of a suture insertion assist device in Appendix G. Such device allows for easy penetration of drug-loaded sutures at precise depths into the skin. See Appendix G figures G.10-G.14 that show the design and the entire process of suture insertion using this device. Most results presented in this paper were conducted either in DES gelatin-based skin model or ex-vivo skin tissue. To further explore this type of drug-delivery platform, experiments will need to be performed in real animal models, especially for month-long continuous delivery. Such experiments could raise new challenges that will be addressed in future work.

F.6 Experimental Section/Methods

Drug-loaded injectable suture fabrication: first, we evaluated the drug-loading capacity of different available thread type: polyester threads, cotton threads, polyester sutures, and Polysorb^{TM} sutures. Specifically, the wet and dry weights of threads were compared. All threads were first plasma treated for 10 minutes. Then, they were weighed before being submerged in deionized (DI) water overnight. The threads are then weighed again after being in water overnight. Difference in weight before and after submerging threads in water is then calculated to obtain loading capacity ($\mu g\ mm^{-1}$).

Visual monitoring of drug release from drug-loaded suture injectables: to elucidate the drug-release mechanism into biological tissue, we visually monitored the diffusion of rhodamine B from a polyester suture based injectable into an agarose gel. A 2-cm polyester suture was plasma treated for 10 minutes then submerged in an aqueous solution of rhodamine B ($1\ mg\ mL^{-1}$)

overnight. The suture was then dried in ambient air for at least 6 hours. Once the suture was dry, it was inserted in an agarose gel (2% w/v agarose in 1X DPBS). Images of the agarose gel were taken at 0, 5, and 10 minutes from inserting the injectable. Furthermore, the release of rhodamine B from an injectable into porcine skin was qualitatively assessed. Two pre-hydrated, 1 cm x 2 cm porcine skin patches were used. On one patch, the dye-loaded polyester suture as injectable was directly in contact with the surface of the skin (no incision). On the other, a horizontal incision was made in the center of the patch in which a injectable was inserted. Images of both patches were obtained prior to the release of the dye and after 30, 60, and 180 seconds of contact. Both patches were then cut through the center of the patch to obtain cross-sectional images.

Dose-controlled release of 5-flurouracil from drug-loaded injectables: we evaluated the total amount of drug released as a function of the length of injectable to demonstrate controlling drug dose by controlling its length. The release profile of 5-FU was obtained by first submerging plasma treated sutures of lengths 0.6 cm, 6 cm, and 60 cm overnight in 4 mg/mL 5-FU solution (in 1X DPBS). The sutures were then dried in ambient air for at least 6 hours. Then, the sutures were submerged in 1X DPBS. UV visible spectroscopy measurements of the solution containing the 5-FU-loaded sutures were obtained at 5, 15, 30, 60, 150, and 240 minutes after submerging the suture in 1X DPBS. It is important, however, to submerge the suture in fresh 1X DPBS after every time point to ensure that drug is not saturated in the solution and that the entire quantity of drug that is loaded gets released. The cumulative amount released is obtained by summing the amount of drug released in the solutions that correspond to the different time points (which is obtained by UV-Vis).

Cancer-cell viability study with chemotherapeutic drug-loaded injectables: we released a cancer drug (5-FU) from sutures into cultured cancer cells (HeLa cells) to demonstrate

biocompatibility and effective, dose-controlled drug release by analyzing cell viability. Loading 5-FU on 2, 3, and 4 cm sutures for cell viability studies follows the aforementioned procedure for obtaining the release profile of 5-FU. However, the sutures are submerged in a 12 mg mL^{-1} aqueous solution of 5-FU instead of 1X DPBS. Once sutures are dry, they were sterilized under UV light for 2 hours then incubated with cultured HeLa cells for 48 hours.

Long-term release in DES gelatin from drug-carrying sutures connected to reservoir: we also monitored long term release profile over weeks from the plasma-treated injectable sutures by connecting it to a drug reservoir. Sutures serve as an open microfluidic channel transporting drug into the skin from capillary action. Gels used in this part of the study are 10 wt. % gelatin in high salt concentration solvent (2:1:1 mol ratio of ethylene glycol:choline chloride:H_2O). This makes for deep eutectic solvent (DES) gel and resembles hydrogels in its physiochemical properties with the benefit that it does not dehydrate readily like a water-based gel.[29-37] For this reason, this DES gelatin gel is better suited to mimic skin to study the drug release than the agarose hydrogel discussed earlier. The DES gelatin-aqueous salt solution was stirred at 85 ^oC until gelatin was completely dissolved and solution was transparent. The solution was then cast into a mold and kept in a 4 ^oC fridge overnight for gel to form and take shape of mold. The physical setup for the reservoir-to-gel delivery experiment is designed to mimic the release of the drug into the skin as follows: an open vial with rhodamine B (drug reservoir), an acrylic disc on top of the vial, a layer of parafilm (skin model) on top of the acrylic disc, a DES gelatin gel on top of the parafilm layer, and a polyester suture as injectable with one end in the dye solution (drug reservoir) and the other in the gel passing through the parafilm and a hole in the center of the acrylic disc (Figure G.3). The injectable suture was plasma treated for 10 minutes then wetted by submerging in DI H_2O for 10 minutes. Then, one end of the suture (attached to a needle) was pushed through the parafilm then the gel. The other end of the suture was submerged in the dye solution. The experimental setup was covered with a transparent box to

minimize the effect of evaporation on the wicking, the dye solution, and the gel. Piercing the gel with the suture is done through the side in contact with the parafilm layer using a needle. The needle and suture are passed through the gel and retrieved on the other side. The needle is detached from the suture and any excess suture that remained outside of the gel was pulled back into the gel by pulling on the suture from the other side. Measurements for this study were based on the change in weight of the dye solution in the vial that serves as a drug reservoir. The weight was converted to volume by measuring the density of the solution. The difference in drug solution volume between time points is attributed mostly to the wicking of dye through the suture and into the gel mimic of skin.

Wearable drug-delivery reservoir: for practical use, a wearable drug-delivery reservoir was 3-D printed that has a hole inlet for refilling the drug on one side and another hole where the injectable suture comes out from and through the skin. A surgical thread-insertion guide was also designed to guide the surgical needle with suture into the skin to the desired depth to which the drugs need to be delivered by the suture. The reservoir part of the device consists of two 3-D printed parts that join and lock with a screw assembly (upper and lower parts). In addition to the screw assembly, an O-ring is placed at the interfacial area where the two parts meet to prevent leakage. Details of the reservoir can be found in Appendix G (Figure G.4-G.9). The suture insertion guide uses the radius of curvature of the needle and keeps the motion of the needle along an arc of a circle. The arc's radius is adjusted to control the penetration depth. The needle guide prevents users or caregivers from accidentally crossing the dermis layer, which would cause pain. Detailed information on the design and the procedure of using the suture insertion guide can be found in Appendix G (Figure G.10 – G.14). To demonstrate drug delivery by sutures using a wearable device, the printed reservoir was filled with an aqueous solution of rhodamine B (1 mg mL^{-1}) and a polyester suture as a soft injectable was secured on the inside of the reservoir on one end of the suture and inserted into a DES gelatin gel serving as skin

mimic on the other. The DES gelatin gel used in this experiment was of the same composition as the ones used in the aforementioned long-term continuous release study. The amount of dye delivered from the reservoir to the gel was based on measuring the increase in gel mass with time. Such increase in mass is attributed to the increased dye content in the gel.

F.7 References

1. Mostafalu, P., et al., *A Textile Dressing for Temporal and Dosage Controlled Drug Delivery.* Advanced Functional Materials, 2017. **27**(41): p. 1-10.
2. Prausnitz, M.R. and R. Langer, *Transdermal drug delivery.* Nature Biotechnology, 2008. **26**(11): p. 1261-1268.
3. Poudel, I., et al., *Vesicular nanocarrier based stimuli-responsive drug delivery systems*. Stimuli-Responsive Nanocarriers. 61-86.
4. Mostafalu, P., et al., *Smart Bandage for Monitoring and Treatment of Chronic Wounds.* Small, 2018. **14**(33): p. 1-9.
5. Hakim, M.L., et al., *Local drug delivery from surgical thread for area-specific anesthesia.* Biomedical Physics & Engineering Express, 2020. **6**(1): p. 015028-015028.
6. Nejad, H.R., et al., *Low-cost and cleanroom-free fabrication of microneedles.* Microsystems & Nanoengineering, 2018. **4**(1).
7. Sadeqi, A., et al. *Cost-effective Fabrication of Chitosan Microneedles for Transdermal Drug Delivery*. in *2018 40th Annual International Conference of the IEEE Engineering in Medicine and Biology Society (EMBC)*. 2018.
8. Sadeqi, A., et al., *Hard polymeric porous microneedles on stretchable substrate for transdermal drug delivery.* Scientific Reports, 2022. **12**(1).

9. Hejri, A., et al., *Subretinal delivery by non-surgical, transscleral injection using a microneedle.* Investigative Ophthalmology & Visual Science, 2023. **64**(8): p. 2625-2625.

10. Choi, Y., et al., *Hepatitis B vaccine delivered by microneedle patch: Immunogenicity in mice and rhesus macaques.* Vaccine, 2023. **41**(24): p. 3663-3672.

11. Hejri, A., et al., *Suprachoroidal Delivery in Rats and Guinea Pigs Using a High-Precision Microneedle Injector.* Translational Vision Science & Technology, 2023. **12**(3): p. 31-31.

12. Romanyuk, A., et al., *Skin Vaccination with Ebola Virus Glycoprotein Using a Polyphosphazene-Based Microneedle Patch Protects Mice against Lethal Challenge.* Journal of Functional Biomaterials, 2022. **14**(1): p. 16.

13. Chen, Q., et al., *Microneedle Patches Loaded with Nanovesicles for Glucose Transporter-Mediated Insulin Delivery.* ACS Nano, 2022. **16**(11): p. 18223-18231.

14. Li, W., et al., *Core-shell microneedle patch for six-month controlled-release contraceptive delivery.* Journal of Controlled Release, 2022. **347**: p. 489-499.

15. Murty, R., et al., *Angled Insertion of Microneedles for Targeted Antigen Delivery to the Epidermis.* Pharmaceutics, 2022. **14**(2): p. 347.

16. Azizoglu, E., O. Ozer, and M.R. Prausnitz, *Fabrication of pure-drug microneedles for delivery of montelukast sodium.* Drug Delivery and Translational Research, 2022. **12**(2): p. 444-458.

17. Xia, D., et al., *An ultra-low-cost electroporator with microneedle electrodes (ePatch) for SARS-CoV-2 vaccination.* Proceedings of the National Academy of Sciences, 2021. **118**(45): p. e2110817118.

18. Li, S., D. Xia, and M.R. Prausnitz, *Efficient Drug Delivery into Skin Using a Biphasic Dissolvable Microneedle Patch with Water-Insoluble Backing.* Advanced Functional Materials, 2021. **31**(44): p. 2103359.

19. Gomaa, Y., et al., *Development of a thermostable oxytocin microneedle patch.* Journal of Controlled Release, 2021. **337**: p. 81-89.

20. Tran, K.T.M., et al., *Transdermal microneedles for the programmable burst release of multiple vaccine payloads.* Nature Biomedical Engineering, 2020. **5**(9): p. 998-1007.

21. Lee, J.H., *Injectable hydrogels delivering therapeutic agents for disease treatment and tissue engineering.* Biomaterials Research, 2018. **22**(1): p. 27.

22. Kiaee, G., et al., *A pH-Mediated Electronic Wound Dressing for Controlled Drug Delivery.* Advanced Healthcare Materials, 2018. **7**(18): p. 1-8.

23. Sonkusale, S. and P. Mostafalu, *Thread-based integrated functional devices*, in *U.S. Patent Application No. 15/749,207*.

24. Tan, W., et al., *Go with the capillary flow. Simple thread-based microfluidics.* Sensors and Actuators, B: Chemical, 2021. **334**(February): p. 129670-129670.

25. Nejad, H.R., A. Sadeqi, and S. Sonkusale. *Thread as a Precise Sampling and Delivery Platform for Implantable or Ingestible Applications*. 2020. The 24th International Conference on Miniaturized Systems for Chemistry and Life Sciences (μTAS 2020).

26. Longley, D.B., D.P. Harkin, and P.G. Johnston, *5-FLUOROURACIL: MECHANISMS OF ACTION AND CLINICAL STRATEGIES.* 2003.

27. Yang, B., et al., *Bilayer dissolving microneedle array containing 5-fluorouracil and triamcinolone with biphasic release profile for hypertrophic scar therapy.* Bioactive Materials, 2021. **6**(8): p. 2400-2411.

28. Halepas, S., X.J. Chen, and E.M. Ferneini, *Thread-Lift Sutures: Anatomy, Technique, and Review of Current Literature.* Journal of Oral and Maxillofacial Surgery, 2020. **78**(5): p. 813-820.

29. Owyeung, R.E., S.R. Sonkusale, and M.J. Panzer, *Influence of Hydrogen Bond Donor Identity and Intentional Water Addition on the Properties of Gelatin-Supported Deep Eutectic Solvent Gels.* Journal of Physical Chemistry B, 2020. **124**(28): p. 5986-5992.

30. Owyeung, R.E., et al., *Highly Flexible Transistor Threads for All-Thread Based Integrated Circuits and Multiplexed Diagnostics.* ACS Applied Materials and Interfaces, 2019. **11**(34): p. 31096-31104.

31. Qin, H., et al., *Highly stretchable and nonvolatile gelatin-supported deep eutectic solvent gel electrolyte-based ionic skins for strain and pressure sensing.* Journal of Materials Chemistry C, 2019. **7**(3): p. 601-608.

32. Rachel, et al., *Free form three dimensional integrated circuits and wearables on a thread using organic eutectogel gated electrochemical transistors.* arXiv pre-print server, 2023.

33. Rachel, O., et al. *Microrheology of gel electrolyte biomaterials based on deep eutectic solvents*. in *Proc.SPIE*. 2020.

34. Owyeung, R.E., S. Sonkusale, and M.J. Panzer, *Opportunities for ionic liquid/ionogel gating of emerging transistor architectures.* Journal of Vacuum Science & Technology B, 2020. **39**(1): p. 011001.

35. Kumar, T., R.E. Owyeung, and S.R. Sonkusale, *Rapid cleanroom-free fabrication of thread based transistors using three-dimensional stencil-based patterning.* Flexible and Printed Electronics, 2021. **6**(1): p. 015007.

36. Owyeung, R., W. Zeng, and S. Sonkusale. *Eutectogel Electrodes for Long-Term Biosignal Monitoring*. in *2022 IEEE Sensors*. 2022.

37. Panzer, M.J., *Holding it together: noncovalent cross-linking strategies for ionogels and eutectogels.* Materials Advances, 2022. **3**(21): p. 7709-7725.

Appendix G: Supplementary Information Concerning Appendix F

This appendix is reproduced form the following publication:

Alsaedi, M. K., Lone, O., Nejad, H. R., Das, R., Owyeung, R. E., Del-Rio-Ruiz, R., Sonkusale, S., Soft Injectable Sutures for Dose-Controlled and Continuous Drug Delivery, *Macromolecular Bioscience*, **2024**, *24*(3), 2300365

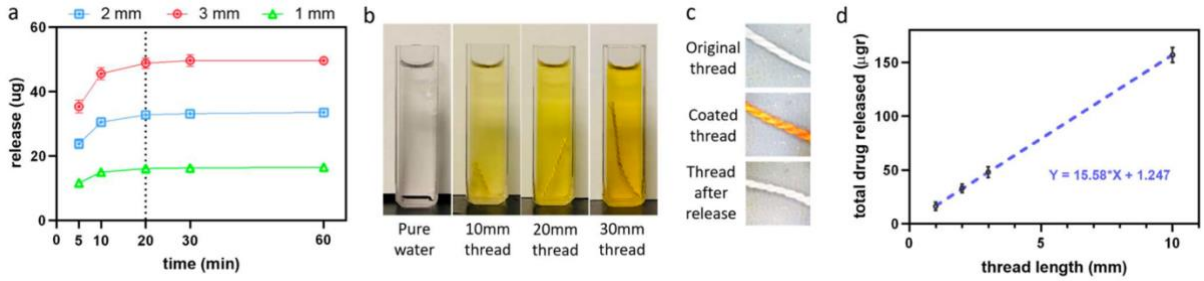


Figure G.1. a) Release profile of cresol red dye (drug model) from polystyrene threads of different lengths, b) qualitative assessment of total drug released from polystyrene threads of different lengths, c) color of thread before coating, after coating, and after dye release, d) correlation between total drug released and different length of the thread. This figure was previously published by members of our group as part of a conference paper (H.R. Nejad, A. Sadeqi, and S. Sonkusale, The 24th International Conference on Miniaturized Systems for Chemistry and Life Sciences (µTAS 2020).[25]

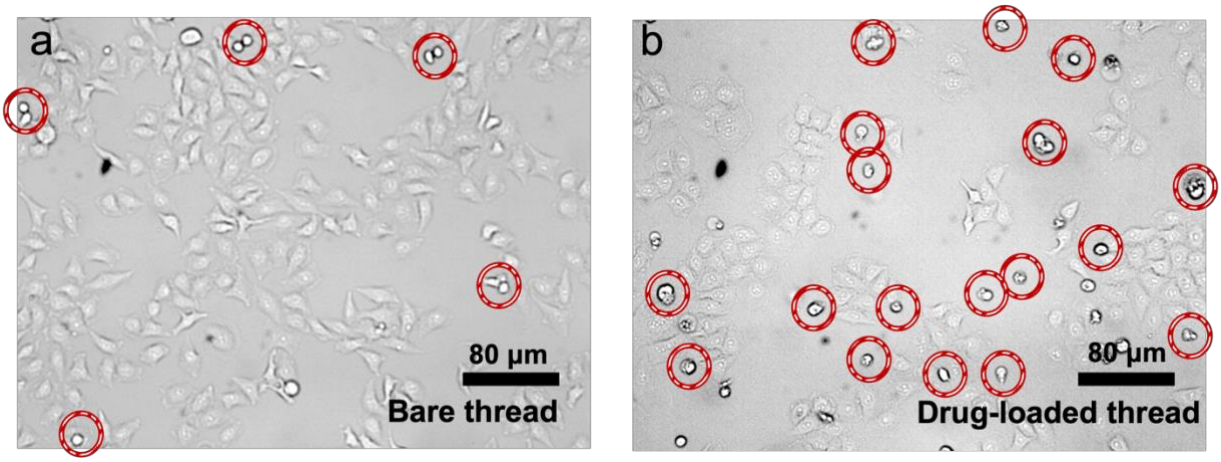


Figure G.2. Microscopic images of cultured HeLa cells (dead cells circled in red) after 48 hours of incubation with a) a bare polyester suture and b) a drug-loaded suture.

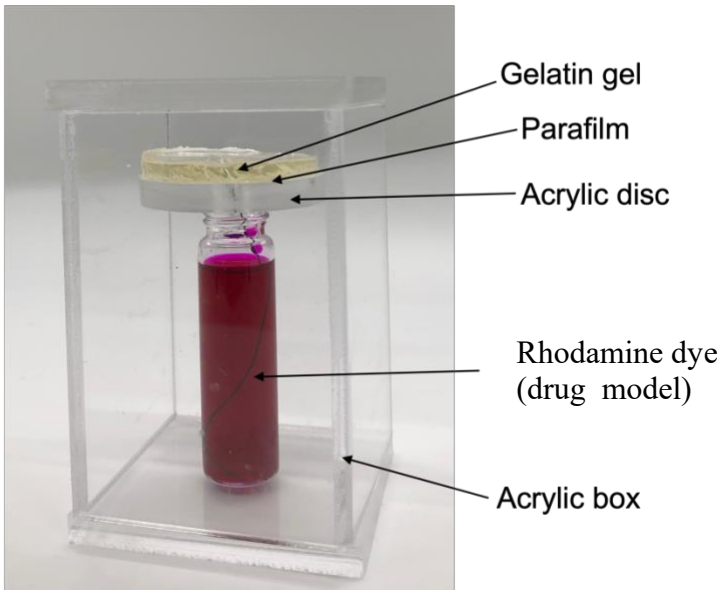


Figure G.3. Experimental setup for long-term continuous delivery. Gelatin gel and parafilm constistute a skin tissue model. Acrylic disc offers physical support. Acrylic box prevents evaporation and contamination.

G.1. Drug-carrying reservoir design:

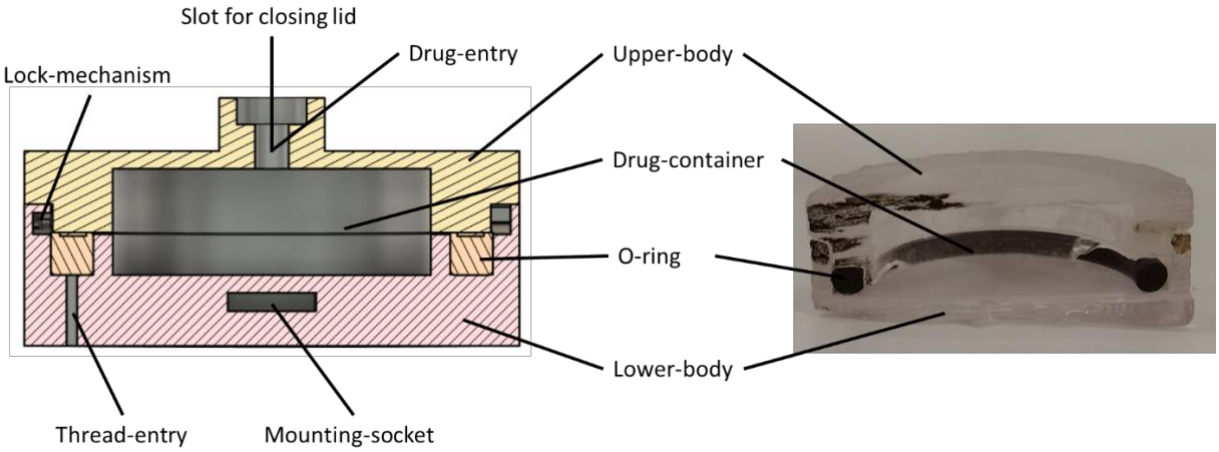


Figure G.4. Cross-section photos of the reservoir design (left) and the 3-D printed reservoir (right). Left image breakdown: yellow is the top part, pink is the lower part, and orange is the O-ring.

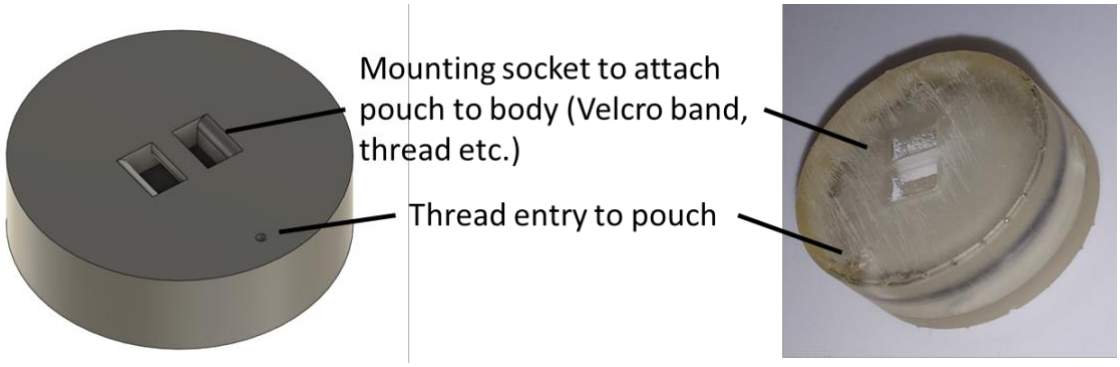


Figure G.5. Design of (left) and 3-D printed socket (right) in which the lower part of the reservoir is placed to facilitate wearing the device. For example, inserting a velcro strap will allow for wrapping the reservoir around the arm as shown in Figure F.1.

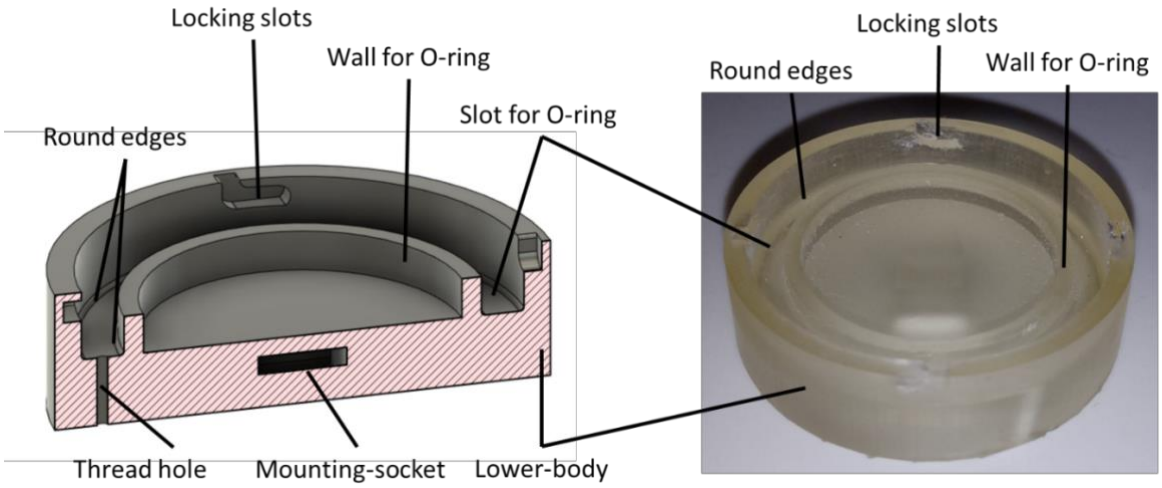


Figure G.6. Design cross-section of (left) and 3-D printed (right) lower part of the reservoir.

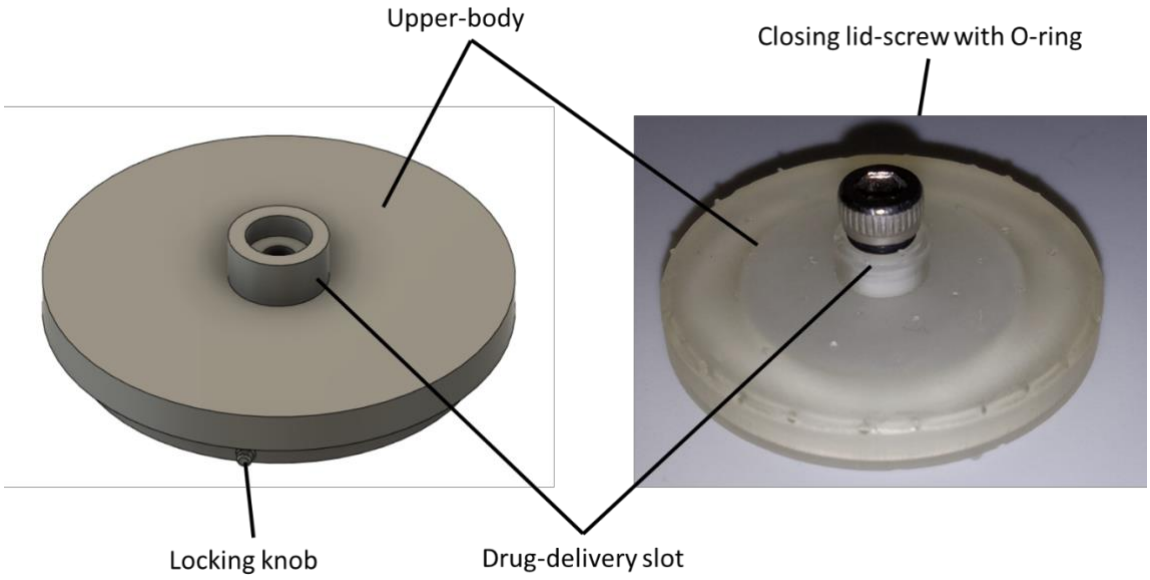


Figure G.7. Design of (left) and 3-D printed upper part of the device. The locking knob locks the reservoir by sliding in the locking slots in the lower part (visible in Fig. G.6). The closing lid can be opened to refill the reservoir with desired drug.

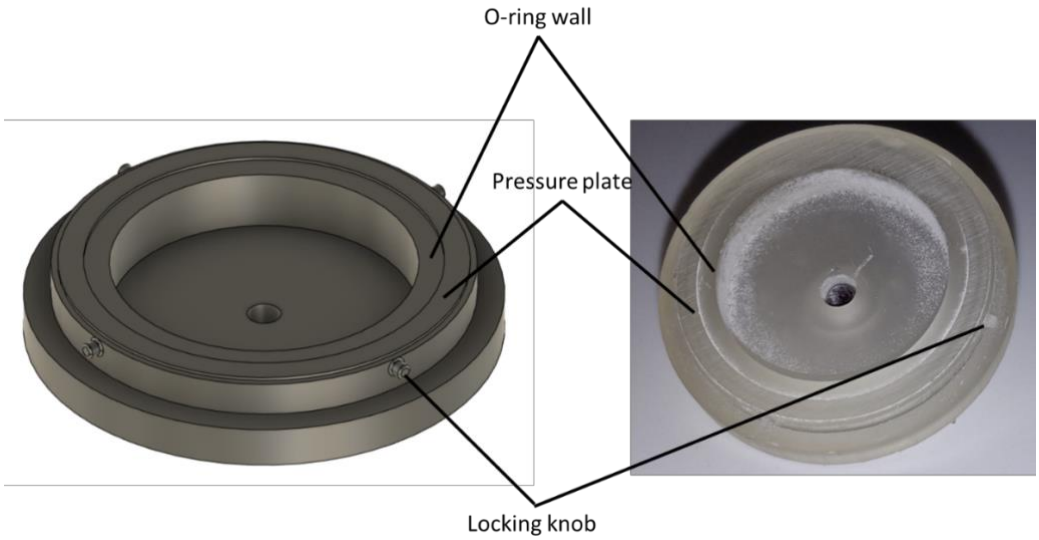


Figure G.8. Design of (left) and 3D-printed part that goes into the inside of the upper part (Fig. G.7) that gets in contact with the lower part and holds the O-ring from the top.

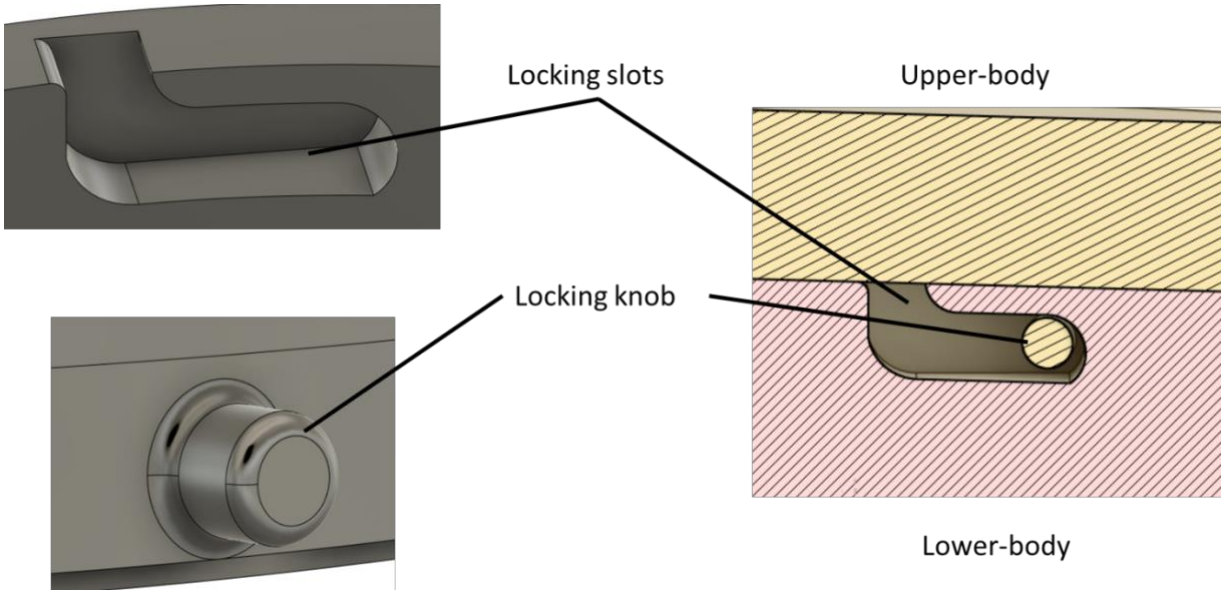


Figure G.9. Locking knobs and slots that keep the reservoir sealed. The knobs slide into the slots by physically rotating the top and bottom part in opposite angular directions. This locks the reservoir in place.

G.2. Needle Insertion Assist Device:

The following figures (Figure G.10-G.14) discuss a suture-insertion assist device to help caregivers to administer the suture-based injectable into the skin at any desired depth. The assist device consists of a holder for the curved needle held at a programmed distance (level) from the skin (Fig. G.10-G.12). This distance level can be adjusted to dictate the depth of insertion. Simple rotation of the assembly automatically inserts the needle and the suture into the skin (Fig. G.14) – the depth dictating the extent of penetration of drug carrying suture into the skin. When connected to the wearable reservoir (Fig. G.14 and Fig F.1(b) and (d)), the entire platform will provide a convenient administration of long-term drug delivery.

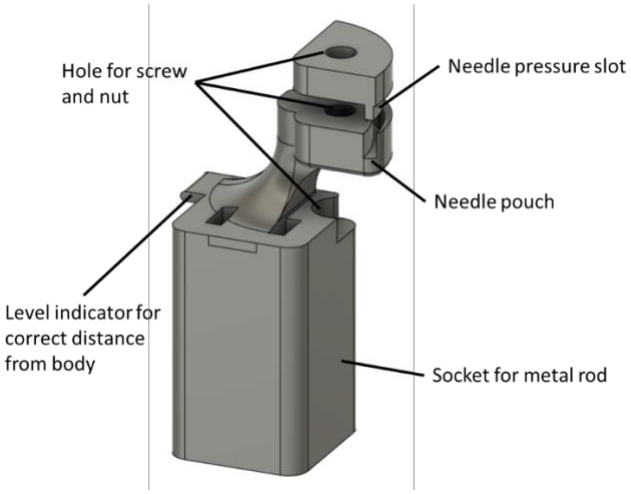


Figure G.10. Design of the needle guide placed upright for clarity. The surface facing the skin is on the left.

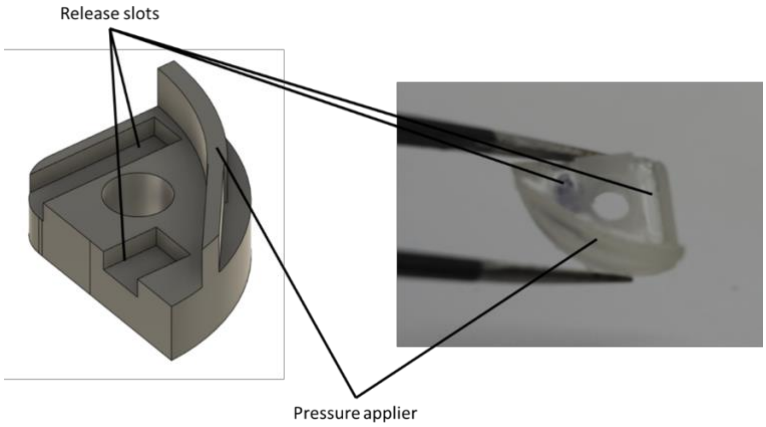


Figure G.11. A close-up of the needle holding compartment in the needle guide.

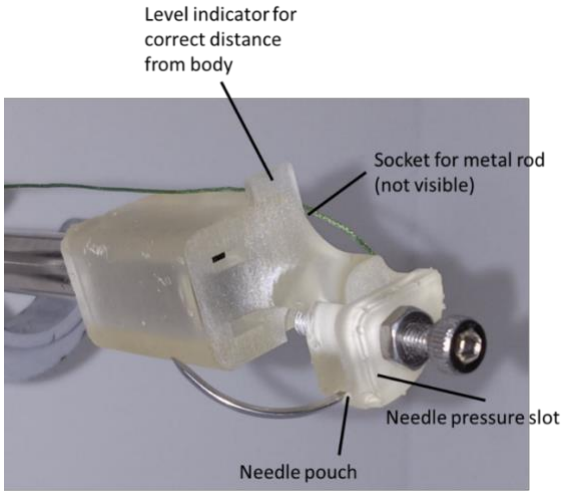


Figure G.12. 3-D printed needle guide with a suture (green) and a curved needle.

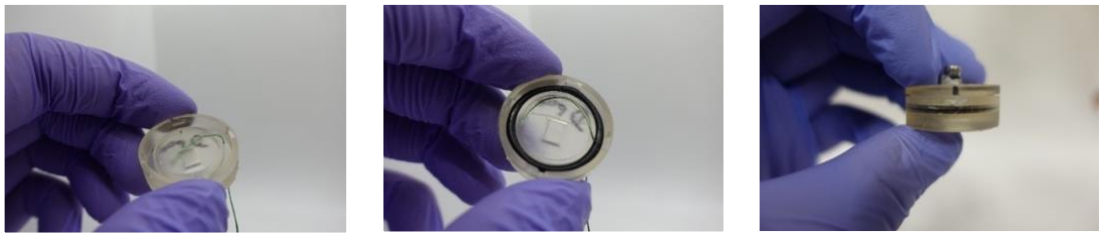


Figure G.13. Reservoir assembly (left to right): Insert the none-needle suture end into the reservoir through the thread hole. Place and press the O-ring into the designated slot while ensuring the thread end is inside the inner wall. Close the reservoir. Then press and turn the upper part to lock and seal the reservoir.



Figure G.14. Procedure to administer the drug carrying suture using the Assist device: Using needle guide and piercing through skin (top left to bottom right): Place the needle in the needle guide and screw the bolt such that the needle is fixated. Place the needle guide at the correct height. Use the built-in skin level for a skin depth of 1 mm. Rotate the needle guide for the needle to pierce the skin. Once the needle resurfaces, unscrew the bolt and lift the upper lid with a pair of tweezers (use the release slots to slide the tweezers in). The needle should now be free from the guide and can be grabbed with a needle holder and pulled. Pull the thread to the end such that there is no gap between the reservoir and the skin. The leftover thread can be cut, and the incision can be closed with a bandage. On the reservoir, the lid can be unscrewed, and, with a Teflon Filter, the reservoir can be filled with the desired drug. After filling, screw the lid back on.